

**Alma Mater Studiorum – Università di Bologna**

**DOTTORATO DI RICERCA IN**

**CHIMICA**

**Ciclo XXIX**

**Settore Concorsuale di afferenza: 03/B1**

**Settore Scientifico disciplinare: CHIM/03**

**PHOTOACTIVE MOLECULES IN SUPRAMOLECULAR  
ARCHITECTURES AND PHOTOREDOX REACTIONS**

**Presentata da: Marianna Marchini**

**Coordinatore Dottorato**

**Prof. Aldo Roda**

**Relatore**

**Prof. Paola Ceroni**

**Esame finale anno 2017**



*“La scienza è il capitano, e la pratica sono i soldati.*

*Studia prima la scienza, e poi séguita la pratica, nata da essa scienza.*

*Quelli che s’innamoran di pratica senza scienza son come ’l nocchier ch’entra in navilio senza timone o bussola, che mai ha certezza dove si vada.”*

Leonardo Da Vinci in *L’uomo e la natura*





# Abstract

My PhD research activity was mainly focused on two different fields: the study of the formation of supramolecular architectures and the investigation of the photophysical behaviour of different photocatalysts in organic reactions.

The first supramolecular system shown in this thesis derives from a shape-persistent molecule, featuring four bipyridinium units, that upon reduction undergoes intermolecular pimerization because of the rigid architecture of the molecule. The pimerization process has been investigated by a variety of techniques, like electrochemistry, absorption measurements, electronic paramagnetic resonance (EPR), gamma and pulse radiolysis, and compared with the behavior of a model compound, one of the four identical subunits of the tetramer. We demonstrated that there is an increase of the apparent pimerization constant by increasing the concentration of reduced bipyridinium units, due to the fact that pimerization is favored in the tetrahedrally shaped molecule because of a cooperative mechanism.

The same tetramer, with non-methylated bipyridium units, is able to form a supramolecular architecture upon complexation with four ruthenium porphyrins: the resulting multichromophoric system features a shape-persistent arrangement of the chromophores. The system was fully characterized from the photophysical point of view: when the supramolecular system is formed, the quenching of both the tetramer's fluorescence and porphyrin's phosphorescence occurs. We hypothesize the presence of a CT state energetically located under the triplet state of the porphyrin, and an electron transfer could occur from the lowest singlet and the lowest triplet of the tetramer and porphyrin, respectively. Finally, the crystal structure of the assembly was resolved.

During my PhD, I spent four months at the ETH, in Zurich, working in the group of Prof. Schlüter. Throughout my stay, I worked on the design, synthesis and characterization of a 2D polymer obtained at the air-water interface with Langmuir-Blodgett technique. The monomer used had a porphyrin core, bipyridine moieties (necessary for the metal complexation with Ni(II) and formation of polymeric structure) and hydrophilic chains (that should

force the monomer to a planar conformation). The films obtained were then characterized with atomic force microscopy, scanning electron microscopy and UV-Vis measurements.

In the field of photocatalysis, I studied four photoredox reactions, two of them photocatalyzed by a metal complex, and the other two by an organic chromophore.

The first photoredox reaction studied provides an efficient access to indole 2- and 3-carboxylates in a single step (with good yields under mild reaction conditions), i.e. the direct photocatalytic carboxylation with  $\text{CBr}_4/\text{MeOH}$ , visible light and  $[\text{Ru}(\text{bpy})_3](\text{PF}_6)_2$  as photocatalyst.

In the second reaction, the complex  $[\text{Fe}(\text{bpy})_3]\text{Br}_2$  is involved in the enantioselective organocatalytic photoredox alkylation of aldehydes with various  $\alpha$ -bromo carbonyl compounds, in presence of visible light. The idea was to replace the rare and expensive  $[\text{Ru}(\text{bpy})_3]^{2+}$  complex, already used as photocatalyst in the same reaction by MacMillan and co-workers, with the abundant and cheap iron complex, with the results of high reaction yields of isolated compounds and enantioselectivities.

Then, we moved toward the use of organic dyes as photocatalysts. We found that an iodo-boron-dipyrromethene (iodo-**BODIPY**) dye derivative is able to promote the atom-transfer radical addition (ATRA) between bromoderivatives and alkenes, using ascorbate as sacrificial reductant. This finding expands the possibility to use **BODIPY** dyes to promote photocatalytic reactions in efficient ways.

Finally, we investigated the mechanism of the reduction of aryl halides promoted by a two-photon mechanism by perylene-3,4,9,10-tetracarboxylic diimide derivative: this reaction mechanism was proposed by König and co-workers in 2014, but we found out that the hypothesis of two-photon mechanism was incorrect, since during the irradiation, a degradation of the photocatalyst occurred, and the photoproduct obtained was the photoactive species in the reaction.

# Contents

<b>1</b>	<b>Supramolecular Chemistry</b>	<b>9</b>
1.1	Viologen Based Supramolecular Structures . . . . .	14
1.1.1	Supramolecular Structures Driven by Pimerization of Tetrahedrally Arranged Bipyridinium Units . . . . .	16
1.2	Ruthenium Porphyrin Based Supramolecular Assemblies . . .	41
1.2.1	Tetrahedral Array of Ruthenium Porphyrins with Bipyri- dinium Based Tetramer . . . . .	43
1.3	2D Polymer at the Air/Water Interface . . . . .	60
1.3.1	Towards 2D Polymer with Porphyrin Based Monomer at the Air/Water Interface . . . . .	64
<b>2</b>	<b>Photoredox Reactions</b>	<b>75</b>
2.1	Visible Light Photoredox Catalysis with Metal Complexes . .	81
2.1.1	Visible-Light-Induced Direct Photocatalytic Carboxyla- tion of Indoles with $\text{CBr}_4/\text{MeOH}$ and $[\text{Ru}(\text{bpy})_3](\text{PF}_6)_2$ as Photocatalyst . . . . .	84
2.1.2	Organocatalytic Enantioselective Alkylation of Aldehy- des with $[\text{Fe}(\text{bpy})_3]\text{Br}_2$ Catalyst and Visible Light . . .	93
2.2	Visible Light Photoredox Catalysis with Organic Dyes . . . . .	105
2.2.1	Photocatalytic ATRA Reaction Promoted by Iodo-Bodipy and Sodium Ascorbate . . . . .	119
2.2.2	A Photochemical View on the Two-photon Mechanism of Reduction of Aryl Halides in the Presence of Perylenedi- imide Photocatalyst. . . . .	128
<b>A</b>	<b>Basic Photophysical and Electrochemical Techniques</b>	<b>143</b>
<b>B</b>	<b>Microscopy and Langmuir-Blodgett Techniques</b>	<b>151</b>
<b>C</b>	<b>Methods of Ionizing Radiation Generation and Electron Paramag- netic Resonance</b>	<b>155</b>
<b>D</b>	<b>Permissions</b>	<b>159</b>



*To M&M's, my strength.*



# A Brief History of Light

*“To perform my late promise to you, I shall without further ceremony acquaint you, that in the beginning of the Year 1666 I procured me a Triangular glass-Prisme, to try therewith the celebrated Phaenomena of Colours. And in order thereto having darkened my chamber, and made a small hole in my window-shuts, to let in a convenient quantity of the Suns light, I placed my Prisme at his entrance, that it might be thereby refracted to the opposite wall. It was at first a very pleasing divertisement, to view the vivid and intense colours produced thereby.”*<sup>1</sup> With these words, Isaac Newton in the 1671-72 started off his famous letter to the Royal Society publisher about his new theory about light and colours. He wanted to disprove French natural philosopher Rene Descartes’ theory of light. Indeed Descartes believed that an invisible substance, which he called the plenum, permeated the universe. Much like Aristotle, Descartes believed that light was a perturbation of the plenum, like a wave that travels through water.

Newton, with his famous experiment described in the letter, observed that when a beam of white light strikes a prism with a particular angle, a beam’s portion is reflected while the remainder passes through the prism surface and comes out broken down in different colour. He supposed that light is composed of coloured particles (corpuscular theory), that combine to appear white, and each colour moves with a different speed: the consequence is that each colour undergoes refraction in a different way, changing trajectory and coming out separate from the others. He divided the spectrum (Newton used this term the first time in print in 1671, describing his experiments in optics) in seven different colours: red, orange, yellow, green, blue, indigo and violet. He choose seven colours not for scientific reason, but out of a belief, derived from the ancient Greek sophists, of there being a connection between the colours, the known objects in the solar system, and the days of the week. Newton’s theory remained in force for more than 100 years. When the corpuscular theory failed to adequately explain the diffraction, interference, and polarization of light it was abandoned in favour of Huygens’ wave theory. Indeed the 1690, the Dutch mathematician, astronomer and physicist Christiaan Huygens assumed the existence of some invisible medium (luminiferous aether) filling all empty space between objects. He

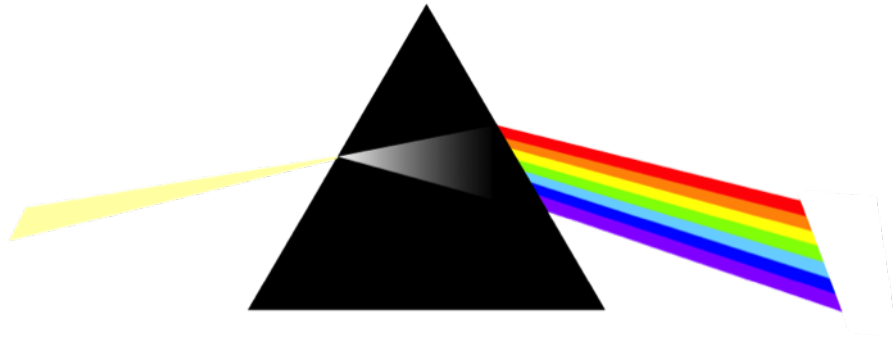


FIGURE 1: Schematic representation of Newton's crucial experiment.

further speculated that light forms when a luminous body causes a series of waves or vibrations in this aether. Those waves then advance forward until they encounter an object. If that object is an eye, the waves stimulate vision. This wave theory of light was first communicated in 1678 to the *Paris Académie des Sciences* and published in 1690 in his *Traité de la lumière*, making it the first mathematical theory of light.<sup>2</sup> Another important discovery dates back to 1800. Sir William Herschel, a British astronomer and composer of German origin, wanted to know how much heat was passed through the different coloured filters he used to observe sunlight. He had noted that filters of different colours seemed to pass different amounts of heat. Herschel thought that the colours themselves might be of varying temperatures and so he devised a clever experiment to investigate his hypothesis. He directed sunlight through a glass prism to create a spectrum and then measured the temperature of each colour, placing a thermometer in a visible colour while other two were placed beyond the spectrum as control samples. As he measured the individual temperatures of the each visible colour, he noticed that all the colours had temperatures higher than the controls. In addition, he found that the temperatures of the colours increased from the violet to the red part of the spectrum. That's why he decided to measure the temperature just beyond the red portion (the colour with higher temperature) of the spectrum, in a region where no sunlight was visible. This region had the highest temperature of all: he had discovered the infrared radiation. A year later, in 1801, Johann Wilhelm Ritter, a German chemist, physicist and philosopher, discovered ultraviolet light. He was working with silver chloride, a salt that turns black when exposed to sunlight. He knew that exposure to blue light caused a greater reaction in silver chloride than exposure to red light. Therefore, he decided to measure the rate at which silver chloride reacted when



---

exposed to different colours of light. With a glass prism he created a spectrum and he placed silver chloride in front of each colour of the spectrum, and he observed that the salt increasingly darkened toward the violet end of the spectrum. Similarly to what Herschel had done, he placed silver chloride in the area just beyond the violet of the sunlight spectrum, in a region where no light was visible. In that condition, the silver chloride displayed an intense reaction: this showed that an invisible form of light, which Ritter called "*Chemical Rays*", existed beyond the violet end of the spectrum.

In the XIX century, the introduction of Maxwell's equations gave to the world one of the most fundamental pieces of scientific research ever undertaken, that played a key role in the formulation and the development of Einstein's special theory of relativity: light is an electromagnetic wave; the visible light is just a tiny part of the whole electromagnetic spectrum. The development of the theory took place starting from basic experimental observations, and leading to the formulations of numerous mathematical equations, notably by Charles-Augustin de Coulomb, Hans Christian Ørsted, Carl Friedrich Gauss, Jean-Baptiste Biot, Félix Savart, André-Marie Ampère, and Michael Faraday. Indeed, in 1847 Michael Faraday suggested light is a high-frequency electromagnetic vibration, which can propagate even in the absence of a medium such as the aether. Faraday had an amazing physical intuition that guided him through his experiments to successfully create a nearly complete model of electromagnetic phenomena. Since he was not at all a mathematician, he was only able to describe this model in words and did not unify his results into a theory. However, his work inspired James C. Maxwell, who discovered that self-propagating electromagnetic waves travel through space at a constant speed, which is equal to the previously measured speed of light. From this, Maxwell in 1862 concluded that light was a form of electromagnetic radiation and in 1873 he published *A Treatise on Electricity and Magnetism*,<sup>3</sup> which contained a full mathematical description of the behavior of electric and magnetic fields, still known as Maxwell's equations. He was actually able to translate Faraday's ideas into mathematics, with vectors that describe the main players of electromagnetism. To understand how Maxwell developed his theory, is necessary to analyze three fundamental papers, published between 1856 and 1864. In the first paper "*On Faraday's Lines of Force*"<sup>4</sup> (in two parts, presented to the Cambridge Society, the 10<sup>th</sup> of December 1855 and the 11<sup>th</sup> of February 1856) he introduced the flow lines of which could be taken as a geometrical representation of the electric or magnetic field, or the current flow. In his next paper "*On Physical Lines of Force*"<sup>5</sup> (in four parts

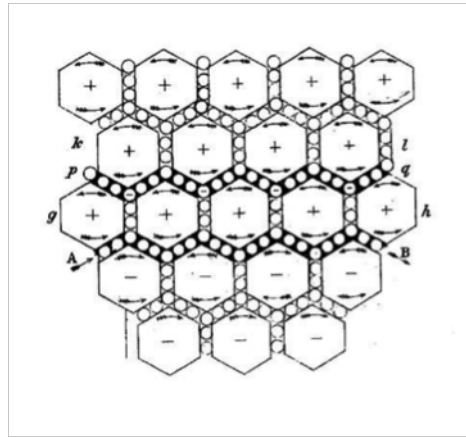


FIGURE 2: Schematic representation of “vortices” drawn by Maxwell in the paper *On physical lines of force* (1861).

1861-1862), he incorporated the known rotational properties of the magnetic field into his model, introducing his famous “vortices”. He imagined the magnetic field as a consequence of vortices whose speed was proportional to the magnetic field itself. The orientation of the magnetic field was given by the vortices’ axis direction. He postulated that the vortices rotate in parallel in opposite direction (figure 2): to allow that, he introduced spheres that rotate, without slithering, with the same speed, avoiding slipping. With a mathematical analysis, he was able to demonstrate the relation between the rotation speed of the vortices (the magnetic field) and the speed whereby the spheres move (how many spheres cross the surface in unit time). Considering the motion of the spheres as electric current, he obtained the Ampère’s circuital law. Later on, he supposed to perturbate the system, and since it was free to evolve, he observed what happened after the perturbation. The vortices are elastic, so they tend to move to equilibrium position. The movement of the spheres produces a magnetic field: this means that displacement currents bring out magnetic effects. He calculated the propagation speed of perturbation and the value he obtained was rather close to the experimentally accepted value of the speed of light. At this stage he declared that light was an electromagnetic phenomenon. In the third paper, *A Dynamical Theory of the Electromagnetic Field*<sup>6</sup> (presented to Royal Society the 8<sup>th</sup> of December 1864 and published an year later), Maxwell attempted to remove from his theory some of the appeals to models and analogies and to lay out a coherent mathematical theory of electromagnetism and an electromagnetic theory of light. He developed also the four famous equations, written in differential

form as followed:

$$\nabla \cdot \mathbf{E} = \frac{\rho}{\epsilon_0} \quad (1)$$

$$\nabla \cdot \mathbf{B} = 0 \quad (2)$$

$$\nabla \times \mathbf{E} = -\frac{\partial \mathbf{B}}{\partial t} \quad (3)$$

$$\nabla \times \mathbf{B} = \mu_0 \left( \mathbf{J} + \epsilon_0 \frac{\partial \mathbf{E}}{\partial t} \right) \quad (4)$$

At the end of XIX, the gap between theoretical prediction and experimental evidences challenged the classical physics, especially when “light” was considered. An idealised model that was considered is the blackbody at thermal equilibrium, an object which absorbs all incident radiation and then emits all this energy again. We can think of the radiating energy as standing waves inside our blackbody cavity. The energy of the radiating waves at a given frequency  $\nu$ , should be proportional to the number of modes at this frequency. Classical physics states that all these modes have the same energy  $kT$  and as the number of modes is proportional to  $\nu^2$ :

$$E \propto \nu^2 kT \quad (5)$$

This implies that we would expect most of the energy at higher frequency, and this energy diverges with frequency. By calculating the total amount of radiated energy, (i.e., the sum of emissions in all frequency ranges), it can be shown that a blackbody would release an infinite amount of energy, contradicting the principles of conservation of energy and indicating that a new model for the behaviour of blackbodies was needed. This paradox was called the “*ultraviolet catastrophe*”. Max Planck, the famous German theoretical physicist, trying to explain the blackbody radiation problem, gave birth to the “Quantum Theory”. Indeed, Planck derived the correct form for the intensity spectral distribution function by making some strange (for the time) assumptions. He realized that light and other electromagnetic waves were emitted in discrete packets of energy, that he called “*quanta*”, which could only take on certain discrete values. Although, quantization was a purely formal assumption in Planck’s work at this time, it’s necessary to wait Albert Einstein’s interpretations in 1905 to fully understand its radical implications. Indeed Einstein was the first scientist who realize that light was made up of photons to explain of the so-called “photoelectric effect”.<sup>7</sup> The name *photon* would have been coined later, by Gilbert Lewis, in an article published in 1926.<sup>8</sup> He wrote “*We are dealing here with a new type of atom, an identifiable*

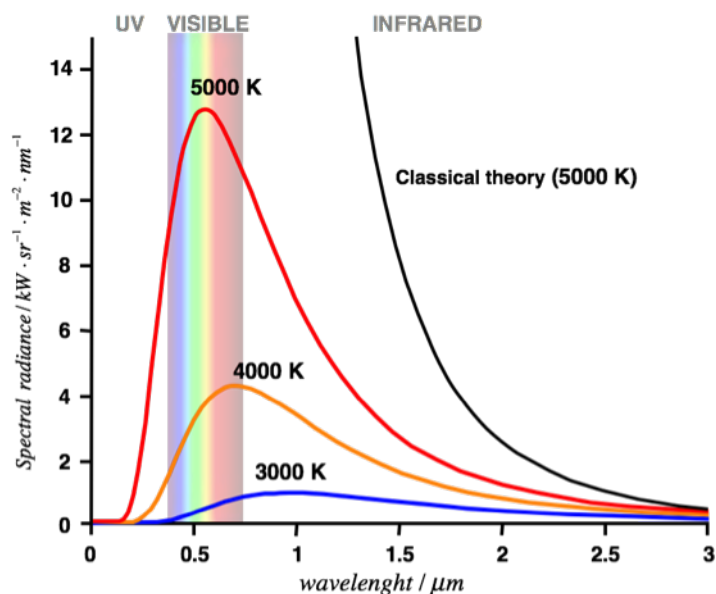


FIGURE 3: Blackbody radiation curves showing peak wavelengths at various temperatures: Planck's law (coloured curves) accurately described blackbody radiation and resolved the ultraviolet catastrophe derived from a classical treatment (black curve).

*entity, uncreatable and indestructable, which acts as the carrier of radiant energy and, after absorption, persist as an essential constituent of the absorbing atom until it is later sent out again bearing a new amount of Energy", and he continues "it would cause confusion to call it merely a quantum [...] I therefore take the liberty of proposing for this hypothetical new atom, which is not light but plays an essential part in every process of radiation, the name photon."* The concept of a photon allowed photochemistry to emerge from its empirical stage. When it was clear that absorption of light corresponds to the capture of a photon by an atom or a molecule, Johannes Stark and Albert Einstein between 1908 and 1913 independently formulated the photoequivalence law, which is nowadays described in the first chapter of any photochemistry book. I'll end this brief "History of light" mentioning the brilliant contribute given in 1933 by the Polish physicist Aleksander Jabłoński. He was a pioneer of molecular photo-physics, creating the concept of the "luminescent centre" and his own theories of concentrational quenching and depolarization of photoluminescence. In 1933 he published a paper in which he proposed a metastable electronic state for the long-lived emission of some dyes. In other words, he described the phosphorescence mechanism and illustrated schematically, with the classical diagram that nowadays we commonly use, the absorption and emission of light. "We can assume therefore that in such molecules there must be at least one

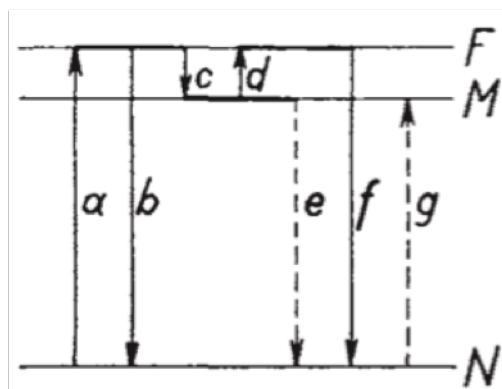


FIGURE 4: Jabłoński diagram of a generic dye, taken from the Nature paper 1933.

*metastable energy level M, situated lower than the level F reached immediately after absorption. From the state F the molecules can pass either to a normal state N, emitting the band FN (fluorescence), or to the metastable state M. The probability of the transition M-N is very small. Therefore when the temperature is sufficiently high, a great majority of molecules will be raised thermally from the level M to F and will be able to emit the band F-N (phosphorescence at room temperature). At low temperatures, direct transitions M-N take place." At the beginning, this diagram was discredited,<sup>9</sup> but to understand how important and innovative it became, still indispensable nowadays to illustrate the electronic states of a molecule and the transitions between them, I'll mention Lewis' words about it, published in 1941: "This simple scheme of Jabłoński has been criticized on several grounds by Pringsheim and Vogels. In their experiments on tryptaflavine in silica gel the phosphorescence phenomena cannot be explained without assuming more than one phosphorescent state. Their experiments do not show whether these two states are excited by the same frequency. In our experiments on crystal violet dissolved in glucose we have found two phosphorescent states, but one is produced by blue light, the other by orange. It seems to us that the scheme of Jabłoński is sufficiently flexible to take care of such complexities as they arise."<sup>10</sup>*



## Chapter 1

# Supramolecular Chemistry

Supramolecular Chemistry, the chemistry of intermolecular bond or the “chemistry beyond the molecule”, involves the investigation of the structures and functions of complex systems formed by molecular units bonded via non-covalent interactions. Such a definition can be extended to a system containing covalently-linked components which satisfy specific conditions: when the intrinsic properties of molecular subunits can be easily identify, it is possible to consider a system with covalently-linked components a supramolecular structure. Supramolecular systems should not be confused with large molecules, but the distinction between them is not straightforward. In a supramolecular system, the essential properties of each component can be known from the study of the separated components (or of suitable model molecules), while in a large molecules, upon fragmentation, the components will completely lose their chemical identity. The degree of interaction be-

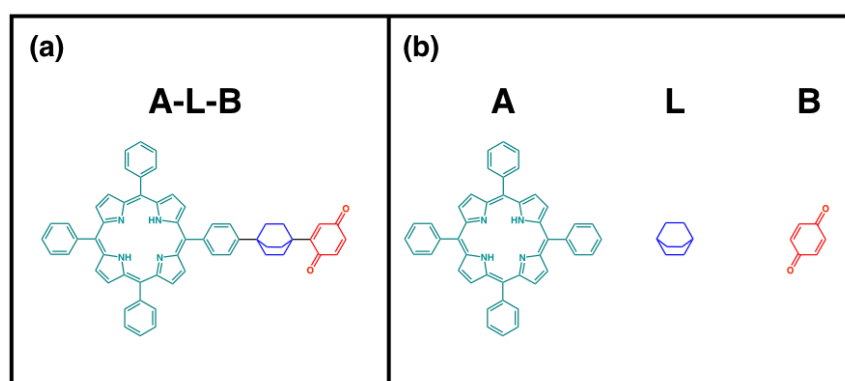


FIGURE 1.1: Covalently linked supramolecule (a) and its molecular components (b).

tween the electronic subsystems of the component units is the key to define a “supramolecule” or “large molecule”: provided that this interaction is small with respect to other energy parameters, any multicomponent system

approaches the ideal concept of a supramolecule. The non-covalent interactions that may be involved in the formation of supramolecular architectures are electrostatic forces (dipole-dipole or ion-dipole), hydrogen bonding, metal coordination, van der Waals and  $\pi$ - $\pi$  interactions. These molecular interactions are weak, but if there is cooperation between them, the molecular association will be efficient. One of the goals in supramolecular chemistry is to design the system in order to obtain the right combination of intermolecular interactions between individual components. The study of how non-covalent forces can lead to the association of two or more molecules is the embodiment of supramolecular chemistry. Most non-covalent interactions are relatively weak (figure 1.3) and form and break without significant activation barriers.

The simplest supramolecular systems therefore involve two molecules interacting with each other, and frequently these are defined as host and guest. The host, the larger of the two chemical entities, has curvature or concavity

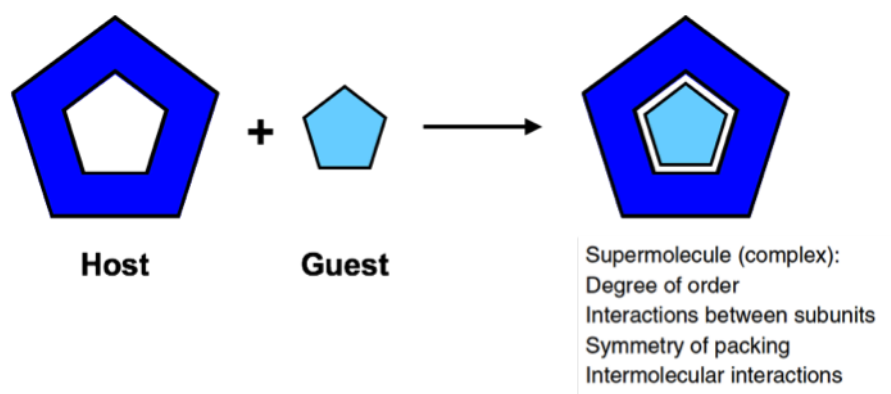


FIGURE 1.2: Schematization of supramolecular “host-guest” complex formation.

(the recognition motif), that define the binding site. In contrast, the smaller guest possesses a convex array of complementary structure which is recognized by the binding site. Many supramolecular systems are under thermodynamic control, so they can be studied as systems at equilibrium: however, self-assembly processes that are governed by kinetics, are becoming topical.<sup>11,12</sup> If the molecular components are photoactive, the formation of the supramolecular structure could perturb the ground and the excited states of the individual species, giving rise to new properties. In this context, we talk about *Supramolecular Photochemistry*.<sup>13</sup> With the formation of the supramolecular architecture, many processes may take place within the components, like



Interactions	Energy (kcal/mol)	Distance Dependence	Stability	Lability	Illustration
Hydrogen Bonding	1-15		Medium	High	$A-H \cdots B$
Ion-Ion	10-60	$1/r$	High	High	$M^{n+} \cdots X^{m-}$
Ion-Dipole	10-50	$1/r^2, 1/r^{4a}$	High	High	
Dipole-Dipole	1-10	$1/r^3, 1/r^{6a}$	Low	High	
Cation- $\pi$	1-20	$1/r^2, 1/r^{4b}$	Medium	High	
$\pi$ - $\pi$ stacking	1-5	$1/r^3, 1/r^{6c}$	Low	High	
Dispersion	1-5	$1/r^6$	Low	High	$Ar \cdots Ar$
Solvent effects <sup>d</sup>	1-10		High	High	$G \cdot S + H \rightleftharpoons S + H \cdot G$

<sup>a</sup>The inverse distance dependence is different for a fixed ion-dipole ( $1/r^2$ ) compared to a freely rotating ion-dipole interaction ( $1/r^4$ ). For dipole-dipole interactions, fixed dipoles have a  $1/r^3$  distance dependence, whereas freely rotating dipoles vary as  $1/r^6$ .

<sup>b</sup>Noncovalent cation- $\pi$  interactions are assumed to be controlled by charge-dipole interactions ( $1/r^2$ ) and by charge-induced dipole interactions ( $1/r^4$ ).

<sup>c</sup> $\pi$  -  $\pi$  interactions are assumed to be controlled by fixed dipole-dipole interactions ( $1/r^3$ ), by freely rotating dipole-dipole interactions ( $1/r^6$ ), and by dispersion interactions ( $1/r^6$ ).

<sup>d</sup>S, solvent; G, guest; H, host.

FIGURE 1.3: Supramolecular recognition interactions. Adapted from Goshe *et al.*, PNAS 2002, 99, 4824

photo-induced energy/electron transfer, cooperative effects and photochemical reactions. As already mentioned, in a supramolecular system the molecular components have well defined individual properties. If the component plays a relevant role in the photophysical behaviour of the supramolecule, its properties must be considered. Active components may participate in various acts such as light absorption and/or emission, intercomponent energy or electron transfer, isomerization, complexation of molecular species or ions, photodeprotonation. The photophysical behaviour of the component *A* is schematically represented in the figure 1.4: the first process is the light absorption, that gives the first excited state  $**A$ ; then non-radiative decay to a lowest "active" state  $*A$  and finally the decay to ground-state *via* radiative ( $k_r$ ), radiationless ( $k_{nr}$ ) and reactive ( $k_p$ ) pathways. It's also important to define  $\nu$  and  $\epsilon$ , the frequency and the molar absorption coefficient

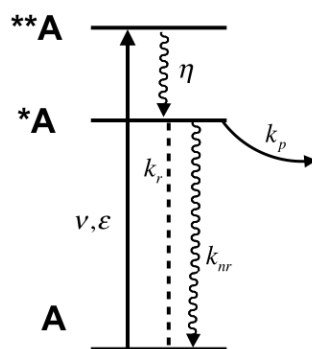


FIGURE 1.4: Photophysical and photochemical processes of a generic molecular component *A*.

of the absorption band respectively, the efficiency of formation of the active excited state ( $\eta$ ), the lifetime of the active excited state ( $\tau = 1/(k_r + k_{nr} + k_p)$ ), finally the quantum yields of emission ( $\Phi_r = k_r \tau$ ) and photoreaction ( $\Phi_p = k_p \tau$ ). Many other properties can be considered to characterize the molecular components, like redox and acid-base properties of the ground and excited state and the coordinative ability towards other species. Since connectors are not active components of the supramolecular system, their main properties are structural, like the degree of rigidity, conformational behaviour or end-to-end distance. It's important to keep in mind that even if the connectors don't have low-lying excited state and low energy levels, they have the important role of connecting the active components in an *electronic* sense: indeed a large part of photophysical processes that take place in a supramolecular array are electron- or energy transfer processes, so a certain degree of electronic interaction between active components is required. It is now evident how important is to attach active components into electronic communication. In the design of a supramolecular system, is important to consider all the above-listed properties of the components: in that contest has an important role the study of isolated components or of some suitable model molecules.

The behaviour of a supramolecule *A.B*, where the dot represents any type of linking interaction, usually differs from the superimposition of those of the single components *A* and *B*, because of the occurrence of intercomponent processes. I'll briefly show below the principal types of intercomponent processes and their characteristic features.

The absorption spectrum of supramolecular system can differ from the sum

of the separate components. It's possible to observe a shift due to perturbation of the single components spectra or new bands can appear: these bands can correspond to the *optical electron-transfer* process (1.1),



This process differs from photoinduced electron transfer, that corresponds to thermal electron transfer following electronic excitation of a single component: in that case light absorption populates an excited state localized on a single component, and electron transfer occurs as a subsequent radiationless process (reaction 1.2).



However, in a supramolecule  $A.B$ , thermal electron transfer to give  $A^+.B^-$  is thermodynamically unfavorable. It is possible to have spontaneous thermal electron in the reverse sense (reaction 1.3): this process is called *back electron-transfer* or *charge recombination*.



The relationship between optical, thermal and photoinduced electron transfer is illustrated in figure 1.5: The photophysical behaviour of the  $A.B$  system

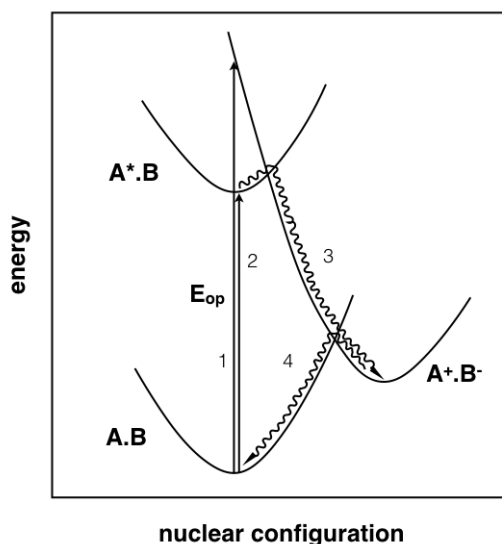
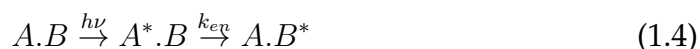


FIGURE 1.5: Relationship between optical (1), photoinduced (2 and 3) and thermal (4) electron transfer processes in a supramolecular system

may differ from the components because of the occurrence of intercomponent electronic energy transfer (1.4)



If the energy transfer process occurs, *A* is quenched and the excited state properties of *B* can be observed. These two phenomena can be described as *quenching* and *sensitization* respectively. A necessary requirement for the energy transfer process is that *B*\* must be equal or lower in energy than *A*\* (energy conservation). For more details, see the book *Supramolecular photochemistry*, by Vincenzo Balzani and Franco Scandola.<sup>13</sup>

In this chapter three different supramolecular systems will be presented:

- a shape-persistent tetramer ( $1^{8+}$ ), that bears four bipyridium units, that under one-electron reduction, give rise to the formation of the supramolecular aggregate;
- multichromophoric systems with a shape-persistent arrangement of the chromophores was obtained from the assembly of the same tetramer, with non-methylated bipyridium units ( $1'^{4+}$ ) and four fluorinated ruthenium porphyrins;
- a porphyrin-based 2D polymer obtained at the air-water interface with Langmuir-Blodgett technique.

## 1.1 Viologen Based Supramolecular Structures

*Viologens*, formed by the diquaternarization of 4,4'-bipyridine, have relatively diverse ranges of properties in terms of their redox chemistry, the electron-poor nature of the viologen dication and the way electrons are delocalized within the radical cation.<sup>14</sup> Knowing that, it is easy to understand why they play a prominent role in contemporary research: they find a variety of applications due to their redox and electrochromic properties and their ability to form intra- and intermolecular charge-transfer complexes. Indeed they can be considered as key components of supramolecular systems, since they are widely employed as electron acceptor recognition sites and redox switching units in supramolecular systems such as dendrimers,<sup>15</sup> rotaxanes, and in electrochromic devices.<sup>16</sup> *Methyl Viologen*, i.e. 1,1'-dimethyl-4,4'-bipyridinium ion, is a representative of this class of compounds.<sup>14</sup> It is well known that

*Methyl Viologen* can undergo two reversible one-electron reduction processes at accessible potentials; the first process lead to the formation of the radical cation, and the second one, occurring at more negative potential affords the neutral quinoidal form. The radical cation exists in aqueous solution in equilibrium with the dimer:<sup>17</sup> the formation of  $\pi$ -bonded dimers obtained by spontaneous and reversible association of  $\pi$ -radicals has been named pimerization. This process can be evidenced by a change in colour from blue, typical of the monoreduced monomeric form, to violet, typical of the pimer species and responsible for the name “viologens” attributed to this bipyridinium-based class of compounds (figure 1.6). This equilibrium between the two

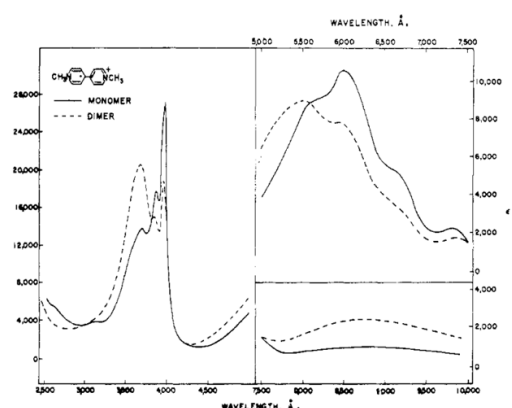


FIGURE 1.6: Comparison between absorption spectrum of *Methyl Viologen* cation radical monomer and dimer in water. Taken from E.M. Kosower, J.L. Cotter, JACS, 1971, 86, 5524.

monoreduced forms, can be used to built a system that can be reversible cycled between diamagnetic (pimer species) and paramagnetic form (non-pimerized species) using non-covalent chemistry. Indeed viologen cation radicals are a well-characterized class of spin-unpaired organic species. Buck and coworkers<sup>18</sup> synthesized a propyl-tethered bis-viologen cation radical that could be switched between paramagnetic and diamagnetic form using the complexation with the macrocycle CB[7] (figure 1.7).<sup>19</sup> The bis-viologen cation was obtained by reduction using sodium dithionite in buffered water: in that condition just a weak EPR signal was detected, attributed to small thermal population of the dissociated paramagnetic diradical. Then varying amounts of the macrocycle are added while the changes in the EPR spectrum were monitored: after addition of 9 equivalents of CB[7] (solubility limit of CB[7] in water), the EPR signal increases significantly. A Job plot was performed to estimate the stoichiometry of the system: they observed the

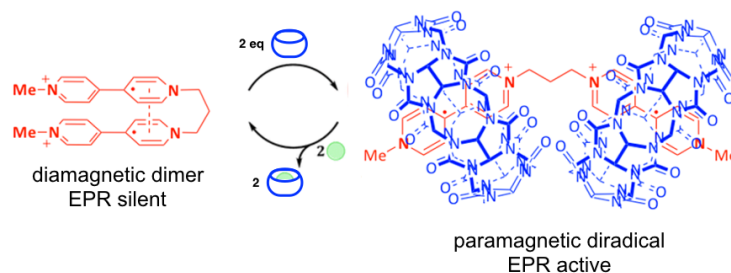


FIGURE 1.7: Reversible cycling between diamagnetic and paramagnetic forms of bis-viologen cation radical using noncovalent chemistry. Adapted from Buck *et al.*, JACS, 2013, 135, 10594-10597.

formation of the ternary complex 1:2 bis-viologen:CB[7]. To test if the paramagnetic complex could be switched back to the diamagnetic form, they used the trimethylaminomethylferrocenyl iodide. Indeed it is well known that this compound is able to form a tight complex to CB[7] in water: it is able to displace the weaker binding with the bis-viologen cation.

### 1.1.1 Supramolecular Structures Driven by Pimerization of Tetrahedrally Arranged Bipyridinium Units

The pimerization constant of *Methyl Viologen* in aqueous solution is quite low ( $385 \text{ M}^{-1}$ ),<sup>17</sup> so that highly concentrated solutions are necessary ( $>0.1 \text{ M}$ ) to form a significant amount of  $\pi$ -dimer (pimer). The presence of *N*-benzyl or *N*-phenyl units instead of the methyl ones enhances the pimerization constant ( $5 \times 10^4 \text{ M}^{-1}$ <sup>20</sup> and  $3.5 \times 10^3 \text{ M}^{-1}$ ,<sup>21</sup> respectively) in aqueous solution because of a more favorable stacking of the aromatic rings and a more hydrophobic character that prevents a good solubility of the monoreduced bipyridinium unit. The stability of the pimer has been enhanced by exploiting different approaches:<sup>22</sup> (i) use of a micelle<sup>23</sup> or a proper host, such as cucurbit[8]uril,<sup>24</sup> or  $\beta$ -cyclodextrin<sup>25</sup> to stabilize the pimer; (ii) mechanical bonding in interlocked systems;<sup>26</sup> (iii) preorganization of two<sup>14</sup> or multiple<sup>27</sup> viologen units in the same scaffold to favor intramolecular pimerization.

In this context we synthesized a shape-persistent molecule featuring four bipyridinium units ( $1^{8+}$  in figure 1.8). The photophysical properties of  $1^{8+}$  have been investigated in comparison with the model compound  $2^{2+}$  in aqueous solution (both compounds as chloride salts).  $1^{8+}$  shows the lowest-energy absorption band with maximum at 317 nm and a fluorescence band with

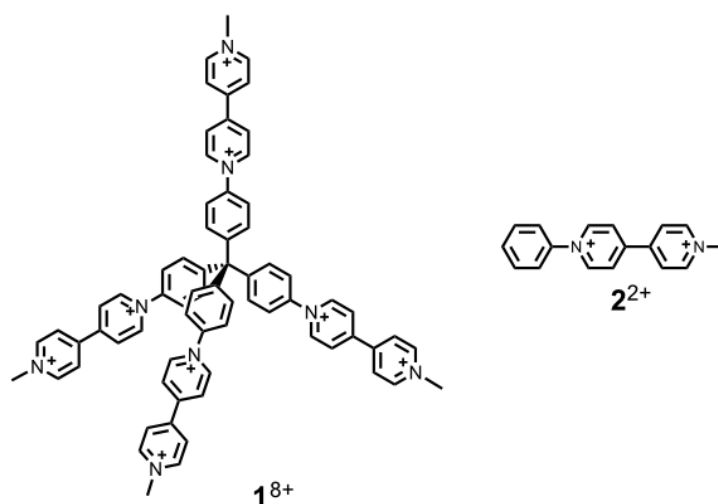


FIGURE 1.8: Chemical structures of the bipyridinium-based compounds  $1^{8+}$  and  $2^{2+}$ .

TABLE 1.1: Photophysical properties of  $1^{8+}$  and  $2^{2+}$  as chloride salts in aqueous solution at 298 K and in MeOH:CH<sub>2</sub>Cl<sub>2</sub> 1:1 (v/v) rigid matrix at 77 K.

	<i>Absorption</i>		<i>Emission</i>				
	298 K		298 K		77K		
	$\lambda/\text{nm}$	$\epsilon/10^4 \text{ M}^{-1}\text{cm}^{-1}$	$\lambda/\text{nm}$	$\Phi_{em}$	$\tau/\text{ns}$	$\lambda/\text{nm}$	$\tau/\text{ns}$
$1^{8+}$	317	3.09	527	0.015	3.3	445	3.2
$2^{2+}$	285	1.31	-	-	-	-	-

maximum at 527 nm ( $\Phi_{em} = 1.5\%$  and  $\tau = 3.3$  ns) at room temperature (figure 1.9). At 77 K in MeOH:CH<sub>2</sub>Cl<sub>2</sub> 1:1 (v/v) rigid matrix, a significant blue shift of the fluorescence band is observed ( $\lambda_{max} = 445$  nm) consistent with a charge-transfer character of the involved electronic transition. The photophysical properties are substantially different from those of the model compound  $2^{2+}$  that shows the lowest-energy absorption band with maximum at 285 nm (table 1.1 followed figure 1.9) and no luminescence.

The luminescent behavior of the tetramer can likely be ascribed to the fact that its rigid structure favors the radiative decays in comparison to the non-emissive  $2^{2+}$ . Therefore,  $1^{8+}$  is not merely the sum of four model compounds: a similar behavior was observed in the case of the analog molecule featuring four pyridylpyridinium units (see section 1.1.2).<sup>28</sup> The experimental absorption spectra of the tetramer and model compound are in good agreement with the computed spectra (1.10).

**Electrochemical Reduction.** The electrochemical investigation was performed

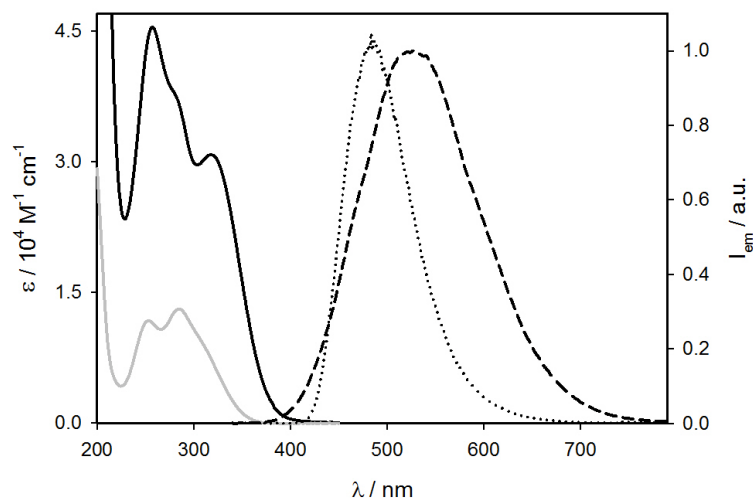


FIGURE 1.9: Absorption spectra (left) of  $1^{8+}$  (black solid line) and  $2^{2+}$  (gray solid line) in aqueous solution as chloride salts; emission spectra (right) of  $1^{8+}$  in aqueous solution at 298 K (black dashed line) and in MeOH:CH<sub>2</sub>Cl<sub>2</sub> 1:1 (v/v) rigid matrix at 77 K (black dotted line).  $\lambda_{em} = 257$  nm.

both in acetonitrile and in aqueous solution by dissolving the investigated compounds as hexafluorophosphate or chloride salts, respectively. The cyclic voltammogram of  $1^{8+}$  in acetonitrile solution shows two reversible redox processes at -0.27 and -0.67 V (vs SCE). Very similar results are obtained in the case of  $2^{2+}$  (figure 1.11). The slightly less negative reduction potentials observed for the tetramer compared to the model may be attributed to weak electrostatic repulsions in the octacationic tetramer, that facilitate reduction. By a bulk electrolysis experiment of  $1^{8+}$  at -0.30 V (vs SCE), we evaluated that in the first reduction process four electrons are exchanged. Since the second voltammetric peak displays similar values of maximum current and no substantial change in the diffusion coefficient of the redox active species is expected, also the second reduction process corresponds to the exchange of four electrons. By performing differential pulse voltammetry, we observed two reduction processes at the same potential values as those reported by cyclic voltammetry in figure 1.11. These results indicate that the reduction of each bipyridinium unit of  $1^{8+}$  is independent, so that the four bipyridinium units are reduced at the same potential value. In acetonitrile no pimerization process was observed, as demonstrated by the spectroelectrochemical experiment (1.12). The absorption spectrum of  $1^{4+}$  is indeed consistent with that of four monoreduced bipyridinium units with no evidence of pimer, which absorbs in the near-infrared (NIR) spectral region. On the other hand,



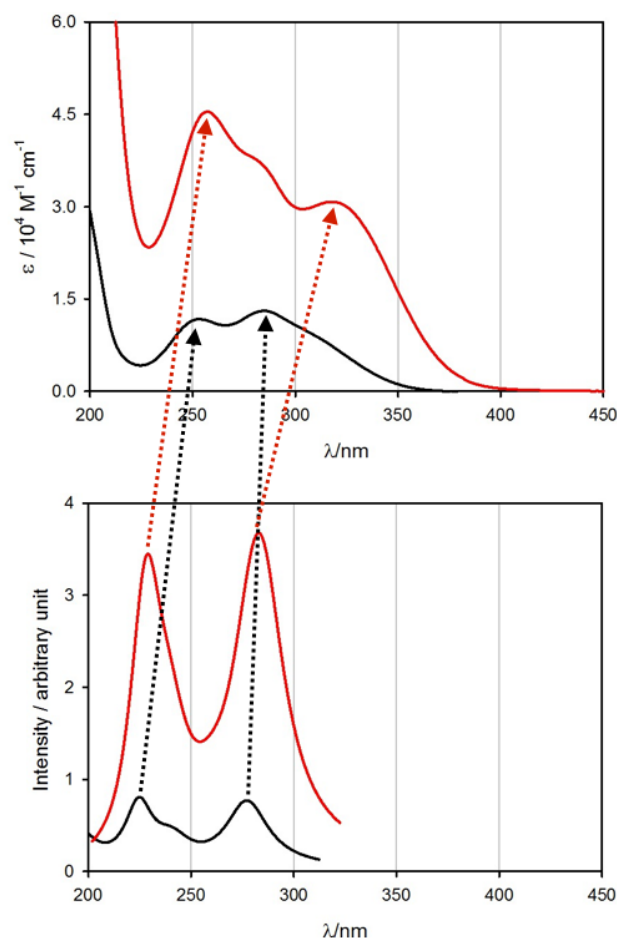


FIGURE 1.10: Comparison between observed (top) and computed (bottom) (TD CAM B3LYP/6-31G\*, see computational details section) absorption spectra of  $1^{8+}$  (red solid lines) and  $2^{2+}$  (black solid lines).

the cyclic voltammograms of both  $1^{8+}$  and  $2^{2+}$  in aqueous solution exhibit chemically irreversible reduction processes at more negative potential values (figure 1.11) and strong adsorption on glassy carbon electrode in the anodic backward scan. Moreover, in the case of  $1^{8+}$  a purple precipitate on the electrode is present after the electrochemical reduction. Spectroelectrochemical experiments could not be performed in aqueous solution because of hydrogen evolution on the Pt grid.

**Chemical Reduction.** It is well known that *viologens* undergo one-electron reduction, in aqueous solution, using sodium dithionite ( $\text{Na}_2\text{S}_2\text{O}_4$ ) as chemical reductant.<sup>29</sup> Our bipyridinium-based compounds show the same behavior. Since the tetramer upon reduction cannot undergo intramolecular pimerization because of the rigid architecture of the molecule, the investigation is thus

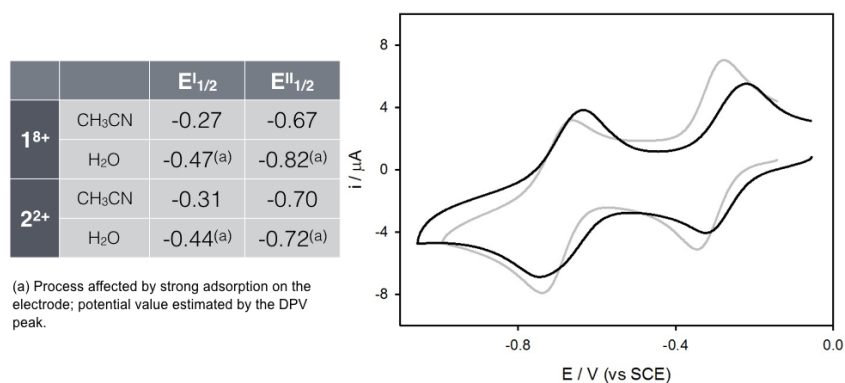


FIGURE 1.11: Cyclic voltammograms of argon-purged CH<sub>3</sub>CN solution  $4.7 \times 10^{-5}$  M of  $1^{8+}$  (black line) or  $4.1 \times 10^{-4}$  M of  $2^{2+}$  (gray line), as hexafluorophosphate salts, in the presence of 0.1 M TEAPF<sub>6</sub>. The current intensity of the model compound has been normalized to that of  $1^{8+}$  for comparison purposes. Scan rate=0.2 V/s; working electrode glassy carbon.

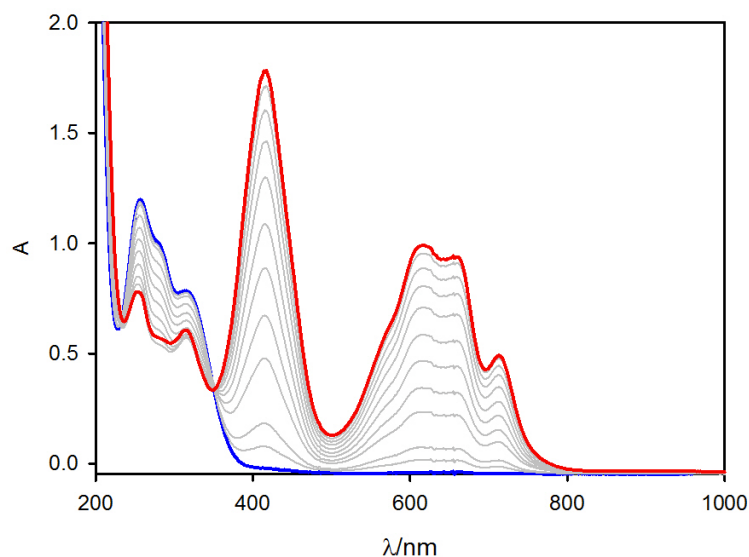


FIGURE 1.12: Absorption spectra of a  $8.2 \times 10^{-5}$  M solution of  $1^{8+}$  as hexafluorophosphate salt in argon-purged CH<sub>3</sub>CN in the presence of TEAPF<sub>6</sub> 0.1 M upon electrochemical reduction at -0.30 V (vs SCE): blue line refers to the initial spectrum and red line to the spectrum at the end of the electrolysis. Path-length of the cell=0.2 cm, working electrode: Pt grid.

focused on the possibility to form a supramolecular structure by intermolecular pimerization of the monoreduced bipyridinium units, as schematically represented in figure 1.13.

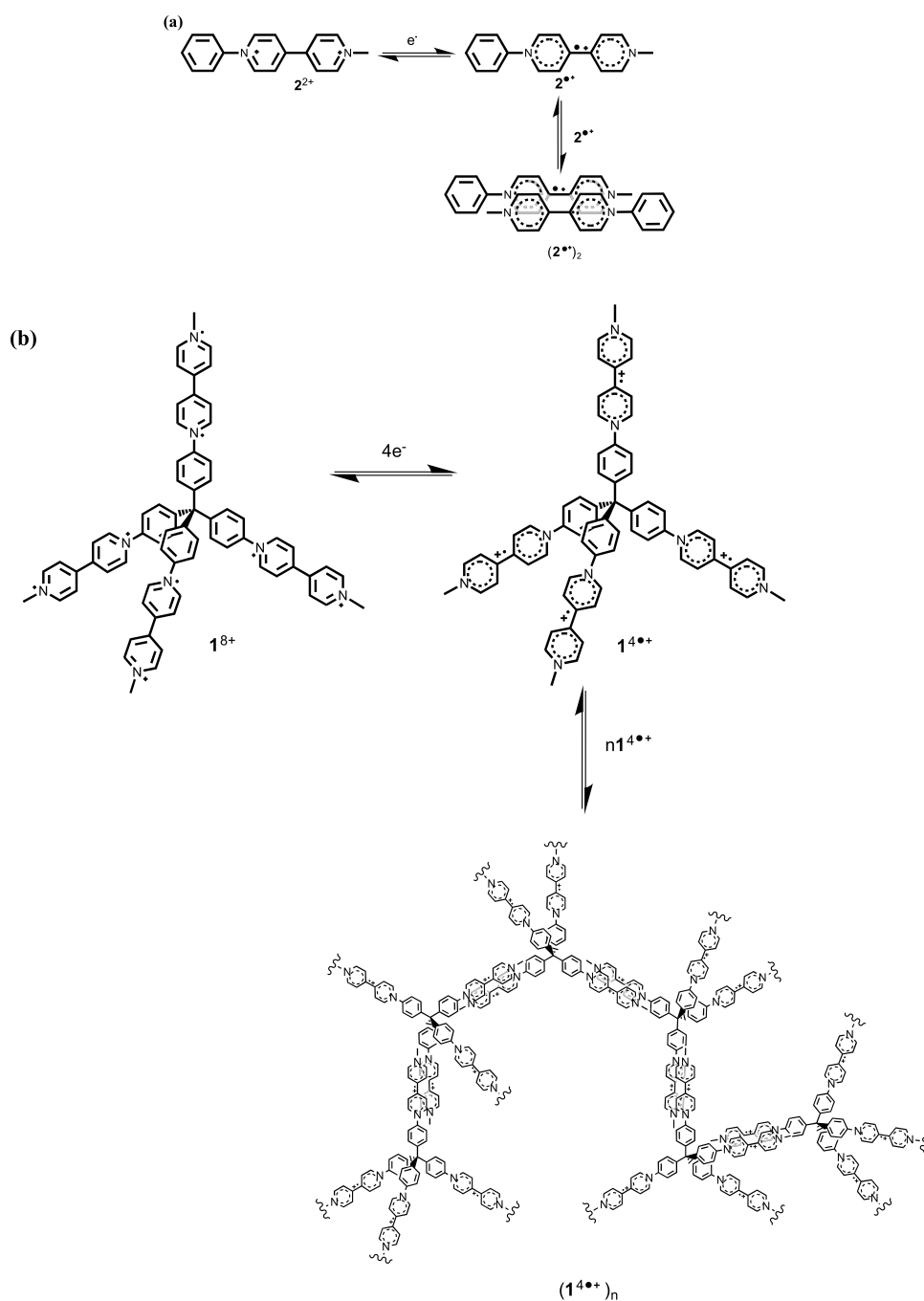


FIGURE 1.13: Intermolecular pimerization of model compound  $2^{2+}$  (a) and  $1^{8+}$  (b). The particular tetrahedral geometry of  $1^{8+}$  can lead to the formation of supramolecular structures because of multiple interactions between the monoreduced bipyridinium units belonging to different  $1^{8+}$  molecules.

Upon addition of a large excess of  $\text{Na}_2\text{S}_2\text{O}_4$  to an aqueous solution  $5.0 \times 10^{-4}$  M of  $2^{2+}$  or  $2.4 \times 10^{-5}$  M of  $1^{8+}$ , the absorption spectra are quite different from those registered upon electrochemical reduction in acetonitrile solution. In particular, two absorption bands without vibrational structure are present in the visible (at ca. 600 nm) and in the NIR spectral region with maximum at 933 and 1160 nm for the reduced species of  $2^{2+}$  and  $1^{8+}$ , respectively. These absorption features are typical of the pimer formed by monoreduced bipyridinium units. The red-shifted maximum observed in the tetramer compared to the model compound is in agreement with the red-shift observed on going from  $2^{2+}$  to  $1^{8+}$  (figure 1.9) and it may also be ascribed to a different structure of the two pimers,<sup>30,31</sup> as suggested by the calculations performed on the model compound and the tetramer (see below).

In the case of the tetramer  $1^{8+}$ , chemical reduction experiments performed with an excess of  $\text{Na}_2\text{S}_2\text{O}_4$  and by changing the concentration of the tetramer in the range  $1.0 \times 10^{-6}$  M -  $7.0 \times 10^{-5}$  M, evidenced the same absorption profile as that reported in figure 1.14 with a linear increase of the absorbance as a function of the tetramer concentration 1.15. In particular the linear increase observed at 1160 nm, where only the pimer absorbs (figure 1.15, plot b), is the clear proof that the formation of the pimer is quantitative and, therefore, we can assume that, under the experimental conditions used to record the spectrum of figure 1.14, only the pimeric form is present by comparison with the spectrum of the monoreduced and non-pimerized species obtained by continuous radiolysis. In the case of the model compound, pimer formation is observed only at a concentration equal or higher than  $5.0 \times 10^{-4}$  M and, also in the presence of a large excess of chemical reductant, complete pimerization does not occur. Therefore, the absorption spectrum reported in figure 1.14 has been estimated by knowing that of the non-pimerized reduced compound obtained by continuous radiolysis.

**EPR Measurements.** Since the pimer is diamagnetic and the monoreduced form non pimerized is paramagnetic, we performed EPR measurements. Radical cation  $2^{\bullet+}$  was prepared by reaction of the diamagnetic monomer precursor  $2^{2+}$ , as chloride salt, with 5-10 equivalents of  $\text{Na}_2\text{S}_2\text{O}_4$  in carefully deoxygenated water solutions. The spectrum, reported in figure 1.16, shows a broad single line ( $\Delta H_{app} = 11$  G) resulting from unresolved hyperfine splittings. Any attempts to resolve the hyperfine structure failed because of the high number of unequivalent magnetic active nuclei (H, N) coupled with the unpaired electron in  $2^{\bullet+}$ . In the absence of hyperfine structure, the signal was

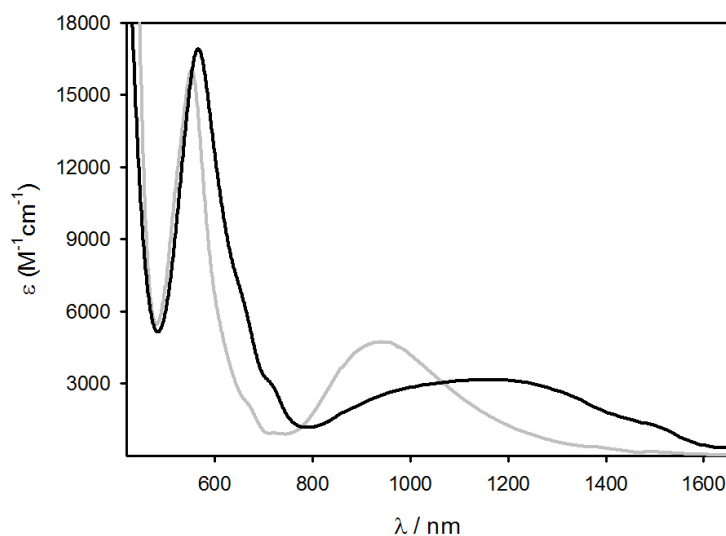


FIGURE 1.14: Absorption spectra of  $1^{8+}$  (black line) and  $2^{2+}$  (gray line) as chloride salts in deaerated aqueous solution upon chemical reduction performed by adding an excess of  $\text{Na}_2\text{S}_2\text{O}_4$  at room temperature. The molar absorption coefficient is reported per pimerized units, i.e. half of the monoreduced bipyridinium units.

assigned to  $2^{\bullet+}$  on the basis of the measured  $g$ -factor = 2.0031. This value is indeed in agreement with previous literature data on viologen radical cation in water.<sup>32,33</sup>

An increase in temperature of the water solution from 298 K to 363 K did not affect the shape of the spectrum, but causes an increase in signal strength, the intensity of which at 358 K was ca. four times higher than that measured at 298 K (figure 1.17). This process was perfectly reversible: no significant deterioration of the EPR signal upon temperature cycling was observed when few cycles were performed. All these observations suggested the presence of a reversible equilibrium between two forms.

I already mention that viologen radical cations in aqueous solution exist in equilibrium (reaction 1.5) with a diamagnetic, EPR silent, pimer.



$$K_{eq} = \frac{[P]}{[M^{\bullet+}]^2} \quad (1.6)$$

The concentration of the monomer radical cation can be calculated at any temperature from double integration of its EPR spectrum. If we assume a

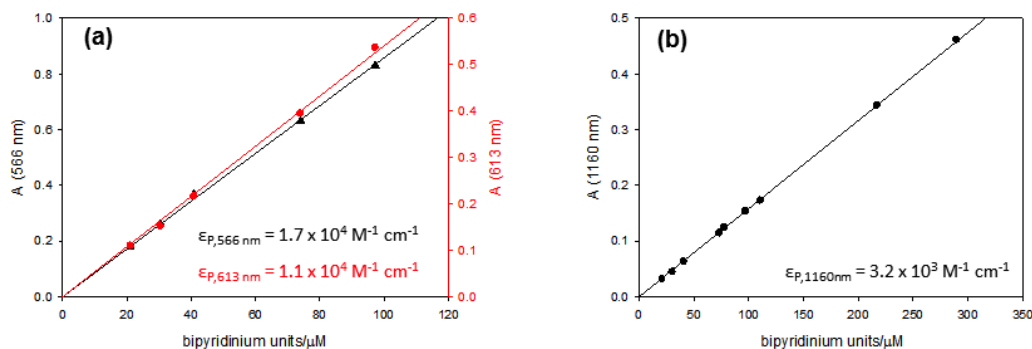


FIGURE 1.15: Linear increase of the absorbance at (a) 566 nm and 613 nm, and (b) 1160 nm as a function of the concentration of the bipyridinium units obtained upon exhaustive chemical reduction of  $1^{8+}$ . From the slopes of the obtained lines it has been calculated the molar absorption coefficients of the pimerized units in the tetramer using the half of the bipyridinium unit concentration.

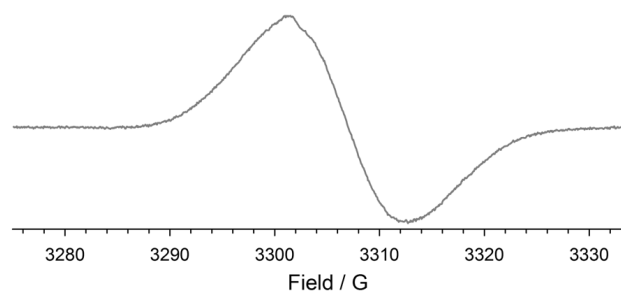


FIGURE 1.16: EPR spectrum of an aqueous solution of  $2^{2+}$  ( $1.0 \times 10^{-3} \text{ M}$ ) upon chemical reduction performed by adding 10 equivalents of  $\text{Na}_2\text{S}_2\text{O}_4$  at 298 K.

complete reduction of starting monomer  $2^{2+}$  in the presence of 5-10 equivalents of  $\text{Na}_2\text{S}_2\text{O}_4$  (at 358 K the radical concentration measured by EPR corresponds to the 80% of the starting concentration), the equilibrium constant can be easily estimated. Values of the equilibrium constant  $K_{eq}$  calculated over the temperature range 298 K - 353 K gives an excellent  $\text{Rln}(K_{eq})$  against  $1/T$  plot (inset figure 1.17), resulting in the thermodynamic values:  $\Delta H^\circ = -12.8 \pm 0.6 \text{ kcal mol}^{-1}$ ,  $\Delta S^\circ = -26 \pm 2 \text{ cal mol}^{-1} \text{ K}^{-1}$ . Although the  $\Delta S^\circ$  value is negative, as one would expect for a dimerization reaction, the variation of enthalpy is significantly favored: at 298 K it indeed leads to  $\Delta G^\circ = -5.0 \text{ kcal mol}^{-1}$  and an equilibrium constant for pimerization  $K_{eq} = 5 \times 10^3 \text{ M}^{-1}$ . We note that the enthalpy variation is consistent with the binding energy determined by calculations which also indicates a favorable pimerization process. The importance of hydrophobic effects was further confirmed by repeating the same EPR experiments in acetonitrile solution. Because of solubility

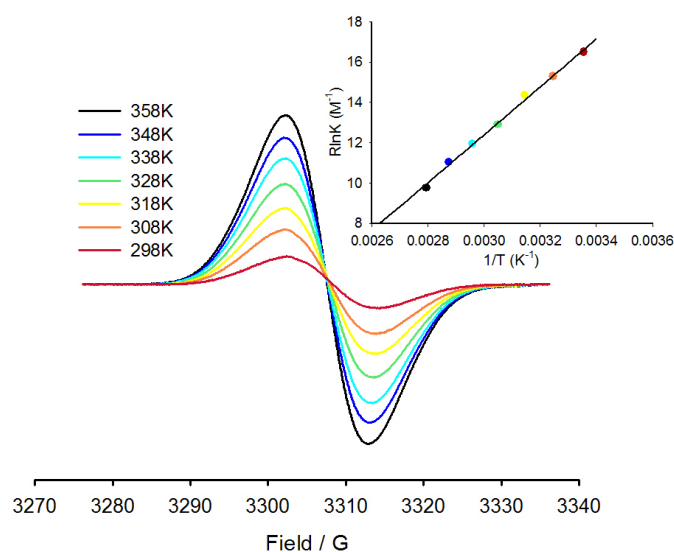


FIGURE 1.17: EPR spectrum of an aqueous solution of  $2^{2+}$  ( $1.0 \times 10^{-3}$  M) upon chemical reduction by addition of 10 equivalents of  $\text{Na}_2\text{S}_2\text{O}_4$  at different temperatures. Inset: plot of  $\ln K_{eq}$  vs  $1/T$ .

reasons, the radical cation  $2^{\bullet+}$  was generated by  $\text{CrCl}_2$  reduction of  $2^{2+}$ , as hexafluorophosphate salt. In this case an intense signal corresponding to 85% reduction of the starting monomer was immediately observed at 298 K. Change of the temperature in the range 298 K - 340 K had a small effect on the spectrum intensity suggesting that in this solvent practically all radicals are present in the monomeric paramagnetic form (figure 1.18). It should be remarked that in water the use of  $\text{CrCl}_2$  as the reducing agent led to the same EPR behavior observed with  $\text{Na}_2\text{S}_2\text{O}_4$ .

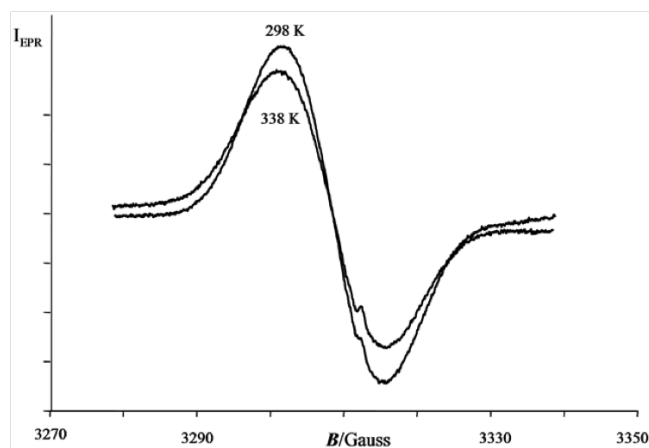


FIGURE 1.18: Radical cation  $2^{\bullet+}$  (0.3 mM,  $[2^{\bullet+}] = 85\%[2^{2+}]$ ) generated by  $\text{CrCl}_2$  recorded at 298K and 338 K in acetonitrile.

We successively passed to investigate the EPR behavior in water of the paramagnetic species formed during the reduction with  $\text{Na}_2\text{S}_2\text{O}_4$  of the tetramer  $1^{8+}$ , as chloride salt. Figure 1.19 reports the EPR spectrum observed after the addition of 10 equivalents of  $\text{Na}_2\text{S}_2\text{O}_4$  respect to  $1^{8+}$  concentration (0.25 mM). The  $\Delta m_s = 1$  region of the EPR spectra consists of only one narrow symmetrical peak ( $\Delta H_{app} = 3$  G), which, on the basis of the corresponding  $g$ -factor (2.0031), was assigned to the monomeric reduced bipyridinium in a doublet state.<sup>34</sup> No evidence of spectral features attributed to higher spin states was observed in the spectrum. The weak signal centered at  $g = 2.0061$  in the spectrum corresponds to  $\text{SO}_2^{\bullet-}$  radical anion.

Exhaustive reduction of the tetramer at the high concentrations necessary for EPR experiments leads to the formation of an insoluble compound. The observed signal at  $g = 2.0031$  must be attributed to monoreduced bipyridinium units not involved in intermolecular radical-radical interactions that occur in the pimer formation. Double integration of this EPR signal showed that the radical units not involved in the pimer formation are about 4% of the total bipyridinium units present in the tetramer. This result evidences that pimerization is almost a quantitative process in agreement with the chemical reduction experiments performed monitoring the absorbance changes.

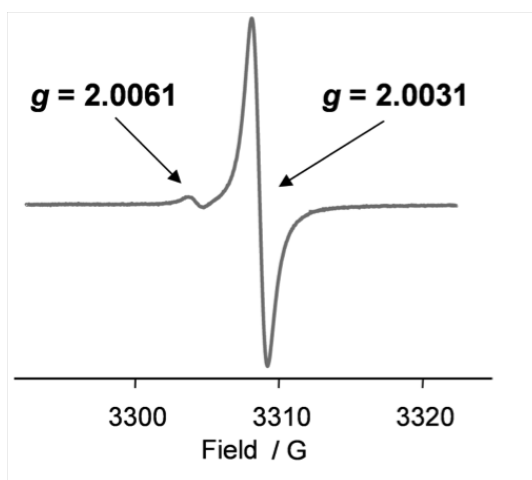


FIGURE 1.19: EPR spectrum of a water sample containing 0.25 mM  $1^{8+}$  and 10 equivalents (respect to the tetramer concentration) of  $\text{Na}_2\text{S}_2\text{O}_4$  at room temperature.

Temperature has no significant effect on both shape and intensity of EPR spectra, on the contrary of the behavior reported for the model compound. Therefore, under these conditions, careful evaluation of the  $K_{eq}$  is prevented because of the precipitation process. When the reduction process is electrochemically performed in the EPR cavity using acetonitrile as the solvent, a



spectrum similar to that obtained with the monomer  $2^{2+}$  is observed under the same experimental conditions (figure 1.20). This signal is due to the monoreduced bipyridinium units which in acetonitrile are not able to pimerize. The spectrum does not show any evidence of intramolecular spin-exchange interaction between two or more viologen fragments connected to the same  $sp^3$  carbon in agreement with the results of the calculations discussed below.

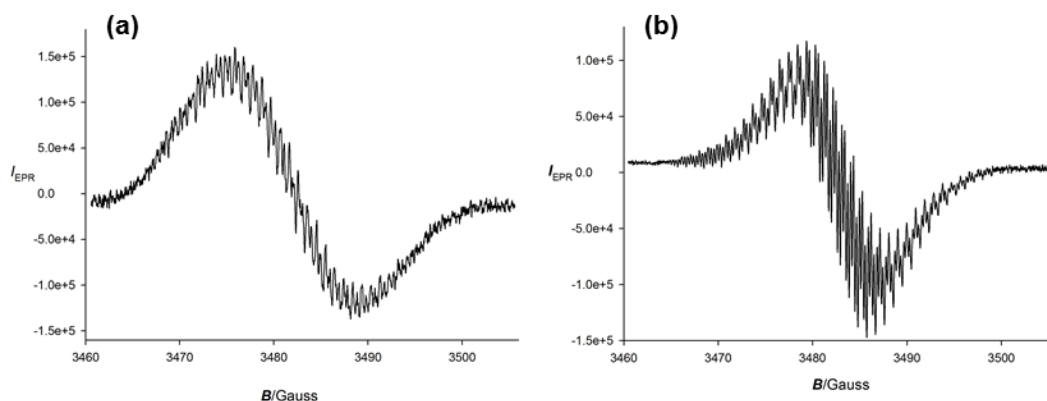
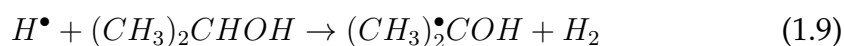
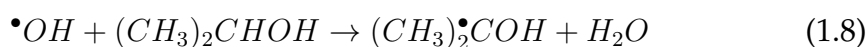
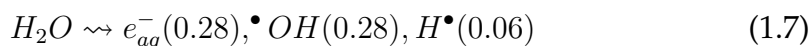


FIGURE 1.20: (a) 1.9 mM  $2^{2+}$  and (b) 0.35 mM  $1^{8+}$  as hexafluorophosphate salts in acetonitrile with 0.1 M  $NH_4PF_6$ , after electrochemical reduction at -2.5 V.

**Continuous Radiolysis.** The situation is different when the reduction is performed in continuous radiolysis. Upon gamma irradiation of argon-purged aqueous solutions containing 0.1 M of 2-propanol,  $e^-_{aq}$  and  $(CH_3)_2\bullet COH$  radicals are generated (equation 1.7 - 1.9); they are capable of reducing rapidly and quantitatively the bipyridinium unit.<sup>35,36</sup> Indeed, in the presence of 0.1 M of 2-propanol,  $\bullet OH$  and  $H\bullet$  radicals are efficiently scavenged (equation 1.8,  $k_2 = 1.9 \times 10^9 \text{ M}^{-1} \text{ s}^{-1}$ , and equation 1.9,  $k_3 = 7.4 \times 10^7 \text{ M}^{-1} \text{ s}^{-1}$ ),<sup>37</sup> and converted to the reducing radical  $(CH_3)_2\bullet COH$ . Thus, under these conditions, the main species present in solution are  $e^-_{aq}$  and  $(CH_3)_2\bullet COH$  with a total radiation yield  $G = 0.62 \mu\text{mol J}^{-1}$ .



Under the above reported experimental conditions, gamma irradiation of a solution containing  $4.8 \times 10^{-5}$  M of  $2^{2+}$ , as chloride salt, causes the reduction of the model compound, clearly evidenced by the typical absorption features of the monoreduced bipyridinium unit (figure 1.21 plot a). The absorption spectrum also shows that no pimer formation occurs even when practically exhaustive reduction is performed (irradiation dose = 65.3 Gy corresponding to  $4.1 \times 10^{-5}$  M of reduced species).

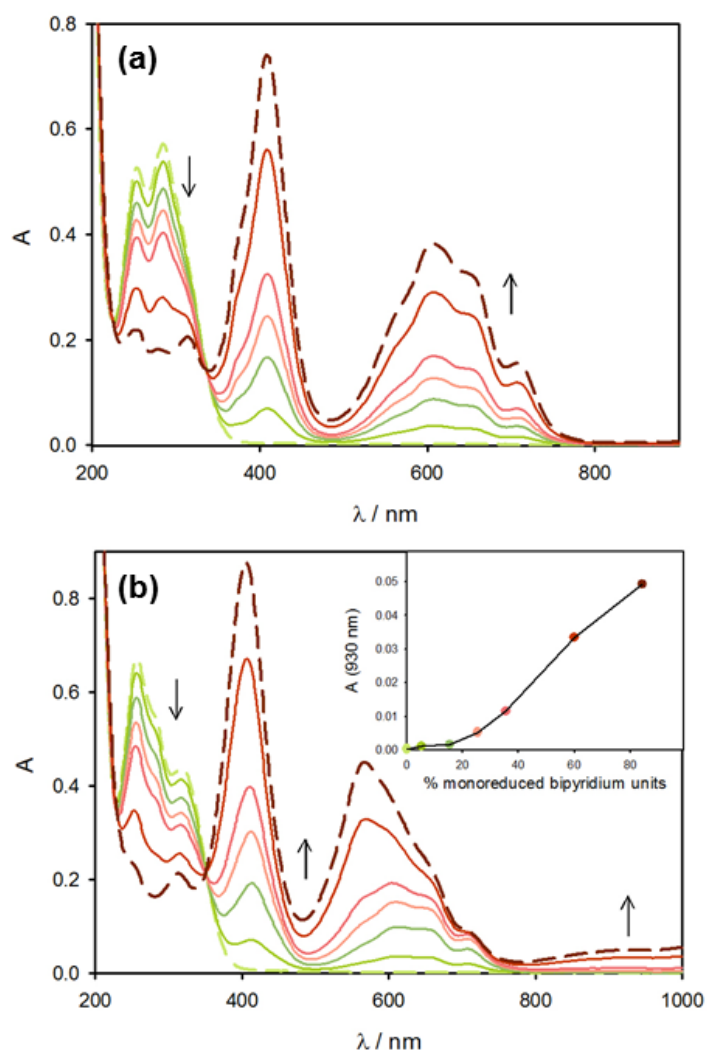


FIGURE 1.21: Spectral changes observed upon gamma irradiation of argon-purged aqueous solutions containing 0.1 M of 2-propanol and (a)  $4.8 \times 10^{-5}$  M of  $2^{2+}$  or (b)  $1.2 \times 10^{-5}$  M of  $1^{8+}$ . Dashed green line: non-irradiated solutions; other lines: each spectrum corresponds to a total irradiation dose of 4.1, 11.9, 19.7, 27.5, and 46.4 Gy, respectively; dashed brown line: after a total irradiation dose of 65.3 Gy. Optical pathlength = 1 cm. Insert of panel (b): absorbance at 930 nm as a function of the percentage of monoreduced bipyridinium units.

A different and quite interesting behavior is observed upon gamma irradiation of a solution containing  $1^{8+}$ , as chloride salt, at a concentration of  $1.2 \times 10^{-5}$  M, which corresponds to  $4.8 \times 10^{-5}$  M of bipyridinium units (i.e., equal to the concentration of  $2^{2+}$  used in the previous experiment). As shown in figure 1.21 plot b, by increasing the amount of the monoreduced bipyridinium (i.e., by increasing the irradiation dose) the typical features of the pimer appear. Because  $1^{8+}$  and  $2^{2+}$  have been irradiated under the same conditions, this finding suggests that the pimer formation is favored by the peculiar structure of  $1^{8+}$ . Interestingly, the pimerization process of  $1^{8+}$  is reversible by changing temperature: upon heating the solution up to  $65^\circ\text{C}$  an absorption spectrum similar to that of the non-pimerized monoreduced bipyridinium units is observed (figure 1.22). The experimental conditions used are quite different from those of the EPR measurements because the  $1^{8+}$  concentration is fifteen times lower and the reduction is not exhaustive (only 35% of the bipyridinium units have been reduced). This result demonstrates

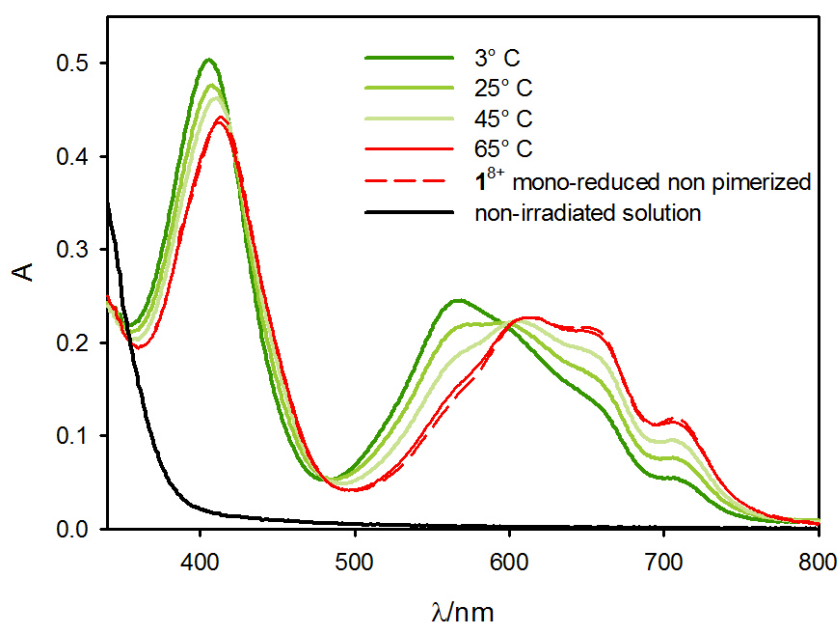


FIGURE 1.22: Spectral changes with increasing temperature of a deoxygenated aqueous solution containing 0.1 M of 2-propanol and  $1.5 \times 10^{-5}$  M of  $1^{8+}$  gamma irradiated with a dose of 46.4 Gy, (ca. 35% of the bipyridinium units have been reduced). black solid line: non-irradiated solution; green solid lines: each spectrum corresponds to 3, 25, and  $45^\circ\text{C}$  respectively; red solid line: spectrum collected at  $65^\circ\text{C}$ ; red dashed line: spectrum of reduced non-pimerized form of  $1^{8+}$ , normalized to the red solid one. Optical pathlength = 1 cm.

that, under the present experimental conditions, pimerization is an equilibrium process, as represented in reaction 1.5. Assuming that  $1^{8+}$  is constituted by four non-interacting bipyridinium units, we can estimate the pimerization constant per bipyridinium unit based on equation 1.6. The equilibrium concentrations of the non-pimerized and pimerized bipyridinium units have been calculated by using the absorption values at 566 and 613 nm (1.21 plot b), the molar absorption coefficients at the two selected wavelengths for the non-pimerized and pimerized bipyridinium units (figure 1.23 and plot a of figure 1.15), and equations 1.10 and 1.11.

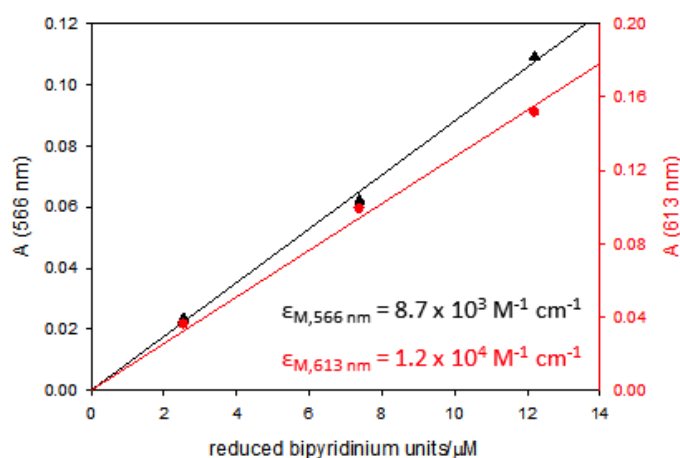


FIGURE 1.23: Linear increase of the absorbance at 566 nm and 613 nm as a function of the concentration of the monoreduced bipyridinium units obtained upon reduction performed by continuous radiolysis of  $1^{8+}$  at low doses (from 4.1 to 19,7 Gy, see figure 1.21 plot b). The slopes of the lines obtained give the molar absorption coefficients of the non-pimerized units in the tetramer.

$$C_M = \frac{A_{613}\epsilon_{P566} - A_{566}\epsilon_{P613}}{\epsilon_{M613}\epsilon_{P566} - \epsilon_{M566}\epsilon_{P613}} \quad (1.10)$$

$$C_P = \frac{A_{566}\epsilon_{M613} - A_{613}\epsilon_{M566}}{\epsilon_{M613}\epsilon_{P566} - \epsilon_{M566}\epsilon_{P613}} \quad (1.11)$$

$C_M$  and  $C_P$  represent the concentration of the non-pimerized and pimerized monoreduced bipyridinium units, respectively;  $A_{566}$  and  $A_{613}$  are the absorption values at 566 and 613 nm, respectively;  $\epsilon_{M566}$  and  $\epsilon_{M613}$  are the molar absorption coefficients of the non-pimerized monoreduced bipyridinium units at 566 and 613 nm, respectively, and  $\epsilon_{P566}$  and  $\epsilon_{P613}$  the molar absorption coefficients of the pimerized units at 566 and 613 nm, respectively. For the tetramer the absorption values at 566 and 613 nm used in the equations are

obtained from the spectra of figure 1.21 plot b corresponding to the last three irradiation doses (27,5, 46,4, and 65.3 Gy); as far as  $\epsilon_{M566}$  and  $\epsilon_{M613}$  are concerned, the values used, namely  $8.7 \times 10^3$  and  $1.2 \times 10^4 \text{M}^{-1} \text{cm}^{-1}$  at 566 nm and 613 nm, respectively, are those estimated from the spectra of figure 1.21 plot b recorded at low irradiation doses (figure 1.23); finally the values of  $\epsilon_{P566}$  and  $\epsilon_{P613}$  are obtained from chemical reduction of  $1^{8+}$  carried out in the presence of an excess of reducing species (figure 1.15 plot a), and correspond to  $1.7 \times 10^4$  and  $1.1 \times 10^4 \text{M}^{-1} \text{cm}^{-1}$  at 566 nm and 613 nm, respectively. Data from chemical reduction of  $1^{8+}$  have been used to perform a similar calculation at 1160 nm (equation 1.12), where the non-pimerized monoreduced bipyridinium does not absorb and the pimerized one has a molar absorption coefficient of  $3.2 \times 10^3 \text{M}^{-1} \text{cm}^{-1}$  (figure 1.15, plot b), estimated again from its exhaustive chemical reduction:

$$C_0 = C_M + 2C_P = C_M + 2 \frac{A_{1160}}{\epsilon_{P1160}} \quad (1.12)$$

The concentrations of the non-pimerized and pimerized monoreduced bipyridinium units so obtained enabled to calculate the apparent equilibrium constant of the pimerization process for  $1^{8+}$  by equation 1.6.

Interestingly, the apparent equilibrium constant changes upon increasing the dose:  $K_{eq} = 2 \times 10^4 \text{M}^{-1}$ ,  $1 \times 10^5 \text{M}^{-1}$ , and  $3 \times 10^5 \text{M}^{-1}$  for 27.5, 46.4, and 65.3 Gy, respectively. This finding indicates that, by increasing the amount of the reduced bipyridinium units, the pimer formation occurs more efficiently, suggesting a cooperative mechanism<sup>38</sup> among the reduced units which is favored by the peculiar structure of  $1^{8+}$ , and supported by the following considerations. As the electrochemical experiments clearly show, the four bipyridinium units contained in  $1^{8+}$  behave independently, therefore their radiolytic reduction has to occur in a statistic way. It means that, increasing the irradiation dose, tetramer molecules with more than one reduced bipyridinium unit are formed (see figure 1.24 and table 1.2). By using this statistic approach we estimated that pimerization begins only when multiple reduction of the same molecule has occurred, specifically when more than 30% and 10% of the molecules have two and three reduced bipyridinium units, respectively.

The presence of multiply reduced molecules is expected to favor the pimerization process that, because of the rigid structure of  $1^{8+}$ , can occur only intermolecularly. Indeed, the fraction of encounter events resulting in pimer

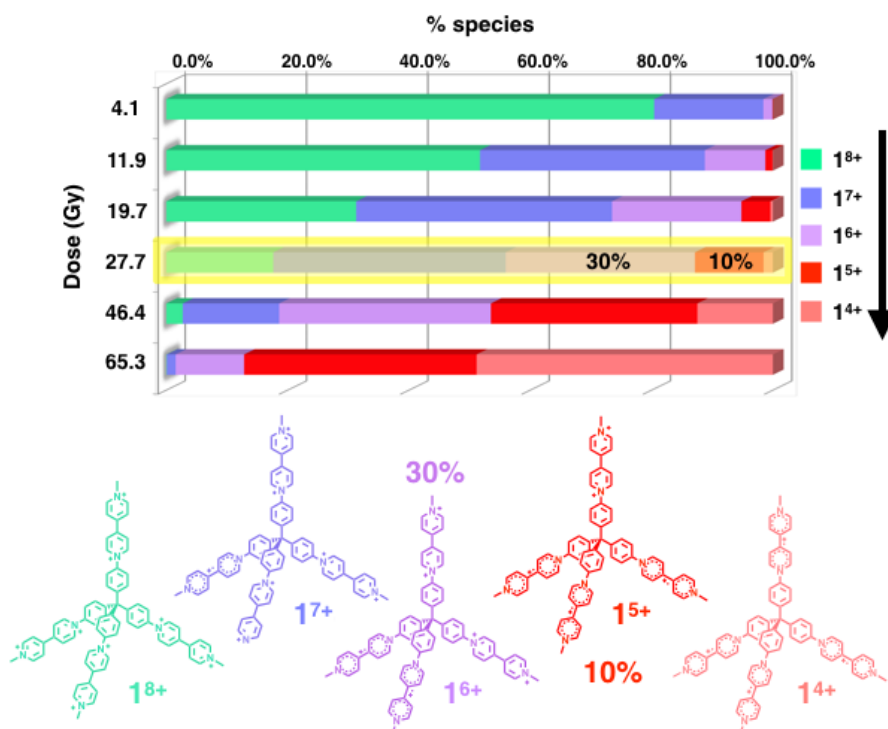


FIGURE 1.24: Statistical distribution of the species present in argon-purged aqueous solution containing 0.1 M of 2-propanol and  $1.2 \times 10^{-5}$  M of  $1^{8+}$ , upon radiolytic reduction, as a function of the irradiation dose.

formation is much higher for tetramer containing four monoreduced bipyrindinium units than for tetramers containing just one monoreduced unit. This expectation is evidenced by the fact that the pimer formation shows an induction period (inset of figure 1.21 plot b and figure 1.25). Such a behavior, not observed in the case of the model compound  $2^{2+}$  (figure 1.25), is in agreement with a cooperative mechanism. Furthermore, each (multiple) reduced molecule is surrounded by a number of reduced molecules that increases by increasing the irradiation dose. Moreover, the increase of the irradiation dose also favors cooperative, multiple intermolecular interactions, that enhance the stabilization of the system, also leading to a hierarchical supramolecular growth. Such a cooperative effect is evidenced by the increase in the apparent equilibrium constant value by increasing the irradiation dose. Finally, because the pimerization is likely enthalpy driven, as supported by the EPR measurements performed on the model compound, the cooperative mechanism<sup>38</sup> is also in agreement with the fact that the process is characterized by a ceiling temperature below which the system pimerizes and above which ( $65^\circ\text{C}$ ) the fraction of the pimerized molecules is zero (figure 1.22). Beside

TABLE 1.2: Statistical distribution of the species present in argon-purged aqueous solution containing 0.1 M of 2-propanol and  $1.2 \times 10^{-5}$  M of  $1^{8+}$ , upon radiolytic reduction, as a function of the irradiation dose.

Dose, Gy	Reduced bipyridinium units, M	$1^{8+}$	$1^{7+}$	$1^{6+}$	$1^{5+}$	$1^{4+}$
4.1	$2.5 \times 10^{-6}$	80.4%	18.0%	1.5%	0.1%	0.0%
11.9	$7.4 \times 10^{-6}$	51.7%	37.1%	10.0%	1.2%	0.1%
19.7	$12.2 \times 10^{-6}$	31.3%	42.2%	21.3%	4.8%	0.4%
27.5	$17.0 \times 10^{-6}$	17.6%	37.1%	31.2%	11.3%	1.5%
46.4	$28.8 \times 10^{-6}$	51.7%	2.7%	34.9%	34.0%	12.4%
65.3	$40.5 \times 10^{-6}$	51.7%	0.1%	11.3%	38.3%	48.8%

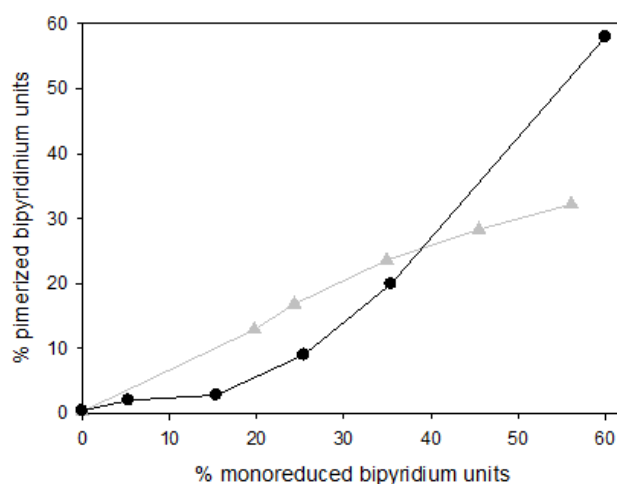


FIGURE 1.25: Percentage of pimerized bipyridinium units as a function of the percentage of monoreduced bipyridinium units of  $2^{2+}$  (grey triangles) and  $1^{8+}$  (black circles).

the structural consideration, the fact that the pimerization process has to occur intermolecularly has been proven by pulse radiolysis experiments.

Continuous radiolysis of a more concentrated solution of  $2^{2+}$ , namely  $1.0 \times 10^{-3}$  M, shows that a partial pimerization occurs as in the case of the chemical reduction (figure 1.26). Under these conditions it was possible to estimate the pimerization constant for  $2^{2+}$  applying equation 1.12 at 933 nm, where only the pimer absorbs: its value, equal to  $5 \times 10^3 \text{ M}^{-1}$ , is in good agreement with that obtained by chemical reduction in EPR measurements.

**Pulse Radiolysis Experiments.** Beside the structural consideration, the fact that the pimerization process has to occur intermolecularly has been

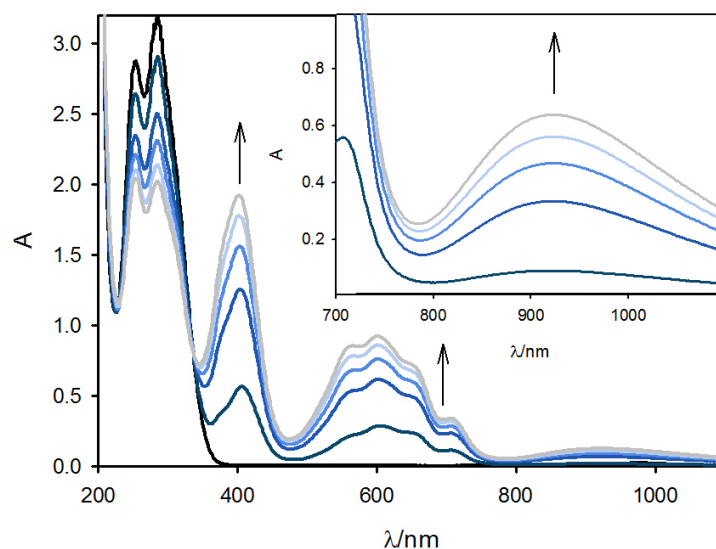


FIGURE 1.26: Spectral changes observed upon gamma irradiation of argon-purged aqueous solutions containing 0.1 M of 2-propanol and  $1.0 \times 10^{-3}$  M of  $2^{2+}$ . Black solid line: non-irradiated solutions; blue solid lines: each spectrum corresponds to a total irradiation dose of 177.7, 392.7, 563.3, and 733.9 Gy, respectively; grey line: after a total irradiation dose of 904.6 Gy. Optical pathlength = 0.2 cm. Insert: same spectra recorder in a cuvette with optical pathlength = 1 cm.

proven by pulse radiolysis experiments. Pulse radiolysis experiments have been performed on argon-purged aqueous solutions containing 0.1 M of 2-propanol to monitor the kinetics of the reduction of  $2^{2+}$  and  $1^{8+}$  induced by  $e^-_{aq}$  and  $(\text{CH}_3)_2\bullet\text{COH}$  and the processes that follow. As expected  $e^-_{aq}$  and  $(\text{CH}_3)_2\bullet\text{COH}$  are capable of reducing the model compound and the tetramer on the time scale of  $\mu\text{s}$  (figure 1.27). The bimolecular rate constants, obtained as reported in figure 1.28, are gathered in table 1.3, where the corresponding rate constants for *Methyl Viologen* are also reported for comparison purposes.

The fast absorption changes observed (figure 1.25) upon radiolytic reduction of both  $2^{2+}$  and  $1^{8+}$  can be unequivocally attributed to the formation of non-pimerized monoreduced bipyridinium. In the case of the model compound the shape does not change over time, whereas for the tetramer it evolves on the ms time scale evidencing absorbance increases at 570 and 1000 nm (figure 1.29) where the pimer exhibits molar absorption coefficients higher than those of the non-pimerized reduced bipyridinium. This process follows a second order kinetics with a rate constant of  $6 \times 10^7 \text{ M}^{-1}\text{s}^{-1}$  (figure 1.29) and can be therefore assigned to the pimerization reaction. Note that in



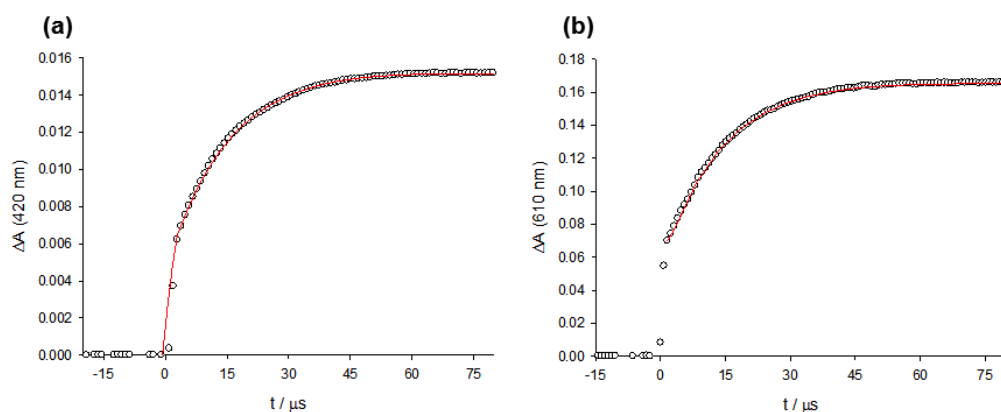


FIGURE 1.27: Time-dependence of absorption at (a) 420 nm and (b) 610 nm after pulse radiolysis of argon-purged aqueous solutions containing 0.1 M of 2-propanol and  $1.0 \times 10^{-5}$  M of  $1^{8+}$  (dose per pulse 20 Gy; optical pathlength = 1 cm). The solid red line represents a first order kinetics fit to the data.

TABLE 1.3: Rate constants for the reactions of the model compound  $2^{2+}$  and the tetramer  $1^{8+}$  with the radiolitically generated reducing species in argon-purged aqueous solution in the presence of 0.1 M of 2-propanol. For comparison purposes the corresponding rate constants involving *Methyl Viologen* ( $MV^{2+}$ ) are also reported.<sup>35 36</sup>

Compound	Reducing species	$k, M^{-1} cm^{-1}$
$2^{2+}$	$e^-_{aq}$	$5.0 \times 10^{10}$
	$(CH_3)_2 \bullet COH$	$3.2 \times 10^9$
$1^{8+}$	$e^-_{aq}$	$7.0 \times 10^{10}$
	$(CH_3)_2 \bullet COH$	$4.6 \times 10^9$
$MV^{2+}$	$e^-_{aq}$	$8.4 \times 10^{10}$
	$(CH_3)_2 \bullet COH$	$2.9 \times 10^9$

pulse radiolysis experiments, because of the very high dose-rate, second order reactions are favored; therefore, pimerization occurs also at doses much lower than in continuous radiolysis experiments, namely involving tetramer molecules in which only one bipyridinium unit is monoreduced. Although these results are preliminary and a more detailed study is in progress, the fact that upon reduction of  $1^{8+}$  the non-pimerized monoreduced bipyridinium is firstly formed and that, on a quite long time scale, the absorption features of the pimer are observed according to a second order kinetics, strongly supports that the pimerization process occurs intermolecularly.

**Computational Study.** To support the experimental data, the equilibrium

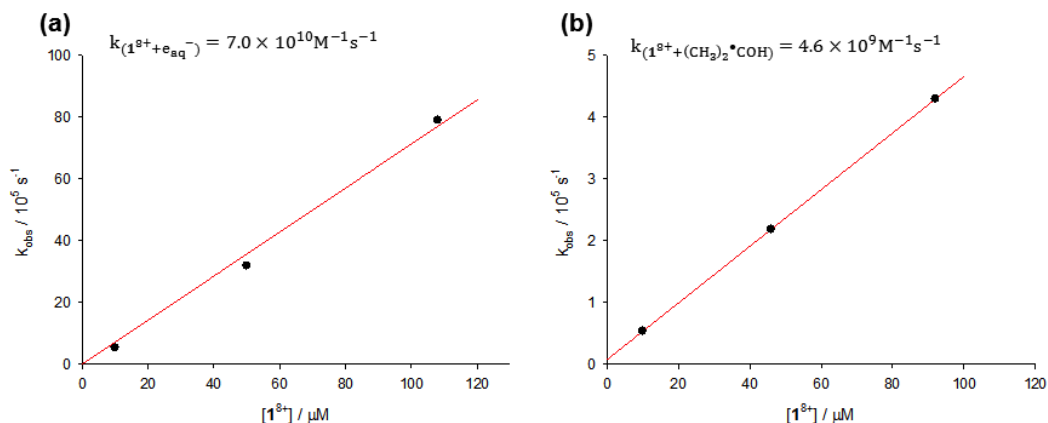


FIGURE 1.28: Dependence of  $k^{obs}$  for the buildup at 420 nm as a function of the  $1^{8+}$  concentration from which the second order rate constants of the reaction with  $e^-_{aq}$  (a) and  $(CH_3)_2\bullet COH$  (b) have been obtained (dose per pulse 20 Gy; optical pathlength = 1 cm).

structures of models for  $1^{8+}$  and  $2^{2+}$  were determined by CAM-B3LYP calculations using the polarizable continuum model (PCM) and water as solvent. The geometry rearrangement in water (compared to the gas phase) leads to a notable change of the computed absorption spectrum of  $1^{8+}$  which agrees with the splitting in two bands of the main feature in the absorption spectrum observed experimentally (figure 1.10). Upon reduction of  $2^{2+}$  to the radical  $2^{\bullet+}$  the system undergoes a remarkable geometry change corresponding to the planarization of the bipyridinium moiety as shown in figure 1.30. The dihedral angle between the two pyridinium rings is only  $4^\circ$  compared to  $41^\circ$  in the dication, in agreement with previous investigations on related viologen radical cations.<sup>39</sup> The planarization is accounted for by considering the shape of the orbital that accommodates the electron upon reduction, also shown in Figure 1.30. The bonding character of the orbital reinforces and shortens the C-C connecting the two pyridinium moieties and imparts a quinoidal structure to the bipyridinium moiety, as confirmed by the geometry optimization and the solid state structure of related viologen radical cations.<sup>40</sup> The same orbital is responsible for the formation of the pimer. Two pimers, labelled *parallel* and *antiparallel* (in the latter the two bipyridinium units point the phenyl group to opposite sides, see figure 1.31), were optimized in water using the M06L functional, which is known to describe accurately  $\pi$ - $\pi$  stacking interactions. A stable structure was obtained for both, as demonstrated by the bonding HOMO orbital, also shown in figure 1.31, which corresponds to the in

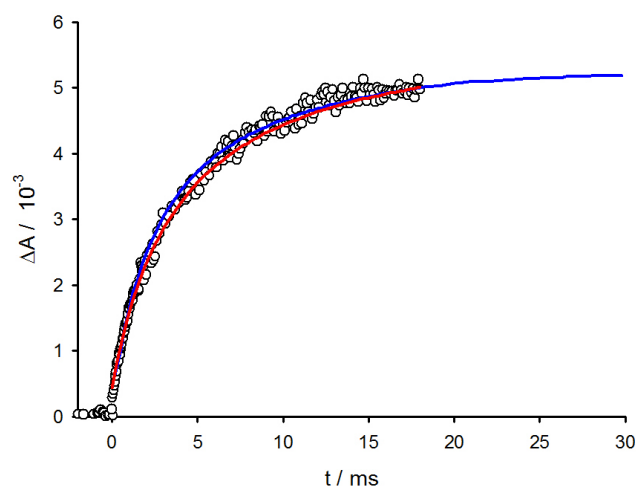


FIGURE 1.29: Time dependence of absorption at 1000 nm after pulse radiolysis of argon-purged aqueous solutions containing 0.1 M of 2-propanol and  $1.0 \times 10^{-5}$  M of  $1^{8+}$  (dose per pulse 7 Gy; optical pathlength = 1 cm). The solid red line represents a second order kinetic fit to the data; the blue line represents the simulation of the trace obtained by using Facsimile™ chemical modeling package in which a second order kinetics equation system was numerically integrated.

phase combination of the orbital in figure 1.30. The computed binding energies (17.11 kcal/mol for the *parallel* pimer and 13.94 kcal/mol for the *antiparallel* pimer) are in line with recent investigations on similar systems.<sup>41</sup> The distance between the two monomers is ca. 3.27 Å for the *antiparallel* pimer and 3.25 Å for the *parallel* pimer, again in line with recent investigations on similar bipyridinium-based radical cation pimers.<sup>39</sup> Upon four-electron reduction of  $1^{8+}$ , each bipyridinium unit of the tetramer undergoes a geometry change corresponding to the planarization as discussed for the model compound. The four monoreduced units are weakly or negligibly interacting as it is indicated by the identical optimized structure and energy of the singlet, triplet and quintet states. A picture of the spin density for the quintet state is shown in figure 1.32: as expected, the four radicals are mainly delocalized on the bipyridinium moieties. The distances between two terminal N on different units is about 20 Å while the distance between two internal N on different units is about 9 Å. Similarly, the distances between carbon atoms bridging the pyridinium rings on two different units are ca. 14 and 16 Å. Owing to the rather large distances and the delocalized nature of the spin (see figure 1.32), a weak interaction is expected in agreement with EPR results discussed above. The pimer formed by two four times reduced tetramers was also investigated and a picture of the optimized structure in water, showing

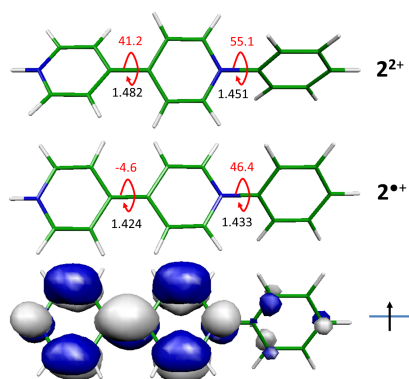


FIGURE 1.30: CAM-B3LYP/6-31G\* optimized geometries in water of  $2^{2+}$  (top) and  $2^{\bullet+}$  (middle) along with the orbital holding the unpaired electron in  $2^{\bullet+}$  (bottom)

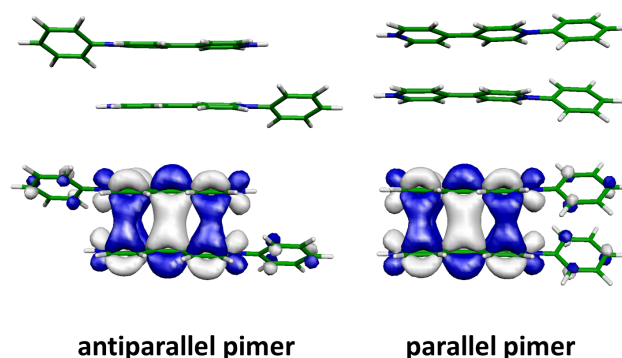


FIGURE 1.31: M06L/6-31G\* optimized geometries in water of the two possible pimers of  $2^{\bullet+}$  (top) and (bottom) shape of the orbital responsible for the pimer binding.

the strongly binding nature of the HOMO orbital, is reported in figure 1.33, plot a. Interestingly, using the M06L functional, the binding energy of the pimer for the tetramer is computed to be 11.40 kcal/mol, which is slightly reduced compared to the *antiparallel* pimer of the monomer (13.94 kcal/mol) at the same level of theory. The similar stability between the pimer formed by the model compound and that of the tetramer is, however, remarkable in view of the highly charged nature of the tetramer (4+) compared with the model compound (1+), which is expected to lead to a noticeable repulsion between the two tetramer species. The distance between the bipyridinium radical cation units in the pimer is 3.26 Å (M06L functional) which is also similar to the pimer formed in the case of the model compound.

To account for the observed absorption spectrum of the pimer in the tetramer compared with that of the model compound, we explored the structures of a multi-pimer system. To reduce the computational cost, we investigated the

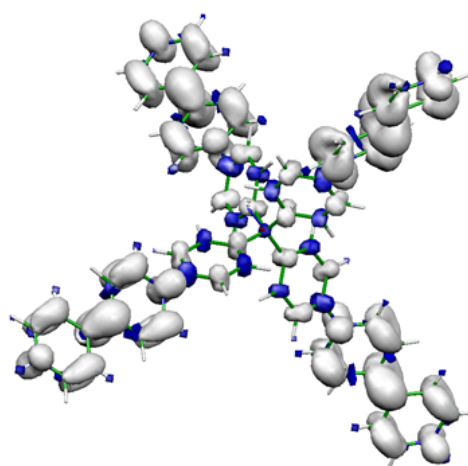


FIGURE 1.32: Computed unpaired spin density distribution in the quintet electronic state of  $1^{\bullet 4+}$

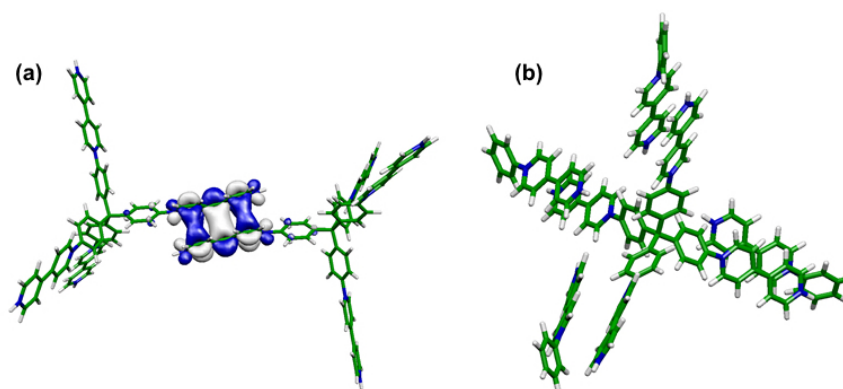


FIGURE 1.33: (a) M06L/6-31G\* optimized geometry in water of the pimer of  $1^{\bullet 4+}$  and shape of the orbital responsible for pimer binding. (b) M06L/6-31G\* optimized geometry in water of the model tetra-pimer formed by the four times reduced tetramer,  $1^{\bullet 4+}$ , and four units of  $2^{\bullet +}$

optimized geometry of a multi-pimer system in which each pimer involves one monoreduced bipyridinium unit of the tetramer and  $2^{\bullet +}$ , instead of a second reduced tetramer species. We investigated mono, bis, tris and tetra-pimer structures and their absorption spectra. All the pimers were stable, included the tetra-pimer (whose optimized geometry is shown in figure 1.33 plot b), despite the repulsion expected between the positive charged moieties. The electronic absorption spectra of all the investigated pimers were computed at TD-CAM-B3LYP level of theory. The spectra of the antiparallel pimer and of the parallel pimer formed by two  $2^{\bullet +}$  are almost identical. The computed spectra of  $2^{\bullet +}$  and its pimer (figure 1.34 plot a) in water are in good agreement with the experimental ones. In particular the low energy band in

the pimer along with the blue shift of the second band in the visible region of the pimer compared with the non-pimerized  $2^{\bullet+}$  is nicely reproduced. The computed absorption spectrum (TD-CAM-B3LYP) of the pimer formed by  $1^{\bullet4+}$  and four  $2^{\bullet+}$ , shown in 1.34 plot b, is in good agreement with the experimental spectrum as far as the two lowest energy transitions (visible and NIR spectral regions) are concerned.

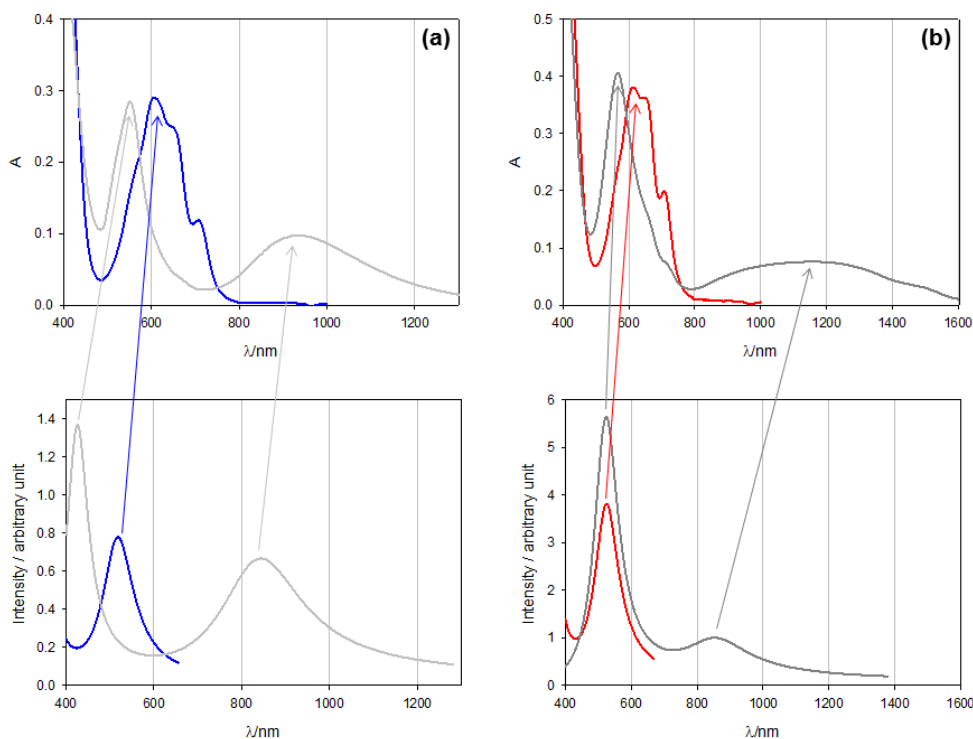


FIGURE 1.34: (a) Top: experimental absorption spectra of isolated radical cation  $2^{\bullet+}$  (blue line) and the pimer (grey line). Bottom: TD-CAM-B3LYP/6-31G\* computed absorption spectra of the isolated radical cation  $2^{\bullet+}$  (blue line) and the pimer (grey line). (b) Top: experimental absorption spectra of the non-pimerized  $1^{\bullet4+}$  (acetonitrile solution, ref line) and of the tetramer-based pimer (aqueous solution, dark grey line). Bottom: TD-CAM-B3LYP/6-31G\* computed absorption spectra of the isolated radical cation  $1^{\bullet4+}$  (ref line) and of the pimer formed by  $1^{\bullet4+}$  and four  $2^{\bullet+}$  (dark grey line).

## 1.2 Ruthenium Porphyrin Based Supramolecular Assemblies

Artificial photosystems mimicking the natural occurring ones play a prominent role in the contemporary research. In particular, the study of multichromophoric systems with a shape-persistent arrangement of the chromophores has gained increasing relevance since new properties may emerge from the interaction between the spatially organized units.<sup>42,43</sup> In this context porphyrins are particularly attractive supramolecular building blocks for their strong absorption in the visible spectral region, light emission and redox properties, as well as for their synthetic versatility: the variety of possible functionalization of the periphery, and the choice of the metal center, allows to tune electronic and photophysical properties and the structural features of these components. Furthermore the axial coordination chemistry of metallo-porphyrins is a useful strategy to create supramolecular porphyrin assemblies. As for many other metallo porphyrins, ruthenium-porphyrins can readily form stable five- and six coordinate complexes with nitrogen. One example of porphyrin array was published in 1999 by Anna Prodi and coworkers.<sup>44</sup> They synthesized a series of stable and inert side-to-face perpendicular arrays with free-base or zinc 4'-pyridylporphyrins and ruthenium porphyrins (figure 1.35). As expected, the study of the photophysi-

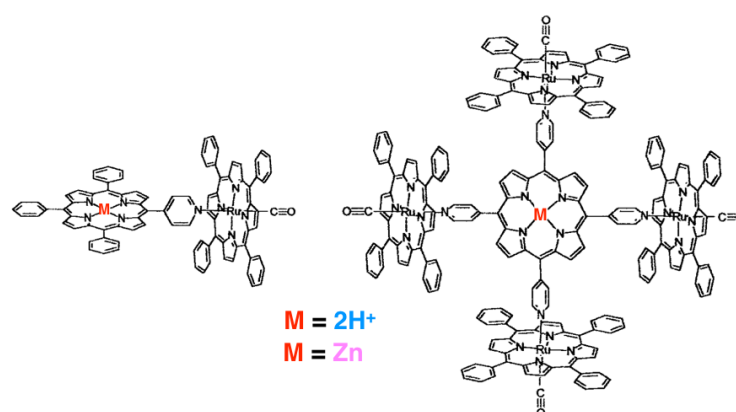


FIGURE 1.35: Schematic structure of the dimeric and pentameric supramolecular assembly. Adapted from Prodi *et al.*, Chem. Eur. J., 1999, 5, 2668 - 2679

cal behaviour of the dimeric and pentameric systems lead to the conclusion that the energy levels and many of the intrinsic properties of the molecular components are maintained within the arrays, but this doesn't mean, however, that the photophysical behavior of the arrays is simply a superposition

of that of the components. Indeed even a small intercomponent perturbation can lead to changes in the kinetics of intracomponent photophysical processes and, as described in the introduction, new intercomponent processes (energy or electron transfer) may occur. Looking at the energy-level diagrams for the pentameric system (figures 1.36), different intercomponent processes (thermodynamically allowed) can be identified for the various arrays. The processes that can occur are highlight in figure 1.36. Because of

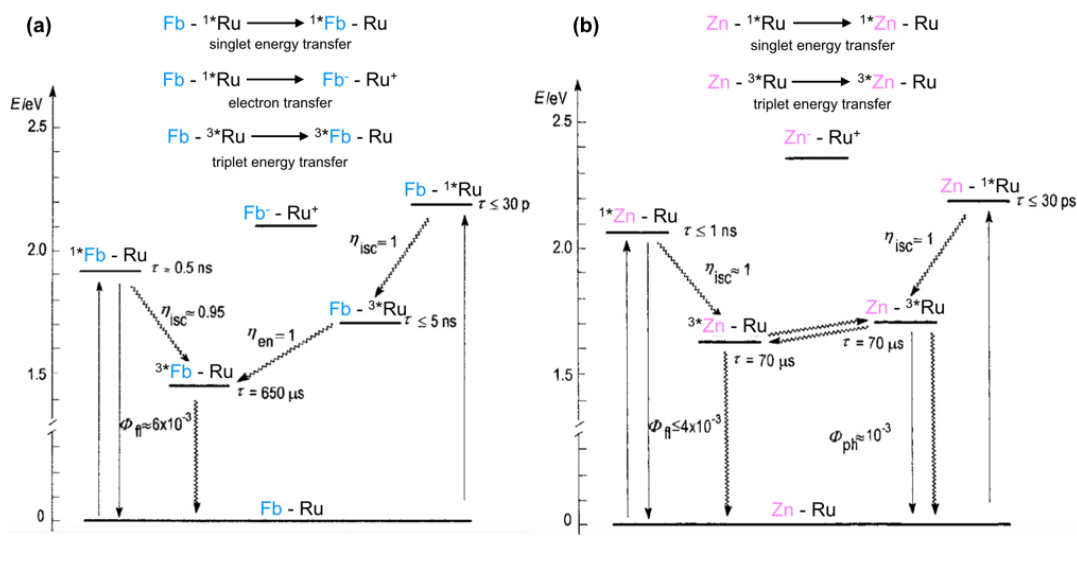


FIGURE 1.36: Energy level diagrams for the pentameric array based on free-base (a) and zinc (b) porphyrin. Adapted from Prodi *et al.*, Chem. Eur. J., 1999, 5, 2668 - 2679

spectral overlap, is not possible the selective excitation of the two molecular components, to check for the occurrence of the intercomponent processes listed above. Even so, the additive character of the spectra permits to evaluate the relative amount of exciting light absorbed, at any wavelength, by the various molecular components. The comparison with the emission spectra of the units shows that fluorescence emission arise from free-base or zinc porphyrin (axial units), since the ruthenium porphyrin are intrinsically non fluorescent. However, the fluorescence from the axial porphyrin unit could, in principle, arise not only from direct excitation of the free-base or zinc porphyrin, but also from singlet energy transfer from the ruthenium ones (figure 1.36). Nevertheless, this does not take place: the fluorescence excitation spectrum of the pentameric array shows the complete lack of ruthenium porphyrin absorption features and the correspondence to the absorption spectrum of free-base porphyrin. Interestingly, the fluorescence that originates from direct excitation of the free-base or zinc porphyrin units in the arrays



is definitely weaker than that of the corresponding monomeric model systems. This decrease was accompanied, by a parallel decrease in fluorescence lifetime: indeed the free-base and zinc porphyrin units become less emitting and shorter lived when the array is formed. Since the electron transfer states are too high (figure 1.36) to be involved in the fluorescence quenching (further proof is the fact that the quenching persists at 77K, in rigid matrix), this decrease can be explained considering the spin-orbit perturbation effect, provided by the ruthenium (heavy-atom effect), responsible of the enhancement of the intersystem crossing process in the axial porphyrin.

To study the behaviour at the triplet level, they detect the phosphorescence of the ruthenium porphyrin unit, that is completely quenched in the assembly: transient absorption experiments demonstrate that the quenching of the triplet state of the ruthenium porphyrin and the sensitization of the free-base one, since the triplet-triplet spectrum of the ruthenium porphyrin is replaced by that of the free-base porphyrin. This is an evidence of a triplet energy transfer process in the system.

In the case of the array with zinc porphyrin, the situation is different since the phosphorescence of the ruthenium porphyrin is still detectable. In transient absorption, the spectrum is comparable with the zinc porphyrin one, but the time scale for the transient decay is shorter than the free zinc porphyrin but longer than the free ruthenium one: this feature can be explain considering the fact that the zinc porphyrin triplet is sufficiently close to the ruthenium triplet to have an equilibration between the two states prior to deactivation.

### 1.2.1 Tetrahedral Array of Ruthenium Porphyrins with Bipyridinium Based Tetramer

The same tetramer used in the formation of the supramolecular system described in section 1.1.1, except for the presence of *N*-methyl group, is involved in the formation of a tetrahedral array of ruthenium porphyrins. This shape-persistent tetramer  $1^{4+}$  is one of the building blocks of the assembly; the other component is a tetrafluorinated ruthenium porphyrin (Ru(CO)FTPP), that was synthesized in Prof. Elisabetta Iengo's group, University of Trieste. As a model system, we considered the association of one of four subunits of the tetramer ( $2^{+}$ ) and the same ruthenium porphyrin (1.37). We decided to use a fluorinated porphyrin for several reason:<sup>45</sup>

- fluorine ionization energy is appreciably higher than for the other halogens and is known to exhibit the highest electronegativity of any atoms; so it is used to alter the electronic properties of the ligand system
- the high strength of bonds between fluorine and most other atoms present in fluorinated compounds provide their special resistance to temperature and oxidants;
- fluorination can alter the solubility of the ligand system;
- selective fluorination can introduce a useful magnetic label that provide excellent signal noise ratio for NMR spectroscopy

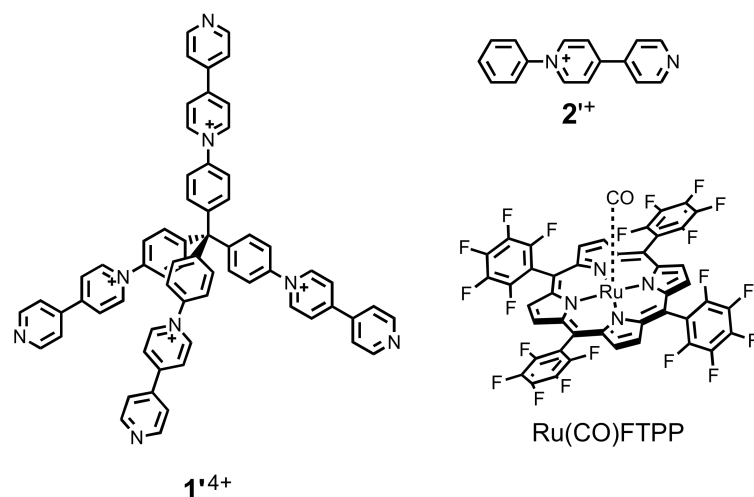


FIGURE 1.37: Chemical structures of the compounds  $1'^{4+}$ ,  $2'^{+}$  and  $\text{Ru}(\text{CO})\text{FTPP}$

The choice of the building blocks as the aim to obtain the formation of the supramolecular arrays, in organic solution (acetone or  $\text{CH}_2\text{Cl}_2$ , at room temperature, since is well known that ruthenium porphyrins are able to axially coordinate pyridine.<sup>46,47</sup> First of all, we studied the photophysical properties of  $1'^{4+}$  and  $2'^{+}$ , as hexafluorophostate salt, in acetonitrile. The absorption spectrum of  $1'^{4+}$  shows a band in the UV spectrum with maximum at 302 nm which is significantly redshifted ( $2350\text{ cm}^{-1}$ ) compared with that expected for four noninteracting units of the model  $2'^{+}$ .<sup>28</sup> Moreover, tetramer  $1'^{4+}$  shows a very strong blue emission band at 464 nm with a  $\Phi_{em} = 40\%$ , compared with an extremely weak emission of the model  $2'^{+}$  at 431 nm (table 1.4).

**Formation of  $2'^{+}:\text{Ru}(\text{CO})\text{FTPP}$  assembly.** There are several techniques to follow the formation of the supramolecular arrays: we used spectrophotometric, spectrofluorimetric and NMR titration (performed in University of

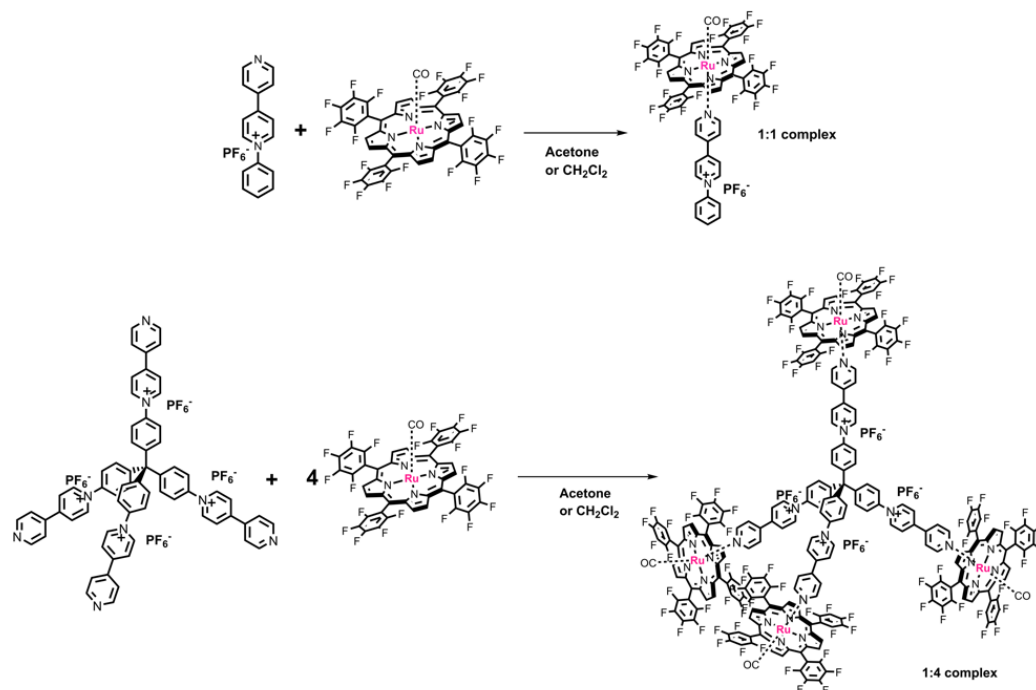


FIGURE 1.38: Schematization of the supramolecular arrays' formation.

TABLE 1.4: Photophysical data of tetramer 1'<sup>4+</sup> and monomer 2'<sup>+</sup> in acetonitrile at 298 K

	Absorption		Emission		
	$\lambda/\text{nm}$	$\epsilon/10^4 \text{ M}^{-1}\text{cm}^{-1}$	$\lambda/\text{nm}$	$\Phi_{em}$	$\tau/\text{ns}$
1' <sup>4+</sup>	302	6.26	464	0.4	3.4
2' <sup>+</sup>	282	2.08	431	0.004	1.7

Trieste). For the spectrophotometric titration, we dissolved the Ru(CO)FTPP in acetone and we add increasing amounts of 2'<sup>+</sup> and 1'<sup>4+</sup>. We decided to replace acetonitrile since it was too coordinating and we were not able to observe the assembly formation. Following variations in absorption spectra is possible to determine the stoichiometry of the system. In the case of model system, we observed variations in the Soret Band (1) and in the Q-bands (2): the Soret-band is red-shifted, but more significant variation are appreciable in the Q-bands region (figure 1.40) The trend obtained from *absorbance* versus 2'<sup>+</sup> *equivalents added* (figure 1.41) show a plateau coming after the addition of ca. 1 equivalent of 2'<sup>+</sup>; that suggests a stoichiometry of 1:1 2'<sup>+</sup>:Ru(CO)FTPP. As expected, a ruthenium porphyrin is able to complex one molecule of 2'<sup>+</sup>.

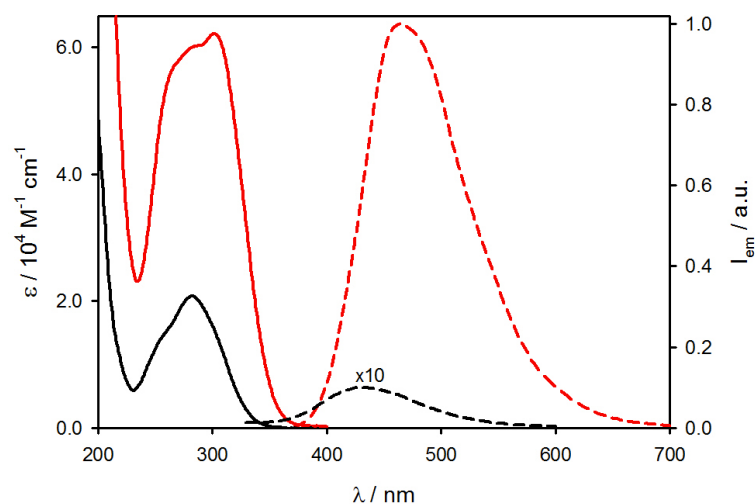


FIGURE 1.39: Absorption (solid lines) and emission spectra (dashed lines) of  $1'^{4+}$  (red lines) and  $2'^{+}$  (black lines) in acetonitrile at 298 K for optically matched solution at the excitation wavelength ( $\lambda_{ex}=285$  nm).

By global fitting of the absorption changes it was estimated that the formation of the supramolecular system had a constant of  $3 \times 10^7 \text{M}^{-1}$ .

$^1\text{H-NMR}$  spectra were exploited to follow the formation of the supramolecular arrays, since the inert and relatively strong nature of the ruthenium-nitrogen bond provides clear spectra with sharp resonances: the coordination of the pyridyl group to the ruthenium center is accompanied by strong up-field shifts of the proton resonances of the axial ligand; this effect decreases as the distance from the perpendicular porphyrin aromatic macrocycle increases. On the other hand, the resonances of the metallo-porphyrin are not particularly affected by axial coordination to the metal center. Moreover, since the single components and the assembled system are in slow exchange with respect to the NMR timescale, it is easy to monitor, at least for the model system, the progressive formation of the assembly, that appears as a set of sharp resonances well distinguishable from those of the free components. Increasing amounts of  $\text{Ru}(\text{CO})\text{FTPP}$  were added to an acetone- $d_6$  solution of  $2'^{+}$  until the total disappearance of the proton signals related to the free ligand in the aromatic region, and concomitant growth of the peaks of the same unit within the assembly: the stoichiometry obtained is  $1:1$

Single crystals suitable for X-Ray diffraction of the model system were obtained by slow diffusion of *n*-hexane into concentrated acetone solutions of  $2'^{+}$  and  $\text{Ru}(\text{CO})\text{FTPP}$ . The model system crystallizes in a monoclinic  $P2_1/n$

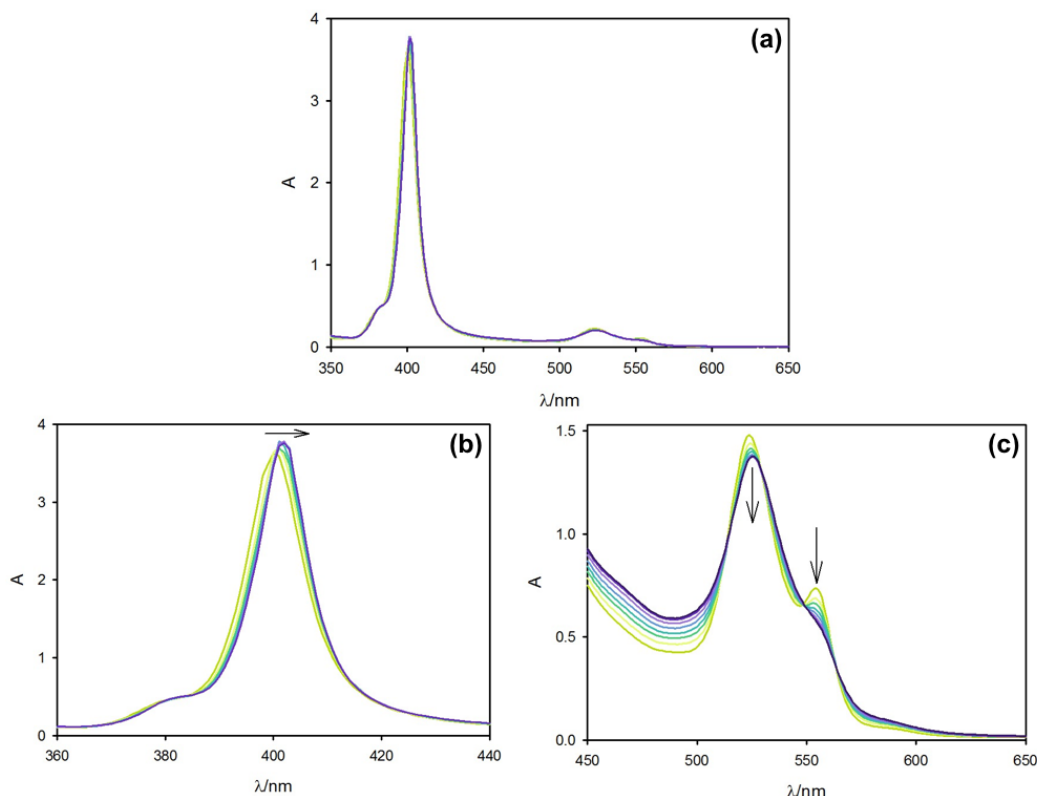


FIGURE 1.40: Complete absorption spectra recorded after increasing amount of 2<sup>+</sup> (up to 2 equivalents) to a Ru(CO)FTPP dissolved in acetone (a). Soret band (b) and Q-bands (c) regions enlarged. The green solid line is the spectrum of the free porphyrin in solution; the violet solid line is the spectrum recorder after the addition of 2 equivalents of 2<sup>+</sup>.

space group with one complex contained in the crystallographic asymmetric unit (figure 1.43, left) and a total of four complexes present in the unit cell. The PF<sub>6</sub><sup>-</sup> counterion is found close to the positively charged pyridinium nitrogen. Notably, the fluorine of the PF<sub>6</sub><sup>-</sup> anions present orthogonal close contacts with the fluorines of the phenyl pertaining to two different neighboring porphyrins, possibly indicating the presence of a weak halogen bonding network. The void space is filled by two acetone and one disordered water molecule, most likely deriving from wet acetone. Another polymorphic crystalline form has been identified during crystals screening. These crystals grown as thinner red plates from the *n*-hexane/acetone mixtures and showed a bigger orthorhombic *Pca*2<sub>1</sub> unit cell. The volume of the cell is three times larger than that found for the other polymorph described above, and contains three independent complexes in the asymmetric unit (figure 1.43, right). The crystal packing appears also different, with close contacts among adjacent complex molecules and smaller cavities surrounding the pyridylpyridinium

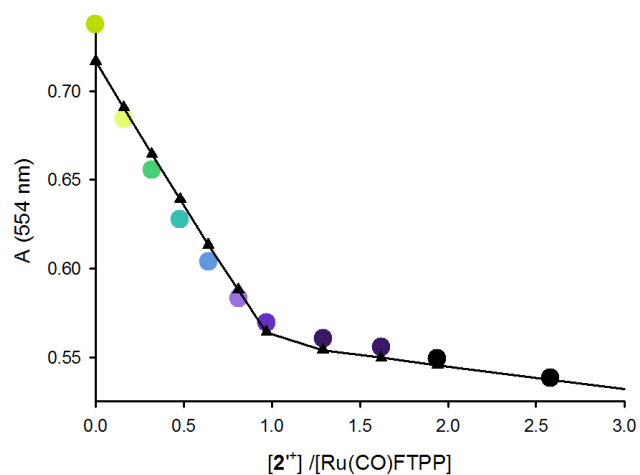


FIGURE 1.41: Global fitting of the absorption changes at 554 nm upon addition of  $2'^+$ .

moieties, in which only five well defined acetone molecules have been identified. Furthermore, large channels, aligned with crystallographic  $a$  axis are filled with disordered solvent. The crystal structure were resolved at the Elettra Synchrotron Institute, Trieste.

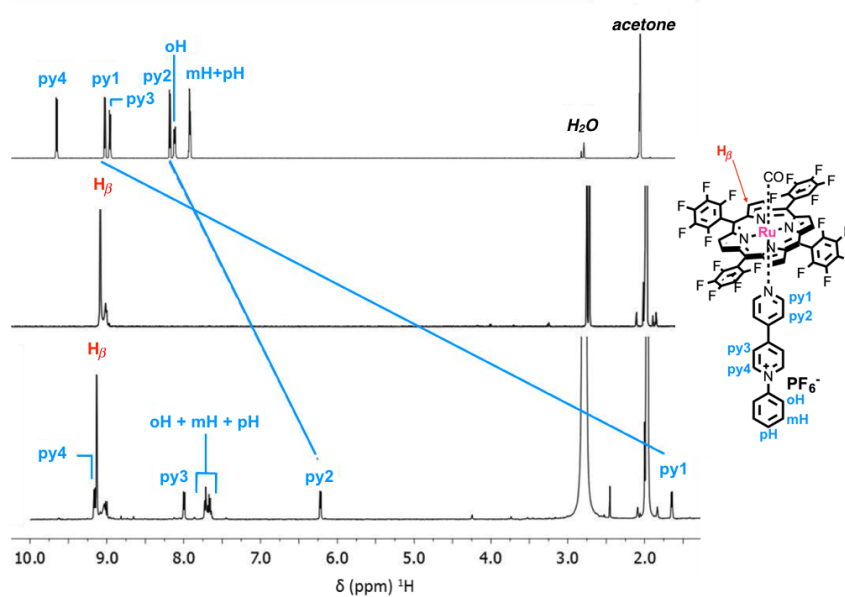


FIGURE 1.42: <sup>1</sup>H-NMR spectra (acetone-d<sub>6</sub>, 500 MHz) of 2<sup>+</sup> (top), Ru(CO)FTPP (center) and assembled system (bottom). Dashed lines highlight the resonances for the proton signals of the scaffold with the largest observed upfield shifts.

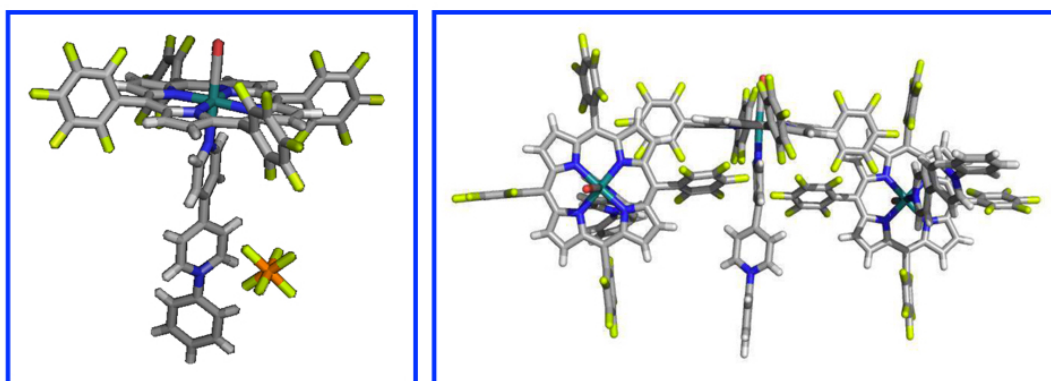


FIGURE 1.43: X-ray crystal structure of model system in the two crystalline polymorph. Stick representation of the crystal packing, the contacts of PF<sub>6</sub><sup>-</sup> anions with the fluorine of two orthogonal pentafluorinated phenyl ring (left); stick representation of the head-to-tail disposition of the three model systems found in the asymmetric units (right).

**Formation of  $1'^{4+}$ :Ru(CO)FTPP assembly.** Once we studied the simplest assembly, we decided to investigate the formation of the supramolecular assembly with the tetramer  $1'^{4+}$  and the Ru(CO)FTPP. As we operated in the case of  $2'^{+}$ , we started with the spectrophotometric titration: we added increasing amounts of  $1'^{4+}$  to a solution of Ru(CO)FTPP, dissolved in acetone. The variation in the absorption spectrum of the Ru(CO)FTPP are similar to those observed in the case of monomer. The Soret-band is red-shifted while in the Q-bands zone a decreasing value of absorbance is evident (figure 1.44, plot b and c). To determine the stoichiometry of the system we considered

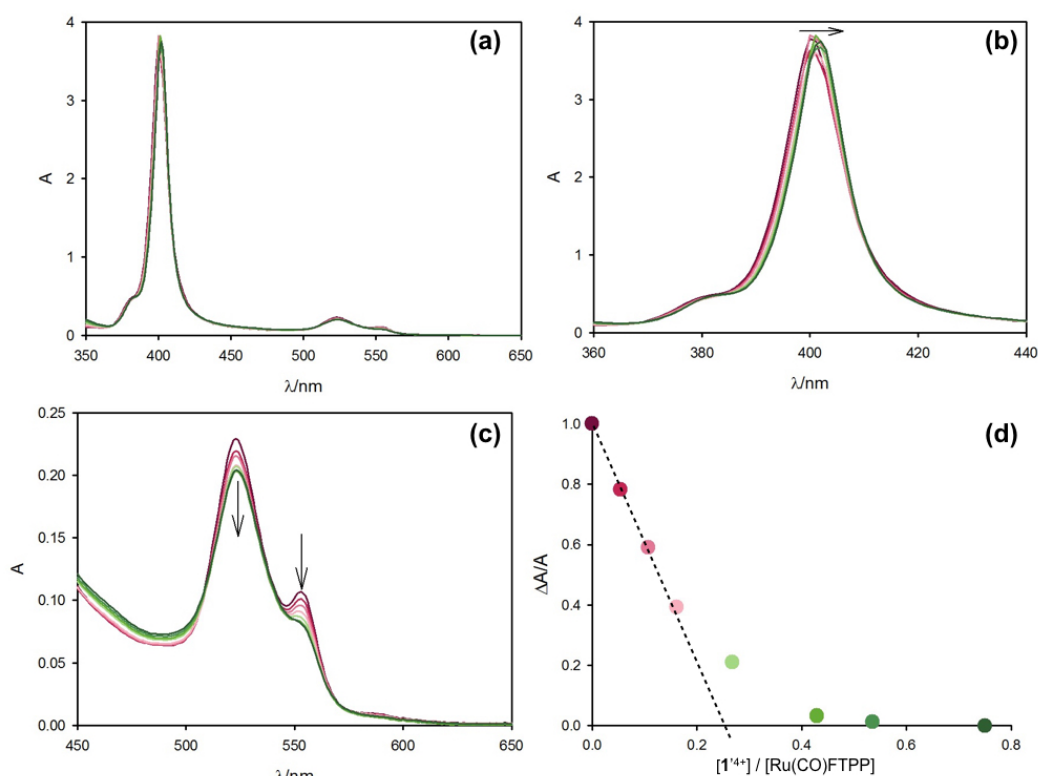


FIGURE 1.44: Complete absorption spectra recorded after increasing amount of  $1'^{4+}$  (up to 0.78 equivalents) to a Ru(CO)FTPP dissolved in acetone (a). Soret band (b) and Q-bands (c) regions enlarged. The violet solid line is the spectrum of the free porphyrin in solution; the dark green solid line is the spectrum recorded after the addition of 0.78 equivalents of  $1'^{4+}$ . Normalized absorption changes at 525 nm upon addition of  $1'^{4+}$  (d).

the trend obtained from *absorbance versus number of tetramer equivalents added*. In that case we saw a plateau coming after the addition of 0.25 equivalent of tetramer: four Ru(CO)FTPP can complex one of the subunits of the tetramer, as expected. The formation of the assembly occurs with a stoichiometry of



1:4  $1^{4+}$ :Ru(CO)FTPP. Since the tetramer  $1^{4+}$  is a good chromophore, is possible to follow the variations in the emission spectrum of the tetramer, when an increasing amount of Ru(CO)FTPP is added in solution. As shown in figure 1.45 plot a, when the concentration of the ruthenium porphyrin increases in solution, an increasing quenching of the tetramer emission occurs. However, the emission spectra are affected by reabsorption of the porphyrin, since the absorption profile of the Ru(CO)FTPP overlaps the emission spectrum of  $1^{4+}$  (figure 1.45 plot a). Nevertheless, if the emission intensity considered is referred to 600 nm, this effect can be ignored. Analyzing the trend *emission intensity versus equivalents of porphyrin added*, we observed that the  $1^{4+}$  fluorescence is completely quenched when less than four equivalents of Ru(CO)FTPP are added. That effect is quite common in spectrofluorimetric titrations: indeed one porphyrin is enough to quench the 65% of the tetramer emission. Since we couldn't find a suitable model for the fitting of the formation of the assembly, we used a simple model, approximate to the real one. We estimated the association constant for the complexation of one subunit and one Ru(CO)FTPP (1:1 stoichiometry), considering four times the concentration of the tetramer. It is a good approximation, as long as the four subunits behave independently in the association with the ruthenium porphyrins. The value obtained is  $4 \times 10^6 \text{ M}^{-1}$ , one order of magnitude lower than the one estimate for the model compound: this could be explained since the subunits are sterically hindered in the tetramer structure.

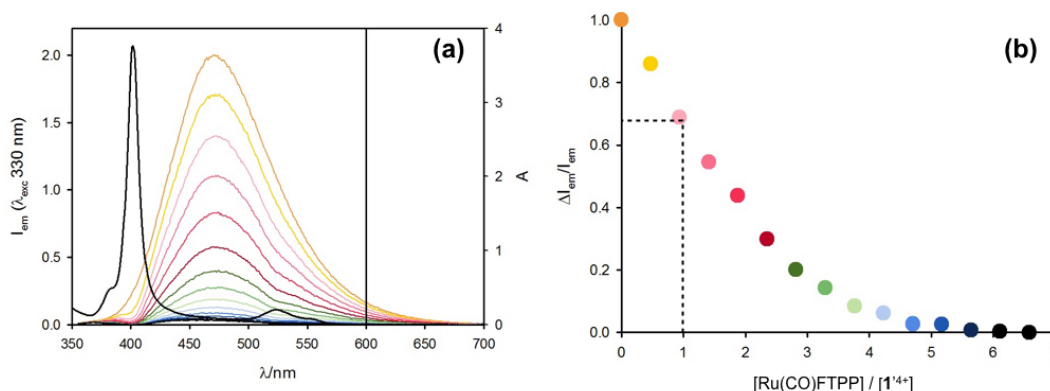


FIGURE 1.45: (a) emission ( $\lambda_{ex}=330 \text{ nm}$ ) spectra of acetone solution of  $1^{4+}$  upon addition of Ru(CO)FTPP: 0 (orange line), 6.5 equivalents per tetramer (dark blue line); the black solid line is the absorption spectrum collected during the spectrophotometric titration, superimposed to evaluate the reabsorption effect. (b) Normalized emission intensity changes at 600 nm upon addition of Ru(CO)FTPP.

Since the ruthenium porphyrin shows a weak phosphorescence emission in de-aerated solution ( $\Phi_{em} = 0.086\%$ ,  $\tau = 0.012$  ms), it's interesting to observe what happens to the phosphorescence emission in the supramolecular system. When we added an excess of tetramer in solution, the phosphorescence is completely quenched (figure 1.46), as it was observed in the case of tetramer's fluorescence emission during the titration (figure 1.45). When the supramolecular system is formed, a quenching of the emission occurs in both cases, tetramer and porphyrin excitation. We hypothesized the presence of a charge-transfer (CT) state energetically located under the triplet state of the porphyrin, and an electron transfer could occur from the singlet and the triplet of the tetramer and porphyrin respectively. To verify our hypothesis

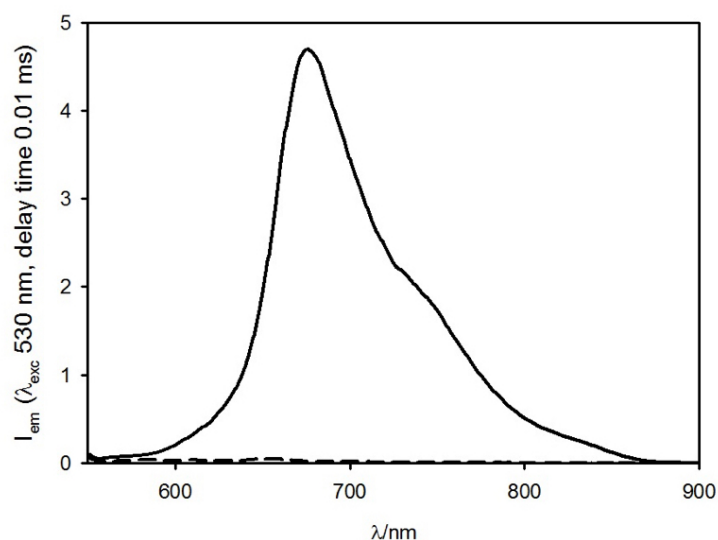


FIGURE 1.46: Phosphorescence emission spectra of the free ruthenium porphyrin in de-oxygenated  $\text{CH}_2\text{Cl}_2$  (black solid line) solution and after the addition of an excess of  $1'4^+$ , added from acetone (black dashed line).

we estimated the energy of the CT state as the sum of energy required for the tetramer reduction and porphyrin oxidation. This can be done from the differential pulse voltammetry of the supramolecular system, in presence of ferrocene as internal standard (figure 1.47, left). We estimated the singlet and triplet state energy of the tetramer and porphyrin respectively, from the 20% of emission maxima; for the energy of the  $S_1$  of the porphyrin, it is a good approximation to consider the absorption maximum of the lowest energy Q-band. Finally, from differential pulse voltammetry measurements we are able to locate the CT state under the triplet of the porphyrin: an electron transfer could occur from both  $S_1$  of the tetramer and  $T_1$  of the porphyrin (figure 1.47, right).

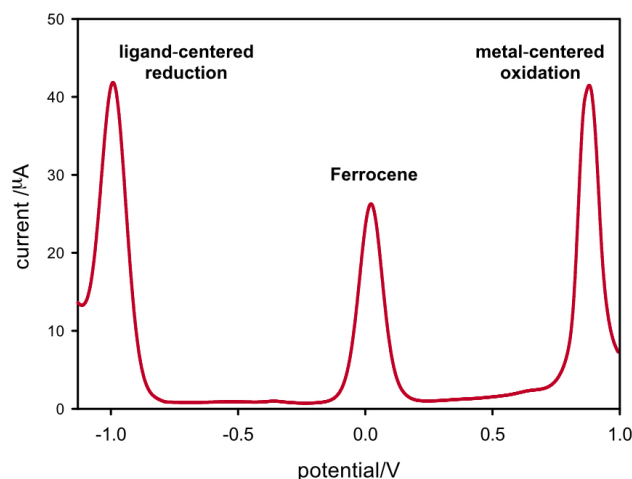


FIGURE 1.47: Differential pulse voltammogram of argon-purged  $\text{CH}_2\text{Cl}_2$  of the supramolecular assembly  $1^{4+}:\text{Ru}(\text{CO})\text{FTPP}$  1:4, in the presence of 0.1 M  $\text{TBAPF}_6$ . Scan rate=0.02 V/s; working electrode glassy carbon. On the right, the Jabłoński diagram of the two components of the assembly with the energy of the electronic states.

A further proof could be obtained by collecting the emission spectra of the free porphyrin and the complexed one, at 77K. Conversely, in that case we are able to see a residual emission, even when an excess of tetramer is added in solution: since the lifetime of the free porphyrin is the same measured for the complexed system ( $\tau = 0.11$  ms), we can attribute this emission to the porphyrin in the assembly. At 77K the emission spectrum is markedly dependent on the rigidity of the medium: this effect, namely *rigidochromic effect*, implicate a repositioning of the *CT*, that now is located above the *T1* of the porphyrin (in that condition no stabilization of the solvent occurs). At that point, the electron transfer is not efficient anymore, and we can still appreciate the phosphorescence of the porphyrin (figure 1.48).

To sum up, if we excite selectively  $1^{4+}$  or the porphyrin, we populate the *S1* states. From the  $1^{4+}$  *S1* state two processes could occur: the energy transfer to the *S1* of the porphyrin, or the direct electron transfer to the *CT* state. From the *S1* porphyrin state an inter system crossing to the *T1*: finally, from here, we can have again the electron transfer to the *CT* (figure 1.49).

The formation of the assembly can also be followed by  $^1\text{H}$  NMR (performed in University of Trieste), with the same procedure just described for the corresponding model system. Up to the addition of four equivalents of  $\text{Ru}(\text{CO})\text{FTPP}$ , the NMR spectra are very crowded and present a large number of peaks, due to the co-existence of intermediate species like excess of free  $1^{4+}$  and partially assembled systems with one up to four coordinated ruthenium-porphyrins

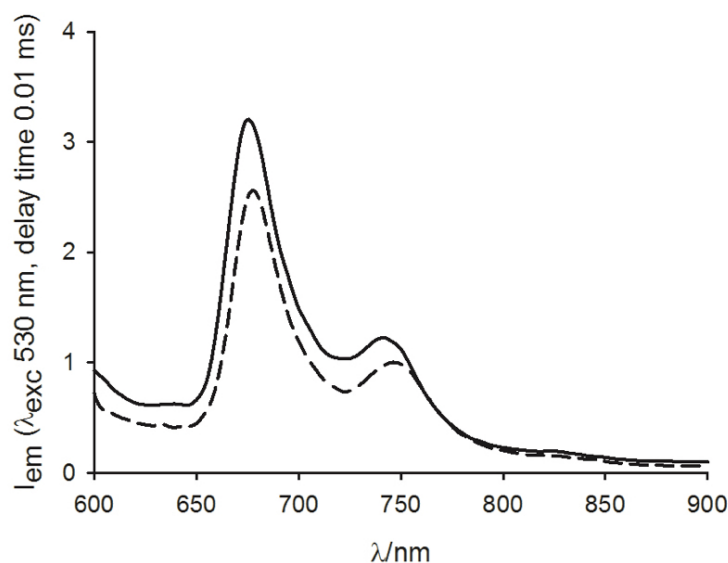


FIGURE 1.48: Phosphorescence emission spectra of the free ruthenium porphyrin in  $\text{CH}_2\text{Cl}_2$  (black solid line) and after the addition of an excess of  $1'^{4+}$ , added from acetone (black dashed line) at 77K.

(figure 1.50). Upon the addition of four equivalents of porphyrin, the  $^1\text{H}$ -spectrum simplifies considerably, both in terms of number and position of the proton signals, that looks very similar to that of the corresponding model system (figure 1.42) despite the signal integration ratio. These spectral features are in agreement with the formation of a highly symmetrical species, in which each one of the four arms of the scaffold is axially bound to one ruthenium-porphyrin center. The spectrum evidenced just one set of signals: that means the four subunits are magnetically equivalent. Respect to the model system, the entity of the upfield shift of the  $1'^{4+}$  proton resonances is larger, as a consequence of the increased shielding effect deriving from the overall contribution of four porphyrins. In the case of  $1'^{4+}:\text{Ru}(\text{CO})\text{FTPP}$  system,  $^{19}\text{F}$ -NMR experiments were also employed, to obtain additional structural information. Indeed, phenyl rings' rotation is slow on the NMR time scale, and they result perpendicular to the porphyrin plane: the two halves of the phenyl rings are not equivalent, because the presence of the CO moiety on one side of the porphyrin, which is strongly bound to the ruthenium center and whose triple bond exert a de-shielding effect on the fluorines pointing in a perpendicular direction. This effect is enhanced in the assembled system, when the subunit of  $1'^{4+}$  coordinate the  $\text{Ru}(\text{CO})\text{FTPP}$ . Accordingly, the ring's half facing the ligand undergoes a further shield effect, so we were able to distinguish which fluorine is oriented towards the opposite plane of the porphyrin and which not (figure 1.51). Again we evidenced just one set

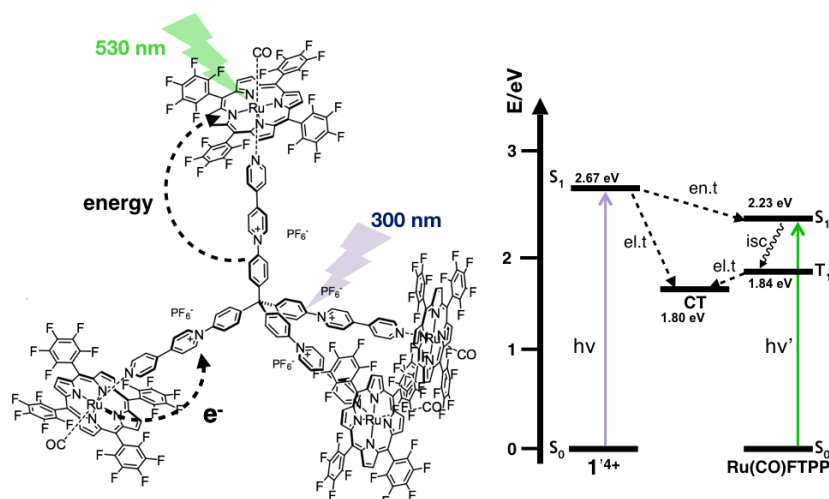


FIGURE 1.49: A schematization of all the photophysical processes that can occur in the supramolecular assembly.

of signals, which means that the four subunits of the tetramer are magnetically equivalent and the system is highly symmetric. Integrating  $^{19}F$ -NMR signal we were able to prove again the formation of 1:4 assembly.

To recover additional information on the size of the supramolecular system, we performed some Diffusion-Ordered Spectroscopy (DOSY) measurements.<sup>48</sup> This technique is widely used to analyze supramolecular assembly, since it allows to estimate the hydrodynamic radius of a species in solution. In appropriate conditions it is possible to appreciate how NMR signals decay as a result of the species diffusion in solution. The mathematical analysis of the decay produces the translational diffusion coefficient, a value inversely proportional to the hydrodynamic radius. This is achieved by combining radio-frequency pulses as used in routine NMR spectroscopy with magnetic field gradients that encode spatial information. The magnetic field  $B$  varies linearly along the  $z$ -axis of a quantity  $G$  representing the gradient intensity. Recording consecutive 1D spectra in which  $G$  is gradually increased, an attenuation of the signals is observed due to the diffusion rate of the species in solution, since during the gradient delay spins move as a consequence of the self-diffusion. The attenuation of the signal is strictly correlated with the diffusion coefficient ( $D_t$ ) of the species generating the analyzed signal through the *Stejskal-Tanner* equation

$$\frac{I}{I_0} = \exp(-D_t \gamma^2 \delta^2 G^2 \Delta) \quad (1.13)$$

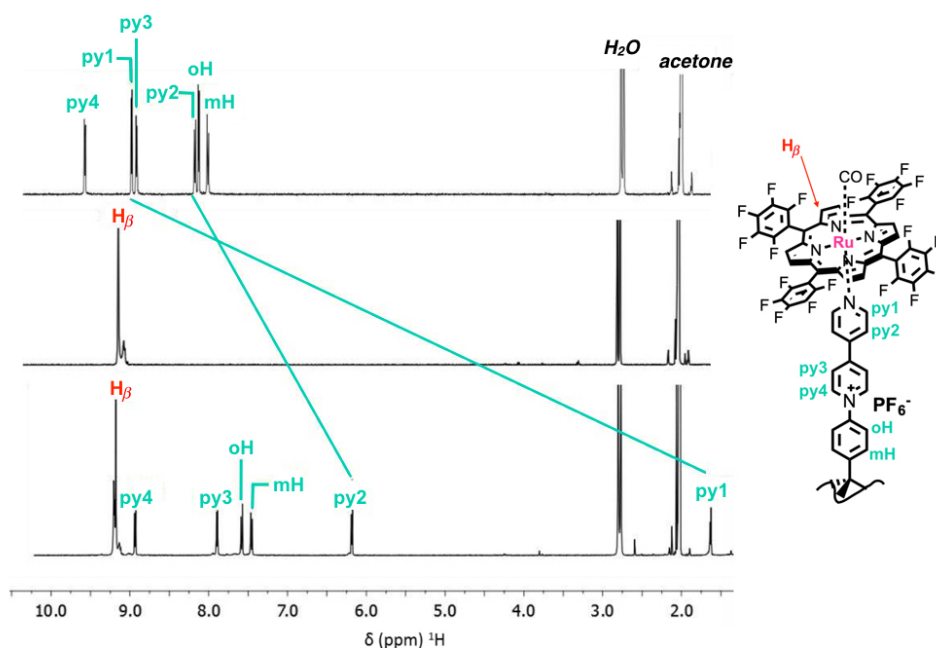


FIGURE 1.50:  $^1\text{H}$ -NMR spectra (acetone- $d_6$ , 500 MHz) of  $1^{4+}$  (top), Ru(CO)FTPP (center) and assembled system (bottom). Dashed lines highlight the resonances for the proton signals of the scaffold with the largest observed upfield shifts. For simplicity, only one of the four arms is depicted, with proton labeling scheme.

where  $I/I_0$  is the relative intensity of the considered signal,  $D_t$  the translational diffusion coefficient of the species generating the signal,  $\gamma$  the gyromagnetic ratio,  $\delta$  the gradient length,  $G$  the gradient intensity and  $\Delta$  the diffusion delay. The experimental parameters  $\gamma$ ,  $\delta$  and  $\Delta$  are constant during the measurements, we can rewrite the equation 1.13 as

$$\frac{I}{I_0} = \exp(-D_t b) \quad (1.14)$$

where  $b$  indicates  $\gamma^2 \delta^2 G^2 \Delta$ .  $D_t$  can be extracted by fitting the experimental decay with a mono-exponential function (1.14) and then, applying the linearization  $-\ln(I/I_0)$  versus  $b$ , the  $D_t$  can be obtained as the slope of the data regression line. To estimate an accurate value of  $D_t$ , the average among the  $D_t$  values obtained from the attenuation of each signal measured in the 1D spectra is calculated, for the considered compound. Data acquired were also processed (using the automatic Bayesian transform processing of the MestReNova<sup>®</sup> software) to obtain a bidimensional plot, in which conventional 1D traces are displayed in one dimension and diffusion rates in the other. The map so obtained in the horizontal rows has species having the

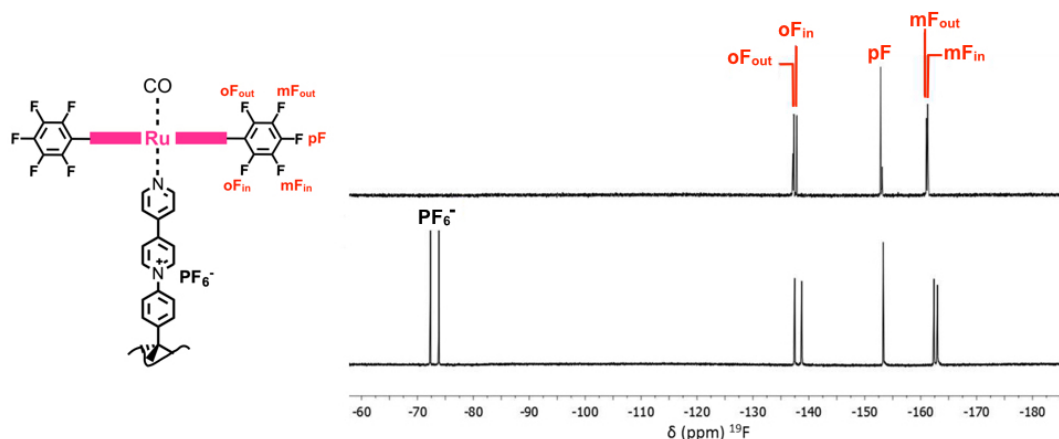


FIGURE 1.51:  $^{19}\text{F}$ -NMR spectra (acetone- $d_6$ , 470.12 MHz) of Ru(CO)FTPP (top) and the assembled system (bottom). The Ru(CO)FTPP is drawn in a side-view perspective to better show the phenyl fluorines in/out average disposition, with respect to the porphyrin plane.

same  $D_t$ , therefore, the same hydrodynamic radius  $r_H$ . All the signals, related to the same molecular system, have the same diffusion coefficient  $D_t$ , so in the 2D map the signals are separate depending on the  $D_t$  value. If all the signals are aligned, it is possible to demonstrate the formation of just one species, in our case bigger than its component. This last feature is also particularly useful to exclude the presence of residual amounts of free building units, that maybe missed from the 1D trace: indeed when the building units display overlapping signals in the free and assembled form, the 2D map is the only way to evidenced the free components presence. The correlation between the diffusion coefficient and the hydrodynamic radius follows the *Stokes-Einstein* equation for linear diffusion:

$$D_t = \frac{kT}{6\pi\eta r_H} \quad (1.15)$$

where  $k$  is the Boltzmann constant,  $T$  is the absolute temperature and  $\eta$  is the fluid viscosity (dependent from solvent and temperature). A species with a diffusion coefficient  $D_t$  diffuses in a given solvent with the same rate of a sphere of  $r_H$ , which can be considered the hydrodynamic radius of the molecule if its shape fits the spherical approximation. If the species has a significant distortion from a spherical shape, the equation can be appropriately modified as follows:

$$D_t = \frac{kT}{f_s c \pi \eta r_H} \quad (1.16)$$



where  $f_s$  is the shape factor and  $c$  the size factor.<sup>49</sup> Usually, unless the system is accurately described by the spherical approximation, the  $r_H$  obtained from the diffusion coefficient is purely qualitative, while the relative comparison between the  $r_H$  values, calculated for the isolated building units and the assembled systems, is quantitatively more meaningful. It is possible to com-

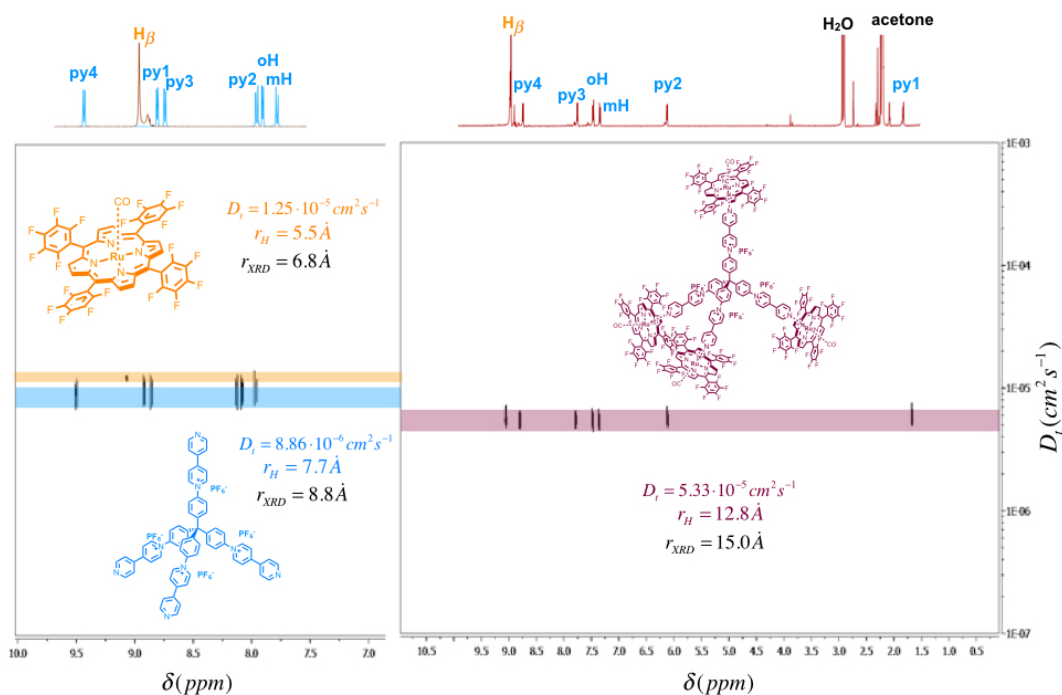


FIGURE 1.52: Comparison between 2D  $^1\text{H}$ -DOSY spectra (Bayesian transform, acetone- $d_6$ , 500 MHz) of Ru(CO)FTPP (orange),  $1^{4+}$  (blue) and the assembled system (dark red). On the horizontal axes, the 1D  $^1\text{H}$  spectrum for the components and the assembly are reported.

pare hydrodynamic radius values, calculated from DOSY experiments, with the values calculated starting from crystallographic data using Hydro++ software ( $r_{XRD}$ ): as known from literature, we found that the hydrodynamic radius obtained from DOSY experiment is more than the 80% of the one calculated from crystallographic data in the three measurements made (for the free porphyrins, the free tetramer and the assembled system).<sup>49</sup>

Finally, we were able to obtain the crystal structure of this supramolecular assembly, in which we have one tetramer and four ruthenium porphyrins. Indeed, despite the big number of crystallization conditions explored, only “fishtail-like” aggregated crystals were isolated, with poor diffraction limits, corresponding to a limited order in the solid state. Some small fragments have been successfully used for the structural characterization of supramolecular assembly: single-crystals with monoclinic  $C2/c$  unit cell were isolated.



The presence of large void channels is consistent with the poor diffracting power of these crystals. The four ruthenium porphyrin units are disposed at the vertexes of a large tetrahedron with sides of unequal lengths, (24.2 Å is the expected for the Ru···Ru distance in an ideal tetrahedron with internal angles of 109.47°) (figure 1.53 left). The crystal packing present small cavities, containing two well-ordered *n*-hexane and one acetone molecules, and larger voids containing a severely disordered solvent content. During screening of various batch of crystals, different crystalline polymorphs were found but they have not been characterized.

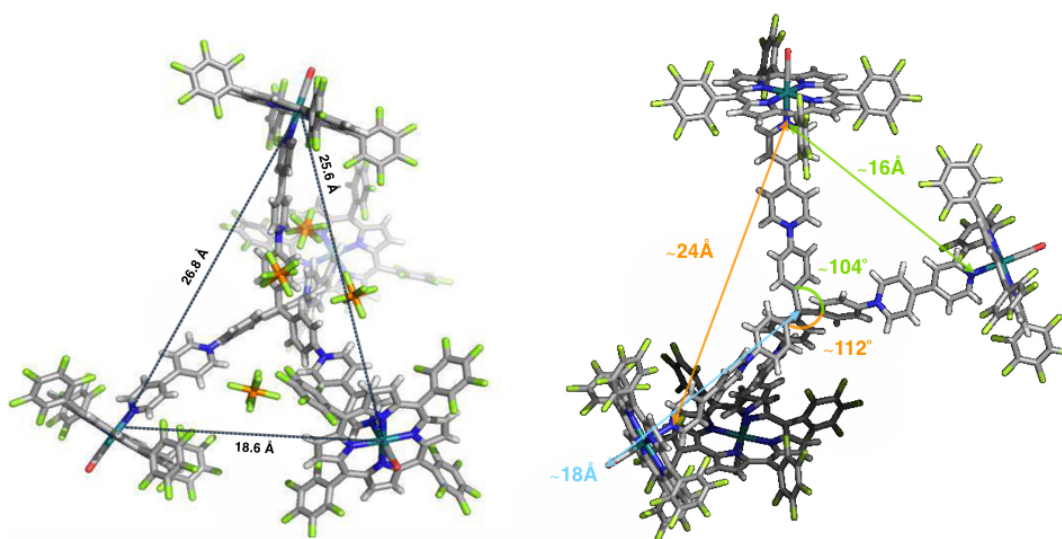


FIGURE 1.53: Stick representation showing the distortion from the ideal tetrahedral geometry found in the solid-state, three of the Ru···Ru distances found (left), N···N distances and central angles (right)

### 1.3 2D Polymer at the Air/Water Interface

During my PhD programme, I spent four months at the ETH in Zurich, working in the group of Prof. A.D. Schlüter, that can be considered a pioneer in the field of 2D polymer. Before talking about the results we obtained during my stay, I'll briefly introduce the concept of "2D polymer" and some important example in the field.

A macromolecule is defined as a 2D polymer when:<sup>50</sup>

- the repeat units are topologically two-dimensional; the monomers should have, at least three binding sites, or, alternatively, 4, 6, 8 so they could tile-cover 2D space;
- repeat units are attached to each other by covalent bonds (preferably with a carbon-carbon nature) or exploiting the metal coordination chemistry;
- covalent bonds are populated highly enough per unit area of the polymer (e.g.  $2 \times 10^8$  repeat units in  $400 \mu\text{m}^2$ );
- polymer molecules are monolayer sheets with a thickness that accounts for the height of the constituent repeat unit.;
- the monolayers must show long-range in-plane periodic order in their constitution.

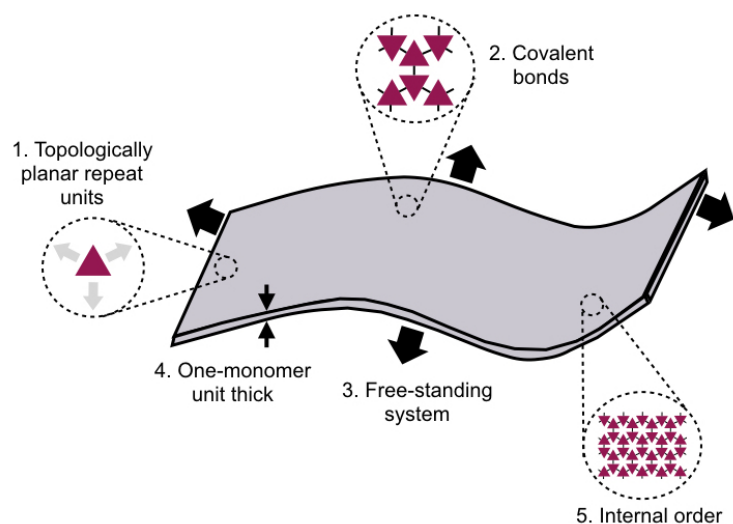


FIGURE 1.54: Schematic representation of a 2D polymer and of the five criteria.

The synthesis of a 2D polymer can be done, at least, with two different approaches. The first one is the single crystal approach, that was introduced for the first in Schlüter's group with the aim of synthesizing the first reported case of a man-made 2D polymer.<sup>51</sup> The monomer, a three-fold symmetry macrocycle shown in figure 1.55, was synthesized and crystallized from tetrachloroethane (TCE) and tetrahydrofuran (THF). The polymerization occurs with a [4+2] cyclo-addition of the adjacent monomers upon irradiation with UV light. Successful exfoliation of the sheets down to monomer thickness was achieved upon exposure of the polymer to N-methyl pyrrolidone (NMP) at 150 °C for 3 days. The thickness of each layer was close to that of the theoretically expected value and was confirmed by atomic force microscopy (AFM) and the monolayers were stable enough to span over holes of a lacey-carbon covered grid.

Another example of the attempts towards creating 2D polymers is through

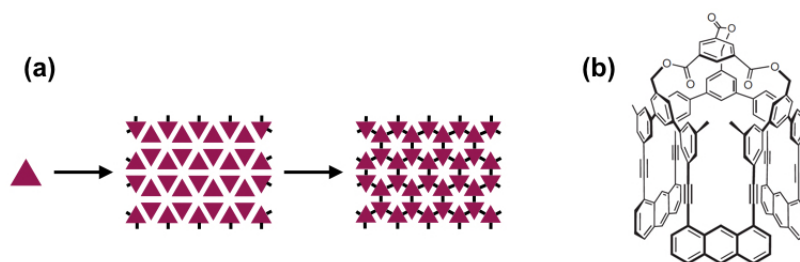


FIGURE 1.55: (a) Formation of a single crystal from a three-fold symmetry monomer, followed by polymerization reaction; (b) chemical structure of the monomer.

the use of air/water interface. In fact surface of water provides a smooth reaction medium which is suitable for obtaining sheets with well-defined structures from amphiphilic molecules.<sup>52</sup> Langmuir films result from the interaction of surfactants trapped at the interface between two dissimilar phases, in our case gas/liquid/ (air/water). Indeed the root-mean-square roughness of water is about 3 Å,<sup>53</sup> value comparable with the structural dimension of an organic molecule: air/water interface is a suitable environment for reaching order on a large scale.

An amphiphilic molecule, insoluble in water, can be spread on a water surface (with the use of a suitable solvent) to form an insoluble monolayer. In these Langmuir films, obtained by applying a compression to the surface, all molecules are concentrated in a one molecule thick layer at the interface (figure 1.56). The most important indicator of the monolayer properties of a material is given by a plot of surface pressure as a function of the area of water

surface available to each molecule. This is carried out at constant temperature and is accordingly known as a surface *pressure/area isotherm*, obtained by compressing the film at a constant rate while continuously monitoring the surface pressure. The isotherm has a shape characteristic of the surfactant involved in film formation. The monitoring of the the surface pressure can be done because of the *Wilhelmy* plate, a thin plate usually on the order of a few square centimeters in area, often made of platinum or glass, which may be roughened to ensure complete wetting. Indeed, the experiment is not affected by the plate material, as long as the plate is oriented perpendicularly to the interface and during the compression is measured the force exerted on it. During a Langmuir experiment, the surface area available is reduced by

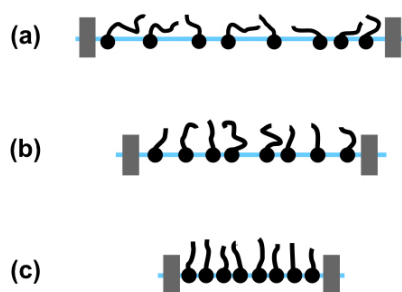


FIGURE 1.56: Schematization of Langmuir monolayer of a generic amphiphilic molecule: (a) expanded, (b) partly compressed, (c) close packed.

sweeping the barriers over the surface, so the surfactant molecules are forced to come closer together and form the ordered monolayer. The accumulation of surface active molecules at the interface tends to reduce the surface tension (figure 1.57). Thus the surface tension is a function of the number of molecules per unit area, and can be affected by compressing a particular monolayer.

Distinct regions (called “phases”) can be defined in a generic isotherm curve. During the compression, the molecules at the interface undergo a transition from a *gaseous “phase”*, with no periodic order, to a *liquid “phase”*, where the first van der Waals interactions among the hydrophobic tails of the amphiphilic molecule is sensed. Further compression takes the molecules to a so called *solid “phase”*: at that point, all the chains are pushed away from the water and are kept parallel to each other with the maximum possible van der Waals interactions (figure 1.57). If the monolayer is still compressed after reaching the “solid state”, the monolayer will collapse into three-dimensional structures. In the isotherm, this collapse is evidenced as a rapid decrease in the surface pressure.

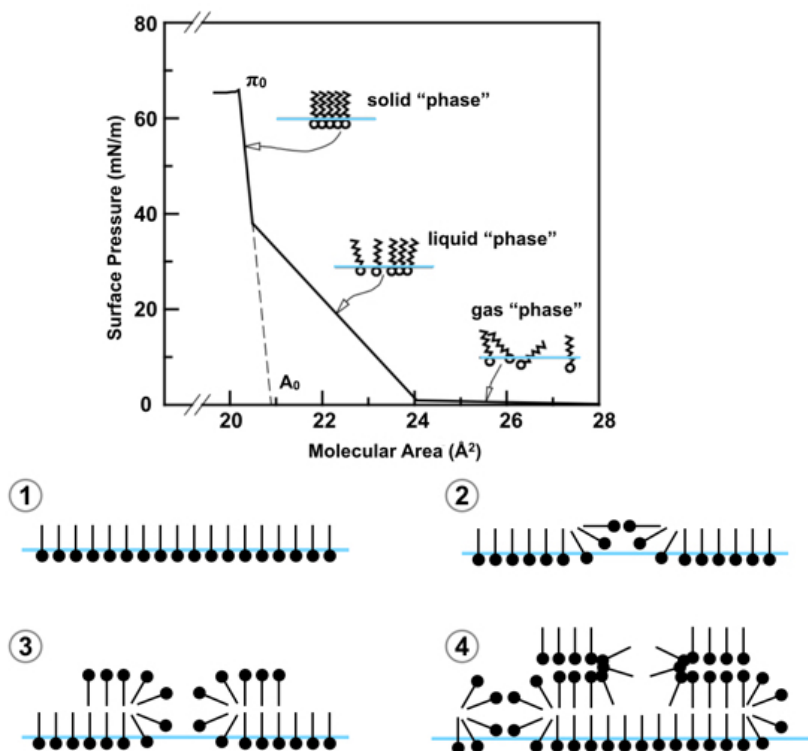


FIGURE 1.57: Top, Isotherm of a generic amphiphilic molecule; bottom, collapse of a monolayer, in four steps.

The different approaches have advantages and disadvantages, in particular: the single crystal approach is limited by the predictability of the crystal structure and the long synthetic procedure (in the case discussed above they performed 25 step synthesis) with the limitation of the lateral size of the polymer, that can't be bigger than the single crystal one. Some of this problem are solved with the second approach, that use the air/water interface: first of all, no lateral size limitation of the polymer, besides the dimension of the through, and the predictability of the monolayer is easier than the former case (amphiphilic monomers are needed, that lie flat at the air/water interface); however, the transfer of the polymer to an appropriate substrate is a crucial process and there are few techniques able to analyze a monolayer, with difficult interpretation of the results.

### 1.3.1 Towards 2D Polymer with Porphyrin Based Monomer at the Air/Water Interface

The approach we decided to use is the polymerization at the air/water interface, with Langmuir through experiments. The design and the synthesis of the monomer EtOx\_por1 used was done in Prof. Schlüter's group. To understand the choice of the monomer, we can divide it in three different level (figure 1.58). The first level (the central core) is a porphyrin, because it's easy to modulate the photophysical properties of this class of compounds, just playing with substituents and metal ion coordinated at the ring core; furthermore the photophysical properties are well known in literature. The second level is based on bipyridine moieties, which are necessary, as I'll explain, for the bond formation between the monomers; that monomer was already studied in the group, but unfortunately it didn't lie flat at the air/water interface. That's the reason why we decided to introduce a third level, that contain hydrophilic glycolic chains, that we expected to be useful to anchor the monomer to a planar conformation. For the polymerization reaction we took advantage of metal coordination (the presence of bipyridine moieties is necessary for the polymerization<sup>54</sup>): the metal ion we decided to use for complexation is nickel(II), because it can gives a square planar coordination geometry and can lead the system to the formation of a 2D network.<sup>55 56 57</sup> The synthesis, performed and optimized by Dai Wenyang,

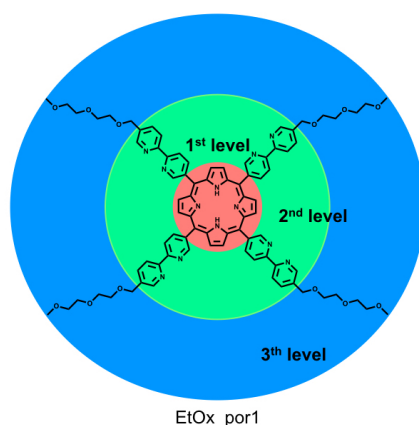


FIGURE 1.58: Chemical structure of the monomer synthesized.

a PhD student in Schlüter's group, is schematically reported in figure 1.59: we started with the commercial available bipyridine and we did a bromination with *N*-bromosuccinimide; then we performed the insertion of the hydrophilic chain, and the substitution of the bromide with an acetyl ester

group. To obtain the corresponding aldehyde we hydrolyzed the product under basic condition and we oxidated the alcohol with Mn(II). The final step is the *Rothemund reaction*, the tetramerization of pyrrole in presence of an aldehyde and propionic acid. The initial step of the *Rothemund reaction* is the carbinol formation: the monomeric carbinol consequently polymerizes into porphyrin and higher oligomers in random manner. The product was purified with gel permeation chromatography (GPC).

Before we started with Langmuir experiment we made some simple con-

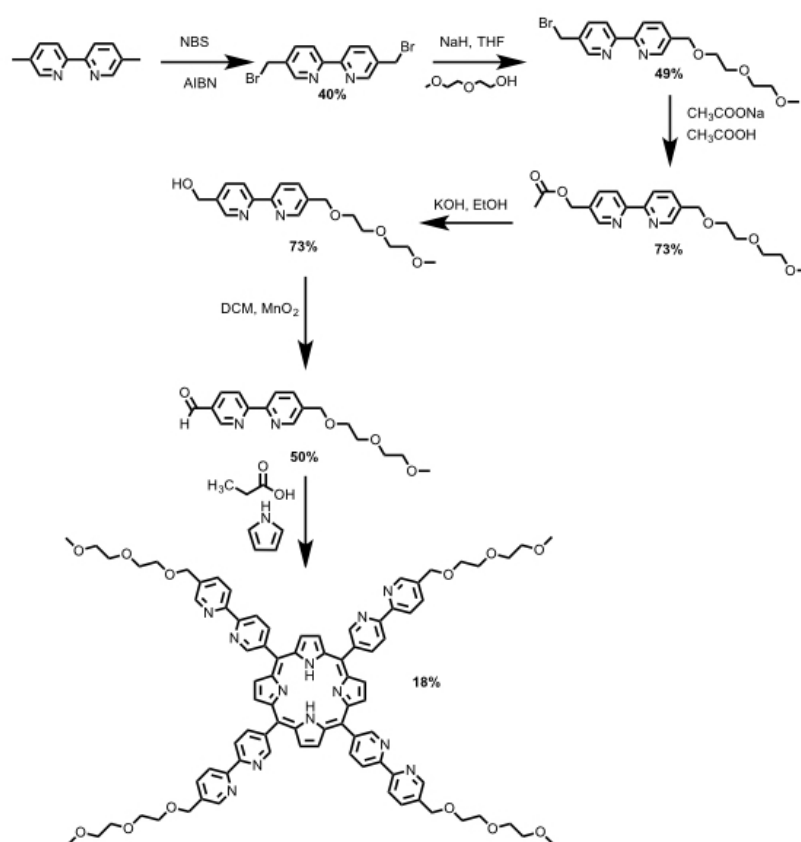


FIGURE 1.59: Scheme of EtOx\_por1 synthesis.

siderations about the geometry of our monomer EtOx\_por1, to have an idea about the value of *mean molecular area* (MMA) we could obtain. We considered the two extreme cases shown in figure 1.60: one is the horizontal orientation, the other is a vertical orientation of EtOx\_por1 at the air/water interface (as assumption, chains don't contribute). If we draw a circle around the monomer, we can calculate the area of the circle and approximate the value obtained with the *mean molecular area*, that is around  $500 \text{ \AA}^2$  for an horizontal orientation (figure 1.60, left); for the vertical orientation, we found  $88.9 \text{ \AA}^2$ ,

considering a van der Waals distance  $d_{vdW}$  of 3.5 Å (figure 1.60, right).

$$MMA \text{ (horizontal orientation)} = r^2\pi \quad (1.17)$$

$$MMA \text{ (vertical orientation)} = 2rd_{vdW} \quad (1.18)$$

The monomer EtOx\_por1 was dissolved in  $\text{CHCl}_3$  and spread at the air/water

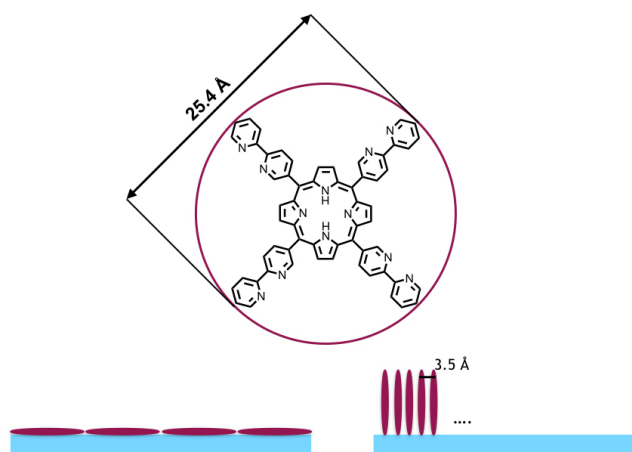


FIGURE 1.60: Geometric consideration on EtOx\_por1: horizontal orientation (left) and vertical orientation (right) of the monomer at the air/water interface.

interface. After 30 minutes (we let the  $\text{CHCl}_3$  evaporates), we compressed the barrier while we were recording the isotherm curve (figure 1.61, plot a). From the curve we were able to estimate the area occupied by each monomer, the MMA, from the intercept between the elongation of the linear part of the curve and x-axis. From this first experiment it was also possible to estimate the surface pressure needed for the formation of the monolayer, from minimum value of the linear part of the isotherm. The value obtained, 10 mNm, is the value that we fixed in every Langmuir experiments that follow. In that condition, we were sure to avoid the collapse of the monolayer. We also compressed and released the system 5 times at 10 mNm, to test the reproducibility of the monolayer formation: since the isotherm collected are superimposable, we concluded that the monomer is not dissolved in water during the compression (figure 1.61, plot b). This is an important feature, since the concentration of the monomer spread at the air/water interface is an important value to estimate correctly the MMA: if we were losing material during the compression, the MMA estimated from the isotherm would have been overestimated. During the compression was also possible to collect Brewster Angle Microscopy (BAM) images: indeed, the Langmuir through was



equipped with a Brewster angle microscope, that is a useful instrument for characterizing in situ thin films: no light is reflected from the air/water interface under Brewster's angle incidence if parallel-polarized light is used. With constant angle of incidence the formation of a monolayer on the water surface modifies Brewster's angle condition and light reflection is observed. The collection of this reflected radiation with a video camera allows the in situ, real time, visualization of the Langmuir monolayer at the air/water interface. The images we took look very similar, up to 20 mN/m pressure applied with the compression of the barrier (figure 1.62): this feature reveals that the monolayer is homogenous already from the beginning, thus the monomer has good spreadability. The MMA obtained is  $93 \text{ \AA}^2$ , value consistent with a vertical orientation: this was in contrast with our expectations: indeed we hypothesized that the monomer EtOx\_por1, with the help of hydrophilic chain, would have lied flat at the air/water interface. Nevertheless we decided to go further, since the film is homogeneous and we hoped that the metal complexation could produce a rearrangement of the monomer at the air/water interface.

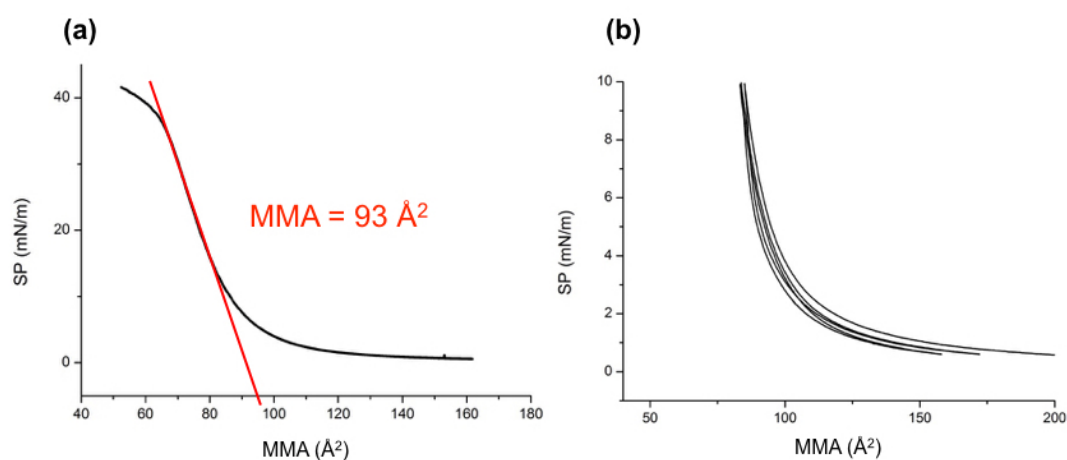


FIGURE 1.61: (a) Surface pressure (SP) *versus* MMA isotherm of monomer EtOx\_por1 at the air/water interface and determination of MMA value; (b) five cycles of compression and release at 10 mN/m.

Once we characterized the monomer monolayer, we decided to polymerize the system: to do that, it is necessary to form the Langmuir monolayer of the monomer and then inject in the through the metal ion as a salt, in large excess (4000 equivalents). In our case, the salt we used was  $\text{Ni}(\text{ClO}_4)_2 \cdot 6\text{H}_2\text{O}$ . After the Ni(II) injection, we waited overnight before the film characterization, since the metal complexation and the equilibration of the system (a rearrangement could occur) could be a long processes. Two different scenarios

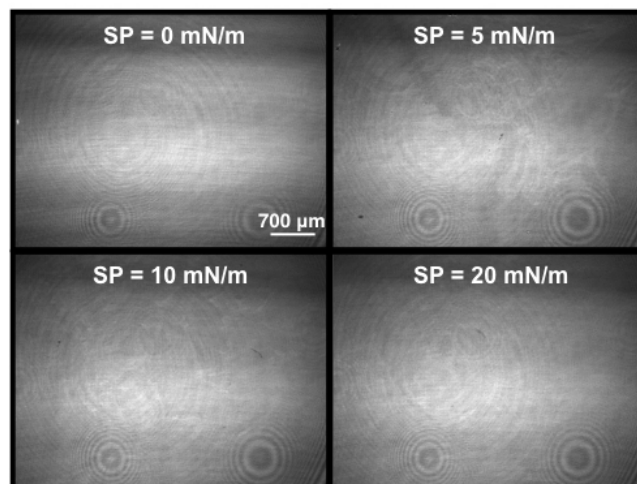


FIGURE 1.62: Series of Brewster angle microscopy images recorder at different surface pressure (0, 5, 10 and 20 mN/m).

can be shown after the injection: the metal ion can diffuse from the sub-phase to the monolayer and lead the monomer to a planar conformation, or can just attach the bottom of the monomer, that remain vertical (figure 1.63). As already mention, an important part of the 2D polymer formation at the

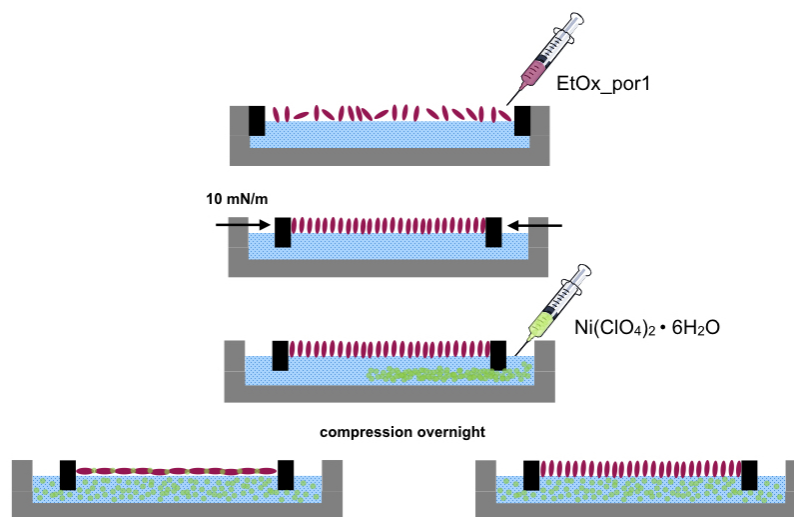


FIGURE 1.63: Schematization of the formation of 2D polymer film with the different orientation of the monomer at the air/water interface.

air/water interface is the film transfer on a substrate. We decided to perform a “horizontal” transfer: the substrate ( $\text{SiO}_2$  for AFM analysis or quartz for UV/Vis spectroscopy) with a piece of mica on it (to create a “fake edge”) was arranged on a platinum basket, dipped in the through before the film

formation. After the compression and, in the case of polymer, the metal complexation, the basket was lifted up very slowly, to avoid the destroy of the monolayer. We let the film dry and, carefully, we removed the mica. In the case of Scanning Electron Microscopy (SEM) grids, to transfer the film we just place prudently the grid on the monolayer (with the help of a tweezer) and with a peace of non-absorbing paper, we removed the grid from the surface, just placing the paper on the grid. After the water evaporation, we were able to analyze the samples. The transfer on SEM grid is important to observe if the film is free-standing: in the figure 1.64, plot a, we could observe that the polymer film is extended for more than  $20 \times 20 \mu\text{m}^2$ , but there are also some cracks. We needed a control experiment to verify if the monomer itself is able to form a film (figure 1.64, plot b): the coverage was not complete, but it was possible to observe the film formation in some areas. That indicates the presence of some interactions between monomer molecules, that are responsible for the free-standing system even when the polymerization reaction is not performed. However, the film is free-standing also in the case of polymerized system (figure 1.64, plot c)

The films transferred on  $\text{SiO}_2$  were characterize with Atomic Force Microscopy

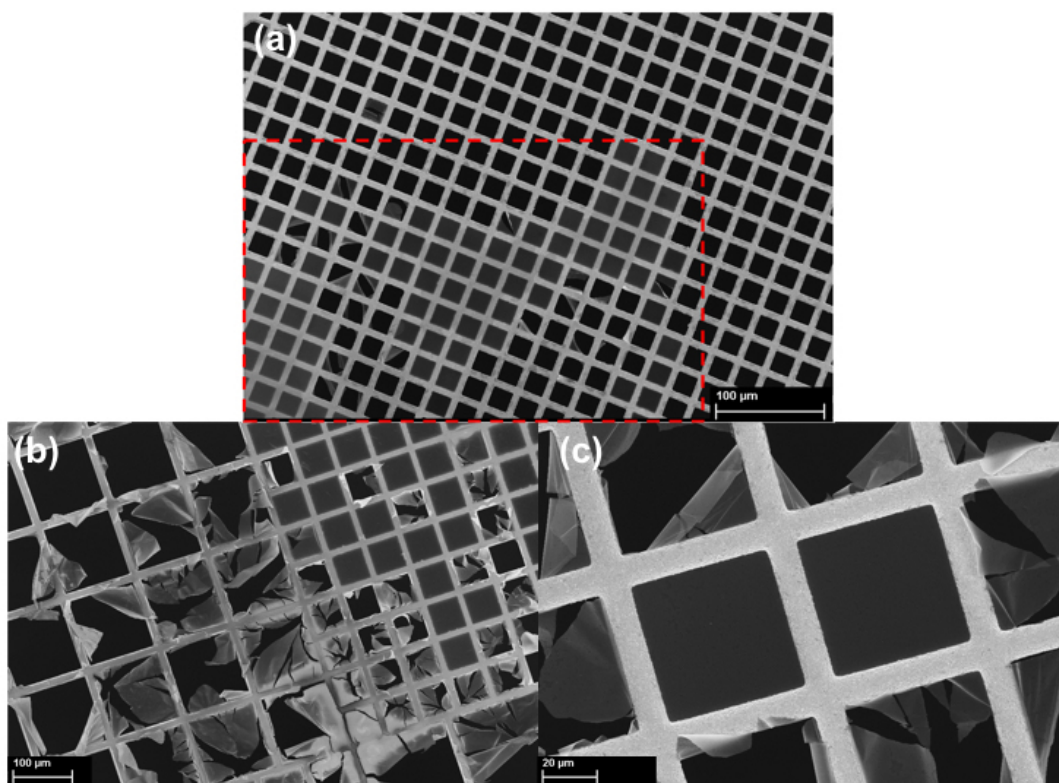


FIGURE 1.64: (a) SEM image of monomer monolayer; the red square evidence the free-standing film. (b) and (c) SEM image of polymer film.

(AFM): this analysis allowed us to estimate the thickness of the monomer and polymer films. In the case of monomer film (figure 1.65, plot a), the thickness measured is  $h_{AFM}$  is 0.5 nm, comparable to an horizontal orientation of the monomer on the substrate. This result is in contrast with the value of MMA estimated from the isotherm, that suggested a vertical orientation. To explain this behaviour, we suppose that, during the transfer, a relaxation of the porphyrin on the substrate occurs, since we don't have the barrier compression anymore. The  $h_{AFM}$  measured in the case of the film obtained after the metal complexation is 1.2 nm: this thickness indicates that the monomers don't lie flat. The relaxation, observed in the case of monomer film, probably doesn't occur because the complexation with nickel stabilizes the system. By simple geometric calculation we estimated, considering a diameter of 25.4 Å, a tilt angle of 30 degrees.

Knowing the photophysical properties of porphyrins, we decided to trans-

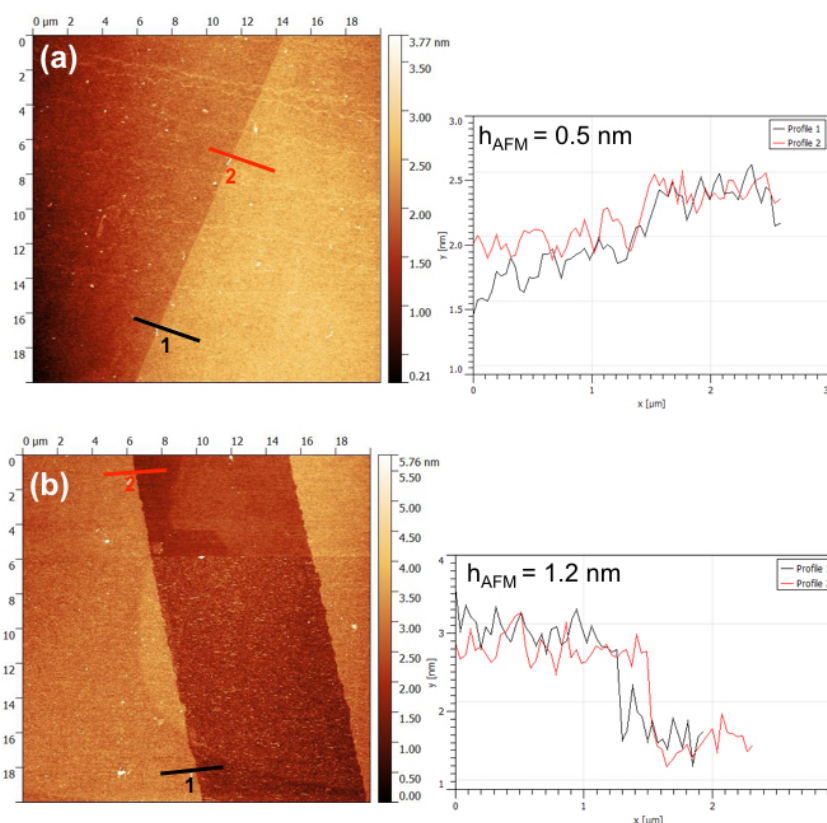


FIGURE 1.65: AFM images of monomer (a) and metal complexed (b) films. Corresponding cross section profile show the thickness of the films, with the use of “fake edge” created with mica.

fer monomer and metal complexed films on quartz substrate, with the aim to collect absorption and emission spectra. As observed in solution after

the addition of Ni(II), the Soret band absorbance decreases when the metal complexation occurs. In the emission spectrum, collected in “front-face” arrangement, we observed a quenching of the porphyrin core fluorescence if the metal ion is added (figure 1.66); the same behaviour was evidenced also in solution. With the film spectra we were able to say if the polymerization occurred, but, however, we didn’t gain information about the ratio of complexation and structural arrangements of the monomers.

To conclude this section, I will show some results, published in 1994 *Suslik*,<sup>58</sup>

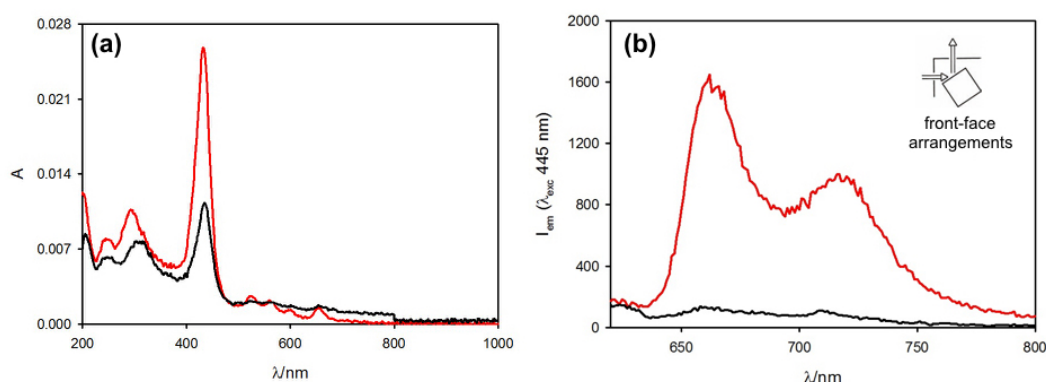


FIGURE 1.66: (a) Absorption spectra of monomer film (red line) and polymer film (black line); quartz substrate was used as reference. (b) Emission spectra, collected in “front-face” arrangement, of the monomer film (red line) and polymer film (black line).

that can be useful to rationalize ours. In the paper, they synthesized a series of nitrophenyl-amidophenyl-substituted porphyrins with hydrophobic tails (figure 1.67). The porphyrin named **por1** has just one long tail, the **por2** has two tails and so on. From the isotherm collected, they observed the formation of good Langmuir films on water. The mean molecular area obtained for the series are shown in table 1.5. Based on single-crystal structures of the simple

TABLE 1.5: Mean Molecular Areas of porphyrins

Porphyrin	Mean Molecular Area ( $\text{\AA}^2$ )
<b>por1</b>	80
<b>por2</b>	120
<b>por3</b>	150
<b>por4</b>	230

tetraphenylporphyrins, the expected mean molecular areas of Langmuir films would be  $90 \text{\AA}^2$  if the porphyrin rings lie vertical to the aqueous surface and



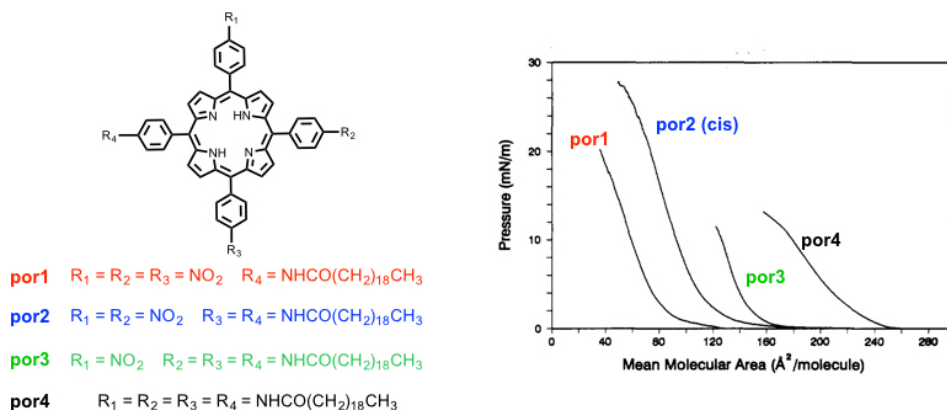


FIGURE 1.67: Chemical structure of the nitrophenyl-amidophenyl-substituted porphyrins synthesized and corresponding SP *versus* MMA isotherms.

$225 \text{ \AA}^2$  if the porphyrin ring lie parallel. As the number of aliphatic chains increases from one to four, the mean molecular areas increases smoothly from the expected value for a vertical orientation up to that for a horizontal orientation. This would seem to imply that the orientation of the porphyrin rings changes from nearly vertical, for a single aliphatic chain, to nearly horizontal for four chains. This variable orientation model is shown schematically in figure 1.68, plot a. However, linear dichroic determinations of the porphyrin orientation demonstrate that this simple hypothesis is incorrect. To test the variable orientation model, they used UV-visible transmission linear dichroism to characterize directly the porphyrin alignment, both on Langmuir trough and after transfer to a glass substrate. Surprisingly, they found that the number of aliphatic chains attached to the porphyrin has no significant effect on the spectroscopically measured tilt angle of the porphyrin, either on trough or after transfer to a glass substrate. The tilt angle measured is the same for all four porphyrins on trough ( $45 \pm 4^\circ$ ) and on the substrate ( $33 \pm 4^\circ$ ). Nevertheless, they found a small difference between in the tilt angle on trough compared to on slide, even though the tilt angles measured on trough were taken at pressures comparable to transfer pressures. They hypothesized a slight relaxation of the porphyrin molecules after transfer to a glass substrate, the same feature we obtained with our system. The fact that the tilt angle is not affected by the presence of the aliphatic chains, is in contrast to the mean molecular areas. This discrepancy can be resolved by a fixed-orientation model in which overlap occurs between adjacent porphyrin rings, as shown schematically in figure 1.68, plot b. This second model takes

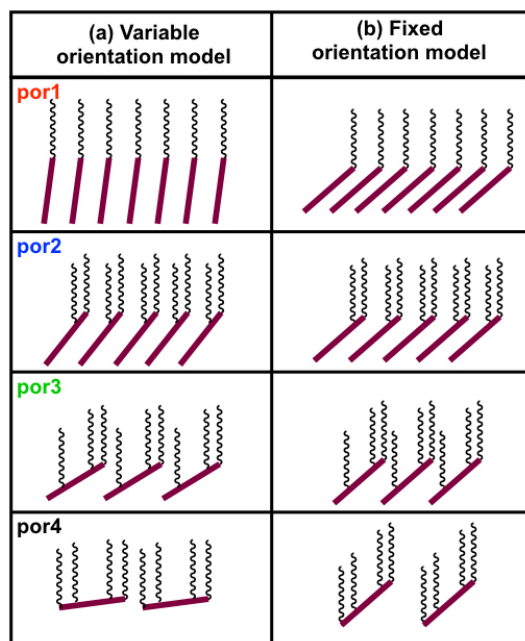


FIGURE 1.68: Schematic models of Langmuir films: (a) variable orientation model in which no overlap of porphyrin rings occurs; (b) fixed orientation model in which porphyrin-porphyrin overlap occurs in the absence of steric constraints from multiple aliphatic chains.

into account the attractive  $\pi$ - $\pi$  interaction between porphyrin rings: this interaction is sufficiently strong that significant pre-aggregation can occur prior to compression of these films. In the absence steric hindrance of the aliphatic chains, the  $\pi$ - $\pi$  stacking permits close packing of the rings; as the number of aliphatic chains on the porphyrin increases, the porphyrin planes must pack more loosely. The orientation of the porphyrins is determined by the  $\pi$ - $\pi$  stacking between the rings and between porphyrins and the water of glass surface, while the differences in the MMA values are determined, independently, by packing constraints imposed by the pendant hydrocarbon chains. In view of this, we might end up the same situation with our porphyrin monomer EtOx\_por1.





## Chapter 2

# Photoredox Reactions

Photocatalysis should be considered more than a type of catalysis, since photocatalytic processes can be used not only to change reaction rates, but also to modify chemical equilibria and, particularly, to convert light into chemical energy. Photocatalysis may involve processes in which light excitation and a catalyst can play separated, concerted or even entangled roles. For all these reasons it is practically impossible to give a comprehensive definition of the term photocatalysis.

Generally speaking, *catalysis* is the increase, in rate, of a chemical reaction, due to the presence of a *catalyst*, an additional substance that participate actively in the reaction mechanism.



The catalyst is not consumed and does not affect the free energy charge and the equilibrium constant. It decreases the activation energy, offering a different path to the reaction, has shown in figure 2.1. In several cases the product

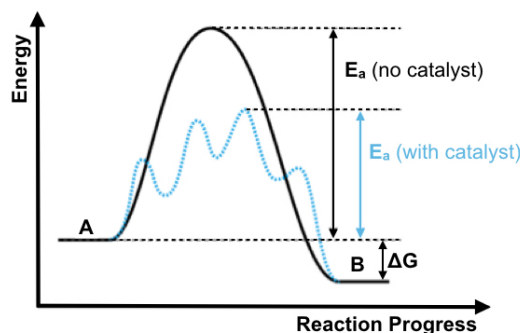


FIGURE 2.1: Generic energy profiles for a reaction in absence (red solid plot) and presence (black solid line) of a catalyst.

of a dark reaction is different from that of the reaction performed under light excitation; when the product is the same, the photochemical reaction is usually much faster than the dark one (2.3).



The decrease of the activation energy for the photochemical reaction is directly connected with the free energy change caused by light excitation, as rationalized by the Marcus theory of electron transfer reactions.<sup>59</sup> As a consequence, the mechanism of a dark reaction that becomes faster under light irradiation (2.3) is completely different from the one catalyzed in the dark (2.2).

An example of a reaction directly catalyzed by light is the oxidation of  $[\text{Ru}(\text{bpy})_3]^{2+}$  by persulfate. This reaction is very slow in the dark, but becomes very fast upon irradiation with visible light; indeed the  $[\text{Ru}(\text{bpy})_3]^{2+}$  is replaced by its excited state  $^*[\text{Ru}(\text{bpy})_3]^{2+}$  (2.2). Since the deactivation of the excited state is

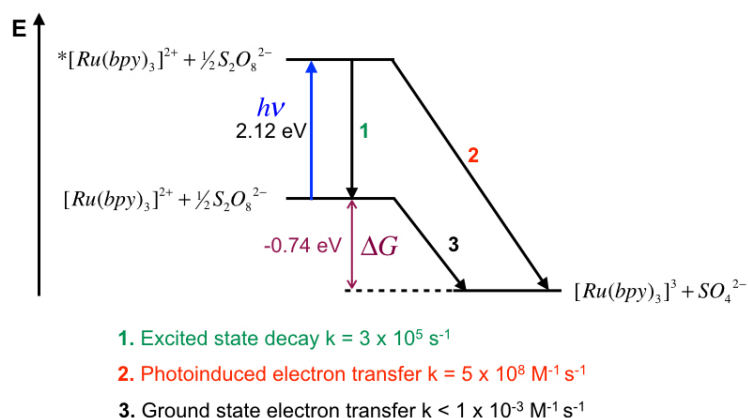


FIGURE 2.2: Photocatalysis of the oxidation of  $[\text{Ru}(\text{bpy})_3]^{2+}$  by persulfate.

really fast ( $3 \times 10^5 \text{ s}^{-1}$ ), the photoreaction must compete with the excited state decay: this feature underlines the importance of the excited state lifetime.

As shown in figure 2.2, the change in free energy from a thermal to a photochemical reaction can increase the reaction rate.

Another important feature of photocatalysis is that of a thermodynamically forbidden reaction that becomes allowed upon light excitation. An example is the reduction of  $\text{Fe}^{3+}$  by  $[\text{Ru}(\text{bpy})_3]^{2+}$ , that cannot take place in the dark, but occurs with very fast rate when the ruthenium complex is excited, since  $^*[\text{Ru}(\text{bpy})_3]^{2+}$  is a much stronger reductant (figure 2.3). Some photocatalytic reactions can require the use of a photosensitizer. The reaction (i) has a high

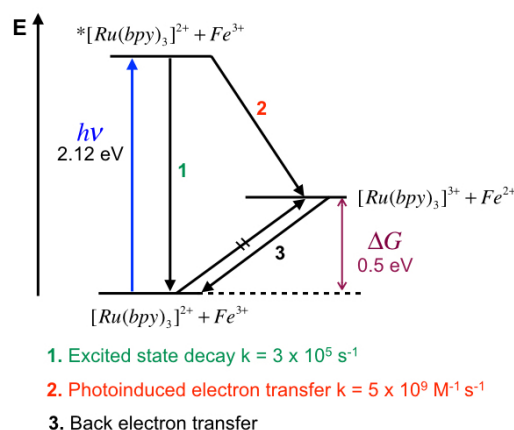
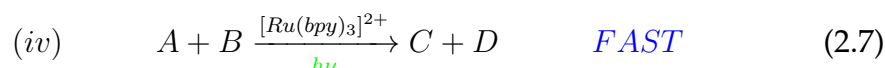
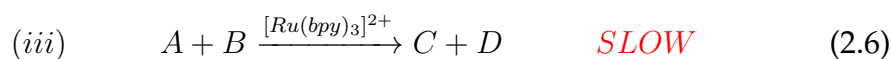
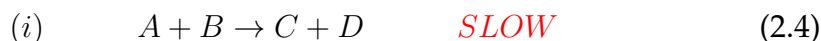


FIGURE 2.3: Photocatalysis of the reduction of  $\text{Fe}^{3+}$  by  $[\text{Ru}(\text{bpy})_3]^{2+}$ .

activation barrier, since it is slow in the dark. To increase the reaction rate it's necessary to excite the reaction mixture with light: indeed this approach doesn't work if A and B don't absorb light (reaction (ii)). If the  $[\text{Ru}(\text{bpy})_3]^{2+}$  is added in solution, nothing happens in dark condition: the reaction (iii) is slow as it was in absence of  $[\text{Ru}(\text{bpy})_3]^{2+}$ : if the reaction mixture is now irradiated with visible light, there is the formation of  $*[\text{Ru}(\text{bpy})_3]^{2+}$  and the reaction is now catalyzed (reaction (iv)); the complex  $[\text{Ru}(\text{bpy})_3]^{2+}$  acts as photosensitizer.



If the reaction is thermodynamically forbidden, when the ruthenium is added to the reaction mixture and visible light is shined, the reaction takes place (figure 2.4, diagram (c) and (d)).

Light as catalyst is extensively used in chemical synthesis. Organic molecules usually absorb ultraviolet light (UV), that is not abundant in the solar radiation (3%) that penetrates the atmosphere. Moreover UV photons are quite high in energy (4.96-3.40 eV), on the order of a C-C bond (bond-dissociation energy at 298 K 3.60-3.69 eV), and can cause decomposition reactions, particularly when relatively weak bonds are present or when the target compounds possess substantial structural complexity. That's the reason why

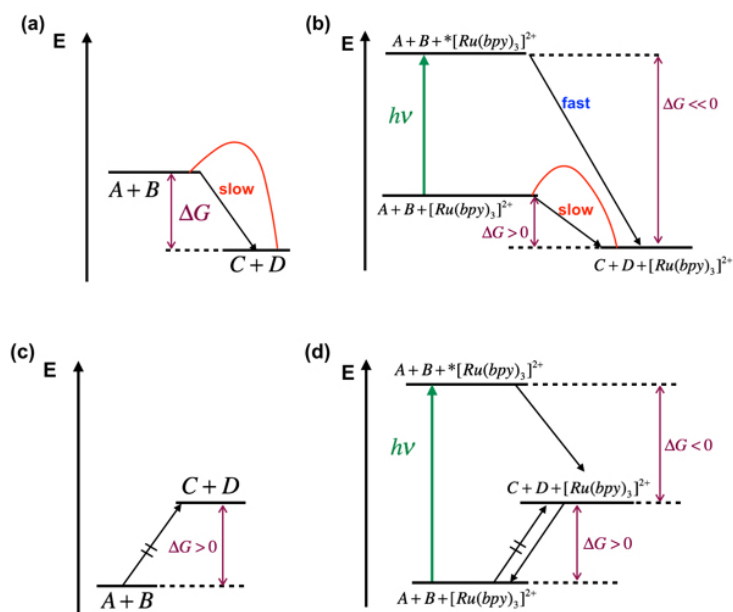


FIGURE 2.4: Schematization of photosensitized reaction thermodynamically allowed ((a) and (b)) and forbidden ((c) and (d)) in dark conditions.

photosensitizer are widely employed in order to take advantage of visible-light excitation: that's the reason why, in any photocatalytic cycle the key step is the absorption of incident light and the formation of the excited state, as a consequence. The excited photocatalyst can act as both a strong oxidant and reductant simultaneously, while in traditional redox reactions, medium can be either oxidative or reductive (but not both); indeed, it is well known that an excited species is both a better electron donor and a better electron acceptor than the ground state species (figure 2.5). Depending on the oxida-

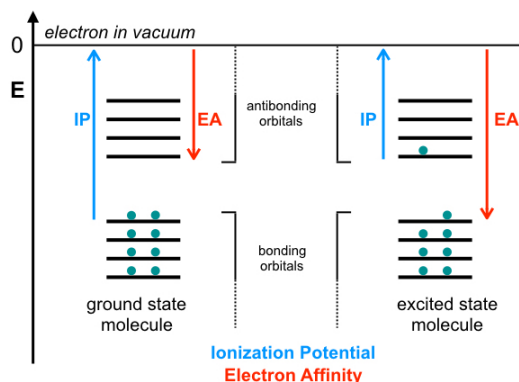


FIGURE 2.5: Orbital scheme for ground state species and excited state species.

tive or reductive mechanism of the reaction, photocatalyst (**cat**) can act as an oxidant or reductant: in an oxidative quenching cycle, the excited state

\***cat** is quenched by donating an electron either to a substrate (**sub**) of the organic reaction, or an oxidant **ox** present in the reaction mixture; in a reductive quenching cycle, \***cat** is quenched by accepting an electron from **sub** or a reductant **red**.<sup>60</sup> The mechanisms shown in figure 2.6 are idealized photoredox reactions proceeding, with photoinduced electron transfer, in which one photon absorption generates one product. Pragmatically, the quantum yields of many photoredox reactions are dramatically lower than 1. However, if an intermediate donates or accepts an electron can initiate a new chain: in that particular case, quantum yields values higher than 1 are possible.<sup>61</sup>

The photoreaction quantum yield  $\Phi_P$  (upon monochromatic excitation), is defined as the moles of photoproduct divided by the moles of photons absorbed by the photocatalyst:

$$\Phi_P = \frac{\text{moles product}}{\text{moles photons absorbed}} \quad (2.8)$$

$$\Phi_P = \frac{\text{moles product}}{q_{p,in} t f_m} \quad (2.9)$$

where  $q_{p,in}$  is the flux of incident photons,  $t$  is the time of irradiation and  $f_m$  is the percentage of the light absorbed by the photocatalyst at the irradiation wavelength. The photon flux of the light source is usually determined by a chemical actinometry (for more details see Appendix A). If the quantum yield is higher than 1, means that more than one mole of product is generated when one mole of photon is absorbed by the photocatalyst, which suggests a chain mechanism for the reaction. Occasionally, some photolytic reactivity

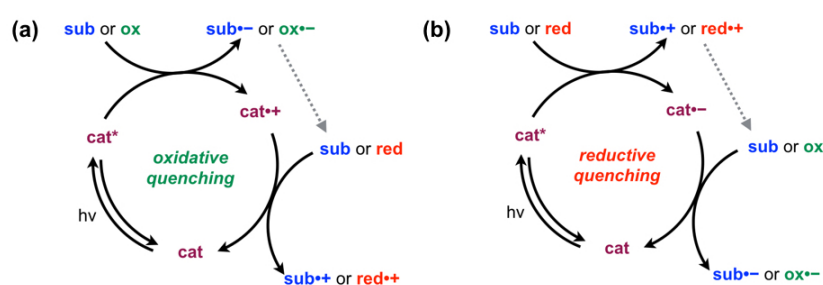


FIGURE 2.6: (a) Oxidative and (b) reductive quenching cycles of a generic photocatalyst **cat**.

can occur even in the absence of a photocatalyst and when the individual reactants are transparent at irradiation wavelengths. In that case, if upon mixing the two reactants, a color change can occur, reveals the formation of an electron donor-acceptor (EDA) complex (alternatively referred to as a

“charge-transfer complex”). These EDA complexes can be responsible for the background activity, since the absorption of a photon at longer wavelengths than the wavelengths of the reactants occurs.<sup>62</sup> Moreover, EDA complex formation can occur between a substrate and the photocatalyst itself, resulting again in a new red-shifted absorbance feature.

Transition metal complexes are widely employed as photocatalysts in organic reactions (the first example was published in 1978),<sup>63 64 65</sup> but more recently, examples of organic reactions catalyzed by organic dyes can be found in literature.<sup>60 66 67</sup>

## 2.1 Visible Light Photoredox Catalysis with Metal Complexes

The first application of photoredox catalysis to organic synthesis date back to 1978:<sup>68</sup> Kellogg and coworkers demonstrated the reduction of sulfonium ions to the corresponding alkanes and thioethers, using *N*-1,4-dihydropyridines as the terminal reductant and  $[\text{Ru}(\text{bpy})_3]\text{Cl}_2$  as photocatalyst. The light source they used was a “normal room lighting”, neon fluorescent lamps at ca. 2 m distance. They added different dyes in solution, like meso-tetrphenylporphine, eosin as disodium salt,  $[\text{Ru}(\text{bpy})_3]\text{Cl}_2$  and followed the variations with <sup>1</sup>H-NMR spectroscopy: they observed that the reduction of sulfonium salts largely accelerated when one of the dyes is present in the reaction mixture; however, the most effective of the dyes was  $[\text{Ru}(\text{bpy})_3]\text{Cl}_2$ . They wrote “ $[\text{Ru}(\text{bpy})_3]\text{Cl}_2$  is known to donate an electron to an acceptor on irradiation in the 450 nm charge transfer band. [...] Detailed mechanistic investigation will be needed to ascertain with certainty whether the dyes are involved in an electron transfer capacity.”

In 1984, Cano-Yelo and Deronzier reported the oxidative photoredox catalyzed reaction of benzylic alcohols to the corresponding aldehydes (*Pschorr* reaction), using aryldiazonium salts as the terminal oxidant for the conversion. The photocatalyst was, again,  $[\text{Ru}(\text{bpy})_3]\text{Cl}_2$ . They found that the *Pschorr* reaction takes place quantitatively with a high quantum yield ( $\phi > 0.4$ ) upon photocatalyst excitation, and the reaction proceeded by a photoinduced electron transfer process.

Polypyridine ruthenium complexes are extensively used as photocatalyst

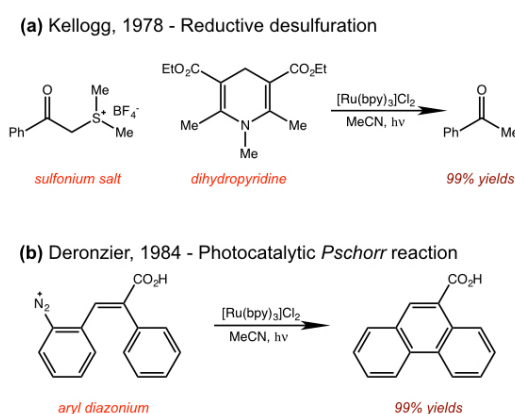


FIGURE 2.7: Scheme of photomediated reduction of sulfonium ions (a) and *Pschorr* reaction (b).

in organic reactions, since the synthesis is easy, they are stable at room temperature and they have excellent photoredox properties.<sup>69</sup> Nevertheless, also iridium polypyridine complexes play a prominent role in the field of photocatalysis. For example, Stephenson and coworker, performed reduction of unactivated alkyl and aryl iodides, using *fac*-Ir(ppy)<sub>3</sub> as visible-light-active photocatalyst (figure 2.8, a).<sup>70</sup> MacMillan published in 2016 a paper in which the combination of photoredox-mediated hydrogen atom transfer and nickel catalysis, permitted a highly selective and general C-H arylation that activates a wide array of C-H bonds as native functional handles for cross-coupling.<sup>71</sup>

The photocatalyst used was [Ir{dF(CF<sub>3</sub>)ppy}<sub>2</sub>(dtbbpy)]PF<sub>6</sub> (dF(CF<sub>3</sub>)ppy = 2-

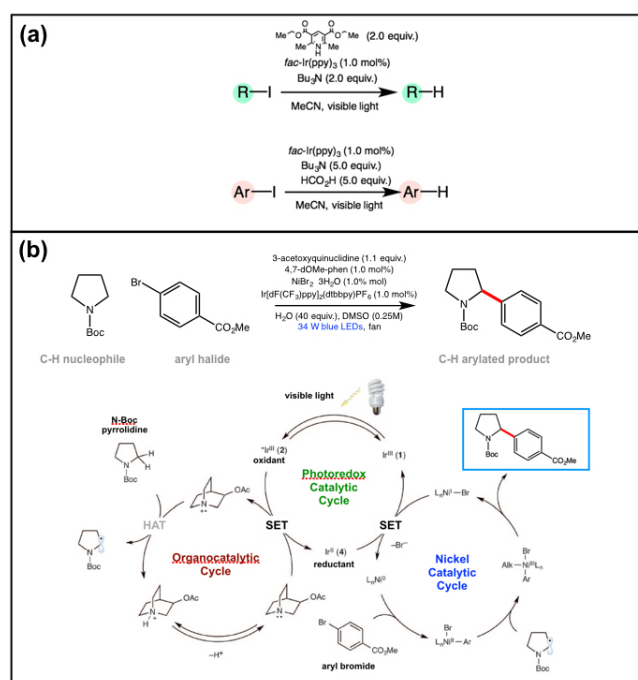


FIGURE 2.8: (a) Reduction of alkyl iodides and aryl iodides; (b) Photoredox, hydrogen atom transfer and Nickel-catalyzed cross-coupling (adapted from Shaw, Megan H. *et al.*, *Science*, 2016, 352, 1304-1308.)

(2,4-difluorophenyl)-5-(trifluoromethyl)pyridine; dtbbpy = 4,4'-di-tert-butyl-2,2'-bipyridine), that upon excitation with a blue LEDs populates the excited state: \*Ir(III) is now able to undergo single-electron transfer with a tertiary amine to generate the amine radical cation. The amine radical cation is now sufficiently electron-deficient to generate hydrogen atom transfer with the nucleophile substrate. Simultaneously, the Ni(0) generated via two reductions by the iridium photocatalyst, can undergo oxidative addition into aryl halide electrophile, forming the intermediate Ni(II)-aryl. This species can



generate Ni(III)-aryl-alkyl complex when intercepts the nucleophile radical which upon reductive elimination lead to the desired C-C bond (figure 2.8, b).

However, even if ruthenium and iridium complexes are the most employed as catalysts in this field, there are examples of photoredox catalysis in which different metal complexes are used. Indeed, heteroleptic copper-based sensitizers, with a bisphosphine and diamine ligand bound to the copper center, are a promising class of photocatalysts:<sup>72</sup> the synthesis of this class of compounds is a single step and they can be formed in situ in the reaction mixture, simplifying the experimental setup. Furthermore, it is possible to tune easily the photoredox properties of these Cu(I)-complexes; indeed the excited state lifetime of the metal center can be lengthen if a rigid bisphosphine is bound to copper, or the diamine ligands can influence the redox potentials of the excited state and the optical properties. An example of photoredox

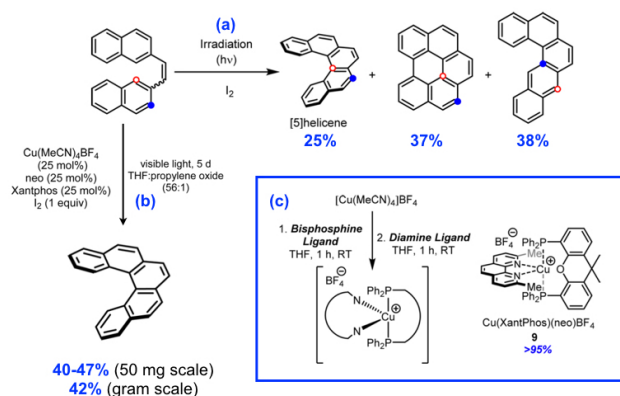


FIGURE 2.9: Synthesis of [5]helicene via UV-mediated photocyclization (reaction (a)) and using the heteroleptic complex  $Cu(XantPhos)(neo)BF_4$  formed in situ (reaction (b)); the reaction (c) is the preparation of the sensitizer in situ.

reaction catalyzed by copper-based complex is the synthesis of [5]helicene: the UV-light mediated method used in presence of the heteroleptic complex  $Cu(XantPhos)(neo)BF_4$ , improved the yield of the reaction, since the elimination of all byproducts occurs (figure 2.9).

In the following section, the study of photocatalyst behaviour in two photoredox reactions will be presented: (i)  $[Ru(bpy)_3](PF_6)_2$  acts as photocatalyst carboxylation of indoles with  $CBr_4/MeOH$ ; (ii)  $[Fe(bpy)_3]Br_2$  and visible light promote the organocatalytic alkylation of aldehydes.

### 2.1.1 Visible-Light-Induced Direct Photocatalytic Carboxylation of Indoles with $\text{CBr}_4/\text{MeOH}$ and $[\text{Ru}(\text{bpy})_3](\text{PF}_6)_2$ as Photocatalyst

Indoles and their derivatives have been widely recognized as a pivotal structural component of a diverse array of natural products and pharmacological agents of various therapeutic actions. Among them, indole C(2)-carboxylates are present as privileged cores in numerous biologically active molecules and still represent crucial building blocks for the synthesis of naturally occurring compounds (figure 2.10). Accordingly, the development of highly

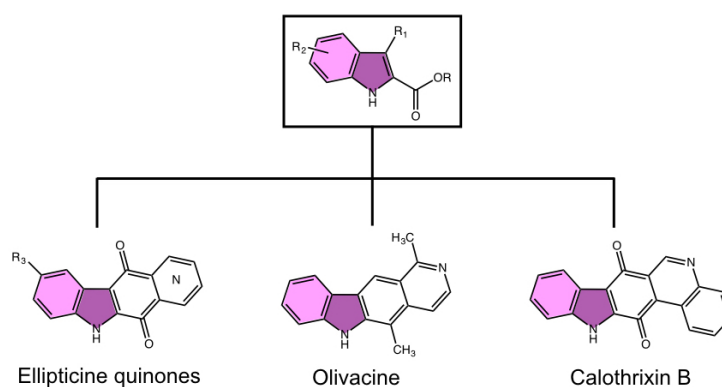


FIGURE 2.10: Representative indole C(2)-carboxylate-based natural products and biologically active compounds.

efficient methods to access direct carboxylation of this pharmacophore, under protecting-group/prefunctionalization-free conditions, still remains an unsolved challenge in organic synthesis. As a matter of fact, besides the *Fisher* indole synthesis,<sup>73</sup> the direct C(2)-carboxylation of indolyl cores frequently involves multiple step sequences based on aggressive reagents (like organolithium compounds),<sup>74</sup> with consequent limitation of substrate scope and moderate yields (figure 2.11, reaction (a)). In this context, we drove our attention to the visible light induced photoredox catalysis, that is already applied in these scenario, since is reported in literature the the synthesis<sup>75</sup> and peripheral functionalization of indoles<sup>76</sup> of metal or organic photosensitizers and electron donor/acceptor complexes. However, no example of photo-assisted regioselective carboxylative CH activation of arenes has been documented so far. In this context we recognized in the tetrahalogenated methanes  $\text{CX}_4$  ( $\text{X} = \text{Cl}, \text{Br}$ ) potential carboxylating agents for arenes, due to their intrinsic attitude of generating electrophilic  $\bullet\text{CX}_3$  radicals ( $\text{CCl}_4 = -0.78 \text{ V vs. SCE}$  and  $\text{CBr}_4 = -0.30 \text{ V vs. SCE}$ )<sup>77,78</sup> by oxidative quenching of

photoexcited photosensitizers. The intercepting of these radical species by aromatic nucleus, followed by alcoholysis, would deliver a rapid entry to mild CH-type carboxylating events (figure 2.11, reaction (b)).<sup>79</sup> To explore

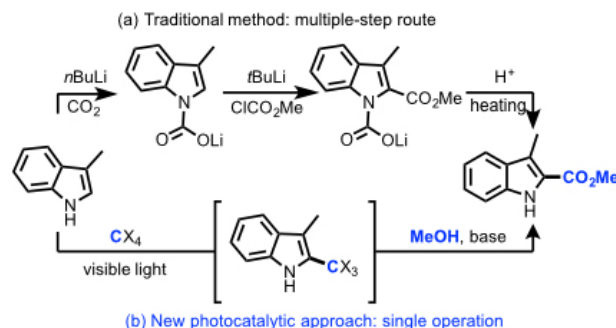
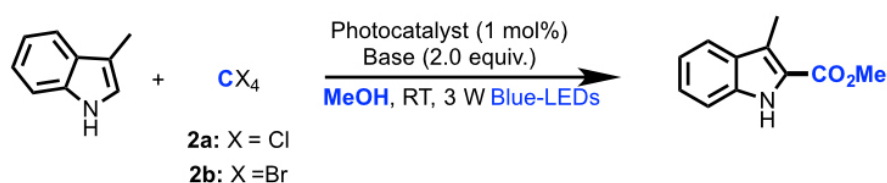


FIGURE 2.11: Synthesis of indole 2-carboxylates with traditional approach (a) and the one we developed (b).

the feasibility of our working plan, we initially investigated the reaction of 3-methylindole and  $\text{CX}_4$  ( $\text{CCl}_4$  or  $\text{CBr}_4$ , 3 equiv.) in the presence of metal photosensitizer (1 mol%), 2,6-di-*tert*-butylpyridine (DTBP 2.0 equiv), blue LEDs (3 W) irradiation, and MeOH as the reaction media (the base was added as a scavenger of the HX delivered during the reaction cycle). Interestingly, while no reaction was observed with  $\text{CCl}_4$ , the use of more easily reducible  $\text{CBr}_4$  furnished the desired product in 32% yield (table 2.1). Next, we further optimized the reaction conditions by performing a survey of parameters involving: nature of the photosensitizer, light source, concentration, and base, identifying the following:  $[\text{Ru}(\text{bpy})_3](\text{PF}_6)_2$  (1 mol%), 7 W blue LEDs at a distance of approximately 5 cm,  $i\text{Pr}_2\text{NH}$  (2 equiv) as the optimal reaction conditions. Here, product was isolated in 90% yield as a single regioisomer upon 6 h irradiation (Table 1, entry 12). Additionally, a sunlight-induced process was also carried out (entry 15), delivering the product in comparable extents (yield: 81%).

With the optimal conditions in hand, we probed the scope of this photocatalytic carboxylation reaction. As summarized in figure 2.12, a series of C(3)-substituted indoles (**1b-1**) were successfully applied to this reaction. The 3-substituted indoles containing linear and branched alkyl groups (i.e. ethyl, cyclopentyl, cyclohexyl) were observed to react smoothly with  $\text{CBr}_4$  delivering products **3b-d** in good yields (70-84%). Focusing on functional-group tolerance, we also subjected N-protected tryptamines (**1e**, **1f**) and tryptophol **1g** to best operating conditions. Gratifyingly, in all cases, the desired acyclic products were recorded in a satisfying manner (yield: 70-82%). It is worth

TABLE 2.1: Optimization of reaction conditions<sup>[a]</sup>.

Entry	Photocatalyst/ <b>2</b>	Base	Time (h)	Yield (% <sup>[b]</sup> )
1	[Ir(diFppy) <sub>2</sub> (dtb-bpy)]PF <sub>6</sub> / <b>2a</b>	DTBP	24	NR
2	[Ru(bpy) <sub>3</sub> ]Cl <sub>2</sub> ·6H <sub>2</sub> O/ <b>2b</b>	DTBP	12	32
3	[Ir(diFppy) <sub>2</sub> (dtb-bpy)]PF <sub>6</sub> / <b>2b</b>	DTBP	72	50
4	fluorescein/ <b>2b</b>	DTBP	48	trace
5	[Ru(bpy) <sub>3</sub> ](PF <sub>6</sub> ) <sub>2</sub> / <b>2b</b>	DTBP	12	42
6	[Ru(bpy) <sub>3</sub> ](PF <sub>6</sub> ) <sub>2</sub> / <b>2b</b>	NaHCO <sub>3</sub>	24	33
7	[Ru(bpy) <sub>3</sub> ](PF <sub>6</sub> ) <sub>2</sub> / <b>2b</b>	Et <sub>3</sub> N	24	25
8	[Ru(bpy) <sub>3</sub> ](PF <sub>6</sub> ) <sub>2</sub> / <b>2b</b>	Cy <sub>2</sub> NH	48	66
9	[Ru(bpy) <sub>3</sub> ](PF <sub>6</sub> ) <sub>2</sub> / <b>2b</b>	<i>i</i> Pr <sub>2</sub> NH	24	73
10 <sup>[c]</sup>	[Ru(bpy) <sub>3</sub> ](PF <sub>6</sub> ) <sub>2</sub> / <b>2b</b>	<i>i</i> Pr <sub>2</sub> NH	48	79
11 <sup>[c,d]</sup>	[Ru(bpy) <sub>3</sub> ](PF <sub>6</sub> ) <sub>2</sub> / <b>2b</b>	<i>i</i> Pr <sub>2</sub> NH	24	81
12 <sup>[c,d,e]</sup>	[Ru(bpy) <sub>3</sub> ](PF <sub>6</sub> ) <sub>2</sub> / <b>2b</b>	<i>i</i> Pr <sub>2</sub> NH	6	90
13 <sup>[c,d,e]</sup>	-/ <b>2b</b>	<i>i</i> Pr <sub>2</sub> NH	24	NR
14 <sup>[c,d,f]</sup>	[Ru(bpy) <sub>3</sub> ](PF <sub>6</sub> ) <sub>2</sub> / <b>2b</b>	<i>i</i> Pr <sub>2</sub> NH	24	trace
15 <sup>[c,d,g]</sup>	[Ru(bpy) <sub>3</sub> ](PF <sub>6</sub> ) <sub>2</sub> / <b>2b</b>	<i>i</i> Pr <sub>2</sub> NH	6	81

[a] Unless noted, reactions were performed on 0.2 mmol scale of 3-methylindole (3-methylindole/**2** 1:3 ratio), in degassed reagent-grade MeOH. [b] Isolated yield. [c] CBr<sub>4</sub>(1.5 equiv) was used. [d] 3-methylindole 0.05M in MeOH. [e] 7 W blue-LEDs was used. [f] In the dark. [g] In the sunlight. NR=no reaction.

noting that the present carboxylative process does not suffer brominating side events (both on the arene and alcoholic moiety **1g**) and that the *N*-Boc (Boc = *tert*-butoxycarbonyl) group is also selectively cleaved during irradiation (*N*-free tryptamine **3f** was isolated as the major compound).

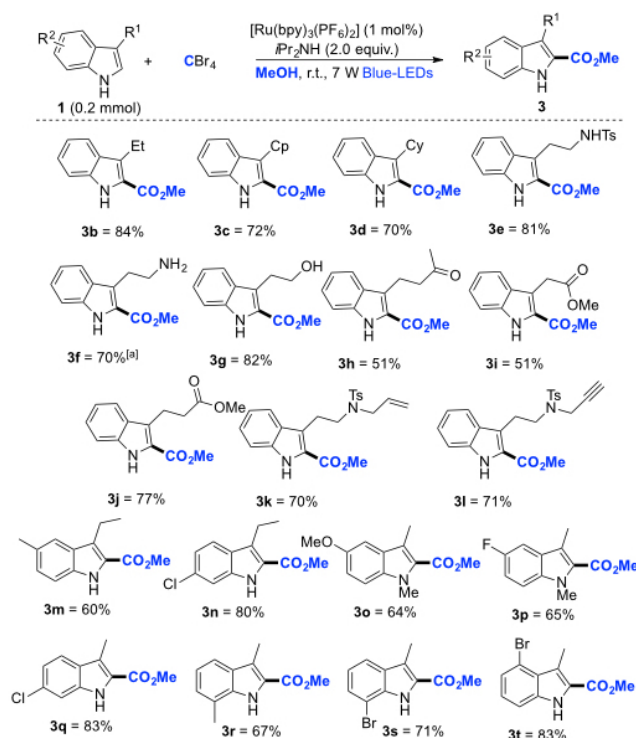


FIGURE 2.12: Generality of the method towards C(3)-substituted indoles (isolated yields are reported for each example). <sup>[a]</sup>*N*-Boc-protected tryptamine **1f** was used as the starting material.

Besides amino and alcohol moieties, a wide range of different functional groups proved tolerance of the working conditions. Indoles carrying ketone (**1h**), ester (**1i**, **1j**), alkene (**1k**), and alkyne (**1l**) substituents were proved competent in our protocol (yield: 51-77%). Furthermore, the impact of the electronic properties of the benzene ring on the final chemical outcome was evaluated. To this aim, substrates containing electron-deficient and -donating groups at the C(4)-, C(5)-, C(6)-, and C(7) arene-position were tested, furnishing the corresponding C(2)-carboxyl-indoles (**3m-t**) in good yields (60-83%). Next, the generality of the process was further substantiated by subjecting a range of C(2)-substituted or -unsubstituted indoles and azaindoles to the best conditions. As highlighted in figure 2.13, 2-substituted indoles carrying Me, Ph, and  $CO_2Et$  units (**4a-d**) successfully participated in the process, providing the corresponding products **5a-d** in 48-62% yields. Analogously, substrates without substituents at C(2)- and C(3)-positions were suitable in this reaction

to furnish indole 3-carboxylates **5e-h** (43-64%). In contrast, the introduction of a substituent at the C(4)-position (that is Br) led to the carboxylation of the C(2) carbon atom exclusively (yield: 50-60%) probably due to the steric hindrance (**5i-j**). In addition, ethyl indole C(2)- and C(3)-carboxylates could also be easily accessible by the use of EtOH as the solvent (**5k-l**, 49-67% yields). Lastly, preliminary encouraging results on different electron-rich heterocycles (like pyrrole, benzofuran, phenol, and thiophene, **5m-r**) were achieved in moderate to good yields (33-77%). Preliminary insights into the reaction

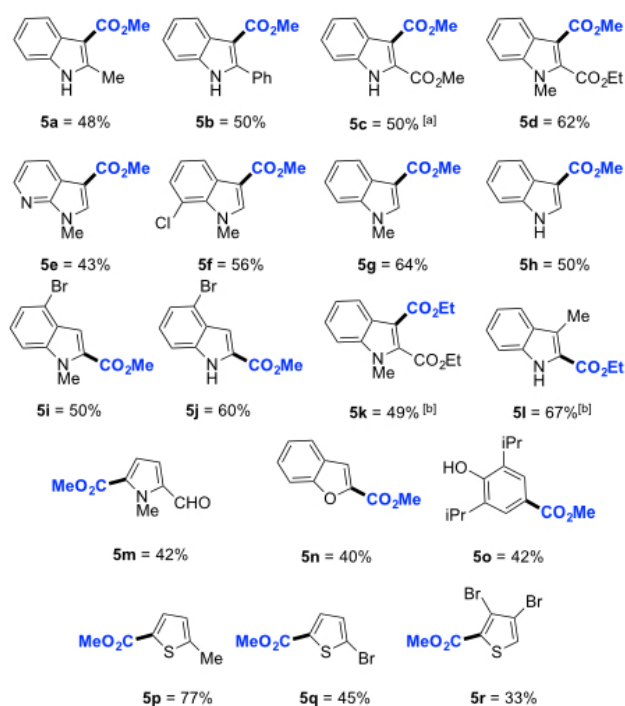


FIGURE 2.13: Substrate scope. The reaction conditions are the same depicted in figure 2.12. <sup>[a]</sup>Complete trans-esterification occurred starting from ethyl indole 2-carboxylate **4c**. <sup>[b]</sup>EtOH was used as the solvent.

mechanism are provided by the additional experiments described in figure 2.14: in particular, the isolation of the bromo derivative **6a** when ethylene glycol was used as the solvent (figure 2.14 (a)), allowed us to observe that the carbon atom of the final carboxylic group comes from  $\text{CBr}_4$  that exerts the initial indole C-H activation, so the alternative carbene-like mechanism can be excluded. In addition, the comparable results obtained by treating **6a** under standard optimized conditions ( $[\text{Ru}(\text{bpy})_3](\text{PF}_6)_2$  (1 mol%), 7 W blue LEDs, at a distance of 5 cm substrate **6a** in MeOH,  $i\text{Pr}_2\text{NH}$  (2 equiv) or simply by stirring **6a** in  $i\text{Pr}_2\text{NH}$  (2 equiv), MeOH at RT for 24 h account for a classic methanolysis reaction as the conclusive chemical event of the

cascade process). The reaction completely stopped in the dark and restarted

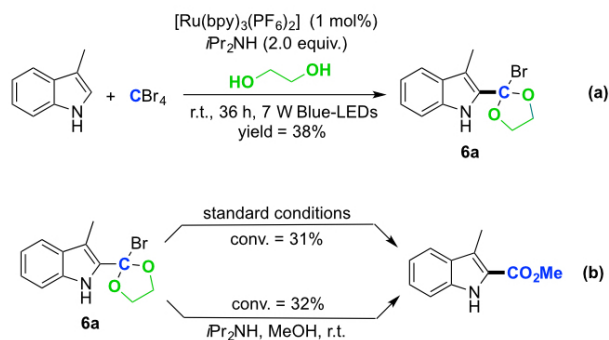


FIGURE 2.14: Carboxylation of 3-methylindole performed in ethylene glycol (a), in standard conditions ((b), top reaction) and by stirring the substrate in  $i\text{Pr}_2\text{NH}$  (2 equiv), MeOH at RT for 24 h ((b), bottom reaction)

when the light source was switched on once again (figure 2.15): this experiment clearly emphasized the pivotal role played by visible light in promoting the process. The reaction was performed with 3-methylindole and  $\text{CBr}_4$  in MeOH under the standard reaction conditions. In the recorded time, 25  $\mu\text{L}$  of the solution was taken from the reaction mixture and injected to Gas-Chromatography (GC) analysis to determine the conversion. To hypothesize

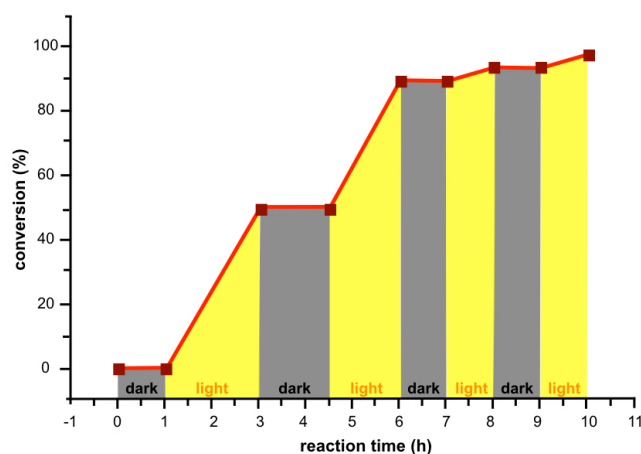


FIGURE 2.15: Experiment of On-Off Switching of the light.

a reaction mechanism, photophysical measurements can be performed, since the catalyst is photoactive. The absorption spectra of 3-methylindole,  $\text{CBr}_4$ ,  $i\text{Pr}_2\text{NH}$ , and the photocatalyst in MeOH is shown in figure 2.16: since none of the other reagents is absorbing visible light, the light excitation performed



with blue LEDs (blue spectrum in figure 2.16) is absorbed by the photocatalyst  $[\text{Ru}(\text{bpy})_3](\text{PF}_6)_2$ . Indeed, the emission profile of the blue LEDs is overlapping only the absorption profile the photocatalyst. Recording absorption

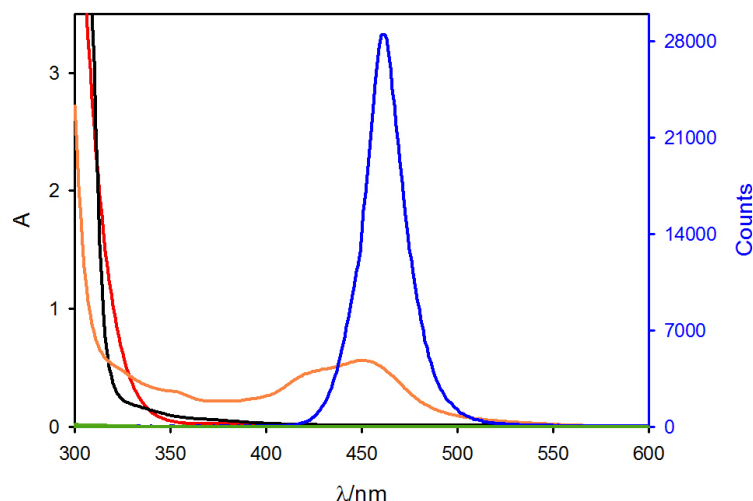


FIGURE 2.16: Absorption spectra of  $i\text{Pr}_2\text{NH}$  0.1 M (green line),  $\text{CBr}_4$  0.075 M (red line), 3-methylindole 0.05 M (black line) and  $[\text{Ru}(\text{bpy})_3](\text{PF}_6)_2$  (orange line)  $3.8 \times 10^{-4}$  M in MeOH. The amount of the species in solution is the same used in reaction mixture condition expect for the photocatalyst that is 2.5 times more diluted. The optical path length of the cuvette used was 0.1 cm. The blue spectrum is the emission profile of the blue LEDs used.

spectra of of the reaction mixture, is possible to follow the stability of the photocatalyst during the irradiation (figure 2.17): we collected the spectra of the reaction when no irradiation was performed (0 min), and after 1 hour, 3, 5, 10, 15 and 20 hours. The reaction was performed in air-tight cuvette (0.1 cm optical path length) equipped with a Teflon stopcock, so we were able to collected the spectra without transferring the solution from a flask to a specific cuvette. We observed that during the irradiation, no significant variation in the absorption spectra of the photocatalyst occurs: this feature suggest that the  $[\text{Ru}(\text{bpy})_3](\text{PF}_6)_2$  is stable during the irradiation, doesn't decompose and can be reused. The quantum yield  $\phi$ , determined by using equation 2.9, is 2.0% (as an average of 2 measurements), much lower than 100%. This result rules out a chain reaction mechanism, as supported also by the *On-Off Switching* experiment described above. The photon flux of the spectrophotometer was determined by standard ferrioxalate actinometry and resulted to be  $4.52 \times 10^{-6}$  Eisnteins/s. For the determination of the moles of products obtained, the same cuvette air-tight cuvette with 0.1 cm optical path length, was filled with 0.3 mL of a MeOH solution containing  $\text{CBr}_4$  0.05 M,



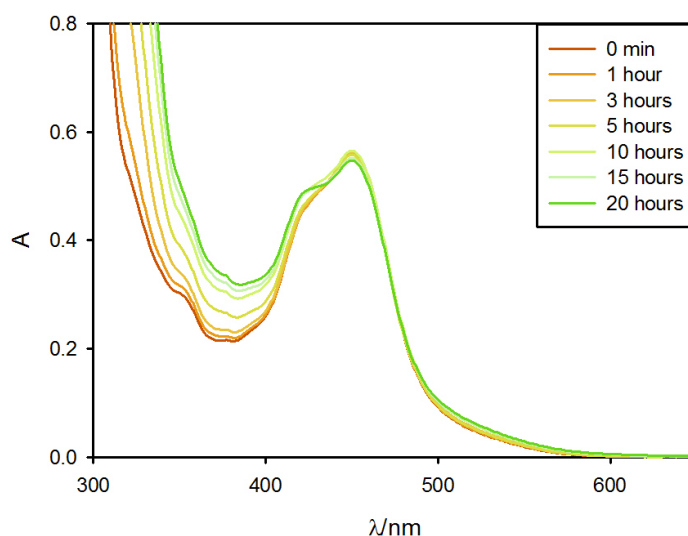


FIGURE 2.17: Reaction mixture in MeOH ( $[\text{Ru}(\text{bpy})_3](\text{PF}_6)_2$   $3.8 \times 10^{-4}$  M,  $i\text{Pr}_2\text{NH}$  0.026 M,  $\text{CBr}_4$  0.02 M, and 3-methylindole 0.013 M) irradiated for 0 min, 1 hour, 3 hours, 5 hours, 10 hours, 15 hours and 20 hours.

3-methylindole 0.075 M,  $i\text{Pr}_2\text{NH}$  0.1 M and  $[\text{Ru}(\text{bpy})_3](\text{PF}_6)_2$   $5.6 \times 10^{-4}$  M. The cuvette was then degassed by purging argon for 20 minutes. The sample was manually stirred and irradiated ( $\lambda = 450$  nm, slit width = 20 nm) for 230 min. After irradiation, the solution was concentrated under reduced pressure and the reaction conversion was determined by crude  $^1\text{H}$ -NMR. Finally, to get better insight on the mechanism, we performed quenching experiments, to determine which component quenched the excited state of the photosensitizer and to obtain the quenching constant. Since no quenching of the emission of the photosensitizer by 3-methylindole and  $i\text{Pr}_2\text{NH}$  was observed at the concentration used in the reaction (consistently, the reaction proceeds also in the absence of the amine with 60% of conversion), we studied the quenching of the excited state by  $\text{CBr}_4$ . We collected the lifetime decay of a degassed solution of  $[\text{Ru}(\text{bpy})_3](\text{PF}_6)_2$  in MeOH after the addition of different amount of  $\text{CBr}_4$  (figure 2.18, plot a). The Stern-Volmer plot shows a linear correlation between the ratio of the luminescent excited state lifetime in the absence ( $\tau_0$ ) and in the presence ( $\tau$ ) of the quencher, the  $\text{CBr}_4$  (figure 2.18, plot b). On the basis of the Stern-Volmer equation (2.10), the quenching constant is estimated as  $5.3 \times 10^6 \text{ M}^{-1}\text{s}^{-1}$ :

$$\frac{\tau_0}{\tau} = 1 + K_{SV}[Q] = 1 + k_Q\tau_0[Q] \quad (2.10)$$

To conclude a plausible mechanism is proposed, as shown in figure 2.19,

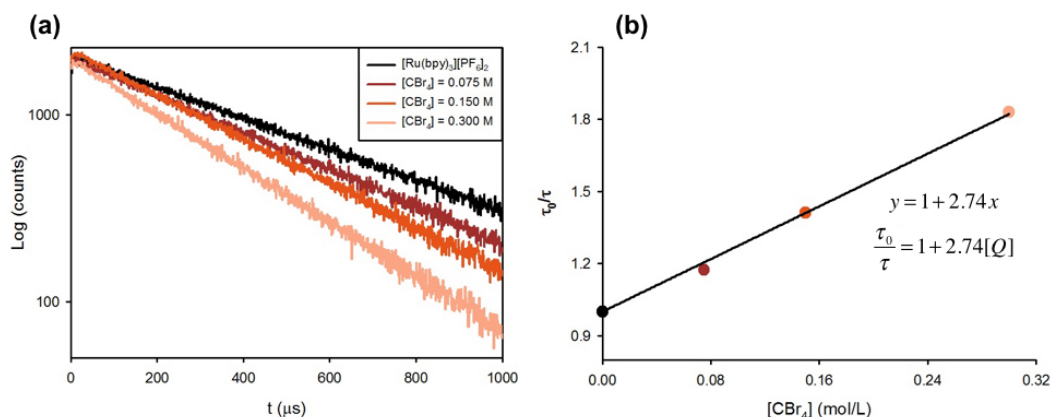


FIGURE 2.18: (a) Lifetime decays of a  $5.0 \times 10^{-5}$  M degassed solution of  $[\text{Ru}(\text{bpy})_3](\text{PF}_6)_2$  in MeOH with different amount of  $\text{CBr}_4$ ; (b) Stern-Volmer quenching plot of the same solution of photosensitizer as a function of  $\text{CBr}_4$  concentration.

using methoxycarboxylation of 3-methylindole as an example of this novel photocatalytic process. Visible-light excitation of the reaction mixture, populate the lowest energy triplet excited state of the photocatalyst,  $^*[\text{Ru}(\text{bpy})_3]^{2+}$ , since none of the other reagents is absorbing visible light (figure 2.16).  $^*[\text{Ru}(\text{bpy})_3]^{2+}$  is quenched by  $\text{CBr}_4$  with a quenching constant: this process is the oxidation of  $^*[\text{Ru}(\text{bpy})_3]^{2+}$  and the reduction of  $\text{CBr}_4$ , which generates  $\cdot\text{CX}_3$  (I) and  $\text{Br}^-$ . Trapping of the electron-deficient radical by 3-methylindole formed a new benzyl radical II, which can be oxidized by  $[\text{Ru}(\text{bpy})_3]^{3+}$  to provide the intermediate III, regenerating the photocatalyst  $[\text{Ru}(\text{bpy})_3]^{2+}$ . Rearomatization of the intermediate III followed by methanolysis furnished the observed product.

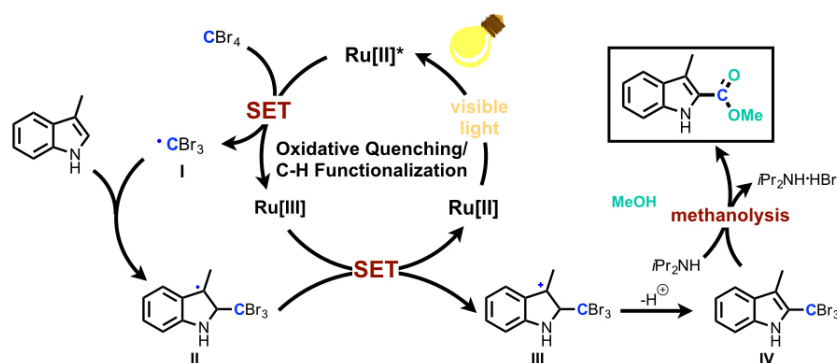


FIGURE 2.19: Hypothesis of reaction mechanism.

### 2.1.2 Organocatalytic Enantioselective Alkylation of Aldehydes with $[\text{Fe}(\text{bpy})_3]\text{Br}_2$ Catalyst and Visible Light

Due to the mild reaction conditions and the high enantiomeric excesses obtained, asymmetric catalysis promoted by visible light, a sustainable and economical source of energy, is emerging as an active new field of investigation. There are basically three leading strategies to promote enantioselective chemical reactions by light with enamine organocatalysts and bromo derivatives,<sup>80</sup> and all of them are based on photoinduced electron transfer (ET) processes. In 2008, MacMillan's group reported the first example of merging visible light induced photoredox catalysis in asymmetric organocatalysis by using  $[\text{Ru}(\text{bpy})_3]^{2+}$  as photosensitizer (figure 2.20 (a)).<sup>81</sup> Chiral enamines formed in situ as nucleophilic partners are able to intercept the radical species generated by the photoredox event. Similarly, radical species can be generated by other photosensitizers as organic dyes, semiconductors, or chiral iridium complexes.<sup>82</sup> A variant for the generation of radical species was disclosed by Melchiorre, who used chiral enamines able to form EDA complexes with benzyl halides electrophiles, absorbing visible light and inducing a charge transfer (figure 2.20 (b)).<sup>62</sup> In all these processes, three general events are occurring in order to drive the chemical reaction:

- (i) a photodriven initiation step;
- (ii) the electron transfer (ET) involving the photosensitizer (or the EDA complexes, or enamine);
- (iii) the oxidation of generated  $\alpha$ -amino radicals to iminium ions.

Most commonly employed photosensitizers are based on rare and expensive ruthenium and iridium complexes, although interesting processes based on copper<sup>72,83</sup> and chromium<sup>84</sup> photosensitizers have been described. In this contest, the use of iron(II) complexes would be in fact quite attractive for photocatalytic stereoselective reactions as iron is inexpensive and very abundant. Photophysical properties of iron(II) tris(bipyridine) complexes were fully investigated. The prototypical  $[\text{Fe}(\text{bpy})_3]^{2+}$  complex displays a MLCT band in the visible region. The lowest energy excited state is a metal-centered (MC) state, which is formed within a hundred femtoseconds from the MLCT excited states and it is not luminescent, due to fast non-radiative decay to the ground state (ca. 650 ps lifetime).<sup>85</sup>  $[\text{Fe}(\text{bpy})_3]^{2+}$  is not a good candidate for dynamic electron-transfer processes because of the extremely short lifetime of the lowest energy excited state. Nevertheless, iron(II) polypyridine

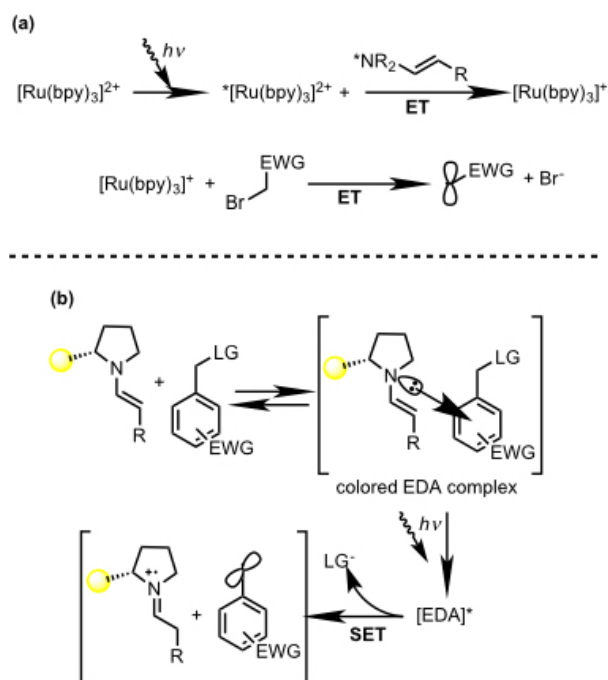


FIGURE 2.20: Strategies in stereoselective photocatalytic addition of bromo derivatives: (a) asymmetric photocatalysis with  $[\text{Ru}(\text{bpy})_3]^{2+}$  and (b) asymmetric photocatalysis induced by EDA complex.

complexes have been reported as photosensitizers of  $\text{TiO}_2$  demonstrating ultrafast electron injection.<sup>86</sup>

In order to investigate the possibility to use iron(II) polypyridyl complexes in photocatalysis, we have selected, as a standard reaction, the  $\alpha$ -alkylation of aldehydes developed by MacMillan (figure 2.21),<sup>87</sup> with the aim of replacing  $[\text{Ru}(\text{bpy})_3]^{2+}$ . Different Fe(II) complexes were tested in the model reaction

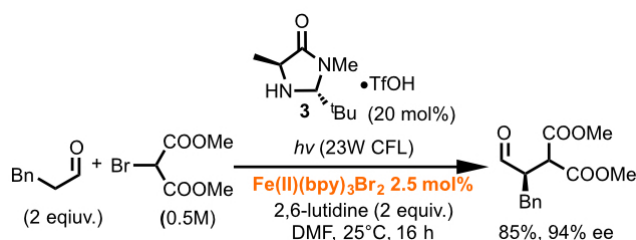


FIGURE 2.21: Optimized conditions for the  $[\text{Fe}(\text{bpy})_3]\text{Br}_2$  photocatalyzed reaction.

with chiral (racemic and enantiopure) organocatalysts:  $[\text{Fe}(\text{bpy})_3]\text{Br}_2$  used in catalytic amount (2.5 mol%) was an efficient photosensitizer for promoting the reaction between hydrocinnamaldehyde and dimethyl bromomalonate, in the presence of 20 mol% of the organocatalyst **3** in figure 2.21 and upon

irradiation with visible light. Isolated yields and enantiomeric excesses obtained were comparable to the reaction promoted by  $[\text{Ru}(\text{bpy})_3]^{2+}$ . Among all the iron complexes investigated,  $[\text{Fe}(\text{bpy})_3]\text{Br}_2$  gave the maximum yields, and from various solvents investigated, *N,N*-dimethylformamide (DMF) was the solvent of choice; enantioselectivity was optimal at room temperature. The reaction was investigated in detail with various aldehydes and bromo derivatives. The salient results are reported in figure 2.22. It was possible to employ in the reaction various bromo-substituted carbonyl compounds as the reaction tolerates various functional and protecting groups. No side reaction is observed with aldehydes bearing alkene functional groups. In

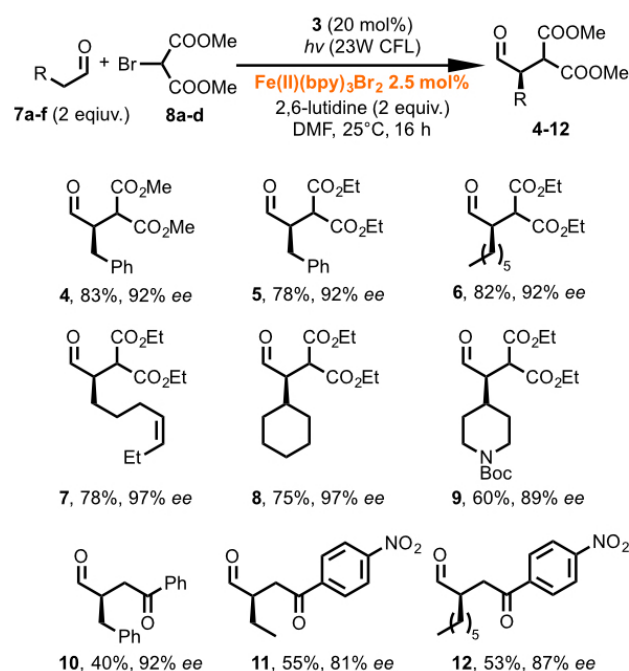


FIGURE 2.22: Scope of the stereoselective alkylation catalyzed by  $[\text{Fe}(\text{bpy})_3]\text{Br}_2$ .

addition, we have investigated the practical use of photoinduced Fe(II) reaction to access useful synthetic intermediates. The addition of bromo ester **8e** to hydrocinnamic aldehydes **7a,g,h** gave in a straightforward manner the lactons **13-15**, key intermediates for the synthesis of biologically active compounds. The lacton **15** was transformed into the natural product **16** by a straightforward transformation as illustrated in figure 2.23.

To clarify mechanistic details about our reaction, we performed some control experiments. Because a CFL lamp emits also in the UV region (figure 2.24), where reagents absorb light (figure 2.28, plot a), we ruled out a UV-induced mechanism by testing the reaction upon visible irradiation ( $\lambda > 420$

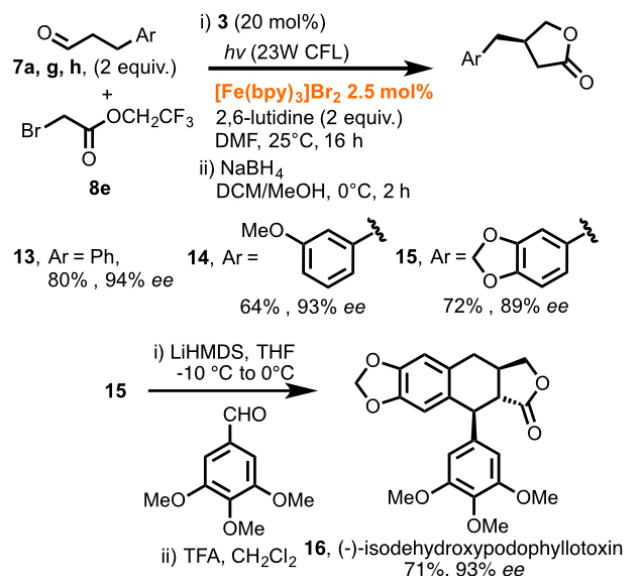


FIGURE 2.23: Preparation of enantioenriched lactones via alkylation of aldehydes and synthesis of (-)-isodehydroxypodophyllotoxin.

nm), where only the photosensitizer  $\text{Fe}(\text{bpy})_3\text{Br}_2$  absorbs light and effectively promotes the reaction. On the other hand, in the presence of the iron sensitizer and in the absence of light, the reaction does not proceed.

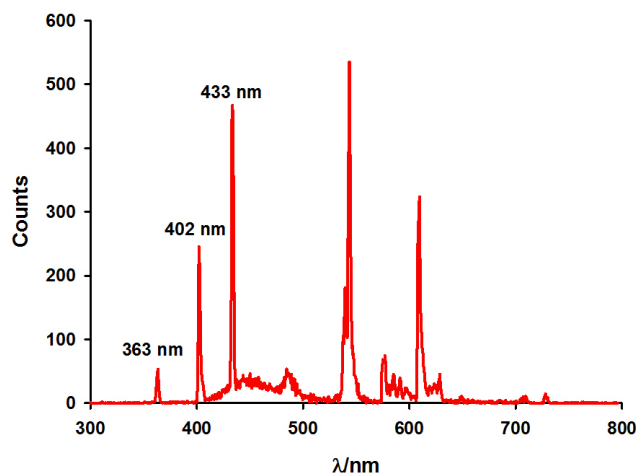


FIGURE 2.24: Emission profile of the 23W Compact Fluorescent lamp used to irradiate the solutions.

In order to prove the formation of radical species under the combined action of light and photocatalyst, we decided to study the formation of radicals with EPR, in the presence of a radical trap. The spin trap experiments

were performed in the presence of *N*-tert-butyl- $\alpha$ -phenylnitrone (PBN) (figure 2.25). In order to get a good EPR signal for the correct characterization of the spin adduct, we initially irradiated the reaction mixture with light containing also near UV ( $\lambda > 320$  nm). Actually, irradiation at these wavelengths of a deoxygenated DMF solution containing bromomalonate **8a** (0.5 M), [Fe(bpy)<sub>3</sub>]Br<sub>2</sub> (10 mol %) and PBN (0.1 M), resulted in a strong EPR signal consisting of a characteristic doublet of triplets (figure 2.26 a). The spectrum was attributed to spin adduct **17** (figure 2.25), resulting from addition of malonate alkyl radical to PBN, as suggested by the values of the EPR parameters ( $a_N = 14.95$  G,  $a_H = 4.75$  G,  $g = 2.0057$ ), which are typical for PBN adducts with alkyl radicals having carbonyl groups in  $\alpha$ -position. We then repeated the same experiment by employing visible light ( $\lambda > 420$  nm), thus mimicking the synthetic reaction conditions (figure 2.26 b). Also, in this case, the signal due to the radical adduct **17** was clearly detected, although the intensity of the signals was weaker with respect to that recorded in the presence of UV-visible light. No signals were observed in the absence of light or after irradiation of a solution containing only the photosensitizer and the spin trap (figure 2.26 c).

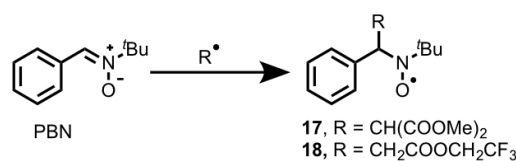


FIGURE 2.25: Radical trap experiment demonstrates the formation of radical induced by photocatalyst and visible light.

A similar trend was also observed in the presence of bromoester **8e**: the PBN-adduct **18** was characterized by slightly different EPR parameters:  $a_N = 14.85$  G,  $a_H = 5.55$  G,  $g = 2.0057$ . In this case, however, the intensities of EPR spectra were lower if compared to those observed in the spectra recorded with bromomalonate **8a** under the same experimental conditions. This indicates that the formation of the less stable alkyl radical from **8e** is more difficult.

From these experiments, it is clear that visible light and [Fe(bpy)<sub>3</sub>]Br<sub>2</sub> are necessary to drive the complete formation of the product. Furthermore, EPR studies with a radical trap evidence the formation of a radical and the reaction is completely shut down in the presence of 2,2,6,6-tetramethyl-1-piperidinyloxy (TEMPO; 20 mol % and 100 mol %). To obtain more information about the mechanism, an experiment with the light turned off and on (figures 2.27,

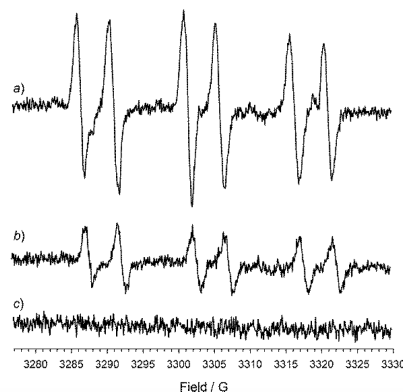


FIGURE 2.26: EPR spectra of spin adduct **17** generated in DMF in the presence of dimethyl bromomalonate **8a** (0.5 M) and PBN (0.1 M) as the spin trap at room temperature. Reaction conditions: (a)  $[\text{Fe}(\text{bpy})_3]\text{Br}_2$  (10 mol %), irradiation with UV-visible light ( $\lambda > 320$  nm); (b)  $[\text{Fe}(\text{bpy})_3][\text{Br}_2]$  (10 mol %), irradiation with visible light ( $\lambda > 420$  nm); (c)  $\text{Fe}(\text{bpy})_3[\text{Br}_2]$  (10 mol %) no irradiation.

plot a and b) was performed and showed that the reaction is proceeding also when the light is switched off, suggesting the existence of a radical chain mechanism.

To understand the photocatalytic mechanism of the reaction, we studied

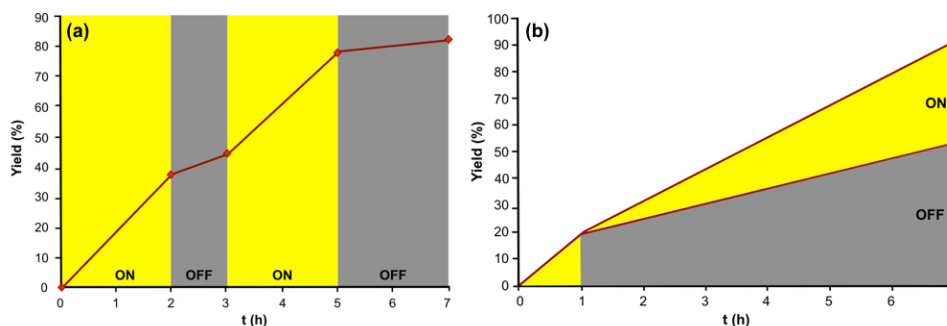


FIGURE 2.27: (a) Successive intervals of irradiation and dark periods. The reaction was performed at r.t with 0.2 mmol of bromomalonate (**8a**), 2 equiv of aldehyde (**7a**) and 2 equiv. of 2,6-lutidine, in the presence of 20 mol% of **3** and 2.5 mol% of  $[\text{Fe}(\text{bpy})_3]\text{Br}_2$  in DMF (0.5 M); yield was determined by GC-MS analysis from an aliquot of the reaction mixture. (b) Two separate but identical reaction were simultaneously performed: the first one was irradiated for 1h and it was kept in the dark for 6 hours. The second one was irradiate for 6 hours. The reactions conditions are the same used for the experiment shown in plot (a).

the reaction from the photophysical point of view. First of all, we collected the absorption spectra of the reaction mixture components: from the figure 2.28, plot a, we can observe that upon visible light irradiation, we excited



selectively the photocatalyst, since the other components don't show significant absorption in the visible region of the light spectrum. Monitoring the reaction with spectrophotometric spectroscopy, allowed us to conclude that no decomposition of the photosensitizer was observed at the end of the reaction (figure 2.28, plot b). Due to the very short lifetime of the lowest

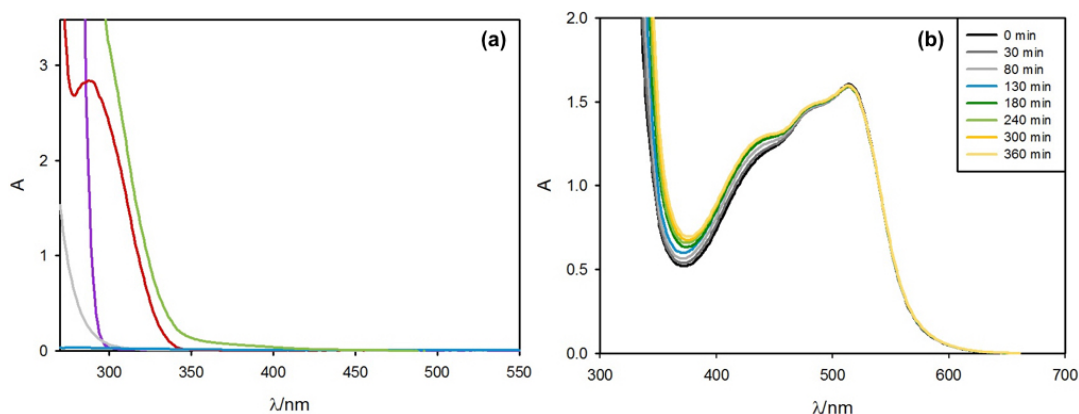


FIGURE 2.28: (a) Absorption spectra of 2,6-lutidine 1 M (violet line), dimethyl bromomalonate **8a** 0.5 M (grey line), 3-phenylpropanal **7a** 1 M (red line), MacMillan catalyst **3** 0.1 M (blue line) and complete reaction mixture without [Fe(bpy)<sub>3</sub>]Br<sub>2</sub> (green line) in DMF; the amount of the species in solution is the same used during the photoreaction. (b) Same reaction mixture of plot a, with the addition of [Fe(bpy)<sub>3</sub>][Br<sub>2</sub>] 1.2 × 10<sup>-3</sup> M in DMF solution, irradiated for 0 min (black line), 30 min, 80 min, 130 min, 180 min, 240 min, 300 min and 360 min (see legend).

energy excited state of the iron(II) complex, we used *femtosecond* laser absorption spectroscopy to monitor the possibility of excited state interactions. Upon irradiation at 510 nm of a 5.7 × 10<sup>-4</sup> M solution of [Fe(bpy)<sub>3</sub>]Br<sub>2</sub> in DMF, the characteristic bleaching of the MLCT absorption band was observed at very short time delay ( $t = 1.2$  ps, figure 2.29 plot a): this transient then decay monotonically to the baseline. The plot of the absorbance change ( $\Delta A$ ) at 535 nm as a function of time, results in a monoexponential decay with a lifetime of 570 ps (figure 2.29 plot b, black solid line) very similar to the literature reported values for the ligand field excited state (MC).<sup>85</sup> Upon addition of dimethyl bromomalonate **8a** (in the range 0.5-6.8M) or enamine **29** (in the range 0.06 M), no appreciable changes in the transient absorption feature were measured (figure 2.29 plot b), so that no detectable quenching process is observed. However, the dual requirement of [Fe(bpy)<sub>3</sub>]Br<sub>2</sub> and light to trigger the catalytic reaction, in spite the absence of efficient quenching process, suggest that the photosensitizer must be capable of promoting, upon excitation, a chain radical reaction in which the photochemical event is only the starting step. Photoalkylation of cis-cyclopropane-substituted aldehyde ( $\pm$ )-

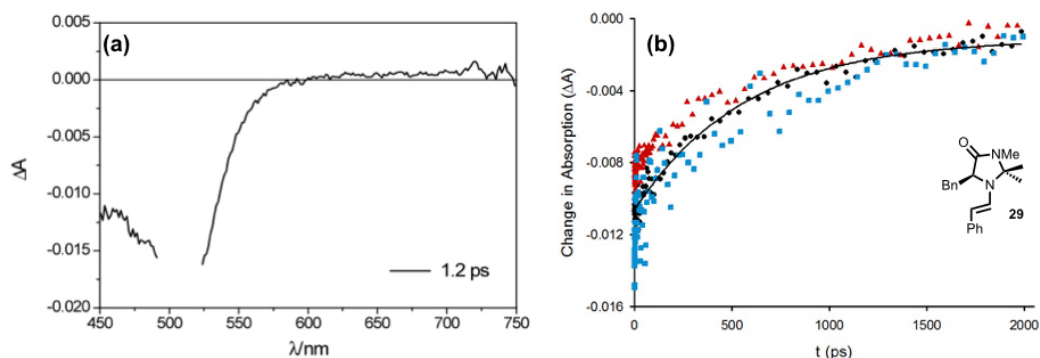


FIGURE 2.29: (a) Transient absorption spectrum at 1.2 ps time-delay obtained by ultrafast spectroscopy (excitation at 510 nm) of  $[\text{Fe}(\text{bpy})_3]\text{Br}_2$   $5.7 \times 10^{-4}$  M in DMF. (b) Exponential decay of absorption changes at 535 nm of  $[\text{Fe}(\text{bpy})_3]\text{Br}_2$  ( $5.7 \times 10^{-4}$  M, black circle),  $[\text{Fe}(\text{bpy})_3]\text{Br}_2$  with dimethyl bromomalonate **8a** 0.5 M (red triangle) and  $[\text{Fe}(\text{bpy})_3]\text{Br}_2$  with enamine **29** 0.06 M (blue square) in DMF stirred solution. The amount of dimethyl bromomalonate **8a** in solution is the same used to perform the photoreaction. The black solid line is the fitting curve of  $[\text{Fe}(\text{bpy})_3]\text{Br}_2$  exponential decay.

*cis-1i* with dimethyl bromomalonate **8a** was performed to demonstrate that reaction proceeded through a traditional enamine catalysis pathway, with the EWG stabilized carbon-centred radical **III** species adding to the generated enamine **II** as the propagation step (**Path A**). If the reaction proceeded through a radical-cation pathway (**Path B**), the cyclopropylcarbiny radical **VI** formed after electron transfer process should undergo fast ring-opening **VII** and ring closing prior to C-C bond formation leading to the thermodynamically more stable intermediate **VIII** and consequentially to the product ( $\pm$ )-*trans-20*. When ( $\pm$ )-*cis-1i* was subjected to the photocatalytic alkylation protocol with bromide **8a** the ( $\pm$ )-*cis-20* product was exclusively formed, provides a strong evidence that an enamine addition mechanism (**Path A**) is operating. Therefore, we propose that the reaction is proceeding through a radical chain propagation pathway (see figure 2.31). The addition of the radical **XII** to enamine **XI** is the enantiodiscriminating step. The  $[\text{Fe}(\text{bpy})_3]\text{Br}_2$  photosensitizer acts as a reductant for initiating the chain mechanism. The ability of the amidoalkyl radical **XIII** to behave as strong reducing agent induces the reduction of bromomalonate, regenerating the radical **XII**.

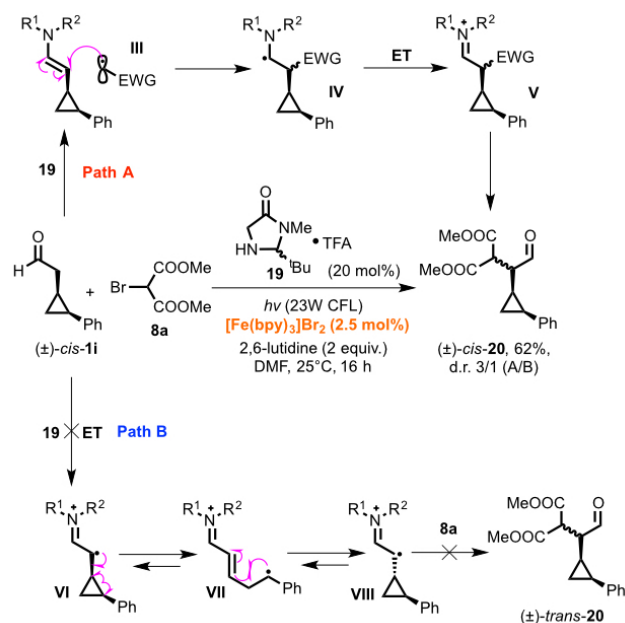


FIGURE 2.30: Alkylation reaction performed in the presence of a radical clock, with the two possible pathways.

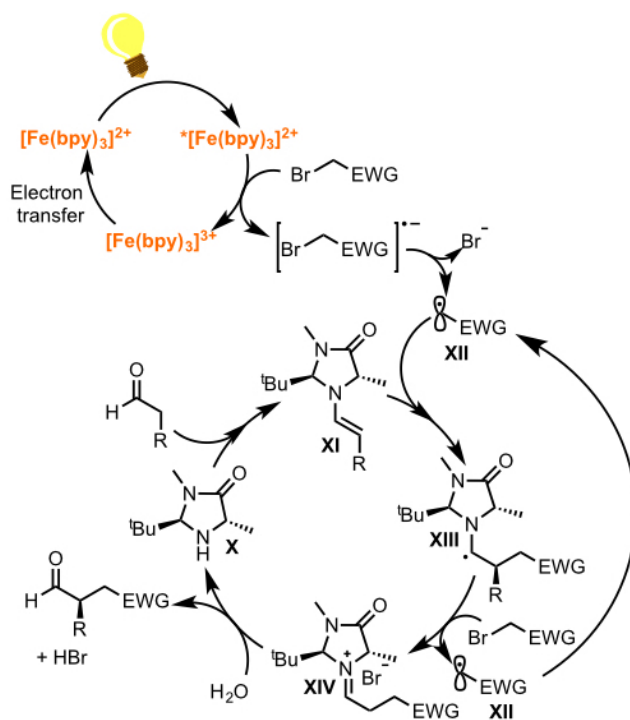


FIGURE 2.31: Suggested catalytic cycle for the Fe(II) alkylation.

TABLE 2.2: Effect of photosensitizer nature.

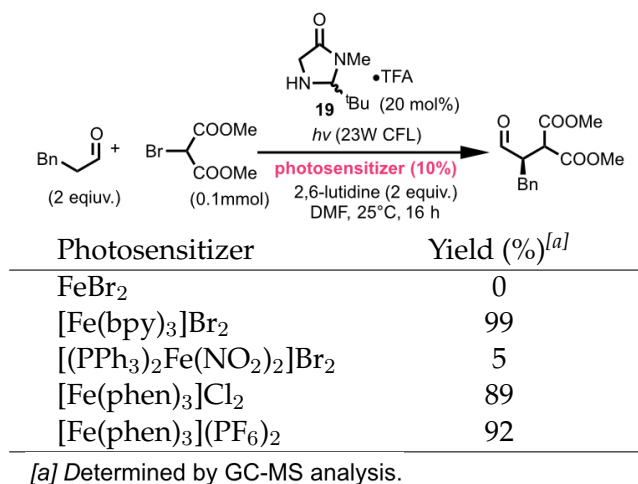


TABLE 2.3: Effect of solvent.

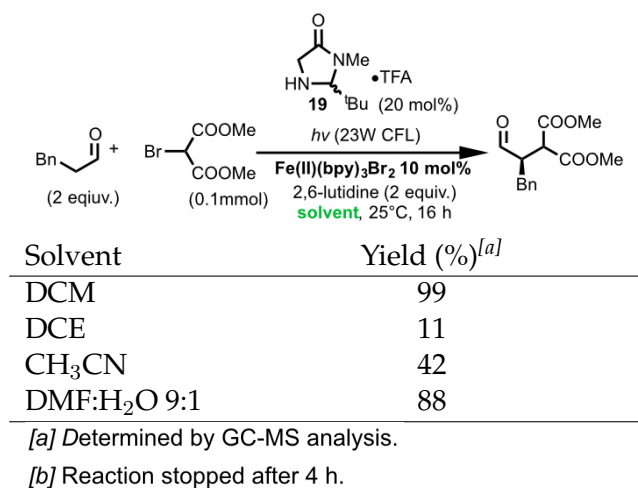


TABLE 2.4: Effect of organocatalyst.

Reaction conditions:  $h\nu$  (23W CFL),  $\text{Fe}(\text{bpy})_3\text{Br}_2$  (10 mol%), 2,6-lutidine, DMF, 25°C, 16 h.

Organocatalyst structures and associated HX:

- A**: HX = none
- 3**: HX = TfOH
- C**: HX = TFA
- D**: HX = HCl
- E**: HX = TFA
- F**: HX = TfOH
- G**: HX = TfOH
- H**: HX = TfOH
- I**: HX = TFA
- J**: Ar =  $(\text{CF}_3)_2\text{-C}_6\text{H}_3$

Organocatalyst	Yield (%) <sup>[a]</sup>	ee (%) <sup>[b]</sup>
<b>A</b>	29	93
<b>3</b>	79	93
<b>B</b>	52	73
<b>A + LutTFA</b> <sup>[c]</sup>	77	81
<b>A + LutTfOH</b> <sup>[d]</sup>	65	93
<b>C</b>	32	89
<b>D</b>	63	62
<b>E</b>	73	83
<b>F</b>	76	58
<b>G</b>	54	36
<b>H</b>	28	n.d.
<b>I</b>	20	-70

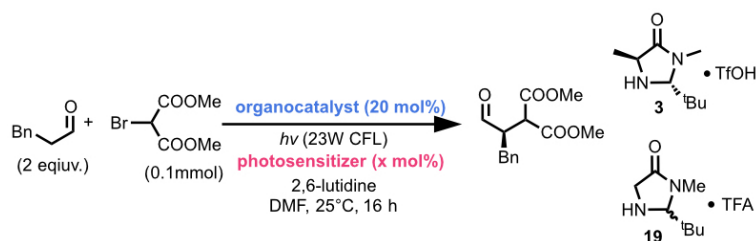
[a] Determined by GC-MS analysis. [b] Determined by HPLC analysis on chiral stationary phase. [c] Lutidinium trifluoroacetate. [d] Lutidiniumtriflate.

TABLE 2.5: Effect of concentration and iron catalyst loading.

Photosensitizer loading (mol %)	Concentration of bromomalonate ( <b>8a</b> )(M)	Yield (%) <sup>[a]</sup>	ee (%) <sup>[b]</sup>
10	0.1	79	93
10	0.5	81	92
5	0.5	74	93
5	0.2	61	93
2.5	0.5	89	93
1	0.5	79	92

[a] Determined by GC-MS analysis. [b] Determined by HPLC analysis on chiral stationary phase.

TABLE 2.6: Light effect.



	Photosensitizer (mol %)	Light	Time (h)	Yield (%) <sup>[a]</sup>	ee (%) <sup>[b]</sup>
<b>19</b>	-	23W CFL	16	95 <sup>[c]</sup>	-
<b>19</b>	-	$\lambda > 420$ nm, 250W	6	0	-
<b>19</b>	[Fe(bpy) <sub>3</sub> ]Br <sub>2</sub> (0.004 %mol)	$\lambda > 420$ nm, 250W	10	82	-
<b>19</b>	[Fe(bpy) <sub>3</sub> ]Br <sub>2</sub> (0.25 %mol)	$\lambda > 420$ nm, 250W	6	87	-
<b>3</b>	[Fe(bpy) <sub>3</sub> ]Br <sub>2</sub> (0.25 %mol)	$\lambda > 420$ nm, 250W	6	49	93
<b>3</b>	[Fe(bpy) <sub>3</sub> ]Br <sub>2</sub> (2.5 %mol)	23W CFL	16	89	93
<b>3</b>	[Fe(bpy) <sub>3</sub> ]Br <sub>2</sub> (2.5 %mol)	no	16	0	-
<b>3</b>	-	$\lambda > 420$ nm, 23W	16	0	-
<b>3</b>	-	23W CFL	16	32 <sup>[c]</sup>	93

[a] Determined by GC-MS analysis. [b] Determined by HPLC analysis on chiral stationary phase. [c] As reported by Melchiorre, photoexcited state of enamines are able to transfer electron to bromomalonates starting a radical-chain reaction under not filtered CFL light. Better yields were obtained with the catalyst **19** are due to the less sterical hindrance.

## 2.2 Visible Light Photoredox Catalysis with Organic Dyes

As illustrated in section 2.1, the majority of literature photocatalysis papers are predominantly focused on the synthetic applications of transition metal-based chromophores, such as ruthenium and iridium polypyridine complexes. The use of photocatalytic organic chromophores to organic synthesis is somewhat less familiar, but certain, is an inexpensive and metal-free alternative to transition metal complexes.

Based on the classification that Nathan A. Romero *et al* made,<sup>60</sup> arranged by catalyst class, I will show an example organic reaction catalyzed by the most common organic dyes:

- cyanoarenes: polycyano-benzenes, naphthalene and anthracenes;
- benzophenones and quinones
- quinoliniums
- xanthenes dyes: fluorescein and rhodamines
- phenothiazines
- other organic dyes: in particular perylene diimides and BODIPY dyes

**Cyanoarenes: Polycyano-benzenes, Naphthalene and Anthracenes.** Cyanoarenes, such as 1,4-dicyanobenzene (*p*-DCB), 1,4-dicyanonaphthalene (DCN) and 9,10-dicyanoanthracene (DCA), have large singlet excited state energies, which, even when paired with moderately large ground state reduction potentials ranging from -0.7 to -1.7 V, render them capable of oxidizing compounds with oxidation potentials exceeding +2.0 V. The radical anions resulting from photoinduced electron transfer are moderate to good reductants. The cyanoarenes with increased aromatic moiety (like DCN and DCA) are most useful, as they absorb in the near UV and visible and possess longer singlet lifetimes than simple cyanobenzenes. Dicyanoarenes are effective catalysts for net  $\alpha$ -arylation reactions of ketones. In need  $\alpha$ -arylation of ketones is an important carbon-carbon bond formation strategy that could be utilized for the rapid access of an otherwise inaccessible molecule. Pandey and coworkers demonstrated a series of oxidative annulation reactions of silyl enol ethers with pendant electron-rich aromatics.<sup>88</sup> They used DCN as photocatalyst to obtain a different cyclization modes to form 5-8 membered ring systems, via

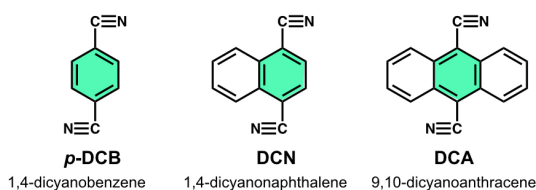


FIGURE 2.32: Chemical structure of the most used cyanoarenes.

*endo*- and *exo*-type of annulations under anaerobic conditions. To have a successful cyclization, the aromatic ketones must bear one or two methoxy substituents. The proposed mechanism, involve a single electron oxidation of the silyl enol ether substrate **I**, followed by cyclization to the radical cation **III** (figure 2.33). Then, the radical cation loses of trimethylsilyl cation and a second single electron oxidation leads to cyclohexadienyl cation **IV**. Finally, **IV** intermediate loses a proton to furnish the ketone adduct (**II**). The regeneration of the photocatalyst, that is responsible of the silyl enol ether substrate oxidation, is proposed to occur via single electron oxidation of **DCN** anion radical by molecular oxygen: hydrogen peroxide is produced as the side product as an overall two-electron oxidation process.

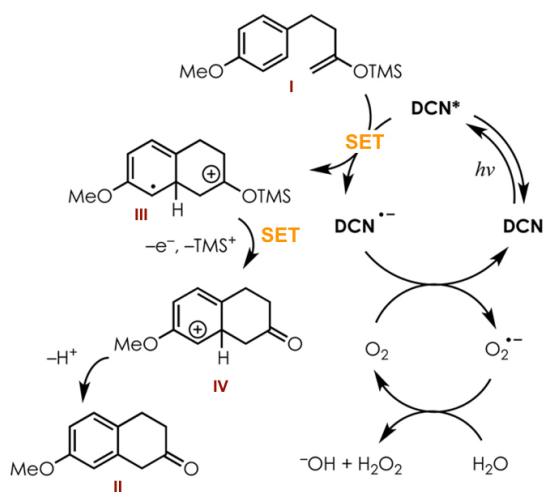


FIGURE 2.33: Mechanism of oxidative  $\alpha$ -arylation of ketones.

**Benzophenones and Quinones.** Benzophenone can be considered as an archetypal example of organic dyes which undergo rapid intersystem crossing with high efficiency ( $k_{ISC} \sim \times 10^{11} \text{s}^{-1}$ ,  $\phi_{ISC} = 1.0$ ), which is characteristic of carbonyl compounds whose  $S_1(n, \pi^*)$ , and  $T_2(\pi, \pi^*)$  are close in energy (see figure 2.35). Indeed, other benzophenone derivatives (including xanthone



XO, thioxanthone TXO, and fluorenone FLN) exhibit quantum yields formation of  $T_1$  close to unity and share similar reactivity patterns. These photophysical features ensure the fact that benzophenone and its derivatives are some of the most effective mediators of triplet energy transfer. The typical

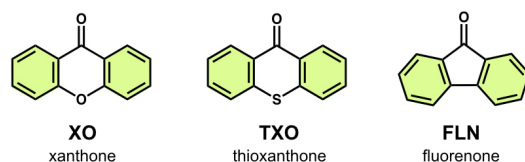


FIGURE 2.34: Chemical structure of the most used benzophenones.

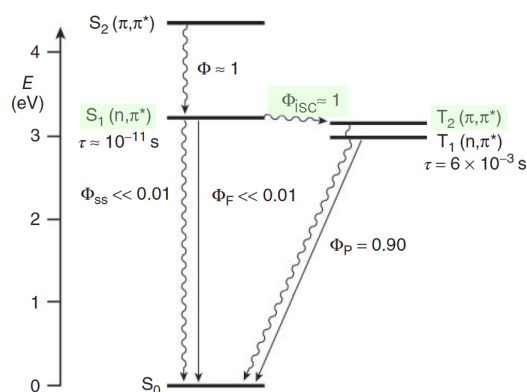


FIGURE 2.35: Energy state diagram for benzophenone. Adapter from V. Balzani, P. Ceroni and A. Juris, *Photochemistry and Photophysics*, 2014, Wiley-VCH, p 87.

reactivity of benzophenone triplets is *hydrogen atom transfer* (HAT), since benzophenones are only moderate oxidants and poor reductants in the  $T_1$  state. This process of photoinduced hydrogen atom transfer, or PHAT, can be seen as sequential single electron transfer (SET) and proton transfer (PT) steps, results in ketyl radical of the type **BPH $\cdot$** . In some cases, the two steps are not dynamically distinguishable, especially in the well-studied hydrogen atom abstraction from alkyl amines (figure 2.36). One common synthetic application of benzophenones found in earlier examples of photoredox catalysis is the generation and addition of carbon-centered radicals precursors, like alcohols, acetals, and even alkanes, to enones.<sup>89</sup>

Generally, quinones are weak absorbers in the visible region ( $\sim 400$  nm). In terms of photophysics and reactivity, benzannulated quinones such as naphthoquinone and anthraquinone behave like benzophenones. For example, anthraquinone (**AQ**) and its derivatives undergo fast intersystem crossing to the triplet states, followed by an efficiently hydrogen atom abstraction to

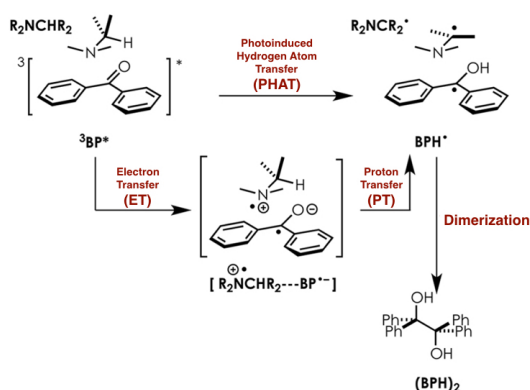


FIGURE 2.36: Photoinduced hydrogen atom transfer (PHAT) process of excited state of benzophenones.

form the semiquinone radicals  $\text{AQH}^\bullet$ : conversely to benzophenones, anthraquinones can perform a second hydrogen atom abstraction and proceed to the anthraquinol of the type  $\text{AQH}_2$  almost quantitatively; the introduction of oxygen into the solution, allow the complete recovery of the quinone (figure 2.37). Finally, quinones are reduced at significantly more positive potentials than benzophenones; this feature makes quinones excellent electron acceptors even in the triplet state. One interesting application of quinones in

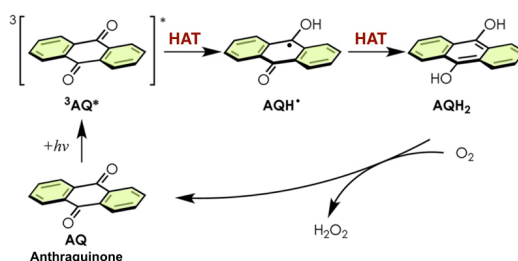


FIGURE 2.37: Photoinduced hydrogen atom transfer (PHAT) process of excited state of anthraquinone.

photocatalysis is the C-H hydroxylation of benzene and halobenzenes: 2,3-dichloro-5,6-dicyano-1,4-benzoquinone (**DDQ**) is well known for its use as an organic oxidant: however, its ground state reduction potential, although anomalously high, is insufficient to oxidize unreactive substrates, such as benzene. In this contest, Fukuzumi and co-workers took advantage of the fact that **DDQ** is a stronger oxidant when promoted to an excited state and were able to accomplish the catalytic coupling of substituted benzenes (figure 2.38) and  $\text{H}_2\text{O}$  to the corresponding phenols in 93% yield.<sup>90</sup> In the proposed mechanism,  $\text{H}_2\text{O}$  adds to the benzene cation radical **V** generated by PET with  ${}^3\text{DDQ}^*$ . Then we have the protonation of  $\text{DDQ}^{\bullet-}$ , which produces quinolyl

radical **DDQH<sup>•</sup>**, responsible for the HAT process from the cyclohexadienyl radical **V** in the aromatization step that furnishes the phenol product. The fully reduced **DDQH<sub>2</sub>** generated in this way is oxidized to **DDQ** by chemical oxidation with nitrogen dioxide (NO<sub>2</sub>), producing H<sub>2</sub>O and nitric oxide (NO). Finally, NO is recycled to NO<sub>2</sub> by aerobic oxidation after being initially formed in situ from *t*-BuNO (figure 2.38).

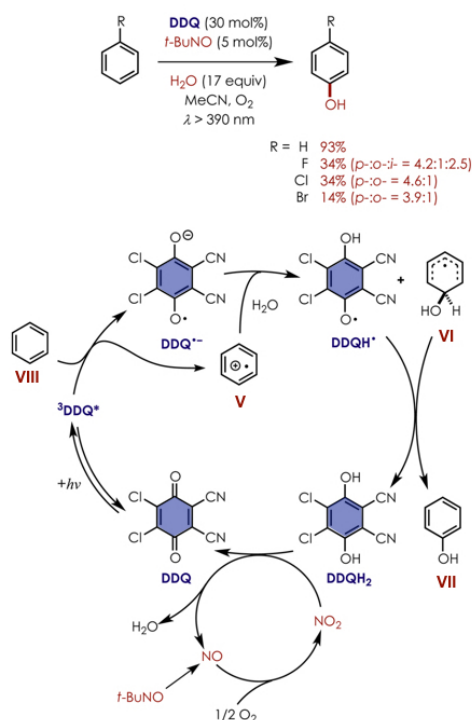


FIGURE 2.38: Proposed mechanism for photoredox catalytic aryl C-H hydroxylation.

**Quinoliniums.** *N*-alkyl quinolinium ions absorb in the near UV (~ 315-350 nm) and are some of the most strong photo-oxidants to be used as photoredox catalysts. Quinoliniums are characterized by high-lying S<sub>1</sub> states (> 3.3 eV) and reduction potentials above -1.0 V, so they are extremely oxidizing in the singlet excited state (> 2.5 V); furthermore, they have long singlet lifetimes and high fluorescence quantum yields. Moreover, upon single electron reduction, their corresponding neutral quinolinyl radicals are generated: they are sufficiently reducing so as to be turned over by relatively weak oxidants, including O<sub>2</sub>.

The dearomatization of the chromophore, due to addition of nucleophiles at the 2- and 4- positions in the ground state cations and radical reactions of quinolinyl radicals at the same positions, limits their application as photoredox catalysts (figure 2.39). That's why quinoliniums usually are substituted at the 2- and 4-positions. The most useful quinolinium is 3-cyano-

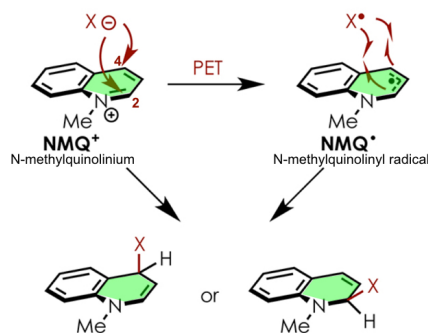


FIGURE 2.39: Deactivation of quinolinium salts by nucleophilic or radical addition.

1-methylquinolinium ( $\text{QuCN}^+$ ), interestingly with substituents at the most electrophilic positions: the  $S_1$  state reduction potential for this compound is reported to be + 2.72 V, make possible electron transfer processes with unreactive hydrocarbons such as benzene [ $E_{ox}(\text{PhH}^{\bullet+}/\text{PhH}) = 2.35$  V vs SCE]; the fluorescence lifetime is 45 ns, significantly longer than the singlet lifetime of most organic photoredox catalysts: that feature, with the high fluorescence quantum yields, suggests minimal effect of nonradiative decay pathways of the singlet state, including inter-system crossing.

Fukuzumi and coworkers, demonstrated the aryl C-H functionalization of benzene and electron-deficient arenes accomplished through the addition of oxygen and fluoride nucleophiles to arene cation radicals with  $\text{O}_2$  as a stoichiometric oxidant. The mechanism proposed is shown in figure 2.40: the generation of arene radical cation is followed by addition of  $\text{H}_2\text{O}$  and deprotonation, to give cyclohexadienyl radical **XII**. Moreover, the benzene cation radical **X** forms a reversible  $\pi$ -complex **XI** with a neutral benzene molecule before nucleophile addition could occur. Aromatization to phenol **XIII** is accomplished by hydroperoxyl radical  $\text{HO}_2^\bullet$  produced by  $\text{O}_2$ -mediated turnover of quinolinyl radical  $\text{QuCN}^\bullet$  and protonation of superoxide.

**Acridiniums.** The acridinium class of chromophores can be seen as benzanulated analogous of quinolinium: at the 2-position of quinolinium there is an additional aromatic ring, that should obstructs nucleophile addition; since the  $\pi$ -system is increased, acridinium chromophores are characterized by a shift in the absorption spectrum towards the visible region. Ground state reduction potential of acridinium ions is approximately -0.5 V vs SCE, with the consequence that the excited state reduction potentials are large and positive, above +2.0 V for the singlet state acridiniums; indeed they are powerful oxidants in the singlet excited state. Moreover, the corresponding acridinyl

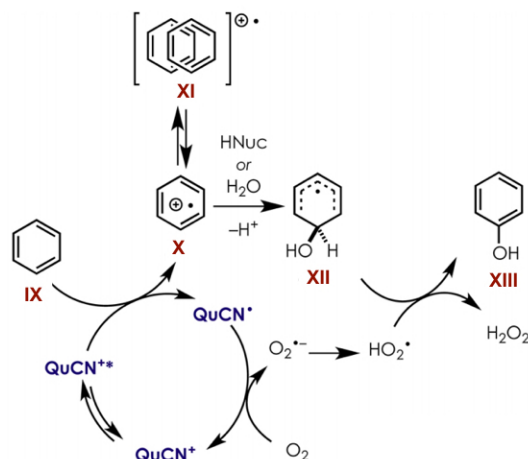


FIGURE 2.40: Proposed mechanism for QuCN<sup>+</sup>-mediated aryl C-H functionalization reactions.

radicals formed upon single electron transfer are weak reductants. The *N*-Methyl Acridinium (**Acr-Me<sup>+</sup>**) is an example for the photophysical and electrochemical properties of this group. It is a powerful oxidant in the singlet excited state, with a reduction potential  $E^*_{red}[(\mathbf{Acr-Me}^+ / \mathbf{Acr-Me}^\bullet)]$  of + 2.32 V. In addition, the fluorescence quantum yield is 1.0 and the fluorescence lifetime 31 ns. Nevertheless, the nucleophile addition at the 9-position in the ground state cation limited the use of this chromophore as a photocatalyst. The nucleophile addition as well as radical reactions of the acridinyl radical **Acr-Me<sup>•</sup>** lead to the deactivation of acridinium, generating dihydroacridines (figure 2.41). The 9-phenyl substituted acridinium (**Ph-Acr-Me<sup>+</sup>**) showed no evidence of radical-radical reactivity at the 9-position, but unfortunately, the nucleophilic deactivation occurs and furthermore, possesses a drastically shorter singlet lifetime ( $\sim 2.0$  ns) and low quantum yield of fluorescence ( $\phi < 0.09$ ), due to nonradiative decay pathways related to the rotational flexibility of the phenyl substituent. The 9-mesityl-10-methylacridinium (**Mes-Acr-Me<sup>+</sup>**) has become the most widely used acridinium photoredox catalyst, since the protective effect of the methyl substituents on the mesityl group in blocking nucleophile and radical addition to the acridinium/acridinyl radical, rather than the fact that photo-excitation of this acridinium can access a charge-transfer state.

A significant body of work has been devoted to the *anti-Markovnikov* hydrofunctionalization of alkenes using **Mes-Acr-Me<sup>+</sup>** (and related derivatives) as photoredox catalysts.<sup>91</sup> A key advance in that field was the discovery of the

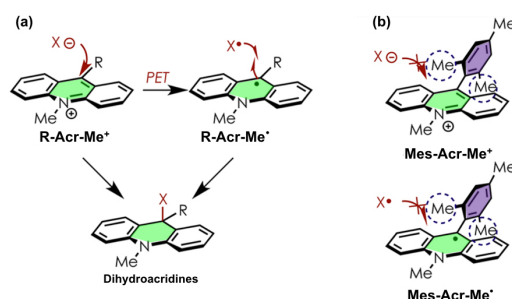


FIGURE 2.41: Deactivation Pathways of Acridiniums and Acridinyl Radicals (a); bulky *Mes*-group blocks addition at 9-position.

improvement of reaction yield due to the use of catalytic amounts of a redox-active hydrogen atom transfer agent, like thiophenol, **PhSH**. The beneficial activity of the HAT catalyst can be understood by considering the figure 2.42. The mechanism proposed is composed by dual catalytic cycles: the PET cycle involves the activity of **Mes-Acr-R<sup>+</sup>** in oxidizing alkenes **iI** to cation radicals **iII**, while the HAT catalyst operates in a separate cycle in which HAT to **iIII** furnishes the hydrofunctionalization product **iIV**, simultaneously producing the **PhS<sup>•</sup>** radical, responsible for the regeneration of **Mes-Acr-R<sup>+</sup>** by oxidizing **Mes-Acr-R<sup>•</sup>**. The HAT catalyst **PhSH** is obtained by protonation of **PhS<sup>-</sup>** coupled with the deprotonation of the nucleophile-cation radical adduct.

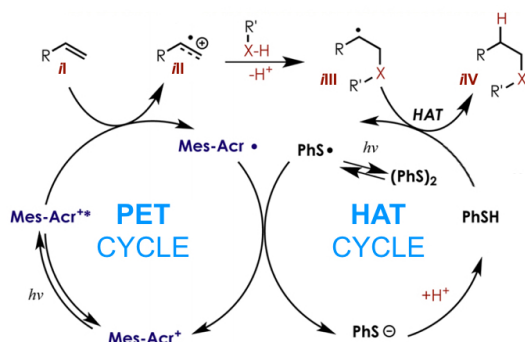


FIGURE 2.42: Proposed mechanism for *anti*-Markovnikov alkene hydrofunctionalization

**Fluorescein and Rhodamines.** The properties of fluorescein (**FL**) and its derivatives have been studied for more than a century. Fluorescein exists in three forms: quinonoid **FLH<sub>2</sub>-a**, lactone **FLH<sub>2</sub>-b**, and zwitterion **FLH<sub>2</sub>-c**. The mono-anion **FLH<sup>-</sup>** is convertible between phenolate **FLH<sup>-</sup>-a** and carboxylate **FLH<sup>-</sup>-b**, while di-anion **FL<sup>2-</sup>** is fully deprotonated (figure 2.43). The absorption wavelength and intensity are pH-dependent (the fully deprotonated

form  $\text{FL}^{2-}$  absorbs at longer wavelengths). Since the neutral form  $\text{FLH}_2\text{-a}$  exists in equilibrium with lactone  $\text{FLH}_2\text{-b}$  that doesn't absorb in the visible, displays diminished absorbance. The most known halogenated analogues of fluorescein are rose bengal (**RB**), most often supplied as the disodium salt ( $\text{RB}^{2-}$ ) and eosin Y (**EY**), found as the neutral ( $\text{EYH}_2$ ), mono- ( $\text{EYH}^-$ ), or disodium salt ( $\text{EY}^{2-}$ ) (figure 2.43). They undergo tautomeric/protolytic equilibria as well, which the consequence of differences in photoredox reactivity. Although significant spectral differences exist for the fluorescein family dependent on ionization, the redox potentials do not appear to differ significantly. Even though  $\text{FL}^{2-}$  has high quantum yield of fluorescence (0.93) with

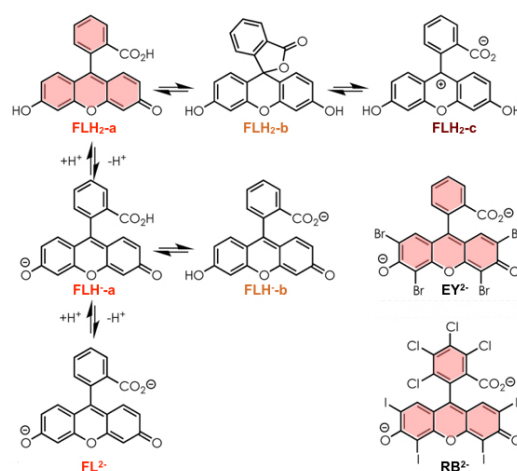


FIGURE 2.43: Equilibria and forms of fluorescein-based dyes.

minimal intersystem crossing to the triplet and a short  $S_1$  lifetime ( $\sim 4$  ns), fluoresceins finds relatively limited use in photoredox catalysis. In contrast, eosin Y and rose bengal undergo fast ISC and the efficiency increases across this series with the degree of halogenation, a trend attributed to the heavy atom effect. These higher  $\phi_{ISC}$  values correspond to short singlet lifetimes ( $\sim 0.5\text{-}2.7$  ns), so the triplet state is the most relevant excited state in photoredox reactions, which can act both as a moderate oxidant and reductant. Halogen substitution also shifts the absorption and emission wavelengths to lower energies and has small effects on redox potentials. The triplet state reduction potentials of eosin Y and rose bengal are approximately equal, around 0.85 V, while the oxidation potentials show that rose bengal is roughly 0.2 V less reducing than eosin Y. Both rose bengal and eosin Y undergo ionization by self-quenching electron-transfer between ground state and excited state. In this way, oxidized and reduced portions can build up in the absence of external redox equivalents.



An example of photoredox catalytic method employing eosin Y in the neutral form ( $\text{EYH}_2$ ) accomplished the synthesis of  $\beta$ -keto sulfoxides **iXIII** from alkenes **iV** and thiols **iVI** under aerobic conditions (figure 2.44).<sup>92</sup> The synthesis worked well with both styrenyl and aliphatic alkene substrates, while the thiol scope was limited to aryl thiols. The first step of the reaction is the oxidation of the aryl thiol **iVI** by the photocatalyst, followed by deprotonation to give thiyl radical **iVIII**. Addition to the alkene **iV** gives radical **iIX**, which is trapped by  $\text{O}_2$  and forms peroxy radical **iXI**. Ultimately,  $\beta$ -keto sulfide **iXII** is generated along with  $\text{H}_2\text{O}_2$ , which is expected to oxidize the sulfide to the observed  $\beta$ -keto sulfoxide product **iXIII**.

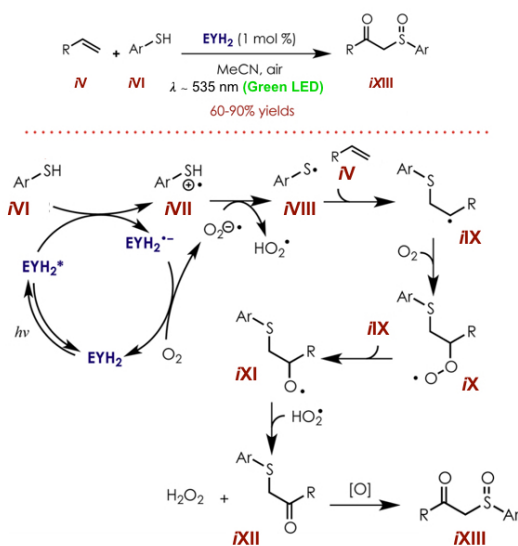


FIGURE 2.44: Mechanism of synthesis of  $\beta$ -keto sulfoxide.

The rhodamines are characterized by photophysical and structural properties similar to the fluorescein analogues. Most rhodamines are highly absorptive but show similar solvent and pH sensitivities to fluoresceins. Rhodamine B (**RhB**) is an exemplar for this class and is supplied in the cationic and neutral forms. This second form exists in a solvent-dependent equilibrium between zwitterion **RhB-a** and spirolactone **RhB-b** (figure 2.45). The cationic and zwitterionic forms have a strong absorption in the visible ( $\sim 550$ - $570$  nm), while the spirolactone form absorbs in the UV and is poorly fluorescent. As triplet formation is typically considered to be negligible due to very low yields of ISC ( $\phi_{ISC} < 0.01$ ), the singlet excited state, is thought to account for most PET reactions of rhodamines, even if it is short-lived, around 2-4 ns. Rhodamine 6G yields the stable radical anion **Rh6G $\cdot^-$**  upon irradiation with



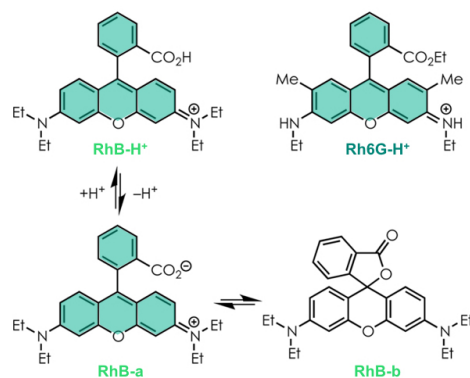


FIGURE 2.45: Forms of two common rhodamine catalysts.

green light, in presence of *N,N*-diisopropylethylamine (DIPEA); since the absorption spectra of **Rh6G** and **Rh6G<sup>•-</sup>** differ significantly (**Rh6G** absorbs in the green and blue regions of the visible-light spectrum, the **Rh6G<sup>•-</sup>** only in the blue region) it is possible to have access to different redox states of **Rh6G** through external control. This particular feature was used by König for the selective activation of aryl-halide bonds for C-H arylation and the sequential conversion of functional groups with different reduction potential, using different light colors as an external control.<sup>93</sup> In the mechanism proposed, **Rh6G<sup>•-</sup>** and **Rh6G<sup>•-\*</sup>** are both active redox species. Upon photoexcitation with green or blue light, **Rh6G** takes an electron from DIPEA to give a radical-anion/radical-cation pair **Rh6G<sup>•-</sup>** and DIPEA<sup>•+</sup>. The ground-state radical anion **Rh6G<sup>•-</sup>** can activate aryl bromide substrates with relatively low reduction potentials. If the irradiation is performed with blue light, **Rh6G<sup>•-\*</sup>** is generated: this species is able to activate aryl with rather high reduction potentials to obtain the aryl radical precursor and regenerating the neutral catalyst. Upon fragmentation of the precursor, the aryl radical is obtained: this species can react with unsaturated compound to yield C-C coupling product, after reoxidation and loss of a proton.

**Phenothiazines.** Compared with the chromophores already mentioned in this section, methylene blue (**MB<sup>+</sup>**) exhibits a red-shifted absorbance near 650-670 nm and high extinction coefficient, 94000 M<sup>-1</sup>cm<sup>-1</sup>. Since the singlet lifetime is really short ( $\tau \sim 1$  ns), the <sup>3</sup>**MB<sup>•\*</sup>** is the most relevant excited state. Indeed, the triplet state of MB is a good oxidant, even if **MB<sup>+</sup>** absorbs at low energy. Furthermore, **MB<sup>+</sup>** doesn't behave strictly by one-electron redox couples, but can proceed from the semi-reduced form **MB<sup>•</sup>** to **MBH** by sequential ET or HAT mechanisms (figure 2.47). Albeit **MB<sup>+</sup>** is suitable photosensitizer for <sup>1</sup>O<sub>2</sub> generation, the photo-induced electron transfer is the

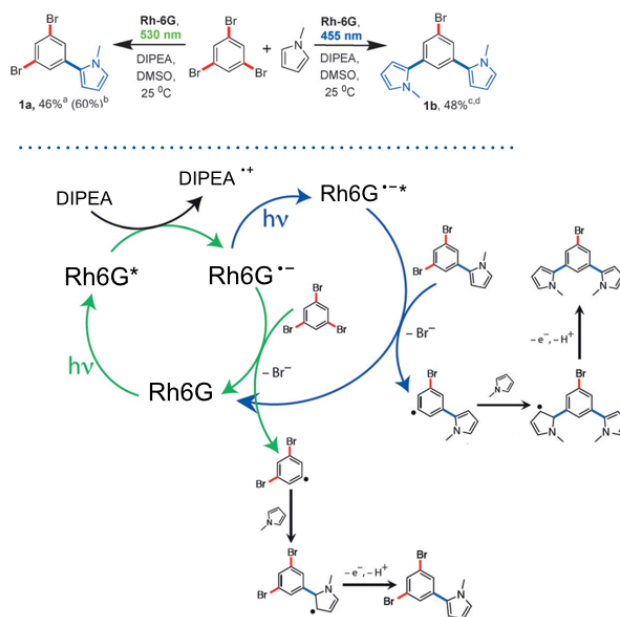


FIGURE 2.46: Proposed mechanism for the photocatalytic activation of aryl bromides involving the ground- and excited-state radical anions of **Rh6G** under green- or blue-light irradiation, respectively.

dominant pathway when electron donors are present in sufficient concentrations.

Methylene blue was used as a photoredox catalyst in the conversion of

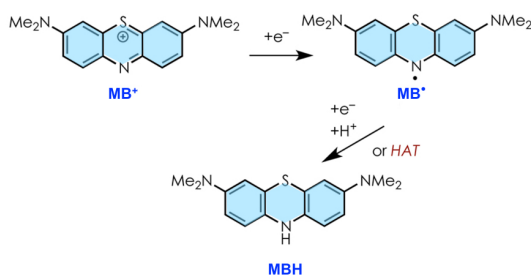


FIGURE 2.47: Two-electron/one-proton reduction of methylene blue (**MB**).

arylbromonic acids to phenols, with *i*Pr<sub>2</sub>NEt as an additive and under an atmosphere of O<sub>2</sub>.<sup>94</sup> Before the methylene blue, the same reaction was performed with [Ru(bpy)<sub>3</sub>]<sup>2+</sup>, but required at least 23 h of irradiation, or eosin Y (**EY-Na<sub>2</sub>**), but high yields were obtained after a 96 h reaction; however the methylene blue catalyzed reaction is complete after 6 h. Laser flash photolysis studies revealed that *i*Pr<sub>2</sub>NEt quenches the triplet state of methylene blue (<sup>3</sup>**MB<sup>•+</sup>**) 40 times faster than the [Ru(bpy)<sub>3</sub>]<sup>2+</sup> one. Singlet oxygen is a negligible mechanistic intermediate (figure 2.48), and the strongly reducing

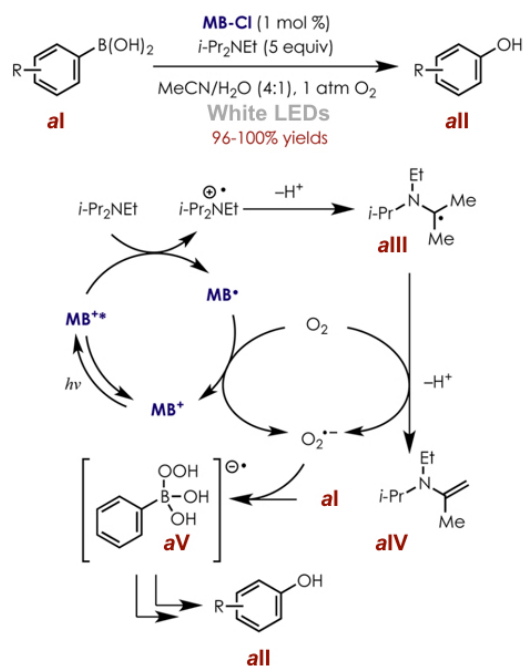


FIGURE 2.48: Oxidative hydroxylation of arylboronic acids with **MB** as photocatalyst.

$\alpha$ -amino radical **aIII** is capable of reducing O<sub>2</sub> along with the semi-reduced **MB<sup>•</sup>**.

**Other organic dyes.** In this category can be included chromophores like phenazinium salts, flavins, perylene diimides and boron-dipyrromethene dyes. I'll talk about boron-dipyrromethene (**BODIPY**) dyes and perylene diimides (**PDI**), since in the next two sections, I'll discuss in details two photoredox reactions performed with **BODIPY** dyes and a **PDI** derivate as photocatalyst. Although **BODIPY** dyes comprise a vast set of light-absorbing and emitting molecules with tunable properties, their use in organic photoredox reactions is extremely limited. One example is the the photoinduced cleavage of *N*-alkyl-4-picolinium esters **aVI** and **aVII** as applied to the photorelease of carboxylic acids (e.g., **aVIII**) and phosphates, in which **BODIPY** dyes are competent photoredox mediators (figure 2.49).<sup>95</sup> In the next section (2.2.1), I'll show an *Atom-Transfer Radical Addition* (ATRA) reaction promoted by iodo-substituted **BODIPY** and sodium ascorbate as reducing agent.

König and co-workers described the hydrodehalogenation of aryl halides using **PDI-a** (figure 2.50) as photocatalyst.<sup>96</sup> The mechanism that they proposed involves a two-photon process, with the consecutive electron-transfer and excitation of the radical anion **PDI<sup>•-</sup>** in order to generate the strong reductant

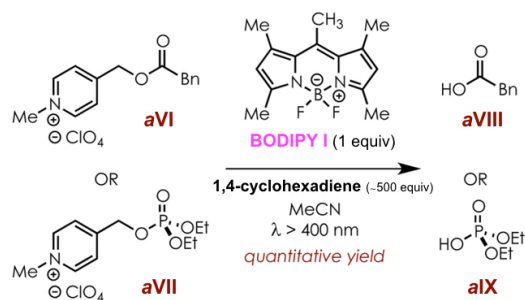


FIGURE 2.49: **BODIPY**-mediated photoinduced cleavage of *N*-methyl picolinium esters.

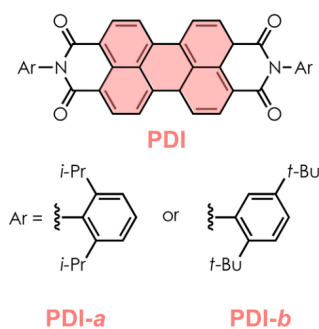


FIGURE 2.50: Chemical structures of two perylene diimides.

**PDI<sup>•-</sup>\***. Nevertheless, I'll explain in details in session 2.2.2, why this proposed mechanism is not correct and the reaction proceed through another pathway.

### 2.2.1 Photocatalytic ATRA Reaction Promoted by Iodo-Bodipy and Sodium Ascorbate

I already mentioned that boron-dipyrromethene (**BODIPY**) compounds (figure 2.51) have been recognized as suitable candidates for photocatalysis due to their photophysical properties: large molar absorption coefficients in the visible spectral region, excellent thermal and photochemical stabilities and high fluorescence quantum yields (an useful tool to investigate the reactivity of the lowest singlet excited state). The Ramaiah research group<sup>97</sup> and Jing/Zhang group<sup>98</sup> recently reported interesting photocatalytic transformations promoted by **BODIPY** dyes. These findings were based on the generation of singlet oxygen by the **BODIPY**-based photocatalysts. In both cases, the introduction of an heavy-atom (such as halogen) in the molecular structure of the dye, leads to the increase of the ISC efficiency, due to the *heavy-atom effect*, that promotes intersystem crossing via spin-orbit coupling. In our case, the result is the increase of the ratio of the phosphorescence and fluorescence quantum yields ( $\phi_P/\phi_F$ ).<sup>99</sup> Knowing that, we synthesized the bodipyVI shown in figure 2.51 and we found that it was an effective photocatalyst for ATRA reactions. This chemistry, pioneered by Kharasch al-

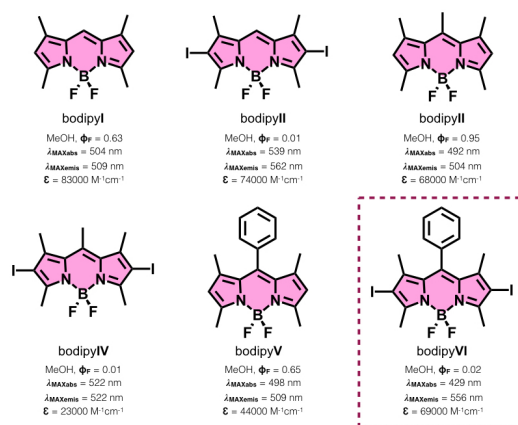


FIGURE 2.51: Relevant **BODIPY** molecules and their photophysical properties.<sup>98</sup>

most 70 years ago,<sup>100</sup> has evolved to become an atom economical and effective methodology for the direct functionalization of alkene substrates. With the idea to use **BODIPY** molecules as photocatalysts to induce an energy transfer process for ATRA reactions, we started our initial explorations by selecting the reaction of diethyl 2-bromo-malonate (**10a**) and 5-hexenol (**11a**). Unfortunately, by exploring various solvents and reaction conditions under 23 W CFL irradiation (emission profile of the lamp is shown in figure 2.24) at

room temperature, all experiments were unsuccessful (see ESI). However, we noted the drastic color change when the reaction was performed in the presence of  $\text{Et}_3\text{N}$ , but the reaction was not proceeding (figure 2.53). However, a complete conversion was achieved when the model reaction was performed in the presence of 0.35 equiv. of sodium ascorbate in DMF/ $\text{H}_2\text{O}$  as reaction solvent (figure 2.52)<sup>101</sup> and the presence of LiBr was beneficial for the isolated yield.

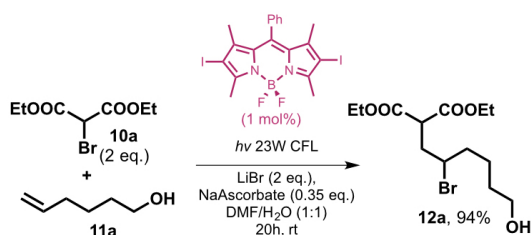


FIGURE 2.52: Optimized reaction conditions.

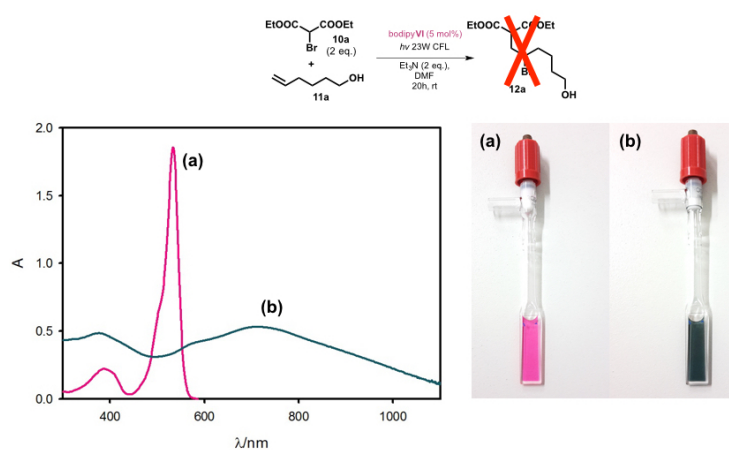


FIGURE 2.53: Absorption spectra of reaction mixture containing **11a** 0.01 M, **10a** 0.005 M, bodipy**VI**  $2.5 \times 10^{-4}$  M (pink solid line), and upon addition of  $\text{Et}_3\text{N}$  0.01 M and irradiation with 23W Compact Fluorescent lamp (blue solid line) in DMF (cuvette optical path length 0.1 cm). The amount of the species in solution is a hundred times more diluted respect to the reaction mixture.

While the bodipy**VI** was an effective catalyst, the employment of catalyst bodipy**V** was found to give no reaction. The photochemical ATRA reaction showed a good synthetic potential: indeed, as shown in figure 2.54, different substituted organic halides (**10b-l**) underwent the desired reaction with **11a** to provide adducts **12b-l** in moderate to good isolated yields. This method allows the direct introduction of functional groups other than an ester: indeed

bromoacetonitrile, carbon tetrachloride and perfluorohexyl iodide are compelling substrates. The novelty, compared to previously reported methodolo-

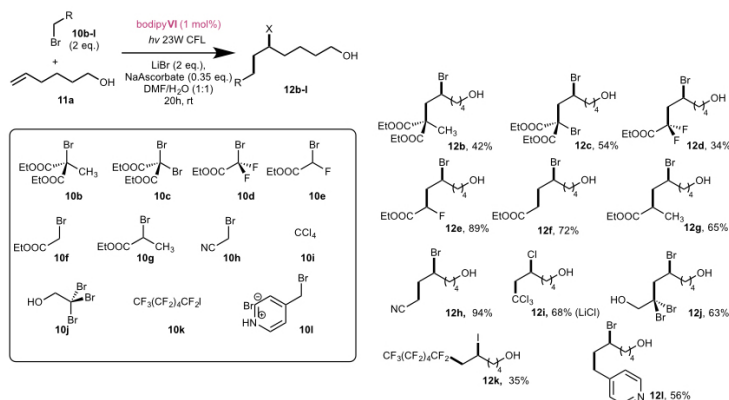


FIGURE 2.54: Scope of the photochemical ATRA reaction promoted by bodipyVI with different halides and substrate **11a**.

gies, is the successful use of bromoacetate and haloalkyl pyridine salt to generate the corresponding radicals and add them to the alkene in good yields (**12f** and **12l**). Next, we studied the reactivity of different olefins with **10a** (figure 2.54). Both terminal olefins and the inherently less reactive internal cyclic alkenes, including cyclohexene, and cyclooctene, were reactive substrates. The lower yields compared to other protocols are caused only by the limited substrate solubility in the solvent mixture, whose choice is dictated by the need to dissolve sodium ascorbate and photocatalyst. Our protocol is clearly more competitive with alkenes showing a better solubility in aqueous media. Despite these problems, the protocol gave moderate yields with all the substrates tested, thus enabling the construction of complex frameworks **13b-k** from simple precursors. The naturally occurring (*R*)-limonene and (-)- $\beta$ -pinene can be successfully employed in the ATRA process, furnishing, respectively, adducts **13j** and **13k**. The determination of the ascorbate mode of action is of great interest because it would open new ways and possibilities for the design and application of **BODIPY** dyes in photochemical processes. In order to determine the reaction mechanism, we performed several experiments on the model reaction depicted in figure 2.52. Control experiments highlighted that both visible light irradiation and the presence of bodipyVI are necessary to promote the reaction. To remove the eventual contribution of the UV component of the CFL lamp, we performed the reaction using White LEDs with  $\lambda \geq 400$  nm, obtaining the desired product in a comparable yield to the standard conditions (see table 2.7, 2.8, 2.9 and 2.10). Since



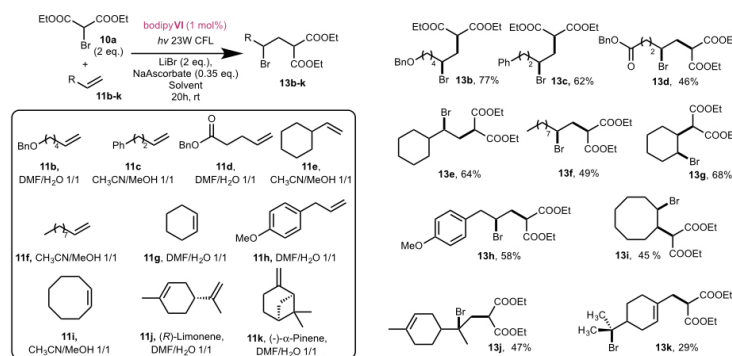


FIGURE 2.55: Scope of the photochemical ATRA reaction promoted by bodipyVI with different alkenes and substrate **10a**.

none of the components of the reaction mixture absorb visible light with the exception of bodipyVI (figure 2.56, plot a), during the excitation, the photocatalyst is the only component that absorbs light and promotes the ATRA reaction. That's the reason why we studied the photophysical properties of bodipyVI<sup>102 103</sup> and the quenching of its lowest excited states, to gain better insights into the reaction mechanism. BodipyVI shows a fluorescence band with a maximum at 529 nm and a weak phosphorescence band at 760 nm ((figure 2.56, plot b)) with a lifetime of 0.22 ms. As expected, the presence of iodo-substituents promotes intersystem crossing to populate the phosphorescent  $T_1$  excited state, as previously observed for different iodo-derivatives of BODIPY dyes.<sup>104</sup> Upon addition of the reagents to a solution of bodipyVI in DMF:H<sub>2</sub>O 1:1 (v/v), up to the concentration used in the photoreaction, no significant quenching of the photocatalyst fluorescence was observed. On the other hand, sodium ascorbate and diethyl 2-bromo-malonate **10a** bring about a decrease of the phosphorescence quantum yield and the corresponding lifetime, while no quenching is observed upon addition of the olefin **11b**. Using the classic Stern-Volmer plot (equation 2.10) we estimated the corresponding quenching constants for **10a** and sodium ascorbate (figure 2.57). Under the experimental conditions used in the photoreaction, the lifetime of the phosphorescent excited state of bodipyVI is quenched 2.5 times when **10a** 0.5 M with lithium bromide 0.5 M is added (without lithium salt, no quenching is observed) and  $10^4$  times in presence of sodium ascorbate 0.088 M (buffered at pH 5<sup>105</sup>), with a quenching constant  $k_q = 5.5 \times 10^8 \text{ M}^{-1} \text{ s}^{-1}$ .

We can thus conclude that, under the experimental conditions used, sodium ascorbate is the main quencher of the lowest triplet excited state of bodipyVI and we propose the catalytic mechanism depicted in figure 2.58. The photocatalyst is reduced to [bodipyVI]<sup>•-</sup> using sodium ascorbate as the electron



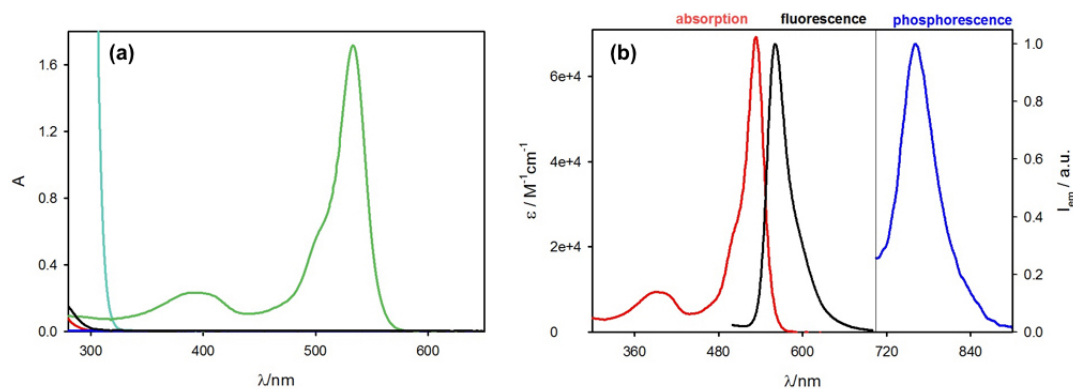


FIGURE 2.56: Plot (a). Absorption spectra of 5-hexenol 0.25 M (blue solid line), diethyl 2-bromo-malonate **10a** 0.5 M (red solid line), sodium ascorbate 0.088 M (light blue solid line), lithium bromide 0.5 M (black solid line) and bodipy**VI**  $2.5 \times 10^{-4}$  M (green solid line) in DMF:H<sub>2</sub>O ratio 1:1 (cuvette optical path length 0.1 cm). The amount of the species in solution is the same used in reaction mixture condition, a part from bodipy**VI**, that is ten times more diluted. Plot (b). Absorption (red solid line) and fluorescence emission (black solid line,  $\lambda_{ex}$  405 nm) spectra of bodipy**VI** in DMF at 298 K. The phosphorescence emission spectrum (blue solid lines) was obtained after five freeze-pump cycles ( $\lambda_{ex}$  525 nm, cuvette optical path length 1 cm)

donor: now it has a sufficiently strong reduction potential (-1 to -1.54 V vs SCE) to effectively convert the alkyl halides (-0.5 to -1 V vs SCE) to electrophilic free radicals, which undergo addition to alkenes. The ATRA product, can subsequently be formed via two different routes: either by propagation (**path A**) or by oxidation to the cation followed by nucleophilic trapping (**path B**). For ATRA using classical radical initiators, propagation has been shown to be an operative mechanism (pathway A).

The propagation pathway A was furthermore supported by the absence of mixed Cl/Br products obtained by conducting the reaction between CCl<sub>4</sub> and **11a** in the presence of excess LiBr (2.5 equiv.) (figure 2.59). We observed exclusively product **12i** derived from the chlorine addition, while Stephenson reported a mixture of Cl/Br products **12i/12i'** under his reaction conditions.<sup>106</sup> The model photo-organocatalytic ATRA reaction was completely inhibited by the presence of oxygen: indeed the oxygen efficiently quenches the phosphorescent excited state of the photocatalyst (no phosphorescence is observed in air-equilibrated solution) and, even if the radical anion of bodipy**VI** is formed, it will react with oxygen. Since the opening of the reaction flask (under a flow of inert gas) to take samples for GC or HPLC analysis

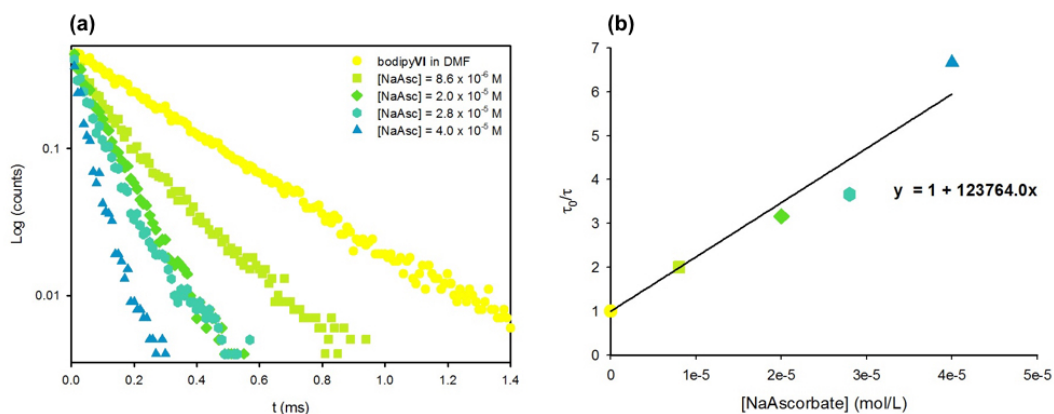


FIGURE 2.57: (a) Lifetime decays of a  $2.5 \times 10^{-5}$  M degassed solution of bodipyVI in DMF with different amount of sodium ascorbate; (b) Stern-Volmer quenching plot of the same solution of photosensitizer as a function of sodium ascorbate concentration.

caused the immediate quenching of the reaction, no information were obtained alternating periods of light irradiation and complete darkness, in order to verify the presence of a radical chain mechanism. In addition, if the reaction was performed in the presence of catalytic or stoichiometric amounts of TEMPO or bis(1,1-dimethylethyl)-4-methylphenol (BHT), no products or other adducts were detected by GC-MS analysis, confirming the presence of catalytic radical intermediates.

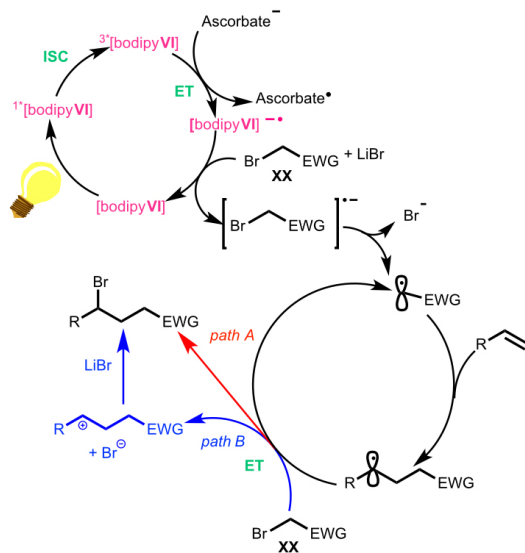


FIGURE 2.58: Proposed mechanistic pathway for the bodipyVI promoted ATRA reaction.

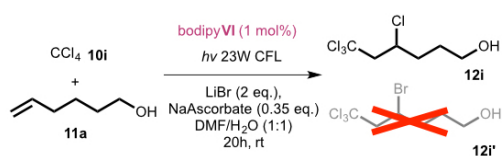
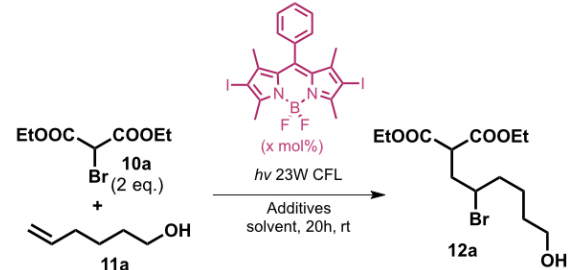


FIGURE 2.59: Control experiment to discriminate between the propagation reaction pathway A and the radical polar crossover pathway B.

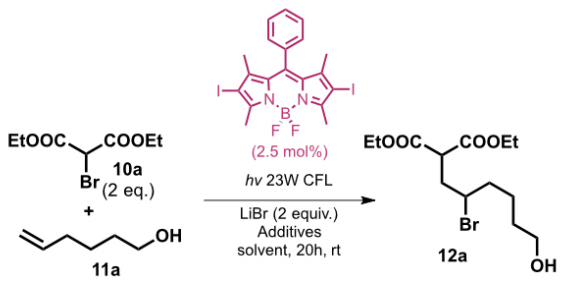
TABLE 2.7: Optimization of reaction conditions.



Photosensitizer (mol%)	LiBr	Additive	Solvent	Product <b>12a</b> <sup>[a]</sup>
5	-	2,6-lutidine (1 equiv.)	CH <sub>3</sub> CN	X
2.5	2 equiv.	-	DMF:H <sub>2</sub> O 1:4	X
2.5	2 equiv.	-	DMF	X
5	2 equiv.	TEA (2 equiv.)	DMF	X
2.5	2 equiv.	TEA (0.35 equiv.)	DMF	X

<sup>[a]</sup> Determined by <sup>1</sup>H-NMR and TLC of the crude.

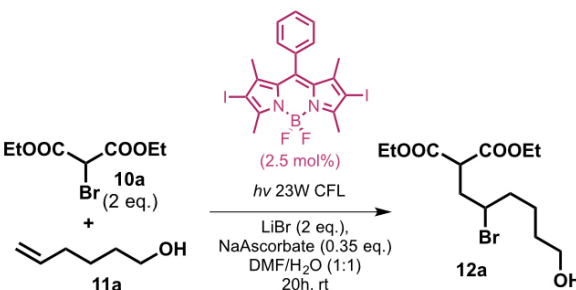
TABLE 2.8: Optimization of reaction conditions.



Additive	Solvent	Product <b>12a</b> <sup>[a]</sup>
TEA (0.35 equiv.)	DMF	X
NaAscorbate (0.35 equiv.)	DMF:H <sub>2</sub> O 1:4	42%
Hantzsch ester <sup>[b]</sup> (0.35 equiv)	DMF	X
NaAscorbate (1 equiv.)	DMF:H <sub>2</sub> O 1:4	X
2,6-lutidine (2 equiv.)		
NaAscorbate (1 equiv.)	DMF:H <sub>2</sub> O 1:1	97%

<sup>[a]</sup> Determined by <sup>1</sup>H-NMR and TLC of the crude;  
<sup>[b]</sup> Diethyl1,4-dihydro-2,6-dimethyl-3,5-pyridinedicarboxylate.

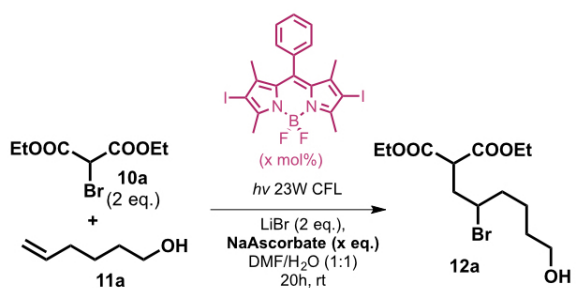
TABLE 2.9: Optimization of reaction conditions.



Photosensitizer	LiBr	NaAscorbate	$h\nu$	air	Product <b>12a</b> <sup>[a]</sup>
yes	yes	yes	yes	no	97%
no	yes	yes	yes	no	X
yes	no	yes	yes	no	56%
yes	yes	no	yes	no	X
yes	yes	yes	no	no	X
yes	yes	yes	yes	yes	X

[a] Determined by <sup>1</sup>H-NMR and TLC of the crude.

TABLE 2.10: Optimization of reaction conditions.



Photosensitizer (mol%)	NaAscorbate (equiv.)	Yield (%)
2.5	1	92%
2.5	1	92%
1	0.35	94%

[a] After column chromatography.

## 2.2.2 A Photochemical View on the Two-photon Mechanism of Reduction of Aryl Halides in the Presence of Perylene-diimide Photocatalyst.

The reduction of unactivated aryl bromides and chlorides is challenging: only recently, it was obtained by visible light photocatalysis exploiting a cyclometalated Ir(III) complex.<sup>107</sup> The reasons are the higher reduction potential of these compounds and the reaction mechanism. Indeed, as extensively studied by Savéant,<sup>108,109</sup> the reduction of aryl iodides is usually concerted with C-I bond cleavage, while for aryl bromides and chlorides, reduction leads to the formation of a radical anion, which then undergoes a rate-determining C-X<sup>•-</sup> bond cleavage. In the case of a reduction in the presence of the photosensitizer **PS**, we can schematize the reaction as shown in figure 2.60: Back electron transfer between **PS**<sup>•+</sup> and Ar-X<sup>•-</sup> competes with aryl

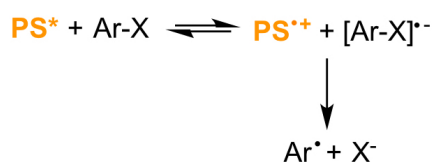
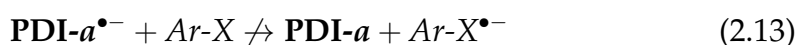
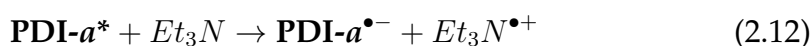


FIGURE 2.60: Schematization of the reduction of aryl halides in presence of a photosensitizer **PS**.

radical formation when X = Br or Cl. Only for aryl iodide the back electron transfer is highly disfavored since reduction and bond cleavage are concerted processes and Ar-X<sup>•-</sup> is eliminated from the electron transfer equilibrium.

In search for more reducing species, the idea of using two photons to get a highly reducing species, Z-scheme mechanism, is very attractive and opens up many opportunities:<sup>107</sup> the first example, published by König *et al.* in 2014,<sup>96</sup> was based on perylene diimides derivative (**PDI-a**) reported in figure 2.50. In that case, the two photocatalysts are the components of the redox couple **PDI-a**/**PDI-a**<sup>•-</sup> (figure 2.61): the radical anion is produced upon irradiation of **PDI-a** in the presence of a sacrificial electron donor, namely triethylamine Et<sub>3</sub>N (figure 2.62).

We can summarize the reaction mechanism as follows:



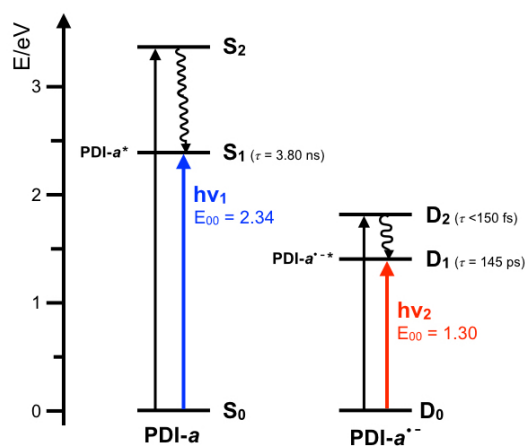
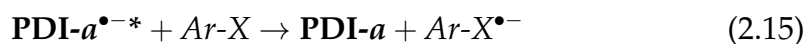
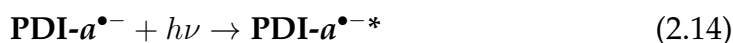


FIGURE 2.61: Jablonski diagram reporting the most relevant electronic states of **PDI-a** and **PDI-a<sup>•-</sup>**.



The same reaction steps are reported in figure 2.62 (a) in terms of electronic states (photochemical point of view) and in 2.62 (b) in terms of redox potentials (electrochemical point of view). The same idea was applied before in the case of a supramolecular triad for photoinduced charge-separation.<sup>110</sup> Excitation of the donor yields the first intramolecular electron transfer and the successive excitation of the radical anion drives a further electron transfer, thermodynamically uphill in the dark.

The idea of using the absorption of two consecutive photons by the two components of a redox couple (Z-scheme mechanism) applied to photocatalysis is really interesting. However, there are two fundamental kinetic concepts need to be considered, to understand if this Z-scheme mechanism can work.

- Molecules have usually several absorption bands, so that the amount of energy injected by photoexcitation can be tuned over a large range of energies. The upper lying electronically excited states, however, usually undergo very fast intramolecular decay (lifetime in the pico- or femto-second time scale), which compete and can, thereby, prevent, the involvement of the excited state in electron transfer reactions. Generally, only the lowest excited state of each spin multiplicity exhibit a lifetime long enough to be involved in electron transfer processes. In the case of **PDI-a** and **PDI-a<sup>•-</sup>**, it means that wherever we excite these species, the lowest  $S_1$  and  $D_1$  excited states are populated, respectively (figure 2.61). As a consequence, the redox potential of **PDI-a<sup>\*</sup>/PDI-a<sup>•-</sup>**

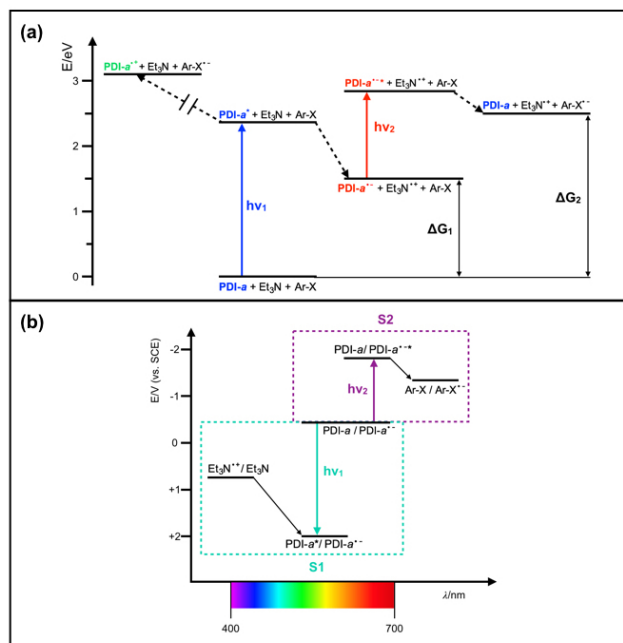


FIGURE 2.62: Reaction steps of the Z-scheme based on **PDI-a/PDI-a<sup>•-</sup>** presented in terms of (a) electronic states (photochemical point of view) and (b) redox potentials (electrochemical point of view).

and **PDI-a/PDI-a<sup>•-</sup>\***, reported in figure 2.62 (a), are estimated based on the electronic energy  $E_{00}$  of the S<sub>1</sub> (2.34 eV) and D<sub>1</sub> (1.30 eV) excited states of **PDI-a\*** and **PDI-a<sup>•-</sup>\***, so that we cannot expect any difference in the reducing power based on the excitation wavelength, even upon excitation at energy higher than 2.34 eV. The **PDI-a<sup>•-</sup>** is not a highly reducing species ( $E(\text{PDI-a/PDI-a}^{\bullet-}) = -0.37 \text{ V vs. SCE}^{96}$ ), but its lowest-energy excited state (**PDI-a<sup>•-</sup>\***) is expected to have  $E(\text{PDI-a/PDI-a}^{\bullet-*})$  ca. +1.7 V vs. SCE, based on the  $E_{00}(\text{PDI-a}^{\bullet-}/\text{PDI-a}^{\bullet-*})$  value of 1.30 eV, estimated by its lowest-energy absorption band.

- Electron transfer in fluid solution can occur only if the excited state A\* and the reaction partner B can encounter, a process that cannot be faster than the diffusion rate constant ( $k_d$ ) in the solvent used. For such dynamic processes, a kinetic analysis shows that the rate constant of the ratio of the excited state lifetime in the absence ( $\tau_0$ ) and presence ( $\tau$ ) of B is given by the well-known Stern-Volmer equation 2.10: based on these kinetic considerations, the photogenerated radical anion **PDI-a<sup>•-</sup>**, exhibiting a lifetime in the range of one hundred picoseconds, is not the best candidate for a dynamic quenching process. Indeed, Wasielesvski



*et al.*<sup>111</sup> reported that the lowest excited state  $D_1$  of  $\text{PDI-}a^{\bullet-}$  has a lifetime of 145 ps. Upon excitation into higher lying  $D_n$  states, a rapid relaxation (within the 150 fs-resolution of the instrument) to the  $D_1$  state occurs without intersystem crossing to a long-lived quartet state.

Based on the Stern-Volmer equation (2.10), if the reaction is diffusion controlled (e.g.,  $k_q = 10^9 \text{ M}^{-1} \text{ s}^{-1}$ ), in the presence of Ar-X  $1.7 \times 10^{-1} \text{ M}$ , only about 2% of the  $\text{PDI-}a^{\bullet-}$  is quenched by the aryl halide. On top of that, the excitation was performed at 455 nm, where the ratio of molar absorption coefficients of  $\text{PDI-}a^{\bullet-}$  with respect to  $\text{PDI-}a$  is ca. 1:9 (figure 2.63). Under the conditions reported in the original paper, slightly less than 50% of  $\text{PDI-}a$  has been converted to  $\text{PDI-}a^{\bullet-}$ , so that the light absorbed by  $\text{PDI-}a^{\bullet-}$  is a very small fraction.

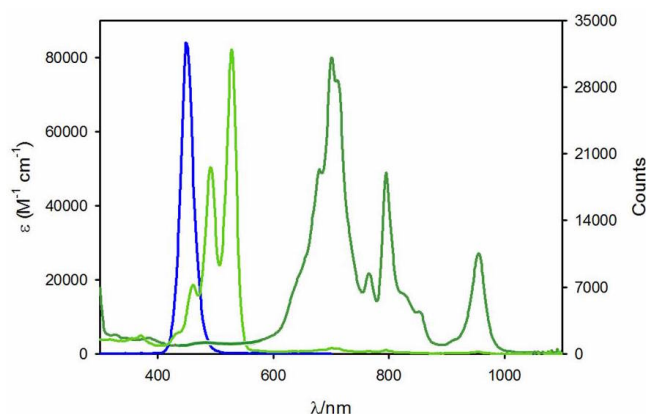


FIGURE 2.63: Absorption spectra  $\text{PDI-}a$  (light green line) and  $\text{PDI-}a^{\bullet-}$  (green line) in DMF. Blue LEDs emission profile (blue line) used as irradiation source.

We decided to investigate the following reaction in a cuvette, in order to monitor the presence of the different chromophores, namely  $\text{PDI-}a$  and  $\text{PDI-}a^{\bullet-}$ , during the reduction of 4'-bromoacetophenone ( $\text{BrAcet}$ ) to acetophenone ( $\text{Acet}$ ).

We performed the experiments under the same experimental conditions used by König *et al.* in the original paper,<sup>96</sup> with regard to solvent, irradiation conditions (we used the blue LEDs in figure 2.63) and concentration of reactants ( $\text{BrAcet}$  0.017 M (1 equiv.) and  $\text{Et}_3\text{N}$  0.13 M (8 equiv.)). The only difference was the amount of  $\text{PDI-}a$  ( $8.0 \times 10^{-4} \text{ M}$  (0.05 equiv.)), which we decreased by a factor of 2 in order to register its absorption spectrum in a 0.1 cm path length cuvette.

Figure 2.64, plot (a) reports the decrease of **PDI-a** absorption upon irradiation at 455 nm for 20 minutes in the presence of 8 equiv. of  $\text{Et}_3\text{N}$ , the resulting formation of **PDI-a** $^{\bullet-}$ , absorbing in the NIR spectral region with maximum at 680 nm, as previously reported:<sup>111</sup> the solution turns from orange to blue (figure 2.65). Figure 2.64, plot (b) reports the following spectral changes upon irradiation up to 6 hours: the absorption features of **PDI-a** $^{\bullet-}$  disappears and a non-structured absorption profile between 600 and 800 nm appears, concomitantly the solution turns brown (figure 2.65).

Using HPLC to monitor the product formation, we were able to correlate the

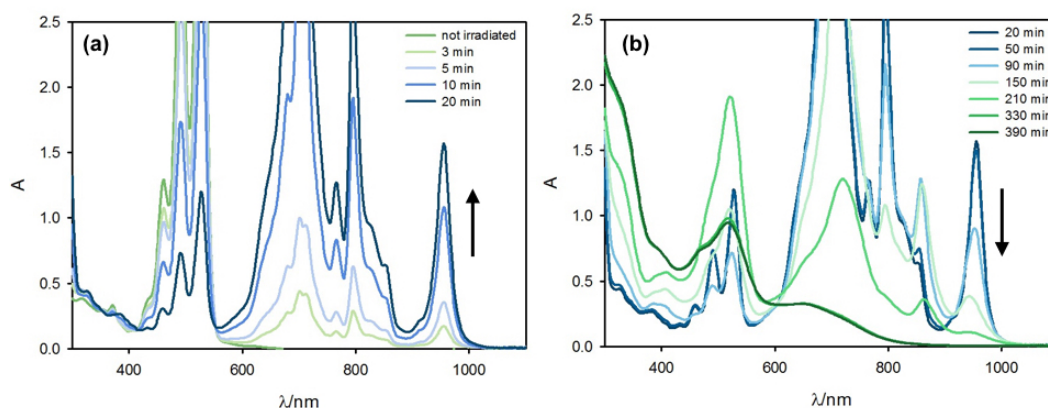


FIGURE 2.64: Absorption spectra of **PDI-a**  $8.0 \times 10^{-4}$  M in degassed DMF solution in the presence of  $\text{Et}_3\text{N}$  0.13 M and **BrAcet** 0.017 M upon irradiation at 455 nm by a blue LEDs in the time interval: (a) 0 - 20 minutes and (b) 20 - 390 minutes.

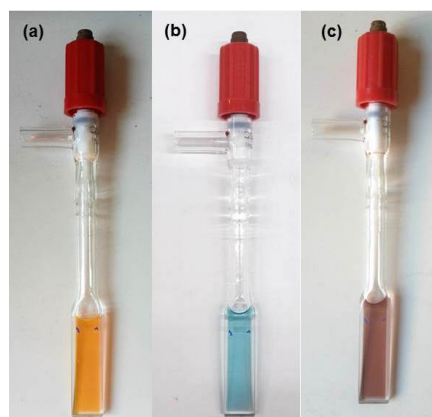


FIGURE 2.65: Reaction mixture before the irradiation (a), after 20 min of irradiation, when the radical anion is formed (b) and after 6 h irradiation (c).

disappearance of **PDI-a** $^{\bullet-}$  with the formation of **Acet** as a function of time (figure 2.67). Two calibration curves were necessary to estimate the amount of **Acet** at high and low conversions (low and high value of the **BrAcet**/**Acet**

ratio) (figure 2.66). Different solution with known ratio of **BrAcet**/**Acet** were injected at HPLC and the area under each peak at three different wavelengths was measured. The correlation between the disappearance of **PDI-a<sup>•-</sup>** and

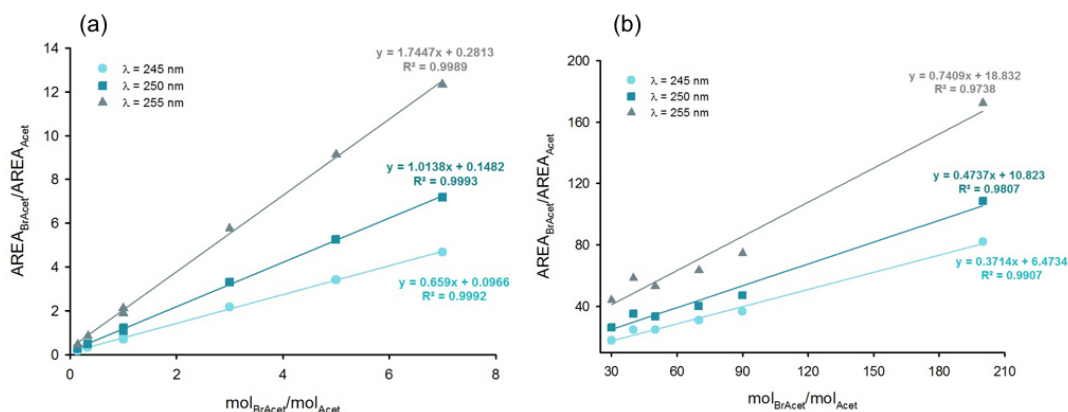


FIGURE 2.66: Calibration curve for high (a) and low (b) conversions at three different wavelengths.

the formation of **Acet** as a function of irradiation time (figure 2.64) is reported in figure 2.67: from the trends is clear that the formation of the product starts when **PDI-a<sup>•-</sup>** is fully decomposed. The disappearance of **PDI-a<sup>•-</sup>** is estimated by the decrease of absorbance value at 954 nm, where the radical anion is only species that absorbs,. From these experiments, we can conclude that

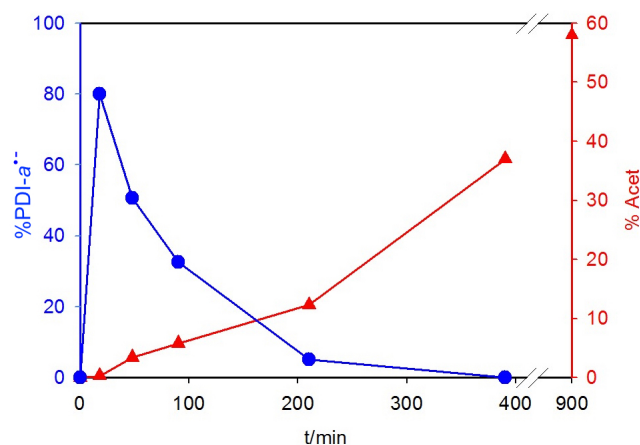


FIGURE 2.67: Irradiation at 455 nm of the reaction mixture (**PDI-a**  $8.0 \times 10^{-4}$  M,  $\text{Et}_3\text{N}$  0.13 M and **BrAcet** 0.017 M) in degassed DMF solution. Percentage of **PDI-a<sup>•-</sup>** (estimated from absorbance at 954 nm during the irradiation of the reaction mixture, blue circles), compared to the initial concentration of **PDI-a**, and percentage of **Acet** formation (estimated with HPLC analysis, red triangles), compared to the initial **BrAcet** concentration, as a function of irradiation time.

the **PDI-a<sup>•-</sup>** is not the photocatalyst for aryl halide reduction: indeed, upon

irradiation of the reaction mixture, the **PDI-a**<sup>•-</sup> disappears and the photoreaction takes place, so we conclude that a photoproduct is the photocatalyst. To get more insights into the mechanism, we performed experiments in different conditions. (i) If we irradiate for 20 minutes, as reported in figure 2.64 plot (a), to form **PDI-a**<sup>•-</sup> and stop irradiation at any time in the interval reported in figure 2.67, the reaction stops: light is necessary for the formation of acetophenone. (ii) In the absence of **BrAcet**, **PDI-a**<sup>•-</sup> is formed upon irradiation of **PDI-a** in the presence of Et<sub>3</sub>N, but it is photostable in solution, as previously observed by Wasielewski, due the very short-lifetime of its lowest excited state; furthermore, after 6 hours of irradiation, if we areated, we were able to recover the initial **PDI-a**. The **BrAcet** is directly involved in the photoreaction of **PDI-a**<sup>•-</sup> (figure 2.68). (iii) Upon chemical reduction of **PDI-a** in

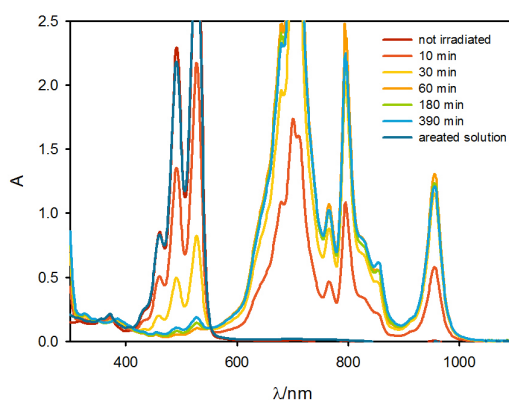


FIGURE 2.68: Absorption spectra of **PDI-a**  $8.0 \times 10^{-4}$  M in degassed DMF solution in the presence of Et<sub>3</sub>N 0.13 M upon irradiation at 455 nm by a blue LEDs up to 390 minutes; the oxygenated solution, after the irradiation, is also reported.

the presence of 8 equivalents of sodium ascorbate, **PDI-a**<sup>•-</sup> is quantitatively formed and upon irradiation at 455 nm, the same spectral changes as those reported in figure 2.64 plot (b) are observed and **Acet** is formed (figure 2.69): Et<sub>3</sub>N is not involved in the photoreaction of **PDI-a**<sup>•-</sup>. We also left the solution in the dark for the same time (6 hours): no variation were observed in the absorption spectra and no formation of **Acet** occurred; even if we generate the **PDI-a**<sup>•-</sup> chemically, the light is necessary to have the formation of the product. (iv) Upon repeating experiment (iii) and changing irradiation wavelength from 455 nm to  $\lambda > 610$  nm, so that only **PDI-a**<sup>•-</sup> is absorbing light, the same results are obtained, in term of conversion and absorption spectra variations (figure 2.70): the photochemical reaction observed is not

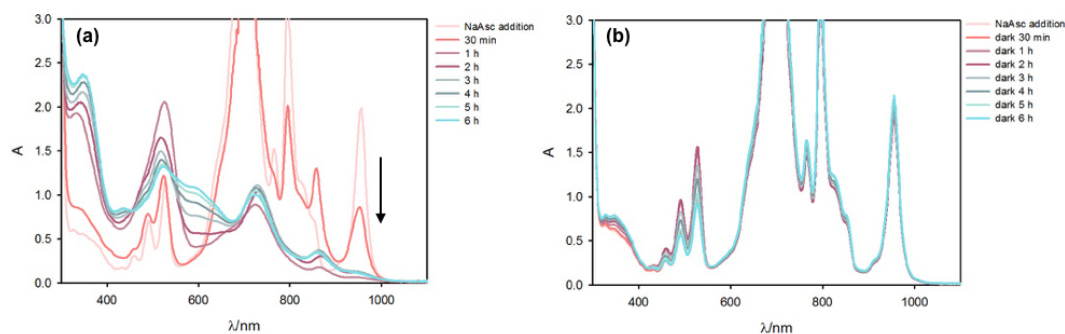


FIGURE 2.69: Absorption spectra of **PDI-a**  $8.0 \times 10^{-4}$  M in degassed DMF solution in the presence of sodium ascorbate 0.13 M and **BrAcet** 0.017 M upon irradiation at 455 nm by a blue LEDs (a) and in the dark (b) in the time interval 0 - 6 hours.

dependent on the irradiation wavelength, as expected from the experimental finding that high-lying excited  $D_n$  states of **PDI-a** $^{\bullet-}$  decays very rapidly by internal conversion to the lowest  $D_1$  state absorbing in the NIR spectral region. (v) We repeated the same experiment with the same concentration

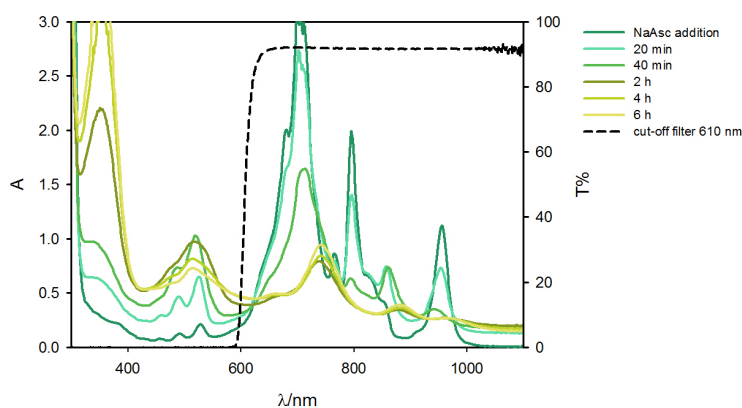


FIGURE 2.70: Absorption spectra of **PDI-a**  $5.0 \times 10^{-4}$  M in degassed DMF solution in the presence of sodium ascorbate 0.13 M and **BrAcet** 0.017 M upon irradiation with CFL 23W lamp with 610 nm cut-off filter (black dashed line) in the time interval 0 - 6 hours.

of **PDI-a** used in the original paper (we were not able to follow absorption variations because the **PDI-a** concentration was too high) and similar results were obtained: the concentration of **PDI-a** is not affecting the reaction mechanism. (vi) Then we decided to change the substrate, to check if it has an active role in the disappearance of **PDI-a** $^{\bullet-}$ : we used 4-Iodobenzaldehyde (**IAld**) instead of **BrAcet** and performed the reaction under the same conditions. Even if the conversion was not comparable with the one reported by König (in 5 hours irradiation he measured 98% conversion, we estimated

10% under same conditions), we observed again the disappearance of **PDI- $a^{\bullet-}$**  (figure 2.71), that does not depend on the substrate used. Unfortunately,

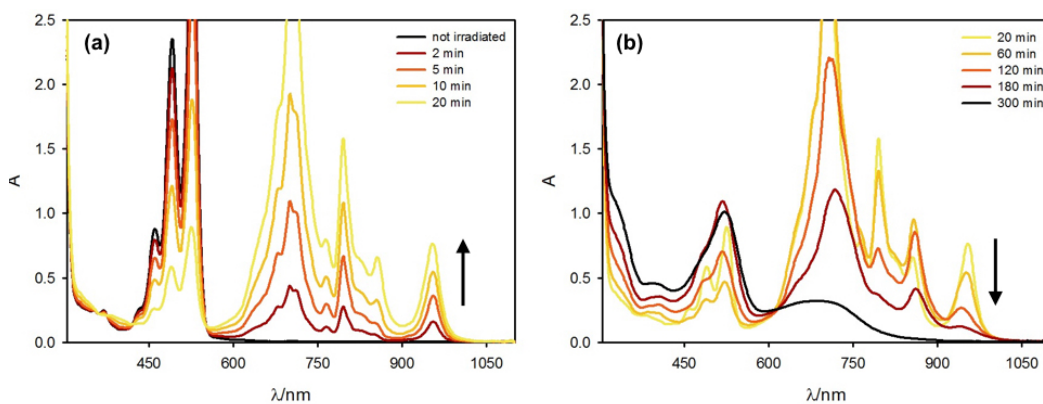


FIGURE 2.71: Absorption spectra of **PDI- $a$**   $8.0 \times 10^{-4}$  M in degassed DMF solution in the presence of  $\text{Et}_3\text{N}$  0.13 M and **IAlId** 0.019 M upon irradiation at 455 nm by a blue LEDs in the time interval: (a) 0 - 20 minutes and (b) 20 - 300 minutes.

we could not isolate the photoproduct that acts as a photocatalyst. Indeed more than one photoproduct exist in the reaction mixture; furthermore, the amount is so not enough to be characterize by NMR and HPLC analysis. We are not able to determine the chemical structure of this photoproduct.

In order to check if the photoreaction of **PDI- $a^{\bullet-}$**  involves an attack to the bay positions,<sup>112</sup> we synthesized the **PDI-Ph** derivative (figure 2.72) and repeated the same experiments. We observed very similar results: **PDI-Ph $^{\bullet-}$**  is formed and then a photodecomposition product needs to be formed to start the reaction of Ar-X.

**EPR measurements.** Further confirmation of the picture outlined by photo-

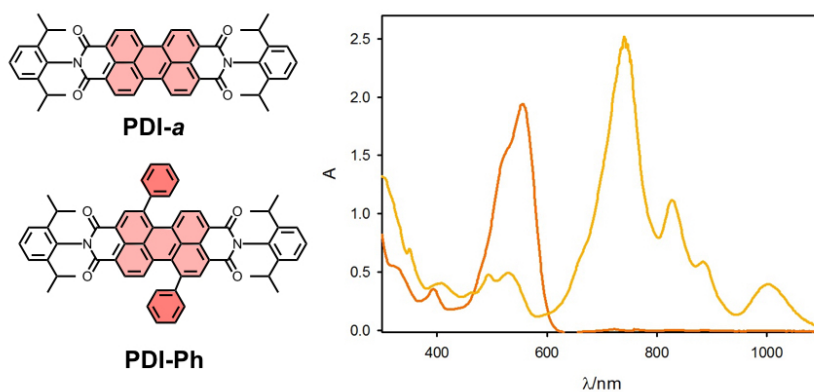


FIGURE 2.72: Chemical Structure of the **PDI-Ph** and absorption spectrum of the neutral (orange line) and radical anion (yellow line) form.



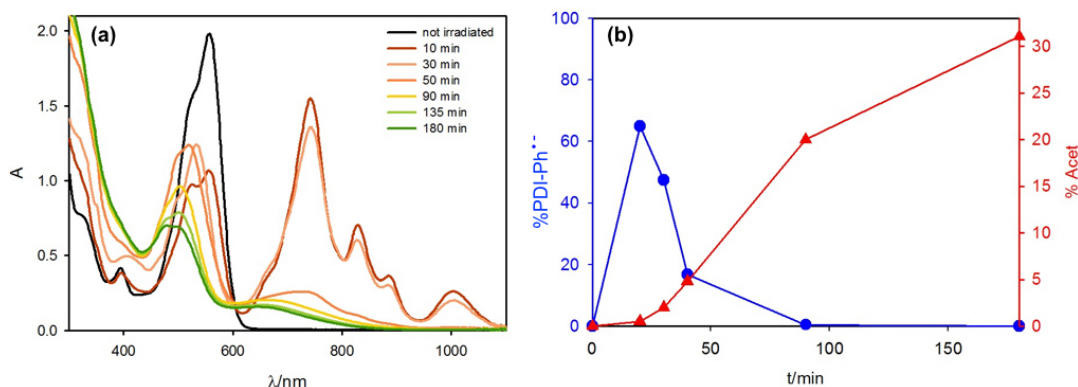


FIGURE 2.73: Absorption spectra of **PDI-Ph**  $8.0 \times 10^{-4}$  M in degassed DMF solution in the presence of  $\text{Et}_3\text{N}$  0.13 M and **BrAcet** 0.017 M upon irradiation at 455 nm by a blue LEDs in the time interval 0 - 180 minutes (a); percentage of **PDI-Ph** $\bullet^-$  (estimated from absorbance at 1003 nm during the irradiation of the reaction mixture, blue circles), compared to the initial concentration of **PDI-Ph**, and percentage of **Acet** formation (estimated with HPLC analysis, red triangles), compared to the initial **BrAcet** concentration, as a function of irradiation time.

chemical experiments was provided by monitoring the reduction of **BrAcet** by using EPR spectroscopy. We initially characterized the paramagnetic species deriving by **PDI-a** under irradiation in the absence of **BrAcet**. Irradiation with visible light ( $\lambda = 450$  nm) of a deoxygenated DMF solution containing **PDI-a** ( $8.0 \times 10^{-4}$  M),  $\text{Et}_3\text{N}$  (0.13 M), resulted in a strong EPR signal consisting of a well resolved hyperfine structure (figure 2.74, plot a). On the basis of spectroscopic parameters ( $a_{2N} = 0.62$  G,  $a_{4H} = 1.75$  G,  $a_{4H} = 0.66$  G,  $a_{2H} = 0.63$  G,  $a_{4H} = 0.55$  G,  $g = 2.0028$ ) the spectrum was attributed to the radical anion of **PDI-a** (**PDI-a** $\bullet^-$ ).<sup>113 114</sup> Further irradiation of the solution containing **PDI-a** $\bullet^-$  did not result in a change in the shape, nor in the disappearance of the EPR signal, thus confirming **PDI-a** $\bullet^-$  is photostable in solution.

Electrochemical reduction of a degassed DMF solution (0.1 M in  $\text{Bu}_4\text{NPF}_6$  as supporting electrolyte) containing only **PDI-a** (figure 2.74, plot b), afforded the same EPR signal observed under irradiation with visible light of **PDI-a** in the presence of  $\text{Et}_3\text{N}$  (figure 2.74, plot a)), this further confirming that the source of the EPR signal is the **PDI-a** $\bullet^-$ . The fate of **PDI-a** $\bullet^-$  was then monitored by mimicking the synthetic reaction conditions, i.e. during the irradiation of a solution containing also the substrate to be reduced. EPR spectroscopy reaffirms that under continuous irradiation of the reaction mixture containing **BrAcet**, the **PDI-a** radical anion initially formed changes to a new paramagnetic species. In figure 2.75 the changes observed in the EPR spectra during irradiation of the reaction mixture are reported. Whereas the

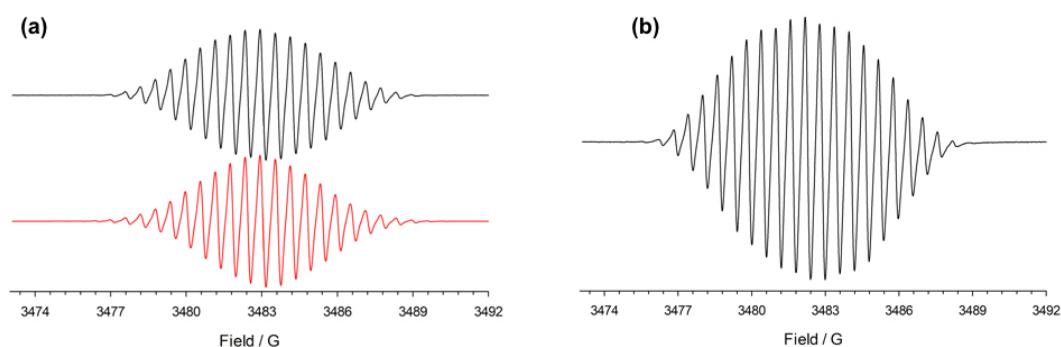


FIGURE 2.74: (a) EPR spectrum (black) obtained during the irradiation of a reaction mixture containing **PDI-a**  $8.0 \times 10^{-4}$  M and  $\text{Et}_3\text{N}$  0.13 M in degassed DMF solution. In red is reported the corresponding theoretical simulation. (b) EPR spectrum obtained during electrochemical reduction of **PDI-a**  $8.0 \times 10^{-4}$  in degassed DMF solution (0.1 M in  $\text{Bu}_4\text{NPF}_6$  as supporting electrolyte).

spectrum of **PDI-a** $\bullet^-$  shows well resolved hyperfine splitting, the spectra recorded after 400 minutes of irradiation do not (figure 2.75). Further irradiation of the reaction mixtures (up to 12 hours) does not produce significant changes in the shape of this new EPR signal.

To conclude, the absorption of two photons by two different chemical species

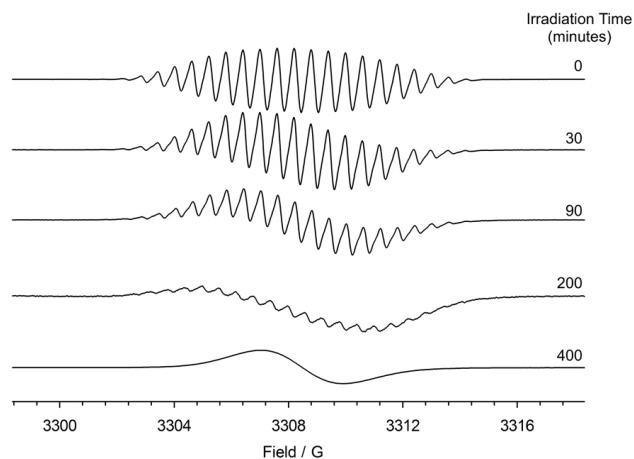


FIGURE 2.75: Time evolution of EPR spectra during irradiation of the reaction mixture containing **PDI-a**  $8.0 \times 10^{-4}$  M,  $\text{Et}_3\text{N}$  0.13 M and **BrAcet** 0.017 M in degassed DMF solution

in order to increase the reducing or oxidizing power in a similar way to the Z-scheme of natural photosynthesis is very appealing, but the product generated by the first photon absorption should exhibit long-lived excited states and high photostability.



## Conclusion

During my PhD, I had the possibility to work on several research projects, gaining different skills. In the field of supramolecular chemistry, we demonstrated the importance of the spatial arrangement of: (i) the reducible units in order to tune their intra- and intermolecular interactions and to drive the hierarchical growth of supramolecular structures by reversible pimerization; (ii) the chromophores in a multichromophoric system in order to control the direction of electron/energy transfer processes between supramolecular components; (iii) the porphyrinic monomers bearing bypyridine moieties, at the air-water interface, in order to control the formation of a 2D-polymer after the complexation with the metal ion.

In the field of photocatalysis, we were able to study in details the behaviour of the various photocatalysts used in the photoredox reactions shown in *Chapter 2*, with spectrophotometric and spectrofluorimetric measurements: by absorption spectra we demonstrated the stability of the photocatalyst during the irradiation (or its degradation) and the selectivity of absorption of the irradiation light; in the case of luminescent photocatalyst, we estimated the quenching constant by different reagents, in order to have more information about the reaction mechanism. Finally, for the reduction of aryl halides catalyzed by perylenediimide derivate, we were able to disprove the two-photon mechanism proposed by König and co-workers (*Science*, 2014, 346, 725 - 728) just monitoring the reaction with absorption spectra and HPLC analysis: after irradiation, the perylenediimide photocatalyst undergoes photodegradation reaction; we supposed that the species so obtained, is the one active in the reduction.



## Appendix A

# Basic Photophysical and Electrochemical Techniques

**Electronic Absorption Spectra.** All the absorption spectra in the UV-Vis region of the light spectrum were recorded at room temperature on solutions contained in quartz cuvettes (optical path length 0.1-1 cm and, Hellma<sup>®</sup> by using a Perkin Elmer LAMBDA 650 double-beam spectrophotometer (figure A.1). In the case of photoredox reactions followed by absorption spectroscopy we used a Cary 50 Bio UV-Vis single-beam spectrophotometer. The precision on the wavelength values was  $\pm 2$  nm. Molar absorption coefficient values were determined using the Lambert-Beer law; the experimental error, mostly due to weighting error, can be estimated to be around 5%. The spectra in the NIR region were recorded with a Perkin Elmer LAMBDA 750 double-beam spectrophotometer.

**Luminescence Spectra.** Fluorescence and phosphorescence emission and

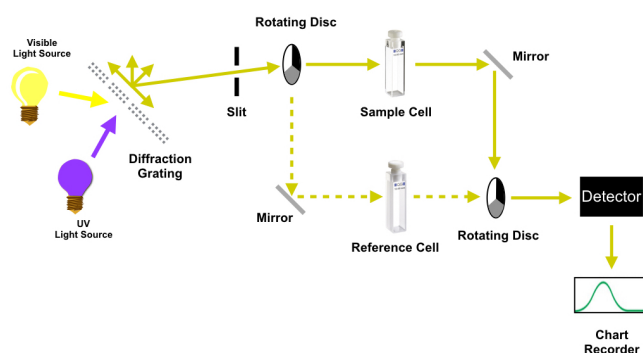


FIGURE A.1: Schematic experimental set-up for a standard double-beam.

excitation spectra in the 250-900 nm range were recorded with Perkin Elmer LS55 spectrofluorometer equipped with Hamamatsu R928 photomultiplier (schematic representation in figure A.2). Room temperature spectra were recorded in spectrofluorometric suprasil quartz cuvettes described for the

electronic absorption spectra. Spectra in frozen matrix at 77 K were taken using quartz tubes with an internal diameter of about 2 mm and a 20 cm length immersed in liquid nitrogen. A transparent dewar (glass or quartz) with a cylindrical terminal part with a 1 cm external diameter was employed. Such a device easily fits into the sample holder of the spectrofluorometers above indicated. The precision on the wavelength values was  $\pm 2$  nm.

**Luminescence Quantum Yield.** Luminescence quantum yields have been

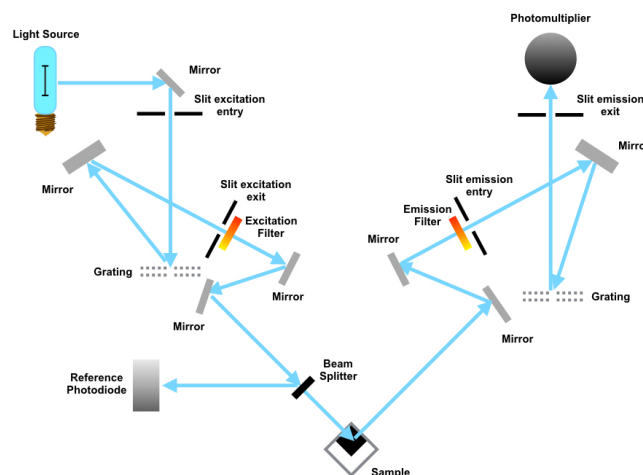


FIGURE A.2: Schematic representation of a standard spectrofluorometer.

determined on solution samples at room temperature referring to the relative method optimized by Demas and Crosby.<sup>115</sup> The quantum yield is expressed as:

$$\Phi_S = \Phi_R \left( \frac{A_S}{A_R} \right) \left( \frac{n_S}{n_R} \right)^2 \quad (\text{A.1})$$

where  $\Phi$ ,  $A$  and  $n$  indicate the luminescence quantum yield, the area subtended by the emission band (in the intensity versus frequency spectrum) and the refractive index of the solvent used for the preparation of the solution, respectively; the subscripts S and R stand for sample and reference, respectively.

Different standards were selected depending on the spectral region of interests, in particular quinine sulphate in 0.5 M  $\text{H}_2\text{SO}_4$  ( $\Phi = 0.55$ ) aqueous solution for the fluorescence of  $2^{2+}$ ,  $1^{8+}$  and  $1^{4+}$ , while Oxazine 1 in ethanol ( $\Phi = 0.15$ ) for the phosphorescence of  $\text{Ru}(\text{CO})\text{FTPP}$ .<sup>116</sup>

**Luminescence lifetime measurements.** Excited state lifetimes in the range 0.5 ns - 10  $\mu\text{s}$  were measured with an Edinburgh Instrument time correlated single-photon counting technique. A schematic view of this instrument is reported in figure A.3. The excitation impulse is obtained by a pulsed diode

laser (300 nm or 405 nm, Picoquant). A photomultiplier tube (Hamamatsu R928P) cooled at  $-20^{\circ}\text{C}$  and suitably amplified is used as stop detector. Lifetimes in the range between  $10\ \mu\text{s}$  and  $5\ \text{s}$  were measured with the same Perkin Elmer LS 55 spectrofluorometer employed for the luminescence spectra acquisition. In this case the excitation pulse is generated by a Xe lamp (5 - 50 Hz) and the emission decay directly recorded. The experimental error on the lifetime measurements is  $\pm 10\%$ .

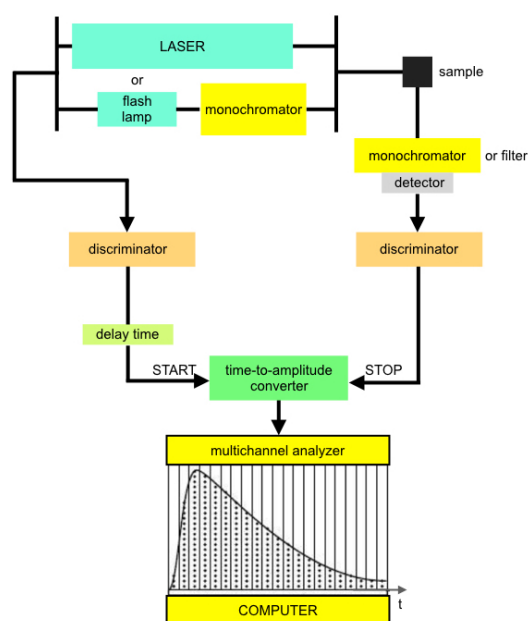


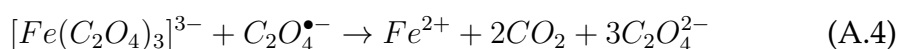
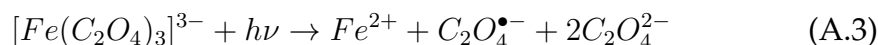
FIGURE A.3: Experimental set-up of the single photon counting.

**Photochemical Quantum Yield Assessment.** The efficiency of a given photochemical process is expressed by its photoreaction quantum yield:

$$\Phi_P = \frac{\text{moles product}}{q_{p,in} t f_m} = \frac{\Delta C V}{q_{p,in} t f_m} \quad (\text{A.2})$$

where  $\Delta C$  represents the concentration of photoproduct obtained during the irradiation,  $V$  is the volume of the irradiated solution,  $q_{p,in}$  is the flux of incident photons (i.e. number of photons emitted by the source),  $t$  is the time of irradiation and  $f_m$  is the mean value of the fraction of absorbed light at the irradiation wavelength. The number of incident photons can be measured by using chemical actinometers, and in particular, was estimated on dilute sample solutions at room temperature by using potassium ferrioxalate as chemical actinometer.<sup>117</sup> Indeed, it is the most practical actinometer for UV and visible light since it can be used up to 500 nm. The photochemical

reaction involved is a photodecomposition described as followed:



The amount of  $Fe^{2+}$  is determined spectrophotometrically by adding *o*-phenantroline and monitoring the formation of the colored tris-phenantroline complex ( $\epsilon = 11100 \text{ M}^{-1} \text{ cm}^{-1}$  at 510 nm), since potassium ferrioxalate is transparent to that wavelength and  $Fe^{3+}$  is not appreciably complexed by *o*-phenantroline. Since the reaction vessel consists of a spectrophotometric quartz cell having a 1cm path length and containing 3 ml of 12 mM ferrioxalate solution, a microversion of the actinometer was performed. The number of incident photons is given by

$$q_{p,in} = \frac{\Delta A_{510nm}}{t} \times Y \times N_A \quad (A.5)$$

where the factor  $Y$  includes the yield of the actinometer at a precise irradiation wavelength, the  $\epsilon$  of the complex  $[Fe(\text{phen})_3]^{2+}$  at 510 nm and the ratio between the product of the irradiated volume and the final volume after addition of *o*-phenantroline and the aliquot of the irradiated solution used for  $Fe^{2+}$  determination.

**Cyclic Voltammetry and Differential Pulse Voltammetry.** Among potentiostatic methods, voltammetric techniques<sup>118</sup> consist on the application of a potential scan to the working electrode and then the current response of the cell is measured. In cyclic voltammetry (CV) the potential applied to the working electrode is changed linearly with time within a defined potential range then a reverse scan is applied, as shown in figure A.4. For an elec-

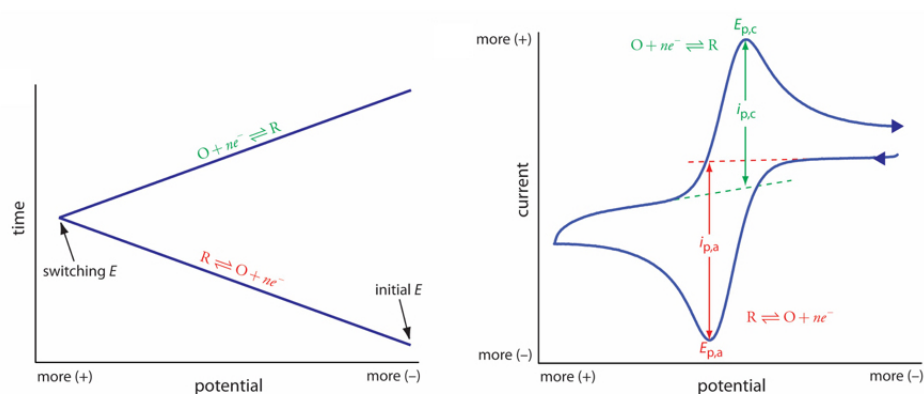


FIGURE A.4: Potential excitation function and current vs potential response for cyclic voltammetry.

trochemically reversible redox process in an unstirred solution containing a supporting electrolyte, hypothesizing a condition of semi-infinite linear diffusion (that is the case found with planar electrode of conventional size), the peak current  $i_p$  is given by

$$i_p = 0.4463 (nF)^{3/2} (RT)^{-1/2} AD_{ox}^{1/2} C_{ox} v^{1/2} \quad (\text{A.6})$$

where  $A$  represents the surface area of the electrode,  $D_{ox}$  and  $C_{ox}$  are the diffusion coefficient and the concentration of the of the electroactive species,  $v$  the scan rate and  $n$  refers to the number of transferred electrons. If the potential difference between cathodic and anodic peaks is  $\leq 59$  mV at 298 K, the average of the cathodic and anodic peak potential yields the *halfwave potential* ( $E_{1/2}$ ) for the redox couple. In contrast, when an irreversible process takes place, the considerations above are not applicable: in the case of irreversible processes the potential value of the corresponding DPV peak was considered.

In contrast to cyclic voltammetry, differential pulse voltammetry (DPV) is a more sensitive technique, having a detection limit of  $10^{-8}$  M. This voltammetric technique<sup>119</sup> is based on the application of a series of regular potential pulses over a base potential: in this case the value of the applied voltage is stepped from the imposed potential range by applying small increments (*step potential*). The applied pulses have the same height with respect to the base potential and the same time duration, as depicted in figure A.5. The most im-

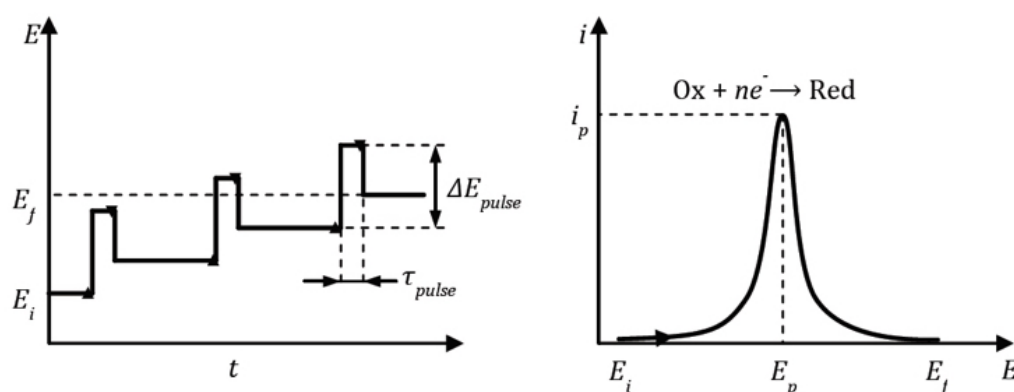


FIGURE A.5: Potential excitation function and current vs potential response for differential pulse voltammetry.

portant parameters for DPV are the height of the potential pulse (modulation amplitude  $\Delta E_{pulse}$ ) and the duration of the potential pulse (modulation time

$\tau_{pulse}$ ). In the case of a reversible process, the potential corresponding to the peak in the voltammogram is independent on the scan rate and is related to the *halfwave potential* by the equation A.7 and the peak on the voltammogram exhibits a symmetrical shape.

$$E_p = E_{1/2} - \frac{\Delta E_{pulse}}{2} \quad (\text{A.7})$$

As for CV, in a diffusion-controlled experiment the current depends on the surface area of the electrode, on the square root of diffusion coefficient of the electroactive species, on its concentration, but also on the height and duration of the applied pulse. In the case of irreversible processes (chemically or electrochemically), the DPV peak is weaker and broader and its shape is not symmetric anymore.

The spectroelectrochemistry (SEC) was born from the combination of electrochemical techniques and UV-Vis spectroscopy:<sup>120</sup> spectroelectrochemical techniques allow in-situ spectroscopic interrogation of electrogenerated complexes and this may permit the study of shorter-lived species and also establish the chemical reversibility of these reactions. The electrochemical techniques commonly used in this contest are potentiometric techniques, in particular, chronoamperometry and chronocoulometry. In chronoamperometry, the potential of the working electrode is stepped and the resulting current from faradaic processes occurring at the electrode is monitored as a function of time; in chronocoulometry the total charge that passes during the time following a potential step is measured as a function of time.

CV and DPV scans were carried out in argon-purged acetonitrile or  $\text{CH}_2\text{Cl}_2$  (Romil Hi-Dry™) and water millipore solutions at room temperature with an EcoChemie Autolab 30 multipurpose instrument interfaced to a personal computer. In acetonitrile and  $\text{CH}_2\text{Cl}_2$  solution the working electrode was a glassy carbon electrode (0.08  $\text{cm}^2$ , Amel); the counter electrode was a Pt spiral and a silver wire was employed as a quasi-reference electrode (QRE). The potentials reported are referred to SCE by measuring the potential with respect to ferrocene (+0.395 in acetonitrile). In aqueous solution a saturated calomel electrode (SCE) was used as reference electrode. The substrate concentrations were in  $10^{-4}$  -  $10^{-5}$  M range; a 0.1 M of supporting electrolyte (TEAPF<sub>6</sub> in acetonitrile, TEAPF<sub>6</sub> in  $\text{CH}_2\text{Cl}_2$  and NaCl in water) was also present. Cyclic voltammograms were obtained with scan rate of 1V/s for the species  $2^{2+}$  and 0.2 V/s for  $1^{8+}$  while the DPV experiments were performed



with a scan rate of 0.02 V/s, a pulse height of 75 mV, and a pulse duration of 40 ms. The errors on the redox potential values are estimated to be  $\pm 10$  mV for reversible processes and  $\pm 20$  mV for irreversible processes.

Spectroelectrochemical experiments were performed in a quartz cell (optical pathlength 0.2 cm) with three electrodes arrangements: the working electrode is a platinum grid (0.8 mm  $\times$  2.8 mm surface area), the counter electrode is a platinum wire (1 mm dia.  $\times$  5 mm length) and a silver wire is used as quasi-reference electrode, positioned very close to the working electrode to minimize Ohmic resistance. The solutions used for spectroelectrochemical experiments were prepared as previously described for cyclic voltammetry. In order to localize the right potential window corresponding to the redox process of interest, a cyclic voltammetry was recorded at 0.2 V/s before the spectroelectrochemistry. The electrolysis potential was varied with 20 - 50 mV steps and UV-Vis-NIR absorption spectra were recorded with an Agilent Technologies 8543 diode array spectrophotometer.



## Appendix B

# Microscopy and Langmuir-Blodgett Techniques

**Atomic Force Microscopy.** Since 1989, the atomic force microscope (AFM) has emerged as a useful tool for studying surface interactions by means of force-distance curves.<sup>121</sup> The heart of the AFM is a cantilever with a micro-fabricated tip that deflects when interacting with the sample surface. That can be scanned by means of a piezoactuator, while the cantilever deflection may be measured in different ways in order to reproduce the sample topography.<sup>122</sup> A general schematization is provided in figure B.1.

There are two principal modes of acquisition of force-distance curves. In the

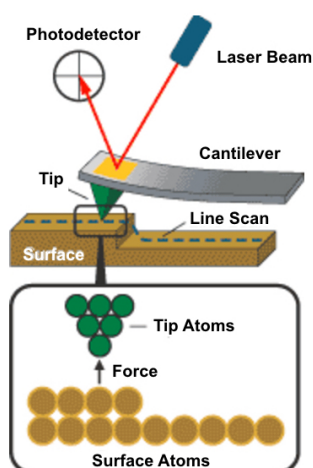


FIGURE B.1: Schematic representation of the tip-sample system in a AFM microscopy.

first mode, called the contact mode, the sample is displaced along the Z axis in discrete steps and the variations in cantilever deflection are collected; in the second mode, called the non-contact mode, the cantilever is allowed to vibrate by an external piezoelectric transducer while the sample is approached

and withdrawn, and the amplitude or the resonance frequency of the cantilever oscillations are collected as a function of tip-sample distance.

AFM images show important information about surface properties with high clarity: in addition, AFM can explore any sufficiently rigid surface either in air or with the sample immersed in a liquid. Indeed with AFM analysis is possible to examine the morphology and distribution of inorganic and organic particles on surfaces as well as evaluation of the thickness and other topographical features.<sup>123</sup>

AFM measurements were carried out on a Dimension FastScan AFM (Bruker, Billerica, Massachusetts). The thickness of the films was determined by tapping mode AFM measurements in the net attractive and net repulsive regimes.

**Scanning Electron Microscopy.** A scanning electron microscope (SEM) uses electrons rather than light, like optical microscope, to generate images and the resolution of an SEM is therefore limited by the wavelength of electrons (standard energy of 5 keV, around 0.55 nm).<sup>124</sup> A scanning electron microscope works by focusing a source of electrons into a fine point that can be scanned over the surface of the object being viewed. When the scanning electrons hit the surface of the material being imaged, several interactions occur. In our case all of the images were generated by collecting secondary electrons, electrons from the material being imaged that get knocked off by the incident electron beam. The secondary electrons are collected by a detector where information from the electrons is used to form an image of the material being viewed.

The SEM grids were placed on a holder (PLANO, G3662) and imaged with FEG-SEM, Zeiss LEO Gemini 1530, Germany microscope with an in-lens detector. Images were recorded at low beam energy (1 - 3 kV) to avoid damaging of the thin films.

**Langmuir Trough.** The Langmuir trough system used is a KSV 2000 System 2 (KSV NIMA, Finland). The system is equipped with a platinum Wilhelmy plate, a dipper and is made of Teflon: the two symmetrical barriers are made of Delrin. Cleaning of the trough was done by rinsing it with millipore water followed by cleaning it with chloroform, ethanol and again chloroform by the use of dust-free papers. The experimental equipment was placed in a Plexiglas box to reduce dust and vibrational influences from the environment. Millipore water was used for the aqueous phase. A typical experimental procedure is as follows: the monomer solution ( $0.5 \text{ mg mL}^{-1}$  in  $\text{CHCl}_3$ ) was warmed to  $20^\circ\text{C}$  and a volume of  $100 \mu\text{l}$  was dropped carefully on the air-water interface. The organic solvent was allowed to evaporate for 30 min.

Compression was then started and maintained at a constant rate of 3 mm min<sup>-1</sup>. The target surface pressure was set to the desired value (10 mN m<sup>-1</sup>). After equilibration for 30 min at the given surface pressure, the metal salt solution was injected from both sides close to the barriers below the interface. Polymerization times of the monomer layer were around 12 hours at the indicated surface pressure. Transfer of polymer from the interface to SiO<sub>2</sub> or quartz substrate was done via horizontal transfer through the interface, with a rate of 0.5 mm min<sup>-1</sup>.

**Brewster Angle Microscopy.** For Brewster angle microscopy (BAM) measurements, a 659 nm laser from the MicroBAM (KSV NIMA, Finland) was used. To allow for total reflection without film, a black glass was placed inside the Langmuir trough (Teflon).



## Appendix C

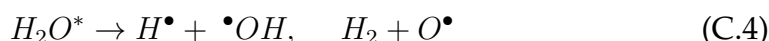
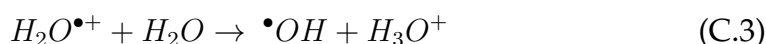
# Methods of Ionizing Radiation Generation and Electron Paramagnetic Resonance

The most commonly used sources of ionizing radiation are  $^{60}\text{Co}$   $\gamma$ -rays, which are photons having energies of 1.17 and 1.33 MeV, or fast electrons from an accelerator with energies typically in the range 2-20 MeV.<sup>125</sup> The dose absorbed by the material is expressed in grays (1 Gy = 1 J kg<sup>-1</sup>) and the dose rate in Gy s<sup>-1</sup>. In each case the result of the interaction of high energy particles with molecules is the ejection of a single electron, which itself may have sufficient energy to cause further ionizations, but which rapidly (< 10<sup>-12</sup> s) reaches thermal equilibrium with the liquid and becomes trapped as a so-called solvated electron ( $e_S^-$ ). In this way, reactive free radicals are generated from stable molecules (M):



An important characteristic of ionizing radiation is that it is absorbed non-selectively so that molecules are ionized according to their relative abundance in the medium of interest. For example, in dilute solution (solute concentration  $\leq 0.1$  M) the ionized molecules are essentially those of the solvent so that knowledge of the radiation chemistry of the solvent. Since our continuous radiolysis experiments were performed in aqueous solution, we will focus our attention of the radiolysis of water. The initial event is the transfer of  $\sim 7 - 100$  eV, an amount of energy sufficient to cause (multiple) ionizations or excitations in water molecules (reaction C.2, 10<sup>-16</sup> s). The positive radical ion  $\text{H}_2\text{O}^{\bullet+}$  is believed to undergo the reaction C.3 by 10<sup>-14</sup> s, the electronically excited states  $\text{H}_2\text{O}^*$  are known to dissociate in the vapor phase by 10<sup>-13</sup>

s (reaction C.4), and the electron is known to be solvated by  $\sim 10^{-12}$  s (reaction C.5). The products of reactions C.3 - C.5 are gather together in small clusters called spurs. Next, these products begin to diffuse randomly and in  $10^{-7}$  s the spurs don't exist anymore and the medium is homogeneous again.



Upon the diffusion through the medium, the radicals can interact with each

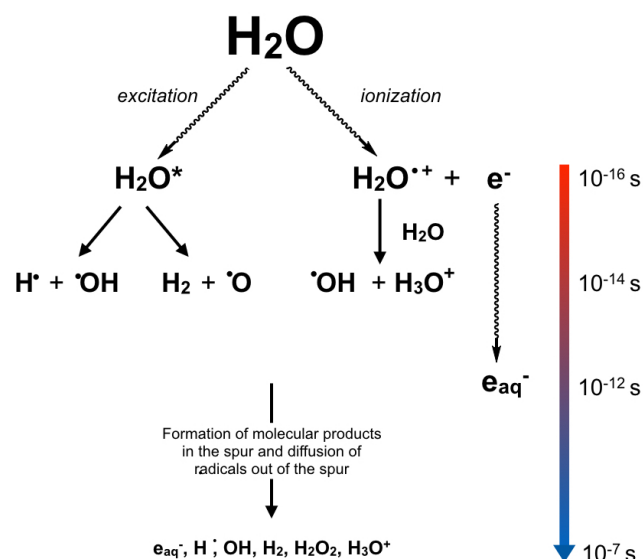


FIGURE C.1: Scheme of reactions of transient species produced by irradiation in water.

other to give molecular products, or they may diffuse away to be picked up by a scavenger: in our case it was 2-propanol, that efficiently scavenges  $\bullet OH$  and  $H\bullet$  (see equation 1.8 and 1.9, chapter 1), and converted to the reducing radical  $(CH_3)_2\bullet COH$ . Thus, under these conditions, the main species present in solution are  $e_{aq}^-$  and  $(CH_3)_2\bullet COH$  with a total radiation yield  $G = 0.62 \mu\text{mol J}^{-1}$ .

**Continuous Radiolysis.** Continuous radiolysis was carried out at room temperature ( $22 \pm 2^\circ\text{C}$ ) on 20 mL samples of argon-purged aqueous solution at natural pH contained in Pyrex cylindrical vessels (total volume 100 mL) fitted with Spectrosil optical cells on a side arm. Irradiations were performed in a  $^{60}\text{Co}$ -Gammacell with a dose rate of  $3.7 \text{ Gy min}^{-1}$ . The absorbed radiation



dose was determined with the Fricke chemical dosimeter by taking  $G(\text{Fe}^{3+}) = 1.61 \mu\text{mol J}^{-1}$ .<sup>126</sup> Absorption spectra were recorded with a Perkin-Elmer lambda 45 UV-Vis spectrophotometer.

**Pulse Radiolysis.** Pulse radiolysis experiments with optical absorption detection were carried out using the LAE-10 linear accelerator of the Institute of Nuclear Chemistry and Technology in Warsaw, Poland. Pulse duration of the LAE-10 was 10 ns and electron energy 10 MeV. As monitoring light source a 150 W xenon arc lamp E7536 (Hamamatsu Photonics K.K) was used. Wavelengths were selected by MSH 301 (Lot Oriel Gruppe) monochromator with resolution 2.4 nm or above 800 nm by bandpass filters (Standa Ltd) with FWHM about 50 nm. Light analysis below 800 nm was performed by means of PMT R955 (Hamamatsu) and above 800 nm by Si amplified diode PDA10A-EC (ThorLabs). Signal from detector was digitized using WaveRunner 6051A (500 MHz, 5 GS/s, LeCroy) or, alternatively, WaveSurfer 104MXs-B (1 GHz, 10 GS/s, LeCroy) oscilloscopes and then it was sent to PC for processing. During the experiments the samples were exposed to as little UV light as possible (using UV cut-off filters) to avoid photodecomposition and/or photobleaching effects, although no evidence of such effects occurring was found within the time frames monitored. Near infrared wavelengths were cut-off by water filter. The total dose per pulse was determined, before each series of experiments, with a  $\text{N}_2\text{O}$ -saturated aqueous solution 10 mM KSCN<sup>127</sup> using  $G\epsilon = 5.048 \times 10^{-4} \text{ m}^2 \text{ J}^{-1}$  for the  $(\text{SCN})_2^{\bullet-}$  radical-anion at 472 nm. **Electron Paramagnetic Resonance.** Electron paramagnetic resonance (EPR) is a technique for studying chemical species that have one or more unpaired electrons, such as organic and inorganic free radicals or inorganic complexes possessing a transition metal ion. When a molecule with an unpaired electron is placed in a strong magnetic field, the spin of the unpaired electron can align in two different ways creating two spin states,  $m_s = \pm 1/2$ . The alignment can either be along the direction to the magnetic field, which corresponds to the lower energy state  $m_s = -1/2$  or opposite to the direction of the applied magnetic field  $m_s = +1/2$ . The two alignments have different energies and this difference in energy lifts the degeneracy of the electron spin states.

The unpaired electrons, because of their spin, behave like tiny magnets. When materials containing such electrons are subjected to a strong stationary magnetic field, the magnetic axes of the unpaired electrons, or elementary magnets, partially align themselves with the strong external field. In an EPR experiment the field of the spectrometer magnet is swept linearly to excite some

of the electrons in the lower energy level to the upper energy level, while the sample is exposed to fixed microwave irradiation. The measurement of radiation absorbed, when the microwave frequency are right to produce an EPR resonance, as a function of the changing variable gives an electron paramagnetic resonance spectrum. Such a spectrum, typically a graph of microwave energy absorption versus applied stationary magnetic field, is used to identify paramagnetic substances and to investigate the nature of chemical bonds within molecules by identifying unpaired electrons and their interaction with the immediate surroundings.

The EPR spectra were recorded on a Bruker ESP300 spectrometer equipped with an NMR gaussmeter for field calibration and Bruker ER033M field-frequency lock. The temperature was controlled with a standard variable temperature accessory and was monitored before and after each run with a copper-constantan thermocouple. The instrument settings were as follows: microwave power 0.79 mW, modulation amplitude 1.0 - 0.2 G, modulation frequency 100 kHz, scan time 180 s, 2 K data points. The hyperfine splittings were determined by computer simulation using a Monte Carlo minimization procedure.

When the reduction process is performed in the EPR cavity electrochemically, an homemade electrochemical cell, consisted of an EPR flat cell (Wilmad WG-810) equipped with a  $25 \times 5 \times 0.2$  mm platinum gauze (cathode), and a platinum wire (anode), was used. The current was supplied and controlled by AMEL 2051 general-purpose potentiostat. In a typical experiment, the cell was filled with an acetonitrile solution of the appropriate substrate (ca. 0.5 mM) containing  $\text{NH}_4\text{PF}_6$  (ca 0.1 mM) as supporting electrolyte. After thoroughly purging the solution with  $\text{N}_2$ , spectra were recorded at different potential settings in the range from 0 to -3.0 V.

## Appendix D

# Permissions

### Photocatalytic ATRA reaction promoted by iodo-Bodipy and sodium ascorbate

G. Magagnano, A. Gualandi, M. Marchini, L. Mengozzi, P. Ceroni and P. G. Cozzi, *Chem. Commun.*, 2017, **53**, 1591  
DOI: 10.1039/C6CC09387F

If you are not the author of this article and you wish to reproduce material from it in a third party non-RSC publication you must [formally request permission](#) using RightsLink. Go to our [Instructions for using RightsLink page](#) for details.

Authors contributing to RSC publications (journal articles, books or book chapters) do not need to formally request permission to reproduce material contained in this article provided that the correct acknowledgement is given with the reproduced material.

Reproduced material should be attributed as follows:

- For reproduction of material from NJC:  
Reproduced from Ref. XX with permission from the Centre National de la Recherche Scientifique (CNRS) and The Royal Society of Chemistry.
- For reproduction of material from PCCP:  
Reproduced from Ref. XX with permission from the PCCP Owner Societies.
- For reproduction of material from PPS:  
Reproduced from Ref. XX with permission from the European Society for Photobiology, the European Photochemistry Association, and The Royal Society of Chemistry.
- For reproduction of material from all other RSC journals and books:  
Reproduced from Ref. XX with permission from The Royal Society of Chemistry.

If the material has been adapted instead of reproduced from the original RSC publication "Reproduced from" can be substituted with "Adapted from".

In all cases the Ref. XX is the XXth reference in the list of references.

If you are the author of this article you do not need to formally request permission to reproduce figures, diagrams etc. contained in this article in third party publications or in a thesis or dissertation provided that the correct acknowledgement is given with the reproduced material.

Reproduced material should be attributed as follows:

- For reproduction of material from NJC:  
[Original citation] - Reproduced by permission of The Royal Society of Chemistry (RSC) on behalf of the Centre National de la Recherche Scientifique (CNRS) and the RSC
- For reproduction of material from PCCP:  
[Original citation] - Reproduced by permission of the PCCP Owner Societies
- For reproduction of material from PPS:  
[Original citation] - Reproduced by permission of The Royal Society of Chemistry (RSC) on behalf of the European Society for Photobiology, the European Photochemistry Association, and RSC
- For reproduction of material from all other RSC journals:  
[Original citation] - Reproduced by permission of The Royal Society of Chemistry

If you are the author of this article you still need to obtain permission to reproduce the whole article in a third party publication with the exception of reproduction of the whole article in a thesis or dissertation.

---

**JOHN WILEY AND SONS LICENSE  
TERMS AND CONDITIONS**

Mar 06, 2017

This Agreement between Marianna Marchiini ("You") and John Wiley and Sons ("John Wiley and Sons") consists of your license details and the terms and conditions provided by John Wiley and Sons and Copyright Clearance Center.

License Number	4063060910292
License date	
Licensed Content Publisher	John Wiley and Sons
Licensed Content Publication	Chemistry - A European Journal
Licensed Content Title	Visible-Light-Induced Direct Photocatalytic Carboxylation of Indoles with CBr <sub>4</sub> /MeOH
Licensed Content Author	Qing-Qing Yang, Marianna Marchini, Wen-Jing Xiao, Paola Ceroni, Marco Bandini
Licensed Content Date	Oct 28, 2015
Licensed Content Pages	5
Type of use	Dissertation/Thesis
Requestor type	Author of this Wiley article
Format	Electronic
Portion	Full article
Will you be translating?	No
Title of your thesis / dissertation	Photoactive Molecules in Supramolecular Architectures and Photoredox Reactions
Expected completion date	Apr 2017
Expected size (number of pages)	200
Requestor Location	Marianna Marchiini Via Selmi 2  Bologna, 40126 Italy Attn: Marianna Marchiini
Publisher Tax ID	EU826007151
Billing Type	Invoice
Billing Address	Marianna Marchiini Via Selmi 2  Bologna, Italy 40126 Attn: Marianna Marchiini
Total	0.00 EUR
Terms and Conditions	

**TERMS AND CONDITIONS**

This copyrighted material is owned by or exclusively licensed to John Wiley & Sons, Inc. or one of its group companies (each a "Wiley Company") or handled on behalf of a society with which a Wiley Company has exclusive publishing rights in relation to a particular work (collectively "WILEY"). By clicking "accept" in connection with completing this licensing transaction, you agree that the following terms and conditions apply to this transaction

(along with the billing and payment terms and conditions established by the Copyright Clearance Center Inc., ("CCC's Billing and Payment terms and conditions"), at the time that you opened your RightsLink account (these are available at any time at <http://myaccount.copyright.com>).

#### Terms and Conditions

- The materials you have requested permission to reproduce or reuse (the "Wiley Materials") are protected by copyright.
  - You are hereby granted a personal, non-exclusive, non-sub licensable (on a stand-alone basis), non-transferable, worldwide, limited license to reproduce the Wiley Materials for the purpose specified in the licensing process. This license, and any CONTENT (PDF or image file) purchased as part of your order, is for a one-time use only and limited to any maximum distribution number specified in the license. The first instance of republication or reuse granted by this license must be completed within two years of the date of the grant of this license (although copies prepared before the end date may be distributed thereafter). The Wiley Materials shall not be used in any other manner or for any other purpose, beyond what is granted in the license. Permission is granted subject to an appropriate acknowledgement given to the author, title of the material/book/journal and the publisher. You shall also duplicate the copyright notice that appears in the Wiley publication in your use of the Wiley Material. Permission is also granted on the understanding that nowhere in the text is a previously published source acknowledged for all or part of this Wiley Material. Any third party content is expressly excluded from this permission.
  - With respect to the Wiley Materials, all rights are reserved. Except as expressly granted by the terms of the license, no part of the Wiley Materials may be copied, modified, adapted (except for minor reformatting required by the new Publication), translated, reproduced, transferred or distributed, in any form or by any means, and no derivative works may be made based on the Wiley Materials without the prior permission of the respective copyright owner. For STM Signatory Publishers clearing permission under the terms of the STM Permissions Guidelines only, the terms of the license are extended to include subsequent editions and for editions in other languages, provided such editions are for the work as a whole in situ and does not involve the separate exploitation of the permitted figures or extracts, You may not alter, remove or suppress in any manner any copyright, trademark or other notices displayed by the Wiley Materials. You may not license, rent, sell, loan, lease, pledge, offer as security, transfer or assign the Wiley Materials on a stand-alone basis, or any of the rights granted to you hereunder to any other person.
  - The Wiley Materials and all of the intellectual property rights therein shall at all times remain the exclusive property of John Wiley & Sons Inc, the Wiley Companies, or their respective licensors, and your interest therein is only that of having possession of and the right to reproduce the Wiley Materials pursuant to Section 2 herein during the continuance of this Agreement. You agree that you own no right, title or interest in or to the Wiley Materials or any of the intellectual property rights therein. You shall have no rights hereunder other than the license as provided for above in Section 2. No right, license or interest to any trademark, trade name, service mark or other branding ("Marks") of WILEY or its licensors is granted hereunder, and you agree that you shall not assert any such right, license or interest with respect thereto
  - NEITHER WILEY NOR ITS LICENSORS MAKES ANY WARRANTY OR REPRESENTATION OF ANY KIND TO YOU OR ANY THIRD PARTY, EXPRESS, IMPLIED OR STATUTORY, WITH RESPECT TO THE MATERIALS OR THE ACCURACY OF ANY INFORMATION CONTAINED IN THE MATERIALS, INCLUDING, WITHOUT LIMITATION, ANY IMPLIED WARRANTY OF MERCHANTABILITY, ACCURACY, SATISFACTORY
-

QUALITY, FITNESS FOR A PARTICULAR PURPOSE, USABILITY, INTEGRATION OR NON-INFRINGEMENT AND ALL SUCH WARRANTIES ARE HEREBY EXCLUDED BY WILEY AND ITS LICENSORS AND WAIVED BY YOU.

- WILEY shall have the right to terminate this Agreement immediately upon breach of this Agreement by you.
  - You shall indemnify, defend and hold harmless WILEY, its Licensors and their respective directors, officers, agents and employees, from and against any actual or threatened claims, demands, causes of action or proceedings arising from any breach of this Agreement by you.
  - IN NO EVENT SHALL WILEY OR ITS LICENSORS BE LIABLE TO YOU OR ANY OTHER PARTY OR ANY OTHER PERSON OR ENTITY FOR ANY SPECIAL, CONSEQUENTIAL, INCIDENTAL, INDIRECT, EXEMPLARY OR PUNITIVE DAMAGES, HOWEVER CAUSED, ARISING OUT OF OR IN CONNECTION WITH THE DOWNLOADING, PROVISIONING, VIEWING OR USE OF THE MATERIALS REGARDLESS OF THE FORM OF ACTION, WHETHER FOR BREACH OF CONTRACT, BREACH OF WARRANTY, TORT, NEGLIGENCE, INFRINGEMENT OR OTHERWISE (INCLUDING, WITHOUT LIMITATION, DAMAGES BASED ON LOSS OF PROFITS, DATA, FILES, USE, BUSINESS OPPORTUNITY OR CLAIMS OF THIRD PARTIES), AND WHETHER OR NOT THE PARTY HAS BEEN ADVISED OF THE POSSIBILITY OF SUCH DAMAGES. THIS LIMITATION SHALL APPLY NOTWITHSTANDING ANY FAILURE OF ESSENTIAL PURPOSE OF ANY LIMITED REMEDY PROVIDED HEREIN.
  - Should any provision of this Agreement be held by a court of competent jurisdiction to be illegal, invalid, or unenforceable, that provision shall be deemed amended to achieve as nearly as possible the same economic effect as the original provision, and the legality, validity and enforceability of the remaining provisions of this Agreement shall not be affected or impaired thereby.
  - The failure of either party to enforce any term or condition of this Agreement shall not constitute a waiver of either party's right to enforce each and every term and condition of this Agreement. No breach under this agreement shall be deemed waived or excused by either party unless such waiver or consent is in writing signed by the party granting such waiver or consent. The waiver by or consent of a party to a breach of any provision of this Agreement shall not operate or be construed as a waiver of or consent to any other or subsequent breach by such other party.
  - This Agreement may not be assigned (including by operation of law or otherwise) by you without WILEY's prior written consent.
  - Any fee required for this permission shall be non-refundable after thirty (30) days from receipt by the CCC.
  - These terms and conditions together with CCC's Billing and Payment terms and conditions (which are incorporated herein) form the entire agreement between you and WILEY concerning this licensing transaction and (in the absence of fraud) supersedes all prior agreements and representations of the parties, oral or written. This Agreement may not be amended except in writing signed by both parties. This Agreement shall be binding upon and inure to the benefit of the parties' successors, legal representatives, and authorized assigns.
  - In the event of any conflict between your obligations established by these terms and conditions and those established by CCC's Billing and Payment terms and conditions,
-



these terms and conditions shall prevail.

- WILEY expressly reserves all rights not specifically granted in the combination of (i) the license details provided by you and accepted in the course of this licensing transaction, (ii) these terms and conditions and (iii) CCC's Billing and Payment terms and conditions.
- This Agreement will be void if the Type of Use, Format, Circulation, or Requestor Type was misrepresented during the licensing process.
- This Agreement shall be governed by and construed in accordance with the laws of the State of New York, USA, without regards to such state's conflict of law rules. Any legal action, suit or proceeding arising out of or relating to these Terms and Conditions or the breach thereof shall be instituted in a court of competent jurisdiction in New York County in the State of New York in the United States of America and each party hereby consents and submits to the personal jurisdiction of such court, waives any objection to venue in such court and consents to service of process by registered or certified mail, return receipt requested, at the last known address of such party.

#### WILEY OPEN ACCESS TERMS AND CONDITIONS

Wiley Publishes Open Access Articles in fully Open Access Journals and in Subscription journals offering Online Open. Although most of the fully Open Access journals publish open access articles under the terms of the Creative Commons Attribution (CC BY) License only, the subscription journals and a few of the Open Access Journals offer a choice of Creative Commons Licenses. The license type is clearly identified on the article.

##### **The Creative Commons Attribution License**

The [Creative Commons Attribution License \(CC-BY\)](#) allows users to copy, distribute and transmit an article, adapt the article and make commercial use of the article. The CC-BY license permits commercial and non-

##### **Creative Commons Attribution Non-Commercial License**

The [Creative Commons Attribution Non-Commercial \(CC-BY-NC\) License](#) permits use, distribution and reproduction in any medium, provided the original work is properly cited and is not used for commercial purposes.(see below)

##### **Creative Commons Attribution-Non-Commercial-NoDerivs License**

The [Creative Commons Attribution Non-Commercial-NoDerivs License](#) (CC-BY-NC-ND) permits use, distribution and reproduction in any medium, provided the original work is properly cited, is not used for commercial purposes and no modifications or adaptations are made. (see below)

##### **Use by commercial "for-profit" organizations**

Use of Wiley Open Access articles for commercial, promotional, or marketing purposes requires further explicit permission from Wiley and will be subject to a fee.

Further details can be found on Wiley Online Library








<http://olabout.wiley.com/WileyCDA/Section/id-410895.html>

#### **Other Terms and Conditions:**

v1.10 Last updated September 2015

Questions? [customercare@copyright.com](mailto:customercare@copyright.com) or +1-855-239-3415 (toll free in the US) or +1-978-646-2777.

---

**Title:** Organocatalytic Enantioselective Alkylation of Aldehydes with [Fe(bpy)<sub>3</sub>]Br<sub>2</sub> Catalyst and Visible Light

**Author:** Andrea Gualandi, Marianna Marchini, Luca Mengozzi, et al

**Publication:** ACS Catalysis

**Publisher:** American Chemical Society

**Date:** Oct 1, 2015

Copyright © 2015, American Chemical Society

[LOGIN](#)

If you're a [copyright.com](#) user, you can login to RightsLink using your [copyright.com](#) credentials. Already a [RightsLink user](#) or want to learn more?

**PERMISSION/LICENSE IS GRANTED FOR YOUR ORDER AT NO CHARGE**

This type of permission/license, instead of the standard Terms & Conditions, is sent to you because no fee is being charged for your order. Please note the following:

- Permission is granted for your request in both print and electronic formats, and translations.
- If figures and/or tables were requested, they may be adapted or used in part.
- Please print this page for your records and send a copy of it to your publisher/graduate school.
- Appropriate credit for the requested material should be given as follows: "Reprinted (adapted) with permission from (COMPLETE REFERENCE CITATION). Copyright (YEAR) American Chemical Society." Insert appropriate information in place of the capitalized words.
- One-time permission is granted only for the use specified in your request. No additional uses are granted (such as derivative works or other editions). For any other uses, please submit a new request.

[BACK](#)[CLOSE WINDOW](#)

Copyright © 2017 Copyright Clearance Center, Inc. All Rights Reserved. [Privacy statement](#); [Terms and Conditions](#); Comments? We would like to hear from you. E-mail us at [customercare@copyright.com](mailto:customercare@copyright.com)



# Bibliography

- [1] Newton, I. *Philosophical Transactions of the Royal Society* **1671**, 80, 3075–3087.
- [2] Huygens, C. *Traité de la lumière: avec, un discours de la pesanteur* **1690**,
- [3] Maxwell, J. C. *A Treatise on Electricity And Magnetism*; Oxford: Clarendon Press, 1873; p 504.
- [4] Maxwell, J. C. On Faraday's Lines of Force. *Transactions of the Cambridge Philosophical Society* **1856**, X.
- [5] Maxwell, On the physical lines of magnetic force. 1861.
- [6] Maxwell, J. A Dynamical Theory of the Electromagnetic Field. *Proceedings of the Royal Society of ...* **1863**, 459–512.
- [7] Einstein, A. Über einen die Erzeugung und Verwandlung des Lichtes betreffenden heuristischen Gesichtspunkt. *Annalen der Physik* **1905**, 17, 132–148.
- [8] Lewis, G. The Conservation of Photons. *Nature* **1926**, 118, 874–875.
- [9] Pringsheim, P.; Vogels, H. No Title. *J. de Chim. Physique* **1936**, 33, 395.
- [10] Lewis, G.; Lipkin, D.; Magel, T. Reversible Photochemical Processes in Rigid Media . A Study of the Phosphorescent State. *J. Am. Chem. Soc.* **1941**, 920.
- [11] Mattia, E.; Otto, S. Supramolecular systems chemistry. *Nature Publishing Group* **2015**, 10, 111–119.
- [12] Ragazzon, G.; Baroncini, M.; Silvi, S.; Venturi, M.; Credi, A. Light-powered autonomous and directional molecular motion of a dissipative self-assembling system. *Nature Nanotechnology* **2014**, 10, 70–75.
- [13] Balzani, V.; Scandola, F. *Supramolecular photochemistry*; Ellis Horwood Series in Physical Chemistry, 1991.

- [14] Monk, P. M. *The Viologens: Physicochemical Properties, Synthesis and Application of 4-4'-Bipyridine*; Wiley, New York, 1998.
- [15] Ronconi, C. M.; Stoddart, J. F.; Balzani, V.; Baroncini, M.; Ceroni, P.; Giannante, C.; Venturi, M. Polyviologen dendrimers as hosts and charge-storing devices. *Chemistry - A European Journal* **2008**, *14*, 8365–8373.
- [16] Freitag, M.; Galoppini, E. Cucurbituril Complexes of Viologens Bound to TiO<sub>2</sub> Films. *Langmuir* **2010**, *26*, 8262–8269.
- [17] Kosower, E. M.; Cotter, J. L. Stable Free Radicals. II. The Reduction of 1-Methyl-4-cyanopyridinium Ion to Methylviologen Cation Radical. *Journal of the American Chemical Society* **1964**, *86*, 5524–5527.
- [18] Buck, A. T.; Paletta, J. T.; Khindurangala, S. A.; Beck, C. L.; Winter, A. H. A noncovalently reversible paramagnetic switch in water. *Journal of the American Chemical Society* **2013**, *135*, 10594–10597.
- [19] Kim, H.-J.; Jeon, W. S.; Ko, Y. H.; Kim, K. Inclusion of methylviologen in cucurbit[7]uril. *Proceedings of the National Academy of Sciences of the United States of America* **2002**, *99*, 5007–5011.
- [20] Mayhew, S. G.; Müller, F. Dimerization of the radical cation of Benzyl Viologen in aqueous solution. *Biochemical Society Transactions* **1982**, *10*, 176.2–177.
- [21] Zhang, L.; Zhou, T.-Y.; Tian, J.; Wang, H.; Zhang, D.-W.; Zhao, X.; Liu, Y.; Zhan-Ting, L. Two-dimensional single-layer supramolecular organic framework that is driven by viologen radical cation dimerization and further promoted by cucurbit[8]uril. *Polymer Chemistry* **2014**, *5*, 4715–4721.
- [22] Zhang, D. W.; Tian, J.; Chen, L.; Zhang, L.; Li, Z. T. Dimerization of conjugated radical cations: An emerging non-covalent interaction for self-assembly. *Chemistry - An Asian Journal* **2015**, *10*, 56–68.
- [23] Kaifer, A. E.; Bard, A. J. Micellar effects on the reductive electrochemistry of methylviologen. *The Journal of Physical Chemistry* **1985**, *89*, 4876–4880.
- [24] Jeon, W. S.; Kim, H.-J.; Lee, C.; Kim, K. Control of the stoichiometry in host-guest complexation by redox chemistry of guests: inclusion of methylviologen in cucurbit[8]uril. *Chemical communications (Cambridge, England)* **2002**, 1828–1829.

- [25] Park, J. W.; Choi, N. H.; Kim, J. H. Facile Dimerization of Viologen Radical Cations Covalently Bonded to  $\beta$ -Cyclodextrin and Suppression of the Dimerization by  $\beta$ -Cyclodextrin and Amphiphiles. *The Journal of Physical Chemistry* **1996**, *100*, 769–774.
- [26] Trabolsi, A.; Khashab, N.; Fahrenbach, A. C.; Friedman, D. C.; Colvin, M. T.; Cotí, K. K.; Benítez, D.; Tkatchouk, E.; Olsen, J.-C.; Belowich, M. E.; Carmielli, R.; Khatib, H. a.; Goddard, W. a.; Wasielewski, M. R.; Stoddart, J. F. Radically enhanced molecular recognition. *Nature chemistry* **2010**, *2*, 42–49.
- [27] Heinen, S.; Walder, L. Generation-dependent intramolecular CT complexation in a dendrimer electron sponge consisting of a viologen skeleton. *Angewandte Chemie - International Edition* **2000**, *39*, 806–809.
- [28] Bergamini, G.; Fermi, A.; Marchini, M.; Locritani, M.; Credi, A.; Venturi, M.; Negri, F.; Ceroni, P.; Baroncini, M. A highly luminescent tetramer from a weakly emitting monomer: acid- and redox-controlled multiple complexation by cucurbit[7]uril. *Chemistry (Weinheim an der Bergstrasse, Germany)* **2014**, *20*, 7054–7060.
- [29] Tsukahara, K.; Wilkins, R. G. Kinetics of reduction of eight viologens by dithionite ion. *Journal of the American Chemical Society* **1985**, *107*, 2632–2635.
- [30] Geuder, Wolfram; Hunig, Siegfried; Suchy, A. Single and Double Bridged Viologens and Intramolecular Pimerization of their Cation Radicals. *Tetrahedron* **1986**, *42*, 1665–1677.
- [31] Neta, P.; Richoux, M.-C.; Harriman, A. Intramolecular association of covalently linked viologen radicals. *Journal of the Chemical Society, Faraday Transactions 2* **1985**, *81*, 1427.
- [32] Rieger, A. L.; Rieger, P. H. Magnetic resonance studies of some bipyridylium dication and cation radicals. *The Journal of Physical Chemistry* **1984**, *88*, 5845–5851.
- [33] Bockman, T. M.; Kochi, J. K. Isolation and oxidation-reduction of methylviologen cation radicals. Novel disproportionation in charge-transfer salts by x-ray crystallography. *The Journal of Organic Chemistry* **1990**, *55*, 4127–4135.
- [34] Abe, M. Diradicals. *Chemical Reviews* **2013**, *113*, 7011–7088.

- [35] Venturi, M.; Mulazzani, Q. G.; Hoffman, M. Z. Radiolytically induced one-electron reduction of methylviologen in aqueous solution. Platinum-catalyzed formation of dihydrogen. *Journal of Physical Chemistry* **1984**, *88*, 912–918.
- [36] Venturi, M.; Mulazzani, Q. G.; Hoffman, M. Z. Radiolytically-induced one-electron reduction of methyl viologen in aqueous solution. *Radiat. Phys. Chem.* **1984**, *23*, 229–236.
- [37] Buxton, G. V.; Greenstock, C. L.; Helman, W. P.; Ross, A. B. Critical Review of rate constants for reactions of hydrated electrons, hydrogen atoms and hydroxyl radicals in aqueous solution. *Journal of Physical and Chemical Reference Data* **1988**, *17*, 513.
- [38] De Greef, T. F. A.; Smulders, M. M. J.; Wolffs, M.; Schenning, A. P. H. J.; Sijbesma, R. P.; Meijer, E. W. Supramolecular polymerization. *Chemical Reviews* **2009**, *109*, 5687–5754.
- [39] Bonchio, M.; Carraro, M.; Casella, G.; Causin, V.; Rastrelli, F.; Saielli, G. Thermal behaviour and electrochemical properties of bis(trifluoromethanesulfonyl)amide and dodecatungstosilicate viologen dimers. *Physical Chemistry Chemical Physics* **2012**, *14*, 2710.
- [40] Porter, W. W.; Vaid, T. P. Isolation and characterization of phenyl viologen as a radical cation and neutral molecule. *Journal of Organic Chemistry* **2005**, *70*, 5028–5035.
- [41] Kahlfuss, C.; Méta y, E.; Duclos, M. C.; Lemaire, M.; Oltean, M.; Milet, A.; Saint-Aman, É.; Bucher, C. Reversible dimerization of viologen radicals covalently linked to a calixarene platform: Experimental and theoretical aspects. *Comptes Rendus Chimie* **2014**, *17*, 505–511.
- [42] Diring, S.; Puntoriero, F.; Nastasi, F.; Campagna, S.; Ziessel, R. Star-shaped multichromophoric arrays from bodipy dyes grafted on truxene core. *Journal of the American Chemical Society* **2009**, *131*, 6108–6110.
- [43] Bura, T.; Gullo, M. P.; Ventura, B.; Barbieri, A.; Ziessel, R. Multichromophoric arrays arranged around a triptycene scaffold: Synthesis and photophysics. *Inorganic Chemistry* **2013**, *52*, 8653–8664.
- [44] Prodi, A.; Indelli, M. T.; Kleverlaan, C. J.; Scandola, F.; Alessio, E.; Gianferrara, T.; Marzilli, L. G. Side-to-Face Ruthenium Porphyrin Arrays:

- Photophysical Behavior of Dimeric and Pentameric Systems. *Chemistry - A European Journal* **1999**, *5*, 2668–2679.
- [45] Nenajdenko, V. *Fluorine in Heterocyclic Chemistry Volume 1*; Springer International Publishing, 2014.
- [46] Antipas, A.; Buchler, J. W.; Gouterman, M.; Smith, P. D. Porphyrins. 36. Synthesis and optical and electronic properties of some ruthenium and osmium octaethylporphyrins. *Journal of the American Chemical Society* **1978**, *100*, 3015–3024.
- [47] Kalyanasundaram, K. *Photochemistry of Polypyridine and Porphyrin Complexes*; ACADEMIC PRESS, INC., 1992.
- [48] Johnson Jr., C. S. Diffusion ordered nuclear magnetic resonance spectroscopy: principles and applications. *Progress in Nuclear Magnetic Resonance Spectroscopy* **1999**, *34*, 203–256.
- [49] Macchioni, A.; Ciancaleoni, G.; Zuccaccia, C.; Zuccaccia, D. Determining accurate molecular sizes in solution through NMR diffusion spectroscopy. *Chem. Soc. Rev.* **2008**, 479–489.
- [50] Sakamoto, J.; Van Heijst, J.; Lukin, O.; Schlüter, A. D. Two-dimensional polymers: Just a dream of synthetic chemists? *Angewandte Chemie - International Edition* **2009**, *48*, 1030–1069.
- [51] Kissel, P.; Erni, R.; Schweizer, W. B.; Rossell, M. D.; King, B. T.; Bauer, T.; Götzinger, S.; Schlüter, a. D.; Sakamoto, J. A two-dimensional polymer prepared by organic synthesis. *Nature Chemistry* **2012**, *4*, 287–291.
- [52] Roberts, G. *Langmuir-Blodgett Films*; Springer, 1990.
- [53] Braslau, A.; Deutsch, M.; Pershan, P. S.; Weiss, A. H.; Als-Nielsen, J.; Bohr, J. Surface roughness of water measured by x-ray reflectivity. *Physical Review Letters* **1985**, *54*, 114–117.
- [54] Cabani, S.; Landucci, M. Stability of Zinc(II)- and Nickel(II)-2,2'-Biipyridyl. *Journal of the Chemical Society* **1962**, 278–282.
- [55] Oza, A. Nickel complexes of 1,10-phenanthroline and 2,2'-bipyridyl with strong intermolecular interactions. *Crystal Research and Technology* **1988**, *23*, 385–391.

- [56] Arora, H.; Philouze, C.; Jarjayes, O.; Thomas, F. Co(II), Ni(II), Cu(II) and Zn(II) complexes of a bipyridine bis-phenol conjugate: generation and properties of coordinated radical species. *Dalton Transactions* **2010**, 39, 10088–10098.
- [57] Griend, D. A. V.; Bediako, D. K.; Devries, M. J.; Dejong, N. A.; Heeringa, L. P. Detailed Spectroscopic, Thermodynamic, and Kinetic Characterization of Nickel(II) Complexes with 2,2'-Bipyridine and 1,10-Phenanthroline Attained via Equilibrium-Restricted Factor Analysis. *Inorganic Chemistry* **2008**, 47, 656–662.
- [58] Chou, H.; Chen, C.-T.; Stork, K. F.; Bohn, P. W.; Suslick, K. S. Langmuir-Blodgett Films of Amphiphilic Push-Pull Porphyrins. *The Journal of Physical Chemistry* **1994**, 98, 383–385.
- [59] Marcus, R. A.; Sutin, N. Electron transfers in chemistry and biology. *BBA Reviews On Bioenergetics* **1985**, 811, 265–322.
- [60] Romero, N. A.; Nicewicz, D. A. Organic Photoredox Catalysis. *Chemical Reviews* **2016**, acs.chemrev.6b00057.
- [61] Cismesia, M. A.; Yoon, T. P. Characterizing chain processes in visible light photoredox catalysis. *Chem. Sci.* **2015**, 6, 5426–5434.
- [62] Arceo, E.; Jurberg, I. D.; Alvarez-Fernández, A.; Melchiorre, P. Photochemical activity of a key donor-acceptor complex can drive stereoselective catalytic  $\alpha$ -alkylation of aldehydes. *Nature chemistry* **2013**, 5, 750–6.
- [63] Schultz, D. M.; Yoon, T. P. Solar Synthesis: Prospects in Visible Light Photocatalysis. *Science* **2014**, 343, 1239176.
- [64] Shaw, M. H.; Twilton, J.; MacMillan, D. W. C. Photoredox Catalysis in Organic Chemistry. *The Journal of Organic Chemistry* **2016**, 81, 6898–6926.
- [65] Narayanam, J. M. R.; Stephenson, C. R. J. Visible light photoredox catalysis: applications in organic synthesis. *Chem. Soc. Rev.* **2011**, 40, 102–113.
- [66] Hari, D. P.; Schroll, P.; König, B. Metal-free, visible-light-mediated direct C-H arylation of heteroarenes with aryl diazonium salts. *Journal of the American Chemical Society* **2012**, 134, 2958–2961.

- [67] Pitre, S. P.; McTiernan, C. D.; Scaiano, J. C. Understanding the Kinetics and Spectroscopy of Photoredox Catalysis and Transition-Metal-Free Alternatives. *Accounts of Chemical Research* **2016**, *49*, 1320–1330.
- [68] Hedstrand, D. M.; Kruizinga, W. H.; Kellogg, R. M. Light induced and dye accelerated reductions of phenacyl onium salts by 1,4-dihydropyridines. *Tetrahedron Letters* **1978**, *19*, 1255–1258.
- [69] Juris, A.; Balzani, V.; Barigelletti, F.; Campagna, S.; Belser, P.; von Zelewsky, A. Ru(II) polypyridine complexes: photophysics, photochemistry, electrochemistry, and chemiluminescence. *Coordination Chemistry Reviews* **1988**, *84*, 85–277.
- [70] Nguyen, J. D.; D'Amato, E. M.; Narayanam, J. M. R.; Stephenson, C. R. J. Engaging unactivated alkyl, alkenyl and aryl iodides in visible-light-mediated free radical reactions. *Nature Chemistry* **2012**, *4*, 854–859.
- [71] MacMillan, D. W. C.; Cuthbertson, J. D.; Terrett, J. A.; Shurtleff, V. W.; Shaw, M. H. Native functionality in triple catalytic cross-coupling: sp<sup>3</sup>-C-H bonds as latent nucleophiles. *Science* **2016**, *352*, 1304–1308.
- [72] Hernandez-Perez, A. C.; Collins, S. K. Heteroleptic Cu-Based Sensitizers in Photoredox Catalysis. *Accounts of Chemical Research* **2016**, *49*, 1557–1565.
- [73] Fischer, E.; Jourdan, F. Ueber die Hydrazine der Brenztraubensäure. *Berichte der deutschen chemischen Gesellschaft* **1883**, *16*, 2241–2245.
- [74] Katritzky, A. R.; Akutagawa, K.; Jones, R. A. Carbon Dioxide: A Reagent for the Protection of Nucleophilic Centres and the Simultaneous Activation to Electrophilic Attack-Part Xii. One-Pot Conversion of 3-Methylindole into 2-Formyl-3-Methylindole. *Synthetic Communications* **1988**, *18*, 1151–1158.
- [75] Kandukuri, S. R.; Bahamonde, A.; Chatterjee, I.; Jurberg, I. D.; Escudero-Adán, E. C.; Melchiorre, P. X-ray characterization of an electron donor-acceptor complex that drives the photochemical alkylation of indoles. *Angewandte Chemie - International Edition* **2015**, *54*, 1485–1489.

- [76] Devery III, J. J.; Douglas, J. J.; Nguyen, J. D.; Cole, K. P.; Flowers II, R. A.; Stephenson, C. R. J. Ligand functionalization as a deactivation pathway in a fac-Ir(ppy)<sub>3</sub>-mediated radical addition. *Chem. Sci.* **2015**, *6*, 537–541.
- [77] Mitani, M.; Kuratate, T. Addition Reaction of Polychloro Compounds to Carbon-Carbon Multiple Bonds Catalyzed by Semiconductor Particles under Photoirradiation. *Journal of Organic Chemistry* **1994**, *59*, 1279–1282.
- [78] Fukui, K.; Morokuma, K.; Kato, H.; Yonezawa, T. The polarographic reduction and electronic structures of organic halides. *Bull. Chem. Soc. Japan* **1963**, *36*, 217–222.
- [79] Yang, Q. Q.; Marchini, M.; Xiao, W. J.; Ceroni, P.; Bandini, M. Visible-Light-Induced Direct Photocatalytic Carboxylation of Indoles with CBr<sub>4</sub>/MeOH. *Chemistry - A European Journal* **2015**, *21*, 18052–18056.
- [80] Mukherjee, S.; Yang, J. W.; Hoffmann, S.; List, B. Asymmetric enamine catalysis. *Chemical Reviews* **2007**, *107*, 5471–5569.
- [81] Nicewicz, D. A.; Macmillan, D. W. C. Merging photoredox catalysis with organocatalysis: the direct asymmetric alkylation of aldehydes. *Science* **2008**, *322*, 77–80.
- [82] Huo, H.; Shen, X.; Wang, C.; Zhang, L.; Röse, P.; Chen, L.-A.; Harms, K.; Marsch, M.; Hilt, G.; Meggers, E. Asymmetric photoredox transition-metal catalysis activated by visible light. *Nature* **2014**, *515*, 100–3.
- [83] Paria, S.; Reiser, O. Copper in photocatalysis. *ChemCatChem* **2014**, *6*, 2477–2483.
- [84] Stevenson, S. M.; Shores, M. P.; Ferreira, E. M. Photooxidizing chromium catalysts for promoting radical cation cycloadditions. *Angewandte Chemie - International Edition* **2015**, 6506–6510.
- [85] Cannizzo, A.; Milne, C. J.; Consani, C.; Gawelda, W.; Bressler, C.; van Mourik, F.; Chergui, M. Light-induced spin crossover in Fe(II)-based complexes: The full photocycle unraveled by ultrafast optical and X-ray spectroscopies. *Coordination Chemistry Reviews* **2010**, *254*, 2677–2686.



- [86] Ferrere, S. New Photosensitizers Based upon  $[\text{Fe}(\text{L})_2(\text{CN})_2]$  and  $[\text{Fe}(\text{L})_3]$  (L) Substituted 2,2'-Bipyridine :Yields for the Photosensitization of  $\text{TiO}_2$  and Effects on the Band Selectivity. *Comparative and General Pharmacology* **2000**, *2*, 1083–1089.
- [87] Nicewicz, D. A.; MacMillan, D. W. C. Merging photoredox catalysis with organocatalysis: the direct asymmetric alkylation of aldehydes. *Science (New York, N.Y.)* **2008**, *322*, 77–80.
- [88] Pandey, G.; Karthikeyan, M.; Murugan, a. New Intramolecular  $\alpha$ -Arylation Strategy of Ketones by the Reaction of Silyl Enol Ethers to Photosensitized Electron Transfer Generated Arene Radical Cations: Construction of Benzannulated and Benzospiroannulated Compounds. *The Journal of Organic Chemistry* **1998**, *63*, 2867–2872.
- [89] Manfrotto, C.; Mella, M.; Freccero, M.; Fagnoni, M.; Albini, A. Photochemical Synthesis of 4-Oxobutanal Acetals and of 2-Hydroxycyclobutanone Ketals. *The Journal of Organic Chemistry* **1999**, *64*, 5024–5028.
- [90] Ohkubo, K.; Fujimoto, A.; Fukuzumi, S. Visible-light-induced oxygenation of benzene by the triplet excited state of 2,3-dichloro-5,6-dicyanop-p-benzoquinone. *Journal of the American Chemical Society* **2013**, *135*, 5368–5371.
- [91] Margrey, K. A.; Nicewicz, D. A. A General Approach to Catalytic Alkene Anti-Markovnikov Hydrofunctionalization Reactions via Acridinium Photoredox Catalysis. *Accounts of Chemical Research* **2016**, *49*, 1997–2006.
- [92] Keshari, T.; Yadav, V. K.; Srivastava, V. P.; Yadav, L. D. S. Visible light organophotoredox catalysis: a general approach to beta-keto sulfoxidation of alkenes. *Green Chem.* **2014**, *16*, 3986–3992.
- [93] Ghosh, I.; König, B. Chromoselective Photocatalysis: Controlled Bond Activation through Light-Color Regulation of Redox Potentials. *Angewandte Chemie - International Edition* **2016**, *55*, 7676–7679.
- [94] Pitre, S. P.; McTiernan, C. D.; Ismaili, H.; Scaiano, J. C. Mechanistic insights and kinetic analysis for the oxidative hydroxylation of arylboronic acids by visible light photoredox catalysis: A metal-free alternative. *Journal of the American Chemical Society* **2013**, *135*, 13286–13289.

- [95] Sundararajan, C.; Falvey, D. E. Photorelease of carboxylic acids, amino acids, and phosphates from N-alkylpicolinium esters using photosensitization by high wavelength laser dyes. *Journal of the American Chemical Society* **2005**, *127*, 8000–8001.
- [96] Indrajit Ghosh, Tamal Ghosh, Javier I. Bardagi, B. K. Reduction of aryl halides by consecutive visible light -induced electron transfer processes. *Science* **2014**, *346*, 725–728.
- [97] Adarsh, N.; Shanmugasundaram, M.; Avirah, R. R.; Ramaiah, D. Aza-BODIPY derivatives: Enhanced quantum yields of triplet excited states and the generation of singlet oxygen and their role as facile sustainable photooxygenation catalysts. *Chemistry - A European Journal* **2012**, *18*, 12655–12662.
- [98] Li, W.; Li, L.; Xiao, H.; Qi, R.; Huang, Y.; Xie, Z.; Jing, X.; Zhang, H. Iodo-BODIPY: a visible-light-driven, highly efficient and photostable metal-free organic photocatalyst. *RSC Advances* **2013**, *3*, 13417–13421.
- [99] Koziar, J. C.; Cowan, D. O. Photochemical Heavy-Atom Effects. *Accounts of chemical research* **1978**, *11*, 334–341.
- [100] Kharasch, M.; Jensen, E.; Urry, W. Addition of Carbon Tetrachloride and Chloroform to Olefins. **1945**, *102*, 128.
- [101] Wallentin, C. J.; Nguyen, J. D.; Finkbeiner, P.; Stephenson, C. R. J. Visible light-mediated atom transfer radical addition via oxidative and reductive quenching of photocatalysts. *Journal of the American Chemical Society* **2012**, *134*, 8875–8884.
- [102] Huang, L.; Zhao, J. Iodo-Bodipys as visible-light-absorbing dual-functional photoredox catalysts for preparation of highly functionalized organic compounds by formation of C-C bonds via reductive and oxidative quenching catalytic mechanisms. *RSC Adv.* **2013**, *3*, 23377–23388.
- [103] Zhang, X.-F.; Yang, X.; Niu, K.; Geng, H. Phosphorescence of BODIPY dyes. *Journal of Photochemistry and Photobiology A: Chemistry* **2014**, *285*, 16–20.
- [104] Zhao, J.; Xu, K.; Yang, W.; Wang, Z.; Zhong, F. The triplet excited state of Bodipy: formation, modulation and application. *Chem Soc Rev* **2015**, *44*, 8904–8939.

- [105] Natali, M.; Deponti, E. Photocatalytic hydrogen evolution with ruthenium polypyridine sensitizers: Unveiling the key factors to improve efficiencies. *Dalton Trans.* **2016**, 9136–9147.
- [106] Wallentin, C.-j.; Nguyen, J. D.; Finkbeiner, P.; Robert, C.; Stephenson, Visible Light-Mediated Atom Transfer Radical Addition via Oxidative and Reductive Quenching of Photocatalysts. *Journal of the American Chemical Society* **2012**, *134*, 8875–8884.
- [107] Devery, J. J.; Nguyen, J. D.; Dai, C.; Stephenson, C. R. J. Light-Mediated Reductive Debromination of Unactivated Alkyl and Aryl Bromides. *ACS Catalysis* **2016**, *6*, 5962–5967.
- [108] Pause, L.; Robert, M.; Savéant, J. M. Can single-electron transfer break an aromatic carbon - Heteroatom bond in one step? A novel example of transition between stepwise and concerted mechanisms in the reduction of aromatic iodides [5]. *Journal of the American Chemical Society* **1999**, *121*, 7158–7159.
- [109] Costentin, C.; Robert, M.; Save, J.-m. Cyrille Costentin, Marc Robert, and Jean-Michel Saveant. *Journal of the American Chemical Society* **2004**, 16051–16057.
- [110] Debreczeny, M. P.; Svec, W. A.; Marsh, E. M.; Wasielewski, M. R. Femtosecond optical control of charge shift within electron donor-acceptor arrays: An approach to molecular switches. *Journal of the American Chemical Society* **1996**, *118*, 8174–8175.
- [111] Gosztola, D.; Niemczyk, M. P.; Svec, W.; Lukas, a. S.; Wasielewski, M. R. Excited doublet states of electrochemically generated aromatic imide and diimide radical anions. *Journal of Physical Chemistry A* **2000**, *104*, 6545–6551.
- [112] Sun, G.; Ren, S.; Zhu, X.; Huang, M.; Wan, Y. Direct arylation of pyrroles via indirect electroreductive C-H functionalization using perylene bisimide as an electron-transfer mediator. *Organic Letters* **2016**, *18*, 544–547.
- [113] Tauber, M. J.; Kelley, R. F.; Giaimo, J. M.; Rybtchinski, B.; Wasielewski, M. R. Electron hopping in pi-stacked covalent and self-assembled perylene diimides observed by ENDOR spectroscopy. *Journal of the American Chemical Society* **2006**, *128*, 1782–1783.

- [114] Chen, S.-G.; Branz, H. M.; Eaton, S. S.; Taylor, P. C.; Cormier, R. a.; Gregg, B. a. Substitutional n-Type Doping of an Organic Semiconductor Investigated by Electron Paramagnetic Resonance Spectroscopy. *The Journal of Physical Chemistry B* **2004**, *108*, 17329–17336.
- [115] Crosby, G. A.; Demas, J. N. Measurement of photoluminescence quantum yields. Review. *Journal of Physical Chemistry* **1971**, *75*, 991–1024.
- [116] Würth, C.; Grabolle, M.; Pauli, J.; Spieles, M.; Resch-genger, U. Relative and absolute determination of fluorescence quantum yields of transparent samples. *Nature protocols* **2013**, *8*, 1535–50.
- [117] Hatchard, C. G.; Parker, C. A. A New Sensitive Chemical Actinometer. II. Potassium Ferrioxalate as a Standard Chemical Actinometer. *Proceedings of the Royal Society of London A: Mathematical, Physical and Engineering Sciences* **1956**, *235*, 518–536.
- [118] Bard, A. J.; Faulkner, L. R. *Electrochemical Methods: Fundamentals and Applications, 2nd Edition*; Wiley, New York, 1980.
- [119] Ceroni, P.; Credi, A.; Venturi, M. *Analytical Methods in Supramolecular Chemistry, Electrochemical Methods*; Wiley, New York, 2012.
- [120] Wolfgang Kaim, A. K. *Spectroelectrochemistry*; 2008; pp 31–37.
- [121] Binnig, G.; Quate, C. F. Atomic Force Microscope. *Physical Review Letters* **1986**, *56*, 930–933.
- [122] Cappella, B.; Dietler, G. Force-distance curves by atomic force microscopy. *Surface Science Reports* **1999**, *34*, 1–104.
- [123] Rao, A.; Schoenenberger, M.; Gnecco, E.; Glatzel, T.; Meyer, E.; Brändlin, D.; Scandella, L. Characterization of nanoparticles using Atomic Force Microscopy. *Journal of Physics: Conference Series* **2007**, *61*, 971–976.
- [124] Bindell, J. In *Scanning Electron Microscopy. Encyclopedia of Materials Characterization: Surfaces, Interfaces, Thin Films*; Brundle, R., Evans, C., Eds.; Manning Publication Company, 1992.
- [125] Spothem-Maurizot, M., Mostafavi, M., Douki, T., Belloni, J., Eds. *Radiation Chemistry: from basics to applications in material and life science*; EDP Sciences Collection, 2008.

- 
- [126] Spinks, W. T.; Woods, R. J. *An Introduction to Radiation Chemistry*; Wiley, New York, 1990; p 100.
- [127] Buxton, G. V.; Stuart, C. R. Re-evaluation of the thiocyanate dosimeter for pulse radiolysis. *Journal of the Chemical Society, Faraday Transactions* **1995**, *91*, 279.